Dissertation

submitted to the

Combined Faculty of Mathematics, Engineering and

Natural Sciences

of Heidelberg University, Germany

for the degree of

Doctor of Natural Sciences

Put forward by

Wuji Wang

born in: Beijing, China

Oral examination: 18th July 2024

Three-dimensional view of circumgalactic to interstellar medium around distant radio galaxies

Referees: Dr. Dominika Wylezalek

Prof. Dr. Jochen Heidt

Abstract

High-redshift radio galaxies (HzRGs, $z \gtrsim 2$) represent a unique population of luminous active galactic nuclei (AGN), enabling the simultaneous examination of jet-mode and radiative-mode feedback in massive galaxies. This thesis focuses on the gaseous medium from circumgalactic to interstellar medium (CGM to ISM) scales around the most well-observed HzRGs sample, leveraging multiwavelength 3D information from integral field spectrographs. The lives of galaxies are shaped both by internal processes and their environment. The ISM and CGM are thus key components in galaxy evolution as sites of energy exchange, chemical enrichment and material cycling. Using MUSE, I conducted the first systematic analysis of ~ 100 kpc intrinsic Lyα nebulae (corrected for H I absorption) for the eight HzRGs. Our characterization of CGM gas properties enables a cross-comparison to different quasar species. The ISM within HzRGs however has remained poorly understood prior to the *JWST* era. I have analyzed the warm ionized gas on galactic scales using *JWST*/NIRSpec IFU with sub-kpc resolution, revealing inefficient radiatively driven outflows in one HzRG, potentially implying that jet-mode feedback dominates. Overall, this thesis initiates the 3D analysis of distant AGN, with legacy datasets spanning from the rest frame UV to far infrared (e.g., ALMA).

Zusammenfassung

Hochrotverschobene Radiogalaxien (HzRGs, $z \gtrsim 2$) sind eine einzigartige Population leuchtkräftiger aktiver galaktischer Kerne (AGN) und ermöglichen die gleichzeitige Untersuchung von Jet- und Strahlungsrückkopplungen in massereichen Galaxien. Diese Arbeit befasst sich mit dem gasförmigen Medium vom zirkumgalaktischen bis zum interstellaren Medium (CGM / ISM) rund um die am besten beobachteten HzRGs, wobei 3D Informationen über mehrere Wellenlängen aus integralen Feldspektrographen verwendet werden. Das Leben von Galaxien wird sowohl durch interne Prozesse als auch durch ihre Umgebung geprägt. Das ISM und das CGM sind daher Schlüsselkomponenten in der Galaxienentwicklung als Orte des Energieaustauschs, der chemischen Anreicherung und des Materialkreislaufs. Mit MUSE habe ich die erste systematische Analyse von ~ 100 kpc intrinsischen Lyα Nebeln (korrigiert für H I Absorption) für die acht HzRGs durchgeführt. Unsere Charakterisierung der CGM-Gaseigenschaften ermöglicht einen Vergleich mit verschiedenen Quasararten. Das ISM innerhalb von HzRGs ist jedoch vor der *JWST*-Ära nur wenig verstanden worden. Ich habe das warme ionisierte Gas auf galaktischen Skalen mit *JWST*/NIRSpec IFU Beobachtungen mit sub-kpc-Auflösung analysiert und dabei ineffiziente strahlungsgetriebene Winde in einem HzRG aufgedeckt, was möglicherweise bedeutet, dass die Rückkopplung im Jet-Modus dominiert. Insgesamt leitet diese Arbeit die 3D-Analyse von fernen AGN ein, wobei vorhandene Datensätze von UV-Ruhestrahlung bis zum fernen Infrarot (z. B. ALMA) reichen.

Contents

1 Introduction

1.1 Motivation

Curiosity drives the humankind to purely pursue the mystery of the universe. Once, the entire sky was thought to be a shield adorned with stars. Over generations, our understanding has continuously evolved. With advancements in observing techniques, astronomical knowledge has expanded rapidly: from Galileo Galilei's discovery of Jupiter's satellites over 420 years ago to Edwin Hubble's demonstration of the extragalactic nature of the "nebulae" just a century ago (Hubble, 1925, 1929), and most recently, the "imaging" of supermassive black holes (SMBHs) by the Event Horizon Telescope (EHT) Collaboration (Event Horizon Telescope Collaboration et al., 2022, 2019). Optical lenses have vastly improved our ability to collect photons compared to the naked human eye. Photographic devices, such as film and charge-coupled devices (CCDs), have unveiled deep fields of space. Furthermore, equipment capable of capturing the full electromagnetic spectrum and beyond (i.e., gravitational waves, Abbott et al., 2016) has revealed a much more colorful celestial world than the traditional optical view.

Information provided separately by imagery and spectroscopy is already rich. However, they do not tell the full story efficiently. The integral filed spectrograph (IFS) is the game changer, offering the ability to present a three-dimensional (3D) view simultaneously, which has been available since the 1980s (Bacon et al., 1988). Development accelerated shortly after its infancy (e.g., Allington-Smith et al., 2002; Bacon et al., 2001; Bundy et al., 2015; Davies et al., 2023; Eisenhauer et al., 2003; McDermid et al., 2006; McGregor et al., 2003; Morrissey et al., 2018; Sugai et al., 2004). Among them, the Multi-Unit Spectroscopic Explorer (MUSE, Bacon et al., 2010; Bacon et al., 2014) mounted on VLT, has revealed many aspects of the deep universe over the past decade, among other exciting discoveries. If we broaden the definition of IFS, the Atacama Large Millimeter/submillimeter Array (ALMA) perfectly meets the requirement of exploring space in 3D. In addition to ground-based facilities, the two IFS on board the James Webb Space Telescope (*JWST*) have just begun to refresh our view with their high sensitivity and previously inaccessible wavelength coverage. The given list is not intended to be exhaustive, as this thesis is not an overview of IFS (see Bacon & Monnet, 2017). One thing we know for sure is that IFS will continue to flourish in the future (e.g., Chapman et al., 2018; Thatte et al., 2021).

It is poetic to exchange space with time – a fundamental principle for high-redshift (or high-z) studies, validated by the finite speed of light. By peering into the early universe, we can trace galaxy formation and evolution across billions of years, aiding our understanding of the history of our current living world. In fact, one of the many important goals of IFS from the onset has been to investigate high-redshift galaxies (e.g, Adam et al., 1997; Petitjean et al., 1996). This is also the broad topic of this thesis, throughout which I will explore the evolution of some of the most massive galaxies in distant universe by combining observations from several of the most powerful integral filed units (IFUs). This exploration is crucial for understanding how our living universe has grown into its current shape.

Let's first take a simple look at this interesting phenomenon. The build-up of galaxies can be summarized as gravity pulling gas from intergalactic medium (IGM) to collapse and form stars in dark matter halos. However, numerous processes are at play, demanding scrutiny. Specifically, the study of galaxy evolution involves disentangling gas, dust, stellar populations, black holes and dark matters (see Figure 1.1, left panel, for a simple example). It is a dynamic process where inflow, outflow, and recycling of gas coexit; different stellar generations continuously enrich the medium; radiation and/or shocks from various sources excite and heat up the medium. Situations become more complicated when both actively accrecting SMBHs (active galactic nuclei or AGN[1]) and star formation occur simultaneously. It becomes even more puzzling when considering interactions between different neighboring galaxies and large-scale environments. On the other hand, it is convenient for us to have all these pieces ready for study at once. We choose to do it not because it is easy but because it is hard.

The high-redshift radio galaxies serve as the beacon for investigating the evolution of distant galaxies, offering a comprehensive package. Broadly speaking, they are rich in mysteries with numerous aspects for investigation, making them ideal principal objects for a series of doctoral theses (e.g., De Breuck, 2000; Drouart, 2013; Falkendal, 2018; Galametz, 2010; Gullberg, 2016; Humphrey, 2004; Kolwa, 2019; Kurk, 2003; McCarthy, 1988; Noirot, 2017; Overzier, 2006; Röttgering, 1993; Venemans, 2005; Vernet, 2001; Wylezalek, 2014, this list is not exhaustive). A more detailed introduction will be presented in Section 1.5, and additional information can be found in Sections 2.1, 3.1, and 4.1. The torch is now passed to this thesis work, revealing the gaseous medium around these distant radio galaxies by leveraging the state-of-the-art IFS.

[1]The acronym "AGN" represents both singular and plural forms.

1.2 AGN feedback and galactic medium

First, let's go through some of the key components and processes in the galaxy evolution:

AGN feedback

Evidence points to the prevalence of SMBHs at the centers of galaxies (e.g., Ho, 2008). The discovered relation between the mass of SMBHs ($M_\bullet$) and the stellar mass ($M_\star$) of their hosts implies the co-evolution (e.g., Kormendy & Ho, 2013). How are these two connected to each other despite being governed on physical scales spanning $\sim$8 to 9 orders of magnitude (i.e., a few lighthours verses tens of kiloparsecs)? As shown in Figure 1.1, gas from the reservoir in the dark matter halo fuels both the SMBHs and stars. The SMBHs can grow their mass through accretion. Simultaneously, during this activate phase, the so-called AGN release energy, which can exceed the binding energy of the host galaxies by a factor of $\sim$10 under simple assumptions (e.g., Fabian, 2012). This first-order calculation provides the foundation for the black hole-galaxy co-evolution. The processes where energy output by SMBHs affects the hosts are referred to as AGN feedback. It reduces the efficiency of baryons turning into stars at the higher M_halo end of the systems. The right panel of Figure 1.1 demonstrates this importance by showing the $M_\star/M_\mathrm{halo} - M_\mathrm{halo}$ relations from simulations with and without AGN feedback, as well as a semi-empirical relationship. Stars also assuredly have feedback (stellar feedback) onto the gas reservoir, which is beyond the scope of this thesis (Figure 1.1). In brief, feedback regulates the growth of the galaxies and shapes the universe into the current appearance. Here, we focus on the feedback from AGN.

The naming of AGN has a historical story, with many acronyms still used in up-to-date literature (Netzer, 2013). I do not intend to give a broad overview of what different names represent but only introduce here the ones relevant to the thesis that follows. Broadly speaking, quasars are the AGN with very high bolometric luminosity, i.e, $L_\mathrm{bol} > 10^{45}\,\mathrm{erg\,s^{-1}}$. Type-1 and type-2 are used to differentiate whether or not the broad component of emission lines, such as Balmer lines, (full width at half maximum, FWHM$\gtrsim 10000\,\mathrm{km\,s^{-1}}$) are identified in the spectra, respectively. Assuming the unification model (e.g., Antonucci, 1993), this indicates whether we are directly observing the broad line region (BLR) inside the AGN ionization cone or just the surrounding diffused narrow line region (NLR).

The AGN feedback takes various forms and affects the galactic medium both within and around the host galaxies, influencing star formation and black hole growth (both negatively and positively). Radiation from AGN can drive wind capable of launching multiphase outflows that clear gas, i.e., star formation fuels (e.g., Harrison et al., 2018; Harrison & Ramos Almeida, 2024; Silk & Rees, 1998). This so-called radiative-mode is particularly effective for AGN at high accretion rates, such as quasars. Conversely, the relativistic electron beams, i.e., jets, launched by black holes can also drive the outflows through shock-inflated

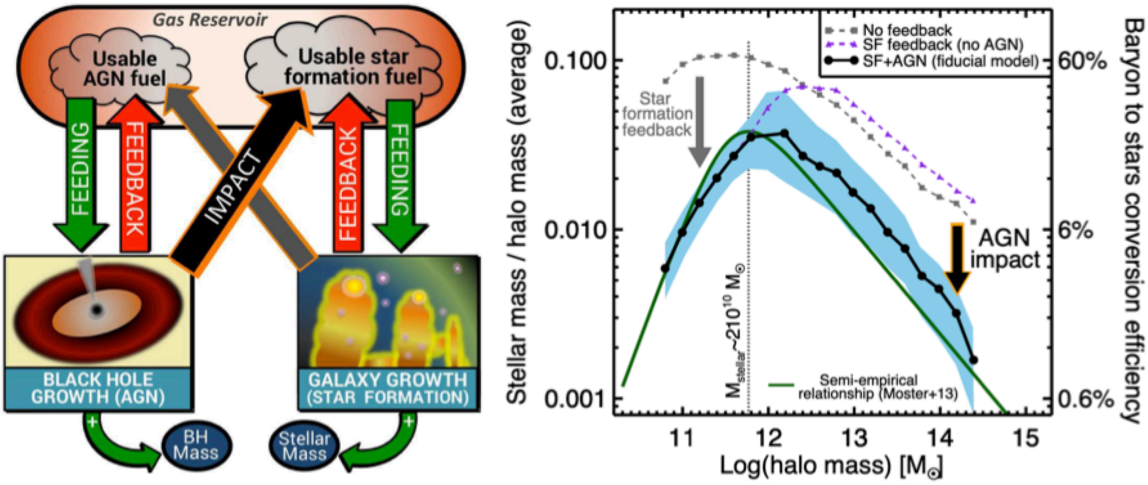

Figure 1.1. Demonstration of feedback processes and their impacts on galaxy formation and evolution. **Left**: A sketch summarizing the interplay between feedback and growth of the black hole and stellar masses. **Right**: Relation between $M_\star/M_{\rm halo}$ and $M_{\rm halo}$. The data are drawn from Somerville et al. (2008) simulations and the Moster et al. (2013) semi-empirical relationship. The figures are taken from Harrison (2017).

bubbles. The injected energy by either the jet or radiation pressure can still disturb the gas when it is not insufficient to accelerate the gas to escape the galactic potential well (e.g., Kukreti et al., 2023; Wagner et al., 2012). Additionally, AGN feedback can radiatively and/or kinetically heat up the gas. The cumulative effect of these processes impacts the gas reservoir and can quench star formation, preventing the appearance of excessively massive $M_\star$ (see Figure 1.1).

Galactic medium

On large scales (hundreds of Megaparsecs), the structure of our universe exhibits homogeneity as predicted by cosmological models and observed in both simulations and observations (e.g., Colless et al., 2001). Zooming in, we find filamentary structures known as cosmic web (see Figure 1.2 inset). At the node of the filaments, i.e., the deep gravitational potential well, galaxies and clusters of galaxies emerge (Umehata et al., 2019). This process is dynamic, involving gas infall, outflow, recycling, and many others scenarios acting together (see Figure 1.2).

It is useful to define the scope focused by this thesis. The gaseous halos around galaxies, particularly the circumgalactic medium (CGM, Tumlinson et al., 2017), play a crucial role in galaxy evolution: fueling galaxies and enduring their feedback. The CGM lacks well-defined boundaries on either side. Typically, we consider the virial radius of the dark matter halo surrounding the galaxy, $R_{\rm vir}$ ($\sim 100\,{\rm kpc}$ for dark halo mass $M_{\rm halo} \sim 10^{12}\,M_\star$, see e.g., Dekel et al., 2013), as the outer boundary beyond which we enter the IGM. Its inner boundary logically lies at the border of the interstellar medium (ISM, $r \sim 15\,\mathrm{kpc}$). Traditional ISM studies can focus on numerous details, disentangling the impacts from stellar populations and galactic nuclei (e.g., Lequeux, 2005; Osterbrock & Ferland, 2006). This thesis focuses on the high-z transition period (see Section 1.3), where current observational techniques cannot reach such resolution, but we are pushing the limits. Additionally, I am inspecting the dynamical processes originating at the galactic center and having effects over $100\,\mathrm{kpc}$, i.e., AGN feedback, for the most powerful species (see Section 1.5). Hence, there is no need for a hard separation, but referring to the objective as the galactic medium, which in our context leans more towards the CGM side.

Now, let's briefly introduce the contents of the galactic medium. Hydrogen, the most abundant element in the baryonic universe, is the major fuel for star formation. Typically, it exists in ionized, neutral and molecular gas phases (H II, H I and H_2). The cold gas phases, H I + H_2, are direct reservoirs for feeding galaxies. Various observational methods can be used to capture the surrounding gaseous medium of host galaxies (see Tumlinson et al., 2017). Lyman-α (Lyα) emission at $\lambda_{\mathrm{rest}} = 1215.67\,\mathrm{\AA}$ is one of the most important probes for studying the early universe, as its observed wavelength falls within the optical window ($z \gtrsim 2$, see Ouchi et al., 2020, for a review). This emission allows us to directly detect the hydrogen gas (H I and H II) around ionizing sources, such as AGN, without any prerequisites (e.g., alignment of background sources). Despite the resonant scattering of Lyα photons, which makes deciphering the global dynamics of hosts challenging, we can still map the emission halos at tens to hundreds of kiloparsecs (e.g., especially around quasars using IFS, Arrigoni Battaia et al., 2019; Cai et al., 2019; Cantalupo et al., 2014). In addition, we can access the distribution and motion of the H I, e.g, through absorption. For cold H_2, observations are typically conducted through proxies (such as CO and [C I] transitions, Carilli & Walter, 2013; Papadopoulos et al., 2004). Radio and sub/millimeter telescopes (VLA and ALMA) serve as ideal tools for detecting this direct star formation fuel (e.g., Riechers et al., 2019; Walter et al., 2014).

In addition to hydrogen, there are other important components in the galactic medium influence the growth of galaxies. Metals, in the astronomical context, represent elements heavier than helium, primarily produced in stellar evolution. Although not abundant in absolute mass fraction, metals play crucial roles in regulating the baryon cycle in the universe. Since the primordial nucleosynthesis and the evolution of Population III stars (extremely metal-poor stars), metals have been accumulated, enriching the galactic medium, and impacting the subsequent build-up of galaxies. Later stages of stellar evolution, such as red giants and supernovae, are directly related to metal ejection with ongoing synthesis. The AGN-driven feedback also contributes to metal redistribution (e.g., Bertemes et al., 2023).

Dust, the micrometer-sized grains, can significantly alter the observed electromagnetic spectra by absorbing and re-emitting photons. It shields the H_2 from destructive ultraviolet (UV) radiation, preserving environments conducive to star formation. For AGN, their dusty toruses are not only a key component in current theoretical model but also contribute a large fraction of the total emis-

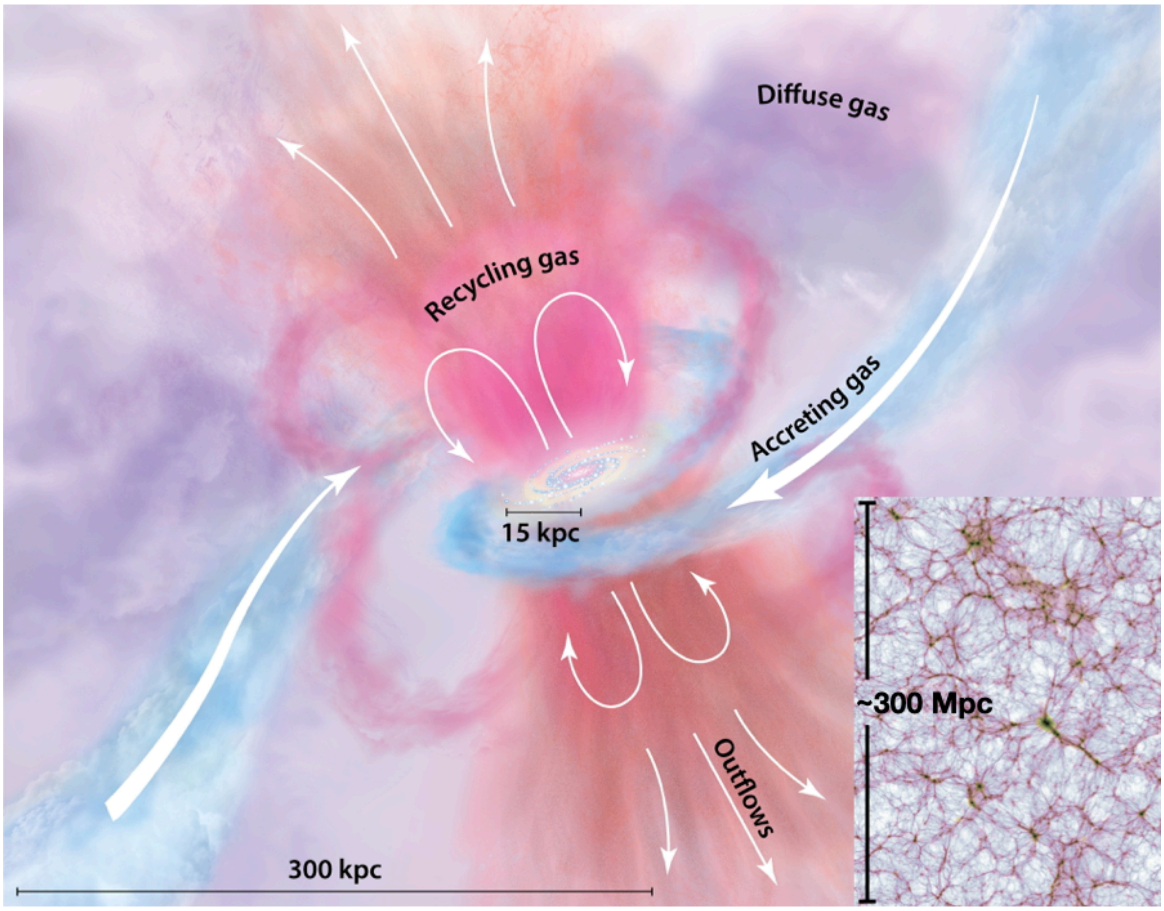

Figure 1.2. Illustration of the CGM gas and key processes. The IGM gas is being accreted onto the central host galaxy to fuel its star formation and black hole growth. The feedback processes are ejecting the gas back to the CGM through outflows. Gas without high velocity is then recycled back to the system. This figure is taken from Tumlinson et al. (2017). The inset shows simulated density distribution of baryons with the projected size of $\sim 300\,\mathrm{Mpc}$ (TNG300 from IllustrisTNG, Credit:TNG Collaboration).

sion in infrared spectral energy distribution (e.g., Beckmann & Shrader, 2012). Some quasar populations exhibit very red colors, highly obscured by dust (e.g., Tsai et al., 2015). From an evolutionary perspective, AGN activities may expel these obscuring materials, transitioning into subsequent stages. Therefore, understanding the full picture of galaxy evolution requires sorting through the various components of active galaxies as comprehensively as possible.

1.3 Cosmic high-Noon

In this section, we introduce a few key concepts of the period focused on in this thesis. Following the epoch of reionization (EoR, $z \sim 6$), the IGM becomes almost fully ionized and transparent to photons. The density of H I + H_2 remains relatively constant until the Cosmic Noon ($z \sim 2-3$), where the molecular gas density experiences a significant boost (Madau & Dickinson, 2014; Péroux & Howk, 2020). Cosmic Noon marks **the time** when the cosmic star formation rate (SFR) density reaches its peak, indicating a direct impact from the the evolution of gas density. Interestingly, the growth (accretion) history of SMBHs also mirrors this evolutionary trend of SFR density (e.g., Heckman & Best, 2014). Simply put, both phenomena are fueled by gas from the IGM through the CGM to ISM and beyond. Consequently, AGN activities also peak during this period, characterized by violent energy, momentum, and matter injection/exchanging. A reasonable deduction is that this feedback slows down star formation and decreases it from the Cosmic Noon to the our current time. This raises questions: How does the universe appear during the period between EoR and Cosmic Noon? What accelerates the feeding to the galaxies? Hence, it is intriguing to examine the **transitional period**, $z \sim 3-6$ (could be referred to as Cosmic high-Noon[2]), and understand how the medium transforms to the boost of H_2 density, leading to an acceleration of star formation.

The focus on the Cosmic high-Noon has been increasing. Recent observations have revealed a higher number density of AGN (e.g., Greene et al., 2024). Evidence suggests that main sequence star-forming galaxies are rich in gas, with a trend of decreasing dust density as redshift increases (Faisst et al., 2020a,b), which may be related to the enrichment history of the galactic medium. Additionally, quenched massive galaxies are detected during this period, exhibiting a deficient gas fraction that appears to be depleted within hundreds of million years (e.g., Suzuki et al., 2022). It is logical to infer that the mechanisms behind this quenching involve energetic impacts on the medium over a very short timescale. One candidate mechanism is powerful radio jets, which can release $\gtrsim 10^{60}\,\mathrm{erg}$ in tens of million years (e.g., Nesvadba et al., 2006). Indeed, as we look further back in time, we will find sources with higher radio power (e.g., $z > 4$, Jarvis et al., 2001). Investigating the medium around these actively energy-injecting sources during the Cosmic high-Noon is precisely the focus of this thesis. There is no need to reiterate the importance and complexity of ISM and CGM studies. This reinforces our motivation to panoramically inves-

[2] https://eas.unige.ch/EAS2023/session.jsp?id=S8

tigate the dynamics and states of the galactic medium within the context of this work, by examining it in full 3D.

1.4 Observational techniques probing high-z

This thesis work utilizes some of the most powerful IFUs to present the observational view of the galactic medium in 3D. One of the most successful tools for observing the ionized CGM tracer, Lyα, is the VLT/MUSE (Bacon et al., 2010). Since its first-light just over a decade ago (Bacon et al., 2014), it has been unveiling the gaseous medium and cosmic filaments in the deep space (e.g., Umehata et al., 2019; Wisotzki et al., 2018). Large survey programs with MUSE have been initiated over the years, presenting various Lyα emitters and nebulae (e.g., Arrigoni Battaia et al., 2019; Bacon et al., 2021; Chen et al., 2020). Although radio galaxies were among the first where giant Lyα emission halo are detected (e.g., Chambers et al., 1990), there is a lack of a sample 3D view of these nebulae. Beyond Lyα, with the relatively broad wavelength coverage of MUSE ($\sim 5000\,\text{Å}$), it can capture all the bright UV line, enabling simultaneous ionization and chemical studies.

Rest frame optical emission lines serve as traditional probes for ionization states and outflows in both AGN and star forming galaxies (Kewley et al., 2006; Veilleux et al., 2005). To observe these lines at the peak of the quasar era, several programs based on Keck/OSIRIS and VLT/SINFONI were carried out (Nesvadba et al., 2017a,b; Vayner et al., 2021a,b, see also Section 1.5). Although the point spread function of the IFS on board the largest ground-based telescopes can reach sub-kiloparsec for Cosmic Noon targets, their sensitivity cannot match observations from space.

The far-infrared singly ionized carbon emission line, [C II]$157.7\,\mu$m ([C II]), is another important tracer of the cold gas reservoir. It can effectively trace organized gas motions (e.g., rotation), as well as mergers and outflows. There have been many efforts made to use ALMA to observe the [C II] in various types of galaxies (e.g., Faisst et al., 2020b; Herrera-Camus et al., 2021; Lelli et al., 2021). Particularly, De Breuck et al. (2022) reported the first detection of [C II] in a high-z radio galaxy (Section 1.5), the SpiderWeb, using single disk observations. This Atacama Pathfinder EXperiment (APEX) detection not only opens the gate to studying the multiphase CGM of these beacons but also pave the road to the 3D view using ALMA.

Era of *JWST*: The *JWST* was launched in Christmas 2021 and commenced science observations in the summer of 2022. Two major IFS are on board, covering the observed frame from near to mid-infrared with medium spectral resolution, namely NIRSpec IFU and MIRI MRS (Argyriou et al., 2023; Böker et al., 2022; Jakobsen et al., 2022; Wells et al., 2015). These instruments present and continue to reveal the medium around AGN from Cosmic Noon all the way to Cosmic Dawn, utilizing the same probes as in the nearby universe. This is made possible by their ability to access wavelengths that were previously inaccessible with high sensitivity (e.g., Jones et al., 2024; Kakkad et al., 2023; Mainieri et al., 2023; Marshall et al., 2023; Perna et al., 2023; Übler et al., 2023; Wylezalek et al., 2022b).

I am fortunate to be at the beginning with access to rich IFS observations. This thesis leverages these observing techniques to offer a unique 3D perspective of the galactic medium.

1.5 High-z radio galaxies

AGN feedback is implicated in the quenching of star formation through momentum and energy injection, although the details remain unclear (Section 1.2, Harrison, 2017). Output from powerful quasars influences their surroundings, extending all the way to CGM scales or beyond. This feedback occurs through radiative and kinematic modes, in the forms of radiation pressure, winds, and radio jets (Fabian, 2012). However, observing these processes across different scales and with various tracers in the early universe is observationally challenging. At the period of interest (Section 1.3), there exist a unique quasar species that allow us to study simultaneously the two modes of feedback, the properties of their host galaxies, and the large scale environments (e.g., galactic medium and cluster).

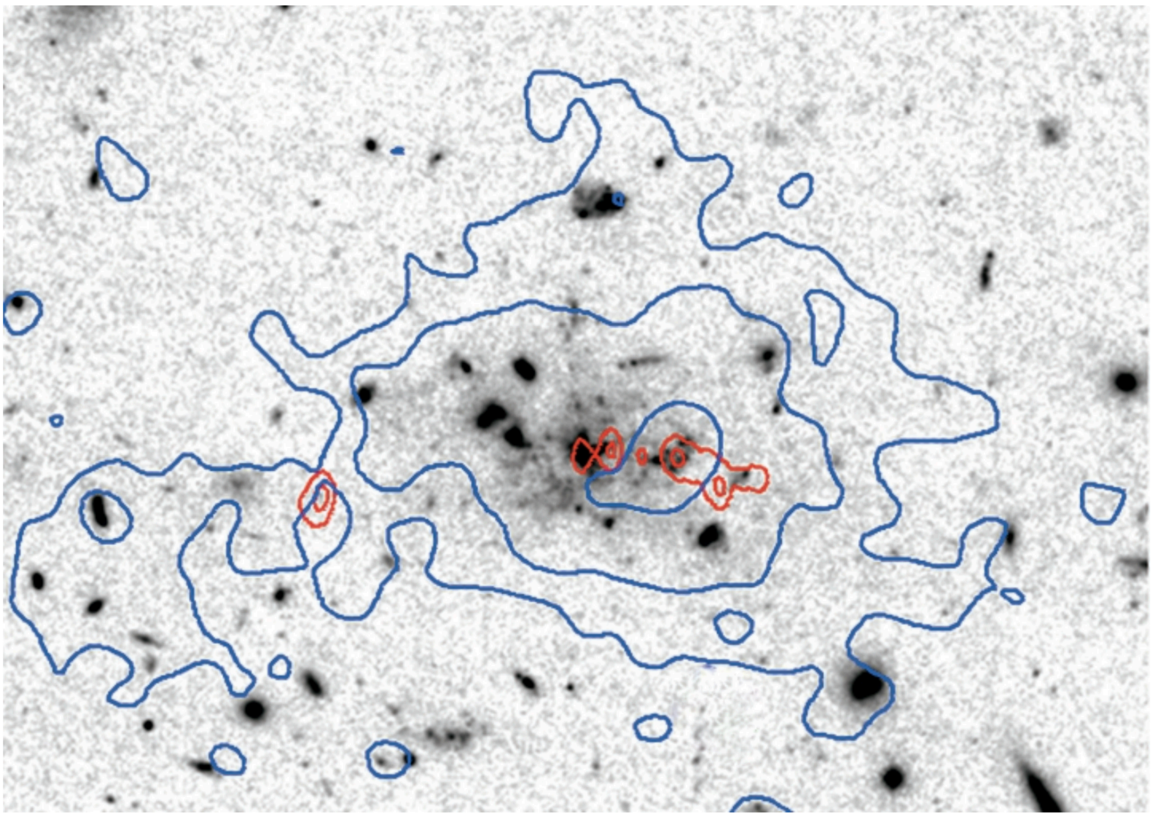

Figure 1.3. An example of the famous HzRG, the Spiderweb galaxy (MRC 1138-262). The grey color image is a *HST*/ACS composite. The red and blue contours are the Lyα nebula and $8\,\mathrm{GHz}$ radio emissions, respectively. The image captures a field of $33'' \times 23''$ ($\sim 270 \times 190\,\mathrm{kpc}^2$). This figure is taken from Miley et al. (2006).

I focus on **the most powerful radio sources** in early universe in this thesis ($L^{\rm rest}_{500\,\rm MHz} > 10^{27}\,\rm W\,MHz$ and $z > 2$, Miley & De Breuck, 2008, see Figure 1.3 for an example). The study of the powerful radio galaxies began over sixty years ago with their detection in various radio surveys and follow-up optical (near-infrared and other bands) studies (see McCarthy, 1993, for a review). Morphologically, most of the radio objects discussed here are of the Fanaroff-Riley II type (FR II, Fanaroff & Riley, 1974; Miley, 1980), exhibiting extended edge-brightened radio morphology. These sources typically extend over tens of kiloparsecs, are brighter than FR Is, and show alignments with UV and optical continuum emissions and gas morphology (e.g., Chambers et al., 1987; McCarthy et al., 1987). Although these earlier radio surveys were flux limited, they are relatively complete for objects at the high luminosity end. This made them an effective means of selecting type-2 AGN when obtaining spectroscopic information was expensive. However, identification was not always straight forward; follow-up polarimetry often played a crucial role (see also Antonucci, 2023). Following the same approach, the objects in this thesis are referred to as **high-z radio galaxies (HzRGs)**, which are radio-loud type-2 quasars.

The local or low-z radio-loud AGN are known to have radio sizes around tens to hundreds of kiloparsecs. They are found to be able to disturb the galactic medium and/or drive multiphase outflows (e.g., Kukreti et al., 2023; Morganti et al., 2021). Cases also show the impact of the jets on megaparsec or intracluster medium (ICM) scales (e.g., jet drives cavity of hot ICM, Bégin et al., 2023; Gitti et al., 2012). However, these radio emissions are at least one order of magnitude lower than the radio jets of HzRGs. Additionally, the conditions of the galactic medium are different at Cosmic (high-)Noon and low-z. Hence, it is crucial to examine these "monsters" to complete the puzzles of both radio-loud AGN feedback and galaxy evolution.

1.5.1 Extended emission-line nebulae and spectroscopy

For over 30 years, we have known about the presence of giant line-emitting halos [3] surrounding HzRGs (see 1.3). They are often referred to as extended emission line regions (EELR), where disturbed kinematics are observed (e.g., van Ojik et al., 1997). As introduced in Section 1.2, Lyα emission is the primary tool for detecting the halo gas. Particularly with the quasar at the center, the luminous ionizing source can illuminate the nebula across hundreds of kiloparsecs. Our understanding of these structures has evolved over time. Let's now summarize several key works focusing on these nebulae.

The high ionization state revealed by the emission lines suggested that AGN is the main powering source of the EELR, instead of stellar population (e.g., McCarthy, 1993). In the late '90s and early 2000s, efforts were made to investigate the details of the ionization conditions and kinematic signatures of the halo gas around radio galaxies. Observations primarily utilized the natural

[3]Through this thesis, the "nebula" and "halo" are used interchangeably which both refer to the extended gaseous medium.

optical window of the Earth's atmosphere. The earlier knowledge was thus acquired by studying the bright rest frame UV lines redshifted into the observed optical range, such as Lyα, N V$\lambda\lambda$1238,1242, C IV$\lambda\lambda$1548,1550, He II$\lambda 1640$, and C III]$\lambda\lambda$1906, 1908, other than traditional optical lines like [O II]$\lambda\lambda$3726, 3729, Hβ, [O III]$\lambda\lambda$4959,5007, and Hα. van Ojik (1995) compiled observed UV emission lines of HzRGs before the era of 8-10 m telescopes. Villar-Martin et al. (1996, 1997) utilized these data to inspect the ionization, contents, and geometry of the EELR through photonionization modeling. These works first explored the UV emission diagnostics in addition to optical ones and then examined the ionizing mechanisms behind the extended nebulae, such as AGN photonionization versus shock ionization. Additionally, these formed part of the basis for studying the chemical composition, i.e., enrichment history, of the high-z gaseous nebulae (e.g., Humphrey et al., 2008b).

While it seems obvious to assume the presence of a quasar at the center based on the high ionization state of the nebulae, additional support is always required. Spectropolarimetry studies are a useful tool in this regard as they can capture the scattered nature of photons from the hidden source (in the case of type-2 objects) by dusty structures. The successful polarization study of the local prototypical high-power radio galaxy, Cygnus A, validated the theory of light scattering from a hidden quasar (e.g., Fosbury et al., 1999; Ogle et al., 1997). Using the polarimeter on Keck, De Breuck et al. (1998) and Vernet et al. (2001) (see also Figure 1.4C) discovered polarized emission from $z \sim 1.5 - 2.5$ radio galaxies, supporting the model of obscured quasars embedded within the dusty medium inside the ionization cone of the high-z radio galaxies, with their lights being scattered to dominate the EELR emissions.

When powerful jets are obviously present, one might intuitively assume that they interact kinematically with the gas, perhaps driving outflows. However, proving this is not straightforward (e.g., Villar-Martín et al., 2000). Evidence of interaction between the jet and gas can be inferred from broad line widths and comparisons of morphologies between emission-line nebulae and radio emissions. Yet, the details of acceleration and ionizing mechanisms are not easily concluded (see previous line ratio diagnostics). Beginning with long-slit spectroscopy of nearby radio galaxies, where observations are more accessible, Villar-Martin et al. (1998) demonstrated potential evidence of jets disturbing gas. In Villar-Martín et al. (1999), the authors reported a strong case where both the broad and narrow gas components exhibited the same (ionization and kinetic) signatures as a shock driven by a jet. The authors made predication that the radio galaxies at higher redshifts could be in similar situations. It is worth noting that the analysis of Villar-Martín et al. (1999) fully leveraged spatial spectroscopic information, which motivated subsequent real IFS observations. Villar-Martín et al. (2003) presented UV spectra of radio galaxies at $z > 2$ observed using the modern largest telescope (Fig. 1.4 AB). These spectra not only revealed the disturbed nature of the high surface brightness halo, probably due to the radio jets, but also discussed the more quiescent and more extended low surface brightness nebulae beyond the radio scope. The authors explored several possibilities of these low brightness nebulae, e.g., rotating gaseous disk or spherical envelope, halos of companions, and infows. Several works followed this path since then. Humphrey et al. (2006) studied these spectra, focusing on the so called jet-gas interaction by considering both ionization and kinematics. Morais et al. (2017) examined two more HzRGs, with the slit being placed in the perpendicular direction of the jet, revealing less perturbed gas kinematics. Though concrete conclusions cannot be drawn due to data limitations and the complex nature of the universe, these long-slit spectra provided excellent starting points for follow-up investigations.

It has been known since the beginning that Lyα nebulae around HzRGs are associated with trough features atop the observed emissions (e.g., Rottgering et al., 1995; van Ojik et al., 1996, 1997, see also Section 2.1). On one hand, the absorption blocks our view of the intrinsic emission, making it difficult to probe the properties of the nebulae. On the other hand, the absorbing gas provide access to the neutral phase of galactic gas, which could be linked with cosmic web, feeding, and/or outflows. These structures (H I absorbers) have been found to be spatially extended, i.e., several tens of kiloparsecs, and are believed to be associated within the potential well of the dark matter halo of the host galaxy. Binette et al. (2000) discussed the nature of the absorber together with the metal ones, i.e., C IV$\lambda\lambda$1548,1550, which are assumed to be in the same gas cloud as the H I. Jarvis et al. (2003) and Wilman et al. (2004) analyzed high-resolution spectra of a sample of HzRGs and discussed the nature of strong and weak absorbers (high and low column density, respectively). Silva et al. (2018a) conducted the long-slit spectroscopic observations of the Lyα and H I absorbers by misaligning the slit from the jet axis, where strong kinematic features are observed (e.g., board line width and blueshifted components). The resonant nature of Lyα, which complicates the investigation of CGM, has urged the requirement of the 3D datasets.

IFU observations of the halos around HzRGs have provided a more comprehensive view. However, the motion and nature of these giant nebulae remain a mystery. Are they part of the rotation structures in the dark matter halo, or are they accreted gas feeding the galaxies from IGM? Villar-Martín et al. (2006) presented some of the first 3D observations using VLT/VIMOS, where evidence of a rotating Lyα halo at $z \approx 2.5$ was found (Figure 1.5A). Humphrey et al. (2008a) conducted the first IFU analysis of the absorbing gas and interpreted that the quiescent gas may be infalling. The operation of MUSE (Section 1.4) has been a game changer for the systematic study of the Lyα halos of HzRGs. Swinbank et al. (2015) made the first effort to spatially correct the H I absorption and studied both the ionized and neutral gas at $z = 4.1$ (Figure 1.5B). Several subsequent works have individually examined the emission nebulae for a few HzRGs using MUSE (e.g., Falkendal et al., 2021; Gullberg et al., 2016; Kolwa et al., 2019; Silva et al., 2018b; Vernet et al., 2017). Yet, the lacking of a sample study has still been needed to pursue comparability with different quasar species on the CGM scale.

While gas motion can leave prints on the shape of the Lyα line profile, it is not always a reliable prob for kinematics. Indeed, interpretations often rely on numerous assumptions and models (Dijkstra, 2014, 2017; Ouchi et al., 2020).

In the optical range, the non-resonant lines (e.g., Balmer lines), especially some of the forbidden lines (e.g., [O III]$\lambda\lambda$4959,5007) are widely used for studying the pattern of AGN feedback onto the galactic medium (e.g., Harrison et al., 2014). Since the operation of VLT/SINFONI (Section 1.4), a series of works targeting HzRGs feedback were carried out. For example, Nesvadba et al. (2007, 2008, 2006) examined the warm ionized ISM gas kinematics in a few HzRGs. These studies revealed the strongly disturbed gas with high-velocity outflowing components, suggesting energetic jets as the favored powering source. Building on this foundation, Nesvadba et al. (2017b) presented a more comprehensive view of 33 HzRGs using SINFONI. The results strongly support the scenario in which jets are the dominant driver of the outflow. Indeed, assuming the Cavagnolo et al. (2010) conversion, the jet powers for similar targets to those in the scope of this thesis range from a few 10^{46} to $\sim 10^{48}\,\mathrm{erg\,s^{-1}}$. In other words, even a tiny fraction of coupling efficiency would suffice for the jets to accomplish their task.

Discussions have been conducted regarding the roles played by AGN radiation in HzRGs (e.g., Nesvadba et al., 2017a, 2006). Their high, quasar-level bolometric luminosities (Drouart et al., 2014; Falkendal et al., 2019) might lead one to intuitively assume that they would also contribute significantly. However, how do AGN photons interact with the medium when high-power jets are also present? There are some pieces of contour-evidence: hydrodynamic simulations of the jet-ISM interactions suggest that high-power jets penetrate the medium rapidly without efficient coupling (e.g., Mukherjee et al., 2016). Maybe radiation instead contributes a comparable fraction to driving outflows. However, caution should be made when comparing observations and simulations (Harrison et al., 2018; Harrison & Ramos Almeida, 2024). Indeed, the traditionally high jet power in simulations, $P_{\mathrm{jet}} \gtrsim 10^{45}\,\mathrm{erg\,s^{-1}}$, is still $\lesssim 2$ lower than that of HzRGs. Moreover, the properties of the gaseous medium in simulations may differ from reality, such as geometry and density. All of these require more sensitive data than that provided by VLT/SINFONI to pursue further investigations.

1.5.2 Living environments and host properties

Up to this point, my focus has been primarily on the gaseous medium and emission-line observations, with a predominant emphasis on ionized and neutral gas. As the beacons for studying feedback and galaxy evolution, the HzRGs are also intriguing in terms of their large-scale environments. Observations have shown that these high-z radio AGN serve as tracers of dense environments. Specifically, they are often found to live in the center of the proto-clusters (e.g., Noirot et al., 2018, 2016; Venemans et al., 2007; Wylezalek et al., 2013, 2014, see also Figure 1.3 as an example). As predicted by cosmology and probed by surveys on larger scales, the baryonic structure formations follow the potential of dark matter. Though this thesis does not directly focus on these megaparsec scales, the feedback from the central radio AGN plays a key part in impacting the companions in their environments. For instance, the output energy increases the efficiency for ram-pressure stripping of gas from the satellite galaxies. These galaxies may undergo merging phases with the massive central one

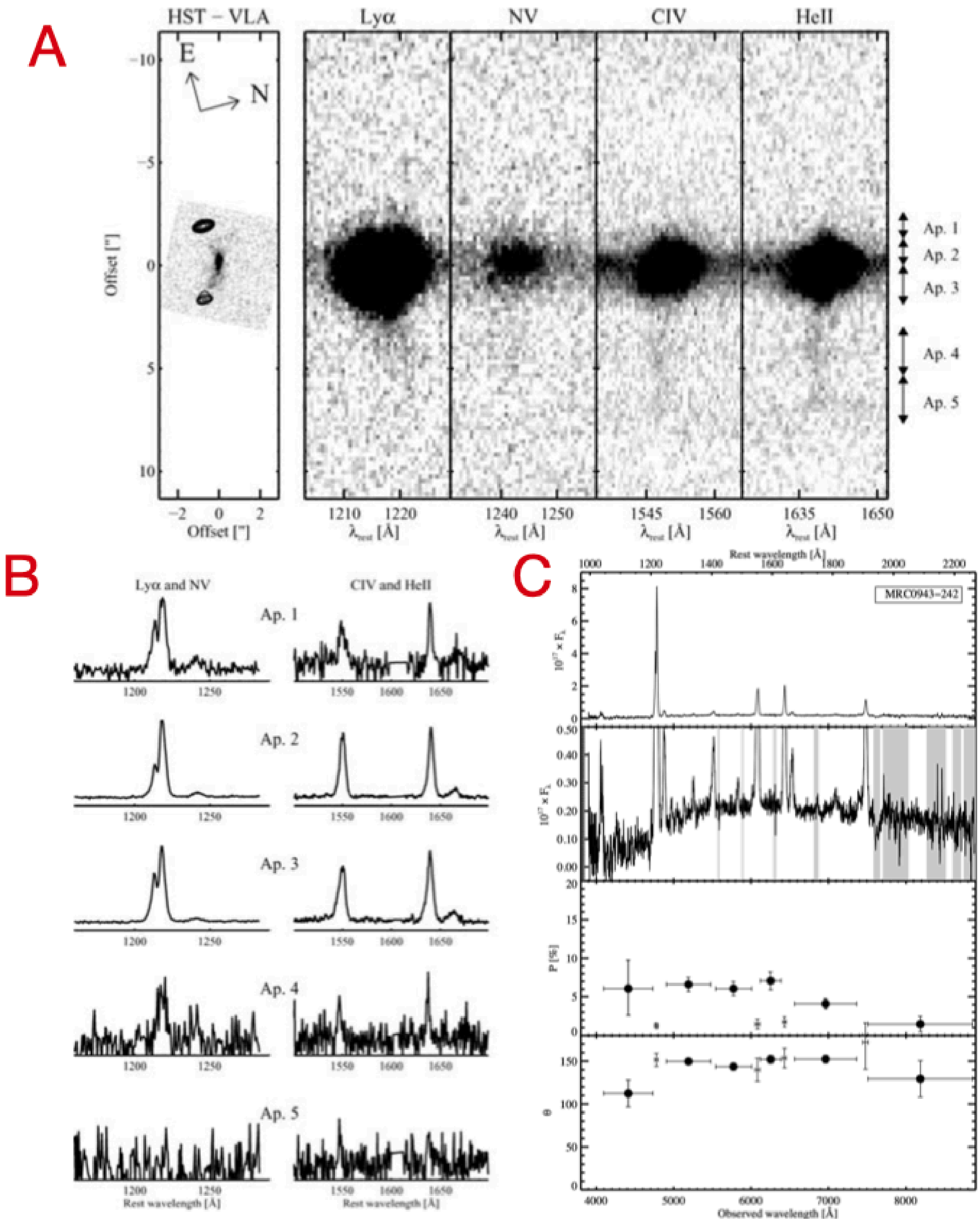

Figure 1.4. Example of the long slit spectroscopic data of the UV emission nebula around MRC0943-242 at $z = 2.923$. **(A)**: HST image (left) and 2D view (right, position-velocity diagram) of the UV emission lines. **(B)**: The 1D spectra extracted from different apertures from panel A. This data probed the UV EELR and quiet halo beyond jet hot spots but with limited spatial information. Both panels A and B are taken from Villar-Martín et al. (2003). **(C)**: The UV spectrum and polarization measurements taken from Vernet et al. (2001) (polarized fraction and position angle of electric vector).

throughout evolution, where the gas fraction will be a crucial parameter determining the significance of this interaction. Therefore, examining the physical space between the center radio AGN and the environment in the (proto-)cluster is essential.

Regarding the host galaxies, multiwavelength photometric analysis confirmed that they are indeed massive in $M_\star$ (De Breuck et al., 2010; Seymour et al., 2007). The majority of them show evidence of quenching, indicated by their position below the star formation main sequence at corresponding redshifts (Falkendal et al., 2019). This is further supported by studies of the molecular gas in HzRGs, which indicate that the jets are ejecting the H_2 (Emonts et al., 2014). Combing this with the aforementioned findings regarding ionized gas, there seems no doubt that the jets are acting as the primary driver.

1.5.3 Open questions

Despite the fruitful knowledge, the view of the gaseous medium remains blurry. We only have a rough idea that the bulk motion of the gas appears to be connected with AGN, especially their powerful jets. On these scales, typically beyond galactic level, the impact from AGN radiation seems secondary. However, what if we focus on the center? What is left behind after the passage of jets? Or before that, what is the chronological order of the two feedback modes taking effect? This is indeed one of the directions of this thesis. On the outer part, our previous understanding of the extended halo was limited by sensitivity. We urgently need a systematic inspection of the CGM nebulae to explore what is further beyond (such as jet hot spots). It would be interesting if connections between radio AGN and their surrounding companions are detected in gaseous medium (e.g., Umehata et al., 2019). It would be even more exciting, if a clearer 3D view of the gas feeding (accretion) could be achieved (e.g., Humphrey et al., 2007; Vernet et al., 2017). To realize these ambitious goals, we need panoramic datasets as well as meticulous analysis technique.

1.5.4 The most well-observed $z \gtrsim 3$ HzRGs sample

In this section, I summarize the sample of eight HzRGs that I will focus on in the rest of this thesis. A relatively comprehensive list of HzRGs (~ 200) was complied in Miley & De Breuck (2008) over a decade ago, where different components and their multiwavelength properties were also discussed. Among those, a sub-sample of well-observed HzRGs is the foundation of this thesis. In addition to the data from early period, relatively recent space and large ground-based telescopes, namely *Hubble* space telescope (HST), *Spitzer* space telescope, *Herschel* space telescope, and VLT, have provided an unprecedented view in terms of both wavelength coverage and sensitivities. These datasets cover rest frame UV to submillimeter with imaging, high resolution spectrograph, and IFUs.

Particularly, observation programs with VLT/MUSE (Chapter 3) initiated the 3D view of the CGM gas around a sample of eight HzRGs at $z \approx 3 - 5$, making them the most well-observed sample. Here, I complied a short table summary of the data covered for these eight, which are the foundation of this thesis (Table 1.1). It, of course, could not be complete without the companion ALMA Band 3 & 4 program targeting the molecular phase of the same sample (Falkendal et al., 2019; Kolwa et al., 2023). Additionally, five out of those were observed in *JWST* Cycle 1 with NIRSpec IFU, whose high sensitivity (a factor of ten) brought us a step closer to understanding the details of the warm ionized gas at the center compared to previous SINFONI data (see Chapter 4 for one and also Roy et al., 2024; Saxena et al., 2024, for another).

Part of these datasets were contributed by me, together with all of my collaborators, during my PhD which will be summarized below. Some of the analysis plans will be shown in Chapter 5. We note that there are also X-ray observations for some of the targets, which are beyond the scope of this work (e.g., Smail et al., 2012). Each of these datasets alone deserves its own paper(s). In joint analysis, they will be the best archives to continuously dig into for the treasure of the universe. Unfortunately, none of them has the full coverage from all instruments. Though we would like to have a completed view, let’s not be too rush but take step firmly towards the ultimate goal.

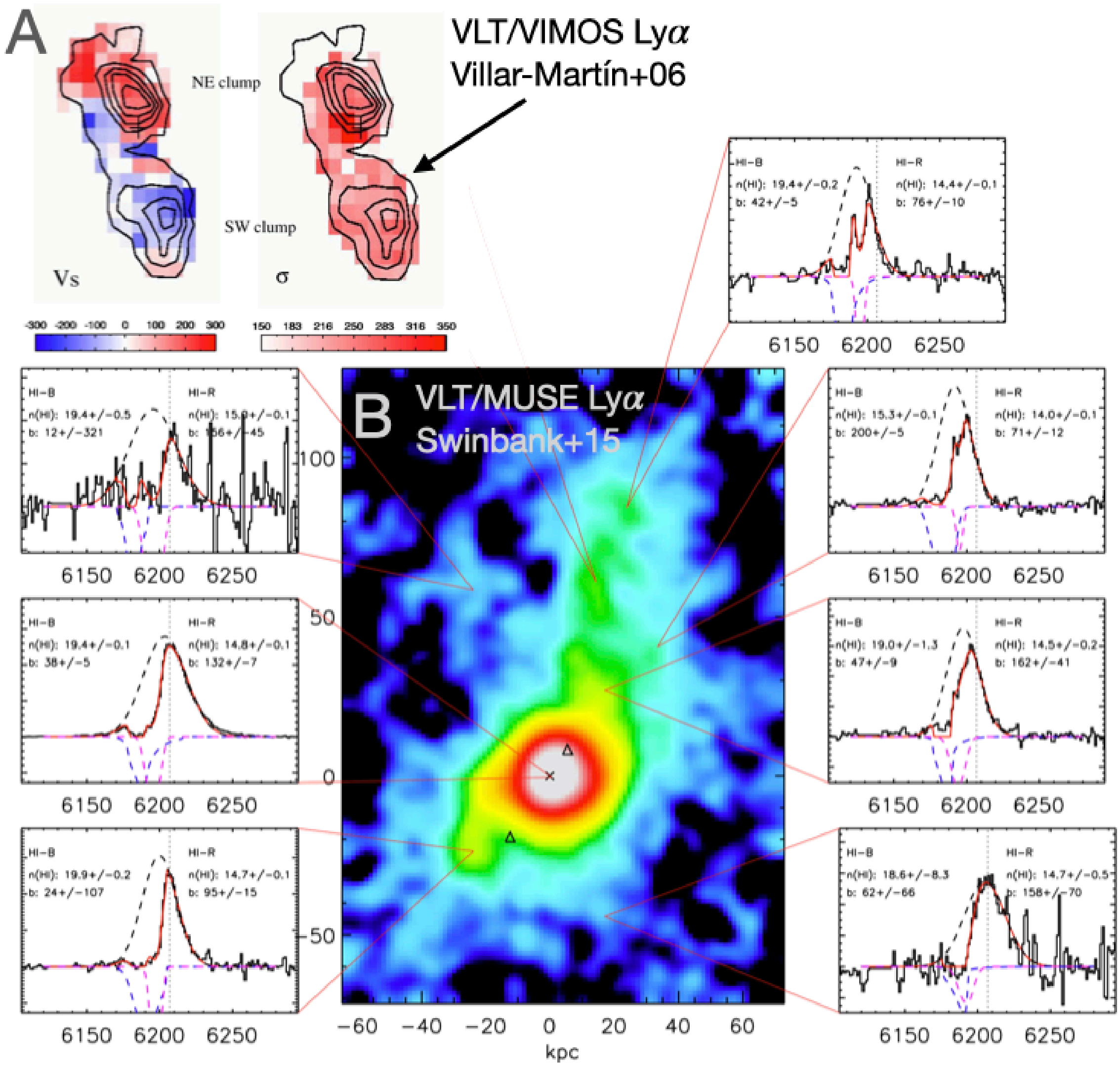

Figure 1.5. Examples of IFU observations of Lyα halo around HzRGs. **(A)**: Lyα velocity shift and velocity dispersion maps of MRC 2104-242 at $z = 2.49$. This VLT/VIMOS data analysis is taken from Villar-Martín et al. (2006). **(B)**: VLT/MUSE observation of the Lyα nebula around TN J1338-1942 at $z = 4.0959$ taken from Swinbank et al. (2015). The IFU reviled the extended absorbing H I on top of the Lyα line over 100 kpc.

Table 1.1. Summary of the rest frame UV to radio observations of the most well-observed $z \approx 3-5$ sample of HzRGs.

radio galaxy	*HST* UV (1)	UVES UV (2)	MUSE UV (3)	SINFONI optical (4)	*JWST* optical (5)	*Spitzer* optical, NIR (6)	*Herschel* MIR (7)	ALMA [C II] (8)	ALMA [C I] (9)	radio MHz-GHz (10)
MRC 0943-242	✓	✓	✓	–†	–	✓	✓	–	✓	✓
MRC 0316-257	✓	✓	✓	✓	–	✓	✓	–	–	✓
TN J0205+2242	–	✓	✓	✓	✓	✓	✓	✓✳	✓	✓
TN J0121+1320	–	✓	✓	✓	✓	✓	✓	✓	✓	✓
4C+03.24	✓	✓	✓	✓	✓	✓	✓	✓✳	✓	✓
4C+19.71	✓	–	✓	✓	✓	✓	✓	✓	✓	✓
TN J1338-1942	✓	✓	✓	✓	✓	✓	✓	✗★	✓	✓
4C+04.11	–	✓	✓	✓	–	✓	✗	–	✓	✓

(1) WFPC2; NICMOS; ACS (e.g., Duncan et al., 2023; Pentericci et al., 2001, 1999; Smail et al., 2012; Vernet et al., 2017). (2) Red arm (e.g., Jarvis et al., 2003; Wilman et al., 2004, Ritter et al. in prep.). (3) WFM (Falkendal et al., 2021; Gullberg et al., 2016; Kolwa et al., 2019; Swinbank et al., 2015; Vernet et al., 2017, see also Chapter 2 & 3). (4) J, H, and K-band (Nesvadba et al., 2017a, 2007, 2008). (5) NIRSpec IFU (Roy et al., 2024; Saxena et al., 2024, Chapter 4). NIRCam for TN J1338-1942 (Duncan et al., 2023). (6) IRAC (also MPIS for MRC 0943-242, De Breuck et al., 2010; Seymour et al., 2007). (7) PACS; SPIRE (e.g., Drouart et al., 2014). (8) Band 8 (Chapter 4 & 5). (9) Band 3 & 4 (Band 6 for MRC 0943-242, e.g., Falkendal et al., 2019, 2021; Kolwa et al., 2023). (10) VLA X and C-band. See Miley & De Breuck (2008) for a summary. Newer VLA (Nesvadba et al., 2017a). MERLIN and e-EVN for 4C+04.11 (Parijskij et al., 2014). (†) The rest frame optical wavelength of MRC 0943-242 was observed by X-Shooter (Silva et al., 2018b). (✳) Due to the program was ranked as a filler, the [C II] integration time was not fulfilled for these two. (★) The redshifted [C II] frequency of TN J1338-1942, 372.34 GHz, is at the edge of ALMA Band 7 such that it is impossible to be observed with the current instrumentation setup.

My contribution other than this thesis

This thesis (and my PhD) initially began with the MUSE sample. As outlined in Section 1.5.4, this sample also has companion (carried out at the similar time as the MUSE) ALMA Band 3 & 4 observations focusing on the [C I](1-0) 492.16 GHz as a proxy for H_2. During my PhD, I also contributed to the analysis of this dataset. The results of which are not included in this thesis but were published in Kolwa et al. (2023). Specifically, I conducted the line fitting of both [C I] and He II (from MUSE) at the position of the host galaxy. This work revealed that the molecular gas mass is low for these radio galaxies, indicating the possible role of powerful jets in gas ejection.

Along my journey, new datasets also came on board. The information contained in those goes far beyond what one PhD work can encompass, making it unrealistic for me to include everything at once. They will be the legacy (or, speaking a bit selfishly, my PhD legacy) for the future analyses of feedback, the gaseous medium, galaxy evolution, etc.

There are three observational programs contributed by me: (i) The observations from MUSE capture the spatial information of the CGM gas using primarily Lyα. However, its medium spectral resolution, $\Delta v \sim 100\,\mathrm{km\,s^{-1}}$, is not sufficient to resolve the narrow absorbers (e.g., Jarvis et al., 2003). Therefore, to complement the MUSE sample, I proposed the VLT/UVES observations (108.21WL, PI: Wuji Wang). Together with the those that already had high-resolution data, we now have the complementary tools for studying the neutral gas (Ritter et al. in prep., Chapter 5). (ii) This thesis only reveals the tip of the (one out of four) iceberg(s) of my NIRSpec IFU sample. My proposal (JWST-GO-1970, PI: Wuji Wang) opened the gate to the detailed feedback studies at Cosmic high-Noon in the most powerful radio-loud AGN. It can and will serve as the basis for many more PhD and Master theses, paving the way for a clearer understanding of the monsters in the early universe. (iii) To fill the gap in spatially resolved ordered gaseous motions and the young star heated cold dust continuum, I proposed the ALMA Band 8 observations for the same sample as my four *JWST* objects (2021.1.00576.S, PI: Wuji Wang). The observations for two, namely 4C+19.71 and TN J0121+1320, were completed and showed clearly detection of [C II] line emission and dust continuum. A tiny piece of this information is included in Chapter 4 which, in my opinion, stimulates more curiosity than it answers questions.

1.6 This thesis

This thesis focuses on the 3D view of the galactic medium around the most well-observed sample of radio-loud AGN at $z \gtrsim 3$. The major part of my work contributes to the systematic technique of reconstructing the intrinsic Lyα emission halos and understanding the CGM gas. In addition, I also dedicated part of my PhD to presenting the unprecedented view of feedback at the center of one HzRG.

A preview is preceded following:

Chapter 2 & 3

Lyα is an important tool for studying the CGM. Its resonant nature offers us the opportunity to trace the ionized gaseous nebulae out to several hundreds of kiloparsecs. These nebulae of HzRGs have long been associated with multiple spatially extended neutral hydrogen clouds (van Ojik et al., 1996, 1997). They are believed to reside between the last scattering surface of Lyα emissions and observers, absorbing photons and leaving troughs on top of the emission spectra. Thanks to IFUs like MUSE, we can correct the absorption in 3D and also study the neutral gas following this treatment.

I established the technique in the pilot study, Chapter 2, focusing on the highest redshift radio galaxy in our sample (4C+04.11 at z=4.5077, Wang et al., 2021b). Along with the analysis, I also developed the optimized reduction procedure which formed the basis for analyzing the entire sample. Beginning with the 1D “master spectrum" extracted at the radio core position, I determined the systemic redshift and tested the emission+absorption fitting approach for Lyα. Following and modifying Swinbank et al. (2015), I generalized the treatment to the extended nebula, recovering spatial information of H I clouds. Combing this with the metal absorption, I proposed that we may witness the redistribution of metals at CGM scale at $z \approx 4.5$ by powerful radio AGN.

Following the pilot study in Chapter 2, I initiated a thorough analysis in Chapter 3 (Wang et al., 2023), focusing on the Lyα nebulae of the eight HzRGs in our MUSE sample. I updated the treatment by (i) including a 3D smooth-based detection method to trace the Lyα nebulae down to the observation limit (Vernet et al., 2017); (ii) using a two-step Voronoi binning to uniformly tessellate the nebulae; (iii) constraining the fitted parameters of the spectra by their neighboring tiles. In this way, I reconstructed the intrinsic emission nebulae (i.e., corrected for absorption).

The Lyα nebulae are ubiquitous around early galaxies (e.g., Wisotzki et al., 2018). Several works have characterized these emission nebulae around radio-loud and radio-quiet type-1 and radio-quiet type-2 quasars in statistical samples across cosmic times observe by IFS (e.g., Arrigoni Battaia et al., 2019; Cai et al., 2019; den Brok et al., 2020; Farina et al., 2019). For radio-loud type-2 quasars, i.e., HzRGs, correcting the H I absorption is necessary before meaningful comparisons to other species can be made. Thus, with the intrinsic Lyα emission of our sample, Chapter 3 linked the gaseous medium around HzRGs on CGM scale, for the first time, with other high$-z$ quasar samples. Several indications from the analysis are discussed. I would like to point out here one interesting idea that: the alignment between the Lyα nebulae and the jet axis beyond the radio hot spots supports the scenario that the large-scale gas distribution (e.g., cosmic web) may bias the orientation along which we observe the the radio jets (e.g., Eales, 1992).

Chapter 4

The capabilities of IFUs on current ground-based telescopes are limited by the Earth's atmosphere in several aspects (e.g., transmission window, sky-line, resolution, etc.). Until the operation of *JWST*, we were missing the detailed view of the ISM of HzRGs. Our program, JWST-GO-1970 (Wang et al., 2021a), made this a reality.

In this chapter (Wang et al., 2024), I focused on one of the most-well studied radio-loud AGN at $z = 3.5892$. Our NIRSpec IFU unveiled the warm ionized ISM in sub-kpc resolution. Exploiting the full 3D information of the cube, I found that the gas has complex morphology around the central $\sim 20\,\mathrm{kpc}$ of the AGN. The ALMA Band 8 dust map agrees with the the optical attenuation of Balmer lines. The kinematics of the gas do not show high velocity shift except near the center. The AGN photoionization dominates in the observed field-of-view. Kinetic calculation suggests that the $L_{\mathrm{bol}} \sim 10^{47}\,\mathrm{erg\,s^{-1}}$ quasar is inefficient in radiatively driving outflow.

Chapter 5

In this final chapter, I will first offer an overview bringing together the 3D views from different instruments. As briefly summarized in Section 1.5.4, we are only seeing tiny pieces of the information buried in the already massive currently available datasets. Thus, I will then suggest some possible directions for the future works on this most-well observed HzRGs sample. Specifically, the analysis of many data have not been published yet at the time of writing, e.g., NIRSpec IFU and ALMA Band 8, which will be the priority. Additionally, I will also provide an outlook for the untouched scope within the ability of current observing techniques.

2

Mapping the "invisible" circumgalactic medium around a $z \sim$4.5 radio galaxy with MUSE

Authors:
Wuji Wang, Dominika Wylezalek, Carlos De Breuck, Joël Vernet, Andrew Humphrey, et al.

Published in *A&A 654, A88 (2021)*.

Wuji Wang is the principal author of this article. The method was developed by Wuji Wang with the assistance from Dr. Kolwa. Wuji Wang, Dr. Vernet, Dr. De Breuck, and Dr. Wylezalek had the idea for the paper. Wuji Wang performed data process, calculations and analysis of the observations. Wuji Wang produced all the figures and tables and wrote the manuscript. All authors collaborated with corrections and suggestions to the manuscript, and Wuji Wang performed the last improvements during the review process.

A&A 654, A88 (2021)
https://doi.org/10.1051/0004-6361/202141558

Astronomy & Astrophysics

Mapping the "invisible" circumgalactic medium around a $z\sim4.5$ radio galaxy with MUSE

Wuji Wang (王无忌)[1,2], Dominika Wylezalek[1,2], Carlos De Breuck[2], Joël Vernet[2], Andrew Humphrey[3], Montserrat Villar Martín[4], Matthew D. Lehnert[5], and Sthabile Kolwa[6,7]

[1] Astronomisches Rechen-Institut, Zentrum für Astronomie der Universität Heidelberg, Mönchhofstr. 12-14, 69120 Heidelberg, Germany
e-mail: wuji.wang@uni-heidelberg.de; wuji.wang_astro@outlook.com
[2] European Southern Observatory, Karl-Schwarzchild-Str. 2, 85748 Garching, Germany
[3] Instituto de Astrofísica e Ciências do Espaço, Universidade do Porto, CAUP, Rua das Estrelas, 4150-762 Porto, Portugal
[4] Centro de Astrobiología, CSIC-INTA, Ctra. de Torrejón a Ajalvir, km 4, 28850 Torrejón de Ardoz, Madrid, Spain
[5] Univ. Lyon, Univ. Lyon1, ENS de Lyon, CNRS, Centre de Recherche Astrophysique de Lyon UMR5574, 69230 Saint-Genis-Laval, France
[6] Inter-University Institute for Data Intensive Astronomy, Department of Astronomy, University of Cape Town, Rondebosch 7701, South Africa
[7] Physics Department, University of Johannesburg, 5 Kingsway Ave, Rossmore, Johannesburg 2092, South Africa

Received 16 June 2021 / Accepted 19 July 2021

ABSTRACT

In this paper we present Multi Unit Spectroscopic Explorer integral field unit spectroscopic observations of the $\sim70\times30\,\mathrm{kpc}^2$ Lyα halo around the radio galaxy 4C04.11 at $z=4.5077$. High-redshift radio galaxies are hosted by some of the most massive galaxies known at any redshift and are unique markers of concomitant powerful active galactic nucleus (AGN) activity and star formation episodes. We map the emission and kinematics of the Lyα across the halo as well as the kinematics and column densities of eight H I absorbing systems at $-3500<\Delta v<0\,\mathrm{km\,s^{-1}}$. We find that the strong absorber at $\Delta v\sim0\,\mathrm{km\,s^{-1}}$ has a high areal coverage ($30\times30\,\mathrm{kpc}^2$), being detected across a large extent of the Lyα halo, a significant column density gradient along the southwest to northeast direction, and a velocity gradient along the radio jet axis. We propose that the absorbing structure, which is also seen in C IV and N V absorption, represents an outflowing metal-enriched shell driven by a previous AGN or star formation episode within the galaxy and is now caught up by the radio jet, leading to jet-gas interactions. These observations provide evidence that feedback from AGN in some of the most massive galaxies in the early Universe may play an important role in redistributing material and metals in their environments.

Key words. galaxies: evolution – galaxies: active – galaxies: high-redshift – galaxies: individual: 4C04.11 – galaxies: halos

1. Introduction

There is significant observational and theoretical evidence that supermassive black holes (SMBHs) in the centers of galaxies play a crucial role in the evolution of their hosts (e.g., Ho 2008). The powerful nuclear activities caused by actively accreting SMBHs – active galactic nuclei (AGN) – can lead to a substantial release of energy (Silk & Rees 1998) and impact the evolution of their host galaxies (Kormendy & Ho 2013; Heckman & Best 2014). The most powerful AGN (quasars, $L_{\mathrm{bol}}>10^{45}\,\mathrm{erg\,s^{-1}}$) can easily heat and photo-ionize their surrounding gas, sometimes even on scales of tens of kiloparsecs, well into the circumgalactic medium (Tumlinson et al. 2017). The detailed mechanisms and timescales relevant to AGN-driven feedback are still not fully understood (Fabian 2012), but large samples of galaxies with high spatial resolution using the modern surveys, primarily at low redshift right now, for example Sloan Digital Sky Survey-IV Mapping Nearby Galaxies at Apache Point Observatory (SDSS-IV MaNGA, e.g., Wylezalek et al. 2018), help in assessing its prevalence and nature. However, it is the epoch at $z\sim2-3$ that marks the peak of both star formation and quasar activity (cosmic noon, $z\sim2-3$; Madau & Dickinson 2014; Förster Schreiber & Wuyts 2020), and probing the feedback processes in AGN at that epoch is essential.

The CGM (see Tumlinson et al. 2017, for a detailed review) is now understood to be a key component in disentangling the feedback processes in active galaxies. It links the smaller-scale interstellar medium (ISM) of the galaxy to the larger-scale intergalactic medium (IGM), not only in a geometrical way but also by acting as the reservoir fueling star formation and the central black hole, where the feedback interacts with the galactic environment and where the gas recycling during galaxy evolution is controlled. This complex environment is multiphase and has been observed in numerous surveys (e.g., Tumlinson et al. 2013; Bordoloi et al. 2014; Peek et al. 2015; Borthakur et al. 2015) at low redshift. A prominent feature of the CGM around active galaxies is the Lyα (Lyman-α) emission line, which is also ubiquitously observed at high redshift (e.g., Haiman & Rees 2001; Reuland et al. 2003; van Breugel et al. 2006; Villar-Martín 2007; Humphrey et al. 2013; Cantalupo et al. 2014; Wisotzki et al. 2016, 2018; Arrigoni Battaia et al. 2018, 2019; Nielsen et al. 2020). Lyα is the transition of the hydrogen electron from the 2p orbit to its ground state. It can happen primarily through collisional excitation and recombination (see Dijkstra 2014, 2017, for a detailed review of Lyα emission mechanisms and radiative transfer). In extragalactic studies, the recombination production of Lyα emission can be generated by photoionization by young stars and/or AGN (fluorescence). This fluorescence emission on larger scales (CGM and IGM) can also be due to UV background radiation. Additionally, collisional excitation can play an important role in the emission seen in outflows and infalling gas (Ouchi et al. 2020). The bright Lyα emission line, along with other UV lines excited by the central or background sources, provides a useful tool for studying the galactic environments in the early Universe. Additionally, H I and metal absorption features observed in the CGM are powerful tracers of feedback signatures as well as tracers of infalling pristine gas (e.g., low metallicity absorption in a $z \sim 2.7$ submillimeter galaxy; Fu et al. 2021). The sensitive integral field spectrographs on the largest ground-based telescopes, such as MUSE (Multi-Unit Spectroscopic Explorer; Bacon et al. 2010, 2014) and KCWI (Keck Cosmic Web Imager; Morrissey et al. 2012; see Cai et al. 2019 for observation of Lyα halos with KCWI), are perfectly suited for mapping these UV features as they move into the optical band for high-redshift sources.

This paper focuses on the population of high-redshift radio galaxies (HzRGs; $L_{500\,\mathrm{MHz}} > 10^{26}\,\mathrm{W\,Hz^{-1}}$ Miley & De Breuck 2008), which are some of the most massive galaxies known at any redshift (with a narrow range in stellar masses of $(1-6) \times 10^{11}\,M_\odot$ for $1 < z < 5.2$; De Breuck et al. 2010). Their energetic radio jets are unique markers of concomitant powerful AGN activity, which place them amongst the most active sources at and near cosmic noon. High-redshift radio galaxies have furthermore been shown to be powerful beacons of dense (proto-)cluster environments in the early Universe (e.g., Le Fevre et al. 1996; Stern et al. 2003; Venemans et al. 2002, 2003, 2004, 2005, 2007; Wylezalek et al. 2013). The quasar-level AGN activity (Miley & De Breuck 2008) at the center is blocked by the thick dusty torus acting as the "coronograph" (Vernet et al. 2001); this makes HzRGs true obscured type-2 quasars, allowing us to probe their host galaxies and CGM without strong AGN contamination (e.g., for unobscured quasars, see Arrigoni Battaia et al. 2019, and for radio-quite type-2 sources, see Cai et al. 2017). Comprehensive studies using near-infrared integral field unit (IFU) instruments show that the ionized gas in HzRGs is highly perturbed ($FWHM \sim 1000\,\mathrm{km\,s^{-1}}$) at kiloparsec scales and is aligned with the radio jets (Nesvadba et al. 2006, 2007, 2008, 2017a,b; Collet et al. 2015, 2016). This implies that the energy and momentum transfer between the central quasar and their ISM is likely due to the jets. Radio-mode feedback may therefore play a fundamental role during the evolution of HzRGs. Recently, Falkendal et al. (2019) combined infrared and millimeter data and deduced a more robust result of a relatively low star formation rate (SFR) for a sample of HzRGs, suggesting evidence of rapid quenching compared to previous studies (e.g., Drouart et al. 2014). Using a small sample of HzRGs, Nesvadba et al. (2011) shows that they are going through a transition phase from active to passive. These observations indicate that HzRGs are on a different track of evolution compared to radio-quiet objects, assembling most of their stellar mass early ($z \sim 3$; Seymour et al. 2007; De Breuck et al. 2010), and that radio jets may actively affect their quenching. However, there is also circumstantial evidence showing that the jet can induce star formation. Humphrey et al. (2006) found that HzRGs ($z > 2$ in the sample) with smaller radio sources and more perturbed gas (emission line) kinematics show lower UV continuum polarization, which could be due to the presence of more luminous young stellar populations and can possibly be explained by the interaction between radio jets and the ISM that enhances star formation. Besides, there is also an anticorrelation between the rest frame submillimeter flux density and radio size in HzRGs (Humphrey et al. 2011), although it is not clear if the physics behind this is feedback-induced star formation, a simultaneous triggering of star formation and the radio-loud AGN activity, or simply environmental effects. Some well-studied HzRGs show evidence of having high SFRs (e.g., 4C41.47 and PKS 0529−549; Nesvadba et al. 2020; Falkendal et al. 2019). In these sources, we may interestingly be witnessing both the jets compressing the gas, leading to enhanced SFRs (e.g., Fragile et al. 2017), and the feedback from the AGN and star formation quenching it (Man et al. 2019).

One of the most prominent features of HzRGs is their gaseous halos, which often reach out to more than 100 kpc from the nucleus, well into the CGM (e.g., van Ojik et al. 1996, 1997; Villar-Martín et al. 2003), and which have different dynamical states (from more perturbed inner regions to quieter outer regions; e.g., Vernet et al. 2017). The halos are observed in all strong emission lines (e.g., Lyα to Hα, McCarthy 1993; Miley & De Breuck 2008) and are metal-enriched, often detected in N Vλ1240 Å and C IVλ1548 Å. The CGM is not only the venue of the feedback but also an essential path from which IGM gas can fuel the growth of SMBHs and star formation, as suggested by various cosmological models (e.g., Springel et al. 2005; Fumagalli et al. 2011). Umehata et al. (2019) observed (proto-)cluster-scale gas filaments that may be tracing infalling gas. Observations of the CGM around HzRGs (e.g., Humphrey et al. 2007, 2008a; Vernet et al. 2017) provide evidence of inflowing gas in both absorption and emission with the scale of $10\,\mathrm{s} \times 10\,\mathrm{s\,kpc^2}$. In addition to the neutral and ionized gas, the molecular and dust phases have also been studied using the Actacama Large Milimeter/submilimeter Array (ALMA; or other millimeter telescopes), which traces the environment of stellar components in the galaxies to show a comprehensive view of galaxy evolution in the early Universe (e.g., Gullberg et al. 2016; Falkendal et al. 2021).

Many HzRGs have deep extended absorbers associated with them (van Ojik et al. 1997). These associated absorbers offer a unique opportunity for probing the neutral CGM, without the requirement of direct ionization by the central AGN (Rottgering et al. 1995; van Ojik et al. 1997; Humphrey et al. 2008a; Jarvis et al. 2003; Wilman et al. 2004; Silva et al. 2018a; Kolwa et al. 2019). The absorbers are usually blueshifted with respect to the host systemic redshift, which can be understood as a potential signature of outflowing gas. Over the past two decades, a series of works have established the picture and have offered evidence for explaining the observed absorption through the scenario of giant expanding shells of gas: Binette et al. (2000) argued that the prototypical H I and C IV absorber in MRC 0943−242 is probably a giant shell enveloping the line-emitting halo. Jarvis et al. (2003) and Wilman et al. (2004) obtained additional data and further developed the expanding shell idea. Before Humphrey et al. (2008a), who published the first IFU study of the properties of an extended HzRG absorber, works on the absorbers had only used long slit spectroscopy placed along the radio axis, meaning that there was no proof, only suspicion, that the H I absorbers are not only extended along the radio jet axis. The result of Humphrey et al. (2008a), therefore, reinforced the giant expanding shell hypothesis. Silva et al. (2018b) studied the Lyα halos of a sample of HzRGs to examine whether extended H I absorbers are usually extended perpendicular to the radio axis. With the long slit spectroscopic data together with a handful of previously published MUSE observations containing extended H I/HzRG absorbers (e.g., Swinbank et al. 2015), it was possible to draw the conclusion that extended H I absorbers of HzRGs are commonly extended perpendicular to the radio axis. In Silva et al. (2018a), the authors measured the line-of-sight velocity as a function of offset from the AGN for the main H I absorber in MRC 0943−242 and detected a radially decreasing blueshift, consistent with an expanding shell centered on the nucleus. More interestingly, around 30% of the detected absorbers are redshifted, and their natures are still unclear. This begs the question of whether they are the cooling inflowing IGM gas that models predict dominates the gas accretion of massive galaxies or are due to the emission line gas in the Lyα halo simply outflowing with a higher line-of-sight velocity than the H I absorber. Absorption features are not unique around type-2 sources like HzRGs; they are also seen in the spectra of type-1 high-redshift quasars (e.g., Arrigoni Battaia et al. 2019). These absorbers may also have an important influence on the inferred intrinsic total flux, which is sometimes neglected (e.g., peak Lyα in Mackenzie et al. 2021).

4C04.11 (RC J0311+0507), at $z \sim 4.5$, is the focusing target of this work. Radio emission of the source was first discovered with the Russian RATAN-600 instrument (the 600 m diameter ring antenna of the Russian Academy of Sciences; Goss et al. 1992). It was observed subsequently by other telescopes in the radio and optical (Kopylov et al. 2006; Parijskij et al. 1996, 2000, 2013, 2014). The source (RC J0311) was then found to be the same one (4C04.11) registered in the older Cambridge surveys (Mills et al. 1958; Gower et al. 1967). We note that Kopylov et al. (2006) first obtained the redshift, $z = 4.514$, of this target using the Lyα line spectrum taken from the Russian 6 m optical telescope (BTA). It is classified as an FR II source based on the radio morphology (Fanaroff & Riley 1974). Previous studies show it has a central SMBH with a mass of $\sim 10^9\,M_\odot$ (Parijskij et al. 2014; Nesvadba et al. 2017a). Kikuta et al. (2017) studied the large-scale environment of 4C04.11 by searching for surrounding Lyα emitters (LAEs) using the Subaru Telescope, which found that 4C04.11 is residing in a low-density region of LAEs. Its X-ray proprieties have been reported by Snios et al. (2020), including the spectrum photon index ($\Gamma = 0.92^{+0.5}_{-0.51}$) and the optical−X-ray power law slope, $\alpha_{\rm OX} = -1.31 \pm 0.08$. That work also reports the absence of extended X-ray structures despite the large radio jet scale.

In this paper we present the results of the MUSE observation for 4C04.11, focusing on the absorption features in its CGM. This radio galaxy is the highest-redshift source in our sample of eight HzRGs with both MUSE and ALMA data. It also has multiple H I and associated metal absorbers on which we can test the absorption mapping ability of MUSE. Hence, this is a pilot work, and upcoming studies will focus on the spatial characteristics of the CGM absorbers of the whole sample. In Sect. 2 we present the observation and the optimized data reduction procedure of the target. The methodology used for analyzing emission line and absorption spectra as well as the spatial mapping is shown in Sect. 3. The results are presented in Sects. 4 and 5 for the 1D spectrum and 2D mapping, respectively. We discuss some physical explanations from the analyzed results in Sect. 6 and propose several models to the observed spatial column density gradient of H I absorber #1 in Sect. 7. Finally, we summarize and conclude in Sect. 8. For this work, we use a flat Lambda cold dark matter cosmology with $H_0 = 71\,\mathrm{km\,s^{-1}\,Mpc^{-1}}$ and $\Omega_{\rm M} = 0.27$. In this cosmology, 1″ corresponds to 6.731 kpc at the redshift of our target, 4.5077.

2. Observations and data reduction

2.1. MUSE Observations

The target of this work, the radio galaxy 4C04.11, was observed by the European Southern Observatory (ESO) Very Large Telescope (VLT) using the instrument MUSE from December 2 to 15, 2015, under the program run 096.B-0752(F) (PI: J. Vernet). The observations were divided into four observing blocks (OBs), where each OB had two exposures of about 30 min each. The total integrated time was 4 h on target. Observations were carried out in the extended wide-field mode of MUSE without the correction from active adaptive optics (WFM-NOAO-E). The wavelength coverage of MUSE is 4750−9300 Å and the field of view (FOV) of $60 \times 60\,\mathrm{arcsec}^2$ with a spatial resolution of $0.2 \times 0.2\,\mathrm{arcsec}^2$ and a 1.25 Å pix^{-1} wavelength sampling. The spectral resolving power of MUSE is approximately $\lambda/\Delta\lambda = 1700$−3400, which is $\Delta\lambda = 2.82$−2.74 Å or $\Delta v = 180$−90 km s^{-1} (blue to red) in terms of resolution (Bacon et al. 2014).

2.2. Optimized data reduction

We are interested particularly in the faint extended line emission in the CGM of 4C04.11. Therefore, we explore different data reduction strategies in order to find an optimized method for further analysis. First, we use MUSE Data Reduction Software (MUSE DRS, version 2.6, the newest version is 2.8.x) pipeline[1] (Weilbacher et al. 2020) by running ESOREX (a command-line tool can be used for executing VLT/VLTI instrument pipeline) for calibration creation, observation preprocessing and observation post-processing. These three reduction stages are completed in the same default procedures for each method before adjusting the reductions. We explore the options of combining the individual exposures using the MUSE DRS pipeline and the MPDAF (MUSE Python Data Analysis Framework; Bacon et al. 2016; Piqueras et al. 2019). Furthermore, we explore the sky subtraction using the pipeline and Zurich Atmosphere Purge (ZAP, a python package developed for MUSE data based on principal component analysis algorithm; Soto et al. 2016).

We evaluate the performance of each reduction method and choose the one that maximizes the signal-to-noise ratio (S/N) for our target by qualitatively comparing the spectra extracted from different data cubes and quantitatively comparing their S/N. We extract spectra from the same apertures as in Sect. 3.1 for each cube, respectively. Then, the S/N is calculated using four wavelength ranges for each spectrum (5600−5900 Å, line-free range; 6567−6864 Å, Lyα emission range; 7400−8000 Å, line-free range; 8300−9200 Å, C IV and He II emission range). The performances of all cubes are similar. In the two line-free ranges, the optimized method (Sect. 2.2) is ∼2% better. As for the emission line ranges, the optimized method is ∼5−10% better. The skyline residuals (e.g., Sect. 4.2) are less severe in the optimized method compared to the other methods, although we still apply masking when analyzing C IV (Sect. 4.2). Through this test, we find the most optimized method for reduction of our observation of 4C04.11: all calibrations are done in the standard way following the pipeline; sky subtraction is done along with the pipeline; each derived exposure data cube goes through ZAP to remove the sky residuals; all exposures are then

[1] https://www.eso.org/sci/facilities/paranal/instruments/muse/doc.html

A&A 654, A88 (2021)

Table 1. Best fitted emission results of the 1D aperture-extracted spectrum using the MCMC method.

Ion	Line center (rest) λ_0 [Å]	Line center (obs.) λ [Å]	Line flux F [10^{-17} erg s^{-1} cm^{-2}]	Line width $FWHM$ [km s^{-1}]
Lyα	1215.67	6694.47 ± 0.59	101.82 ± 4.46	1426 ± 23
Lyα (b.l.)	1215.67	~6693.28	49.92 ± 1.26	3055 ± 38
N V	1238.82	6823.05	1.0 ± 0.2	2087 ± 250
N V (b.l.)	1238.82	~6786.93	4.3 ± 0.2	6034 ± 259
N V	1242.80	6844.97	0.5 ± 0.1	2087 ± 250
N V (b.l.)	1242.80	~6808.73	2.2 ± 0.1	6034 ± 259
C IV	1548.20	8526.98 ± 0.18	3.04 ± 1.01	1264 ± 245
C IV (b.l.)	1548.20	8497.81 ± 3.20	6.27 ± 0.84	2517 ± 143
C IV	1550.77	8541.19 ± 0.18	1.52 ± 0.50	1262 ± 244
C IV (b.l.)	1550.77	8511.97 ± 3.20	3.13 ± 0.42	2513 ± 142
He II	1640.47	9035.23 ± 0.19	8.31 ± 0.15	671 ± 19
O III]	1660.81	9147.24	1.00 ± 0.05	907 ± 68
O III]	1666.15	9176.65	1.50 ± 0.05	907 ± 68

Notes. The blueshifted component is marked as b.l. The reported errors are either the direct 1σ error bar output by the MCMC method or calculated through propagation of uncertainty from the MCMC output. We note that the "best" fitting results reported here from the MCMC method are the median values from the MCMC sampling. The line centers of the systemic N V and O III] emissions are fixed to the redshift determined from He II in this work during the fitting.

combined by MPDAF using the median absolute deviation (MAD)[2] method.

We then perform the astrometric correction to the derived data cube to improve the accuracy of MUSE astrometry. In this step, the *Gaia* Data Release 2 catalog (Gaia Collaboration 2016, 2018) is adopted for acquiring the precise coordinate of the only field star in our MUSE FOV. The position offset is calculated based on this star (fitted with a 2D Gaussian model) and applied to our MUSE observation. This uncertainty estimated in this astrometry correction is 0.007 arcsec for which a large fraction (>98%) comes from the Gaussian fitting of the field star position.

Before we can obtain the data cube for the following scientific analysis, we perform the variance scaling on the variance extension of the data cube using a source-free region of data. The variance extension of the data cube before correction often underestimates the uncertainties due to the incomplete covering of the variance sources (Weilbacher et al. 2020). The variance scale factor is 1.27. The scaled variance extension can then be used for our scientific analysis.

Finally, we note that comparing to the data cube of our target derived using MUSE DRS version 1.6 (S. Kolwa, priv. comm.), our new data cube has a more homogeneous background due to the implemented `auto_calibration` function (see Weilbacher et al. 2020) in version 2.6, which refines the IFU-to-IFU and slice-to-slice flux variations.

We estimate the seeing PSF for the combined optimized data cube to be ~0.97 arcsec in the wavelength range 6573–6819 Å, which is the range of the observed Lyα emission. This is smaller than the extension of the Lyα halo and the H I absorber #1 (Sect. 5). The central part of the Lyα emission halo is not dominated by any unresolved AGN emission such that a further PSF subtraction is not necessary and will not improve the results. The 5σ surface brightness detection limit of our data at 6695.86 Å (peak of Lyα, Table 1) is 5×10^{-18} erg s^{-1} cm^{-2} arcsec^{-2} summed over 6 wavelength channels (7.5 Å) from a 1 arcsec radius aperture. For the spectrum analyzed in this work (Sects. 3.1 and 4), the noise spectrum is also shown, which is the standard deviation derived from the variance extension of the data cube presenting the quality of the reduction.

3. Data analysis

3.1. Single aperture spectrum (master spectrum)

We first extract a spectrum from a large aperture with the goal of using this high S/N spectrum to optimize our analysis and line fitting procedures. The center of the extraction aperture is at (α, δ) = (47°56′59.″6, 5°08′03.″5). This is chosen to be at the pixel with the highest Lyα flux value from the pseudo-narrowband image collapsed between 6704 Å and 6710 Å[3] (Fig. 1 red circle). Next, we extracted three spectra using apertures with radii 0.5, 1 and 1.5 arcsec. By comparing the three spectra, we find that: the line flux (Lyα) ratio for the 0.5 arcsec to 1 arcsec is proportional to their area ratio, which means that the background does not dominate. But the line flux ratio for the 1 arcsec to 1.5 arcsec spectrum is larger than their area ratio, meaning that the contribution of the background is starting to impact the flux measurement. We therefore choose the spectrum extracted from a 1 arcsec aperture centered on the brightest pixel for the following analysis and refer to this spectrum as the "master spectrum" in the remaining parts of the paper.

The master spectrum is shown in Fig. 2 with the upper panel focusing on emission lines and lower panel focusing on the continuum. In the figure, we mark the emission lines with significant detection that our analysis will focus on: Lyα λ1216 (hereafter Lyα), C IV $\lambda\lambda$1548, 1551 (hereafter C IV), He II λ1640 (hereafter He II) and O III]$\lambda\lambda$1660, 1666 (hereafter O III]). We also mark the low S/N N V $\lambda\lambda$1238, 1243 (hereafter N V). The flux of N V is indistinctly low and highly absorbed. Additionally, its position is located in the Lyα wing making it hard to detect in the full spectrum (Sect. 4.3). Using the black dotted lines, we indicate the potential positions of Si IV $\lambda\lambda$1393, 1402 (hereafter Si IV, the overlapped O IV] quintuplet is not shown). We perform the

[2] For an univariate data set $X_1, X_2 \ldots X_n$, MAD = median$|X_i - \widetilde{X}|$, where $\widetilde{X}$ = median(X).

[3] This is also the position of the flux peak for Lyα narrowband image collapsed between larger wavelength range (e.g., 6573–6819 Å covering the entire Lyα line emission) and white light image of 4C04.11.

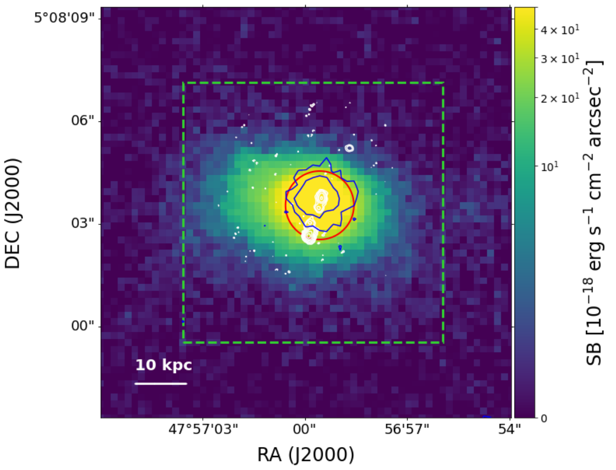

Fig. 1. Lyα narrowband surface brightness (SB) image of 4C04.11 derived from the data cube using 6704−6710 Å in the observed frame. The blue contour indicates the He II emission region. The contour is calculated from the pseudo-narrowband image of He II using 9028−9044 Å in the observed frame with the level of $3\sigma_{\mathrm{He\,II}}$ and $2 \times 3\sigma_{\mathrm{He\,II}}$, where $\sigma_{\mathrm{He\,II}}$ is the standard deviation derived from a source-less region of the He II pseudo-narrowband image. The white contour traces the position of the radio jet observed by MERLIN (Multi-Element-Radio-Link-Interferometer-Network; Parijskij et al. 2013, 2014) with the level of $0.45 \times (-1, 1, 2, 4, 16, 32, 48)$ mJy beam^{-1} following Parijskij et al. (2014). The overlaid red circle with a 1 arcsec radius marks the aperture over which the master spectrum is extracted. The green dashed box shows the FOV of individual panels in Figs. 7 and 8, which is the region we focus on in the spatial mapping in Sect. 5.

fitting of Si IV following Sect. 3.2, but the S/N is so low that the line model is poorly constrained. Hence, we consider it as an un-detection.

3.2. Spectral analysis

We fit models to the observed emission lines to study the physical properties of the gaseous halos of 4C04.11, for example the emitted flux and absorber column density. To do this task properly, we use the Gaussian or Lorentzian model to describe the emission and Voigt-Hjerting function (e.g., Tepper-García 2006, 2007) for the absorption. The fitted function (Eq. (A.8)) is composed of the emission model(s), $F_{\lambda,\mathrm{G}}$ or $F_{\lambda,\mathrm{L}}$ (defined as Eq. (A.2)), multiplied with the convolved Voigt function(s) (Eq. (A.7)). The convolution with the MUSE line-spread function is applied to account for the instrumental resolution. The decision whether Gaussian or Lorentzian function is used for modeling the emission components is made based on several reasons explained in Sect. 4. In Appendix A, we explain the definitions and equations used in our fitting. The underlying assumption made when fitting the Voigt profile to the absorption is that each of the absorbing cloud gas has a covering factor close to unity ($C \simeq 1.0$).

We use different strategies to manage the continua for different lines (see Sect. 4 and Appendix C.1 for details of different lines). The basic idea is to fit the continuum around the emission line with the emission part masked. After the continuum fitting, we then apply the nonlinear least-squares (least-squares for short) algorithm, which preforms with χ^2 minimization to fit the interested spectra. Because of the number of free parameters used in the fitting or/and insensitivity of the algorithm to one (or some) of the variables, several problems appear when running the least-squares method, for example the covariance matrix from which uncertainties of the fitting are derived cannot be produced. Then we apply a more sophisticated method, Markov chain Monte Carlo (MCMC; using the python package `emcee`; Foreman-Mackey et al. 2013), which realizes the fitting through maximizing the likelihood, to better constrain the results and determine the fitting uncertainties. To fulfill this, we perform the MCMC fitting using results from least-squares as initials. We report the results together with the χ^2_ν in Sect. 4[4].

We note that the reported “1σ” uncertainties in this paper are either the direct reported value of the 1σ confidence level from the algorithm (half the difference between the 15.8 and 84.2 percentiles) or the propagated value from this. Due to the large number of free parameters used in the fitting model and the physically limited parameter ranges, we cannot always explore the entire parameter space, that is to say, the fitting procedure seldom gives us the 3σ confidence level. Hence, we take the compromise to report the 1σ confidence level for a reference. Some of the reported formal uncertainties are too small compared to the instrumental limitations, for example the uncertainty of the line center and the spectral resolution of MUSE.

3.3. Spatial mapping method

The MUSE observations allow us to spatially and spectrally map the gaseous halo around 4C04.11. We mainly focus on the morphology, kinematics and absorption column density distribution of Lyα emission because of its high surface brightness. The spatial properties of C IV absorbers are also studied but only in two spatial apertures due to its relatively low S/N. Hence, we describe here the method we use for mapping the Lyα characteristics in this subsection and show the details of C IV together with its result in Sect. 5.2.

The first step is to spatially bin the data of the Lyα emission region to increase the S/N for the following fitting. We adopt the method from Swinbank et al. (2015), which starts at the brightest spatial pixel (spaxel) and bins the spaxels around it until the set S/N or the number of spaxels in one bin threshold is reached. The S/N threshold is set to be 13, which is close to the median value of the spaxel-based S/N in the region enclosed by the green box shown in Fig. 1 and calculated from the wavelength range 6672−6695 Å. This wavelength range is slightly bluer than the peak emission wavelength of Lyα because we are interested in the spatial distribution of the absorbers that are located in the blue wing of Lyα. The largest length of one tessellation bin is 25 spaxels (5 arcsec), which is ~5 times the size of our seeing disk (Sect. 2.2) to include any large-scale structures with low S/N. The commonly used Voronoi binning (Cappellari & Copin 2003) method is not suitable for our purposes due to the high S/N gradient across the Lyα nebula (~150 to ~10 in 20 spaxels). We manually bin some spaxels after running the algorithm to achieve a more homogeneous S/N distribution. There are 64 bins in the final result, which is shown in Fig. F.1.

Next, we fit the Lyα spectrum extracted from each bin following the description in Sect. 3.2, namely we first fit with the least-squares method and then used MCMC to refine the fit. We note that only H I absorbers #1 and #2 (see Sect. 4.1) can be identified in all bins. But for consistency we include all eight absorbers in each fit. To minimize the number of free parameters and keep the fitting of absorbers #3−8 less problematic

[4] Reduced χ^2, $\chi^2_\nu = \frac{\chi^2}{N-N_i}$, which is calculated from the best-fit MCMC model and the data as an indicator of the fitting quality, where N is the number of input data points and N_i being the number of free parameters.

A&A 654, A88 (2021)

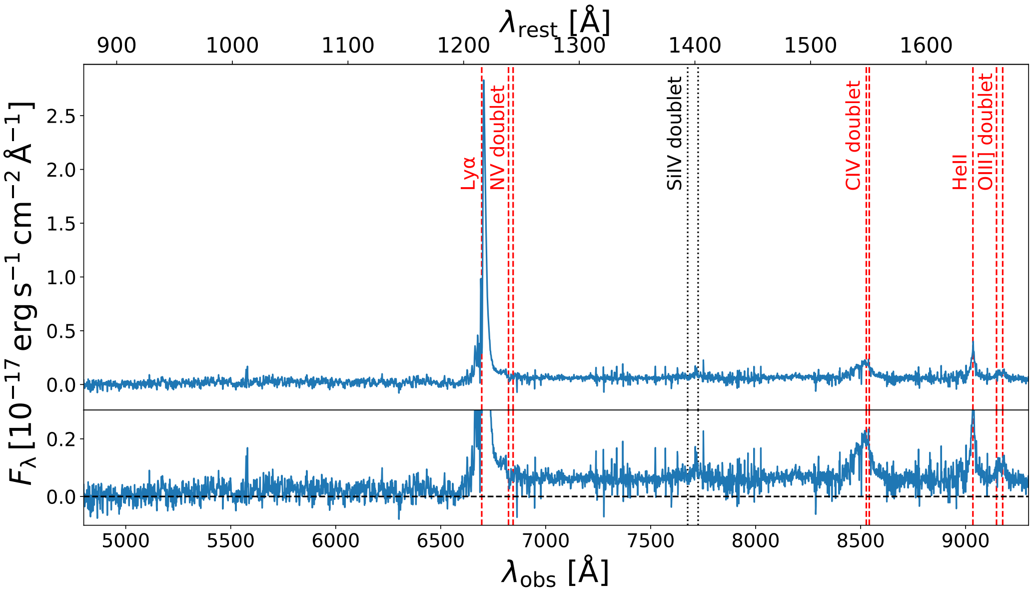

Fig. 2. Rest frame UV spectra of 4C04.11. *Upper panel*: full MUSE spectrum extracted from the central 1 arcsec aperture region. We refer to this spectrum as the master spectrum. The detected UV lines (Lyα, C IV, He II, and O III]) are marked with red dashed lines. We also mark the N V, which has a low S/N, overlaps with the broad Lyα wing, and is not obvious in this full spectrum (see Sect. 4.3). We use the black dotted line to indicate the position of the undetected Si IV. *Lower panel*: same plot as the upper panel but zoomed in to show the continuum. We note that the skyline residuals are seen as regions with higher noise. The horizontal black dashed line marks the zero flux level.

(especially for those bins where they cannot be seen), we fix the positions (velocity shifts) of these 6 absorbers using the values derived from the aperture-extracted Lyα fitting (see Sect. 4.1). We also fix the continuum fitted from each spectrum prior to including the combined Gaussian plus Voigt profiles in the fitting function. The results are presented in Sect. 5.1.

3.4. Photometry data and SED fitting

4C04.11 has multiband photometry available from previous observations, namely, B, V, R, I and K bands reported in Parijskij et al. (2014), 4 bands of ALLWISE (an extended survey of Wide-field Infrared Survey Explorer; Wright et al. 2010; Mainzer et al. 2011) archival data and *Spitzer* IRAC 1 and 2 observation (ID 70135, PI: D. Stern see Wylezalek et al. 2013, 2014, for data reduction and flux measurement). In addition, Snios et al. (2020) reported the *Chandra* 0.5−7 keV X-ray continuum detection of our target. Using these data, we preform a spectral energy distribution (SED) fitting with X-CIGALE (X-ray module for Code Investigating GALaxy Emission; Boquien et al. 2019; Yang et al. 2020, the used photometric data and fitting result are presented in Appendix B) and show the SED fit in the appendix.

We extract the unattenuated stellar emission flux at rest frame 1.6 µm from the fitted SED model from which $M_\star$ is estimated using the extrapolated IR mass-to-light ratio and galaxy age relation (e.g., Fig. 2 in Seymour et al. 2007). The 1.6 µm is a "sweet spot" for deriving $M_\star$ of HzRGs. The flux at shorter wavelengths is dominated by young stellar populations (and contaminated by emission lines) and the shape of the SED beyond the stellar emission bump at around 1−2 µm is dominated by AGN-heated dust. Hence, the flux at ∼1.6 µm is dominated by the bulk of the stellar population. We consider our stellar mass estimate of $M_\star < 6.9 \times 10^{11}\,M_\odot$ as an upper limit due to unaccounted for contributions from AGN-heated dust.

This derived upper limit of the stellar mass is quite high but comparable to other HzRGs ($1 < z < 5.2$, De Breuck et al. 2010). Therefore, taking into account the derived upper limit and the stellar masses from a large sample, we set the $M_\star$ of 4C04.11 to $\sim 2 \times 10^{11}\,M_\odot$ and use this value for following calculation. Galaxies with $M_\star \sim 10^{11}\,M_\odot$ are extremely rare ($\log(\Phi/{\rm dex}^{-1}/{\rm Mpc}^{-3}) \sim 10^{-6}$) at the redshift ($z = 4.5077$) of our object (Davidzon et al. 2017). This indicates that 4C04.11 is a rare galaxy that assembled most of its mass and formed stars when the Universe was very young. It is of great interests to study the different phases of feedback as well as the current environment of such an object.

To estimate the total (baryonic and dark matter) mass of our object, we assume the $M_\star/M_{\rm halo}$ ratio to be 0.02 (see Behroozi et al. 2013). This ratio has a large uncertainty, especially for objects at $z > 4$. For high $M_\star$ objects at high redshift with extremely low number density, it is difficult to predict from simulation works (e.g., Behroozi et al. 2019). The evolutionary trend from Behroozi et al. (2013) shows that this ratio will be higher in the early Universe for objects that are the progenitors of present day massive galaxies (assumed to be applicable to HzRGs, see Sect. 1). Hence, we adopt a conservative value of 0.02, which is the maximum ratio predicted by Behroozi et al. (2013). Then we can calculate the virial radius of the host galaxy, $R_{\rm vir} \simeq 117$ kpc, using

$$R_{\rm vir} \simeq 100\,{\rm kpc}\,(M_{\rm vir}/10^{12}\,M_\odot)^{1/3}(1+z)_3^{-1}, \qquad (1)$$

where $(1+z)_3 = (1+z)/3$ given by Dekel et al. (2013). This is accurate to a few percent for a system at $z \gtrsim 1$.

Using the following equation from the same work,

$$V_{\rm vir} \simeq 200\,{\rm km}\,(M_{\rm vir}/10^{12}\,M_\odot)^{1/3}(1+z)_3^{1/2}, \qquad (2)$$

we also calculate the virial velocity of our target to be $\simeq 583\,{\rm km\,s^{-1}}$. The virial temperature is at the order of 10^7 K. We note that these should be treated as approximation since we only take the $M_\star$ derived from the SED fitting as an upper limit and use the maximum predicted $M_\star/M_{\rm halo}$ ratio value in calculation.

4. Line fitting results

In this section we present the line fitting results of Lyα, N V, C IV + He II and O III]. We remind the readers that the metal absorbers are not as robustly detected as H I absorbers, which have well-defined trough(s) in the spectra in visual check. This is probably due to the depth of the exposure and the spectral resolution. Hence, during the fit, we assume they are at the similar redshift (velocity shift) to the corresponding H I absorbers. The reasons a subset of the absorbers are considered are presented in corresponding subsections (see Sects. 4.2 and 4.3). We refer them as "detection" if their probability distributions in the corner plots (Appendix E) are well constrained. To visually distinguish the better and poorly constrained absorbers, we use the short solid bars and dashed bars with lighter colors in the figures showing the fitting results, respectively.

We also run a test on fitting the C IV and N V without absorption. The overall shape of the C IV could be fitted without absorbers involved. However, the deep trough around 8500 Å, which is too broad to be influenced by skylines (see Fig. 4), cannot be reproduced. As for N V, the algorithm failed to reproduce the systemic emission component. Hence, we believe the absorbing material is enriched and fit the aforementioned two lines with absorbers.

4.1. Lyα

We use a double-Gaussian model to fit and estimate the unabsorbed emission. We note that Lyα is a resonant line, which makes it difficult to trace the intrinsic velocity range where the photons originated from. The double-Gaussian model used is a simple implementation to fit the high emission peak with a broad wing. This two-component fitting is also applied to the C IV and N V but with different velocity shifts (Sects. 4.2 and 4.3). This indicates there are at least two components of gas emission with different physical origins (further discussion in Sect. 6.1).

We present the best-fit model of Lyα in Fig. 3 upper panel with dark magenta line. In the figure, we mark the positions of eight H I absorbers. The best-fit parameters are presented in Table 1 (for emissions) and Table 2 (for absorption). Figure 3 middle panel shows a $N_{\rm H\,I}$ sensitivity test for the model of absorber #1. We vary the column density of absorber #1 from $10^{14}\,{\rm cm^{-2}}$ to $10^{17}\,{\rm cm^{-2}}$ with all other parameters fixed to the best-fit values and find that the profile is only sensitive to the $N_{\rm H\,I}$ near the best fit value (dark magenta line shown in the figure). This test shows that the column density variation in one absorber has little influence on the others unless it is saturated.

We include further details on the Lyα fitting procedure in Appendix C.2. The boundary conditions used for the fitting are also presented in Appendix C.2. In Appendix E we show the corner plot (Fig. E.2) and acceptance fraction plot (Fig. E.1), which traces the correlations between each pair of fitted parameters and quality of the MCMC run, respectively.

Humphrey (2019) studied the contamination of O V] $\lambda\lambda$1213.8,1218.3 (hereafter O V]) and He II λ1215.1 emissions for high-redshift Lyα emitters (Type-2 quasars, HzRGs). In general, the contribution from He II λ1215.1 is insignificant while the O V] emission can contribute 10% (or more) to the Lyα + O V] + He II λ1215.1 flux if certain ionization parameter and metallicity are given. By using the grid model search,

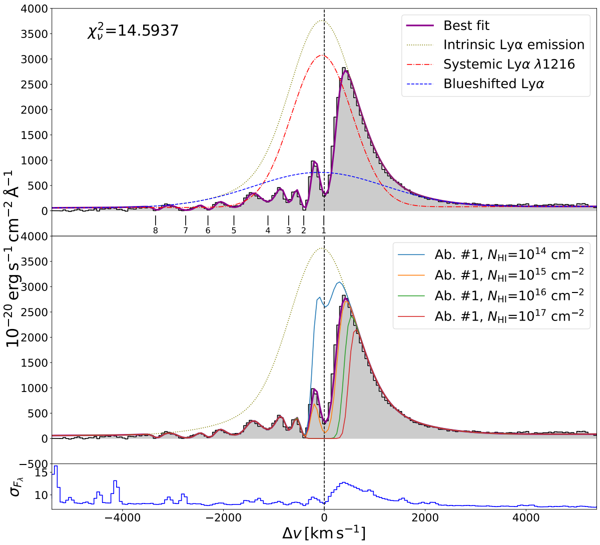

Fig. 3. Lyα fitting result and model sensitivity check. *Upper panel*: best fitting result of the master Lyα line using the MCMC method. The dark magenta line represents the best fit, while the dotted olive line traces the overall Gaussian emission. The systemic emission is shown in a red dotted-dashed line, and the blueshifted emission is marked by a blue dashed line. The positions of all eight absorbers are shown in this panel with black vertical bars. The χ^2_ν is reported as an indicator for the quality of the fit. We note that the small flux excess at $\gtrsim$4000 km s^{-1} is the contribution from N V (Sect. 4.3). *Middle panel*: column density sensitivity check of the Voigt model. The overall intrinsic Gaussian (dotted olive line) and best-fit model (dark magenta line) are the same as in the upper panel. The other lines show how the fitting result will change by only adjusting the column density of absorber #1 to values at $\log(N_{\rm H\,I}/{\rm cm^{-2}}) = 14$, 15, 16, and 17. These lines demonstrate that this fitting is only sensitive to the $N_{\rm H}$ values around the best fitting result. *Lower panel*: standard deviation (noise) of the spectrum derived from the variance extension of the data cube that is used as the weight (inverse) in the fitting. It is shown in the same units as the spectrum and can be used to trace the skylines. We note that the Lyα line suffers less from strong skylines in −4200 to 5500 km s^{-1} compared to Hanuschik (2003).

Humphrey (2019) proposed a correlation between O V] and N V, which can be used to estimate the significance of the contamination. To test how O V] will affect the H I fitting result, which is the primary goal of this work, we run the fit of Lyα including the emission doublet of O V]. In this test, the total O V] flux is fixed to $2.5F_{\rm N\,V}$ according to Humphrey (2019) with $F_{\rm N\,V}$ being the total fitted N V flux (Sect. 4.3) in this work. We also fix the FWHM of O V], a nonresonant line, to the value derived from He II (Sect. 4.2). The results of the 8 H I absorbers, especially the $N_{\rm H\,I}$, are similar to the fitting results without O V]. Therefore, we do not include the O V] into the Lyα fitting in order to avoid introducing more free parameters.

4.2. C IV and He II

The first line we focus on is He II, which is the brightest nonresonant line often used for determination of the systemic redshift of HzRGs observed in optical band (e.g., Swinbank et al. 2015; Kolwa et al. 2019). The nonresonant photons are produced through the cascade recombination of He$^+$; they are not energetic enough to induce other transitions and suffer less from scattering than resonant lines (e.g., Lyα). Previous work (Kopylov et al. 2006) determined the redshift of

Table 2. Best absorption fitting results of the 1D aperture-extracted spectrum using the MCMC method.

Abs. #	Ion	Redshift z	Absorber wav. λ [Å]	Velocity Δv [km s^{-1}]	Column density log(N/cm^{-2})	Doppler b [km s^{-1}]
1	Lyα	4.5075 ± 0.0001	6695.34 ± 0.02	-9 ± 6	14.843 ± 0.004	187 ± 1
	N V	–	6822.84	–	14.99 ± 0.05	387 ± 12
	C IV	4.5083 ± 0.0005	8527.91 ± 0.76	32 ± 38	13.9 ± 0.2	198 ± 43
2	Lyα	4.5002 ± 0.0001	6686.44 ± 0.04	-408 ± 6	15.53 ± 0.14	73 ± 4
	C IV [(a)]	–	8515.37	–	<12.07	–
3	Lyα	4.4947 ± 0.0001	6679.76 ± 0.05	-707 ± 6	14.72 ± 0.01	110 ± 3
	C IV [(a)]	–	8506.86	–	<13.05	–
4	Lyα	4.4872 ± 0.0001	6670.61 ± 0.09	-1116 ± 8	14.85 ± 0.02	265 ± 7
	C IV	4.4872 ± 0.0006	8495.28 ± 0.87	-1114 ± 44	14.24 ± 0.08	271 ± 42
5	Lyα	4.4748 ± 0.0001	6655.54 ± 0.12	-1791 ± 9	14.77 ± 0.01	231 ± 7
6	Lyα	4.4653 ± 0.0001	6644.04 ± 0.14	-2306 ± 10	14.70 ± 0.09	88 ± 10
7	Lyα	4.4572 ± 0.0002	6634.17 ± 0.19	-2748 ± 13	14.81 ± 0.04	165 ± 11
8	Lyα	4.4462 ± 0.0002	6620.83 ± 0.22	-3345 ± 15	<15.46	~40

Notes. The un-reported values and values without uncertainties are fixed parameters during the fit using the values from corresponding H I absorbers. [(a)]The C IV absorber #2 and #3 are poorly constrained (see Appendices C.3 and E.2 and Fig. E.4 for discussion and their probability distributions). We only report the fitted column density results as upper limit.

4C04.11 from the resonant Lyα line, which also heavily suffers from absorption (see Sect. 4.1). Hence, our fitting of the He II will provide a better estimate of the systemic redshift.

C IV and He II are located in the wavelength range that is affected by many strong skylines (Fig. 4, 8200−9300 Å, see Hanuschik 2003, for skylines observed at Paranal). Additionally, this wavelength range is near the edge of spectral coverage of MUSE. To obtain better results from these two low S/N lines, we have to reduce the number of free parameters used during the fitting. For this purpose, we (i) fit C IV together with He II and constrain the line center of the systemic C IV component with the redshift determined from He II; (ii) fix the continuum to a first-order polynomial during the emission and absorption fitting; (iii) use a Lorentzian profile for the systemic He II and C IV to avoid an additional Gaussian component; (iv) include only 4 C IV absorbers and fix the Doppler parameters and redshifts of absorber #2 and #3 (further descriptions are presented in Appendix C.3).

The best-fit model of He II and C IV are presented in Fig. 4 while fitted parameters are shown in Table 1 and Fig. 4 for emission and absorption (only C IV), respectively. The systemic redshift calculated from the intrinsic He II emission is 4.5077 ± 0.0001, which is a significant improvement compared to Kopylov et al. (2006) (~10 Å, in observed frame or -1888 km s^{-1} difference of the He II center wavelength). We detect and report a blueshifted C IV emission component (blue dot-dash and dotted line in Fig. 4) with a relatively high velocity shift of $\Delta v = -1026 \pm 112$ km s^{-1}. The high blueshifted velocity component is also detected in N V (Sect. 4.3, further discussion in Sect. 6.1). The intrinsic C IV (and He II) emission is shown in thick yellow dotted line from which it is clear that the absorption is needed to describe the line profile, especially the trough around 8500 Å. The standard deviation derived from the data reduction is shown in the lower panel of Fig. 4, which is used as weight in the fitting as well as tracer of the skylines. We excluded several regions (shaded yellow) that are affected heavily by skyline residuals during the fit. We note that there are two regions of skylines (overlap with C IV absorbers #1 and #4) that are already given a low weight during the fit. Hence, we do not mask them in order to avoid complicating the absorption fit.

In Appendix E.2, we present the corner plot (Fig. E.4) and acceptance fraction plot (Fig. E.3) which traces the correlations between each pair of fitted parameters and quality of the MCMC run, respectively. From the corner plot, we notice that C IV absorbers #2 and #3 are loosely constrained. Therefore, we only consider the column densities of absorbers #2 and #3 as upper limits (see Appendices C.3 and E.2 for a further discussion). To visually distinguish them from the better constrained absorbers #1 and #4, we use the dashed bars and lighter colors for absorbers #2 and #3 in Fig. 4.

Nesvadba et al. (2017a) analyzed 4C04.11 with SINFONI observation (the Spectrograph for INtegral Field Observations in the Near Infrared; Eisenhauer et al. 2003; Bonnet et al. 2004) which reported the detection of the [O II]$\lambda\lambda$3726, 3729 ([O II]), a nonresonant line, with good S/N (Fig. 11). The redshifts reported by Nesvadba et al. (2017a) based on [O II] fitting are 4.5100 ± 0.0001 and 4.5040 ± 0.0002 for the two narrow Gaussian components used, respectively. Our fitted systemic redshift is in between these two values, which we consider to be reasonable and consistent with the near infrared observation (see Fig. 11). In addition, the authors detect and include a broad blueshifted component ($\Delta v \simeq -240$ km s^{-1}, $FWHM \simeq 1400$ km s^{-1}). We use the Lorentzian profile for the systemic He II because the S/N in this wavelength range of our data is not enough to constrain the fitting with two Gaussian (Appendix C.3). We further discuss this in Sect. 6.1.

The blue wing of He II is too noisy to constrain whether there is a blueshifted component. We present three emission models of the blueshifted He II in Fig. 4 (black dashed, dotted and dash-dotted lines) with velocity shift and FWHM fixed to the blueshifted component of C IV. The line flux of this components are set to be 0.2 (dashed), 0.3 (dotted) and 0.4 (dash-dotted) of the total fitted flux of the blueshifted C IV. From this we can estimate a lower limit of $F_{\rm C\,IV,b.l.}/F_{\rm He\,II,b.l.} \gtrsim 3.3$. We discuss this result further in Sect. 6.1.

4.3. N V

To fit the low S/N N V on top of the broad wing of Lyα and relatively high continuum, we fix the Lyα to the one derived in

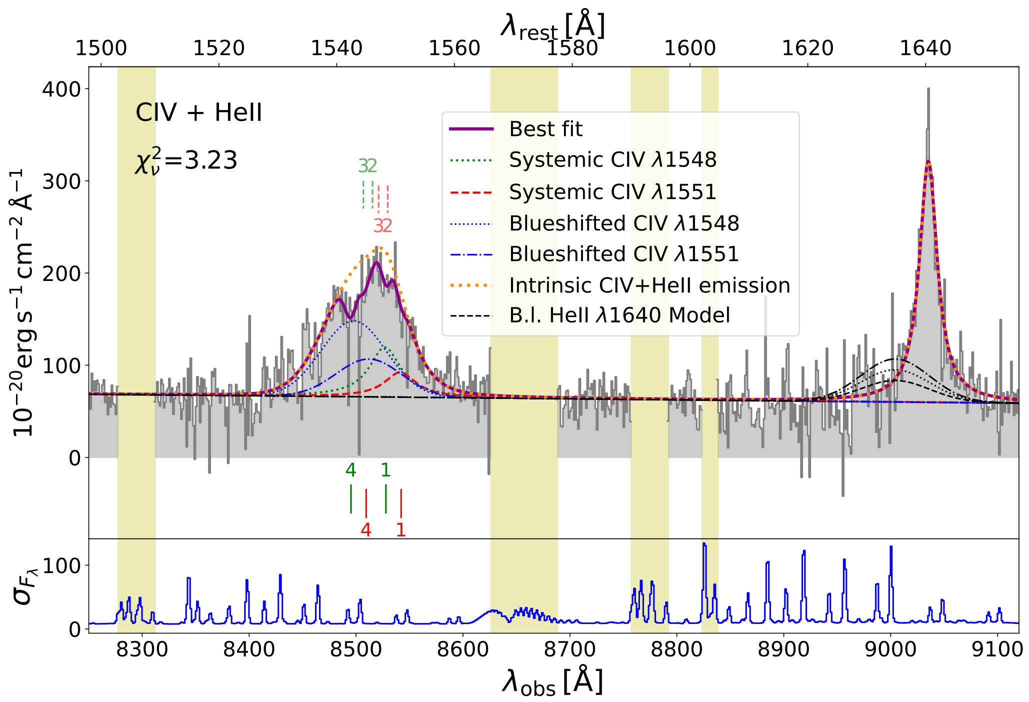

Fig. 4. Best fit of the C IV and He II lines from the master spectrum using the MCMC method. We use the dark magenta line to trace the best fit of these two lines. For the intrinsic C IV and He II, the yellow dotted line is used. We mark the systemic emissions of the C IV doublet in dotted green and dashed red lines and blueshifted emissions in dotted and dot-dash blue lines. The χ^2_ν of the fit is reported to give a hint of the quality of the fit. The yellow shaded regions are excluded during the fit because it is severely affected by skylines (compared with the Hanuschik 2003 data; see also the standard deviation in the *lower panel*, which offers an alternative proof of the positions of the skylines). The short green (red) vertical bars with numbers show the positions of the absorbers on top of the C IVλ1548 (C IVλ1551) line. Absorbers #2 and #3 are marginally constrained (see text), and hence their positions are shown in dashed bars with lighter numbers. The black lines are models of blueshifted He II lines with FWHM and velocity shift fixed to the fitted values from the C IV blueshifted component. The dashed, dotted, and dash-dotted lines show the line flux of 0.2, 0.3, and 0.4 of the total fitted flux of the blueshifted C IV. *Lower panel*: standard deviation (noise) of the spectrum derived from the variance extension of the data cube, which is used as a fitting weight. It is shown in the same units as the spectrum and can be used to trace the skylines.

Sect. 4.1 and use a constant continuum during the N V fitting. The fitting procedure is then carried out following Sect. 3.2 (see Appendix C.4 for details of the N V fitting).

We show the best-fit N V model in Fig. 5 and the fitted parameters in Tables 1 (emissions) and 2 (absorption). The blueshifted emission component is at $\sim-1587\,\mathrm{km\,s^{-1}}$ which is consistent with the C IV blueshifted component[5]. The large value of Doppler parameter, $b\simeq 387\,\mathrm{km\,s^{-1}}$, could be due to unresolved redshifted H I absorber(s) and/or it is influenced by the skyline subtraction. However, we cannot constrain more without deeper and higher-resolution data. We remind the readers that this fit is limited by the low S/N of the data and depends strongly on the Lyα broad wing and it should be treated with caution. In Fig. 5, the positions of the marginally constrained absorber are shown. Given the degeneracy between b and N (e.g., Silva et al. 2018a), the $N_{\mathrm{N\,V},1}$ should be treated as lower limit. The black dashed line in Fig. 5 shows the combined emission structures from all sources (lines and continuum) without absorption. It is clear that at least N V absorber #1 is necessary to fit the data. We note the presence of skylines overlapping with N V (lower panel in Fig. 5), which are already given a low weight in the fitting. Hence, we do not mask them in order to avoid complicating the absorption fitting. We further discuss the interpretation of the emission and absorption results in Sects. 6.1 and 6.3.1, respectively.

In Appendix E.3 we present the corner plot (Fig. E.6) and acceptance fraction plot (Fig. E.5), which traces the correlations between each pair of fitted parameters and quality of the MCMC run, respectively.

4.4. O III]

For 4C04.11, the O III] doublet is detected. Although the O III] is near the He II, we fit them separately in order to avoid introducing more free parameters into the C IV + He II fit, which is one of the major focuses of this work. The fit is preformed following Sect. 3.2 with the line centers and underlying continuum fixed to the systemic redshift implied from He II (Sect. 4.2) and to the model derived in Sect. 4.2, respectively. We present the result of the O III] fitting in Fig. 6 and Table 1. The corner plot and the acceptance rate are shown in Appendix E.4.

5. Spatial mapping

In this section we present the spatial mapping results for Lyα and C IV. The Lyα emission is analyzed by following the method described in Sect. 3.3 and can be studied in detail in both emission and absorption. As mentioned in Sect. 3.3, C IV is detected at low S/N and its quality suffers from skyline contamination.

[5] Though this reported velocity shift is bluer than the one of C IV blueshifted component taking uncertainty into account, the value of $\sim-1500\,\mathrm{km\,s^{-1}}$ will also give C IV a good fit. See Appendix C.4 for more details.

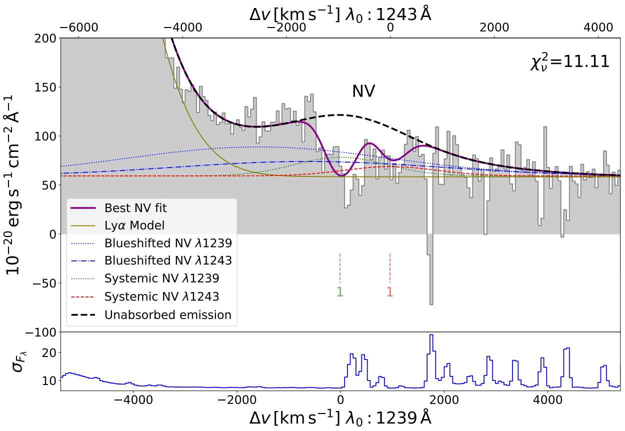

Fig. 5. N V best-fit model from MCMC method. The dark magenta line shows the best N V fit combined with the Lyα from Sect. 4.1. The black dashed line marks all combined emissions without absorption. The systemic emissions are marked in dotted green, and dashed red curves show the doublet. The zero velocities of the systemic emissions for the doublet components are derived from the He II result. The blueshifted components are shown in dotted and dot-dash blue lines for the doublet. The solid olive line shows the Lyα model, which is fixed in the N V fit. The short green (red) vertical bars with numbers show the positions of the absorbers on top of the N Vλ1239 (N Vλ1243) line. The dashed line style and lighter color are used to indicate that N V absorber #1 is marginally constrained (see text). The χ^2_ν of the fit is reported to give a hint of the quality of the fit. *Lower panel*: standard deviation (noise) of the spectrum derived from the variance extension of the data cube that is used as the fitting weight. It is shown in the same units as the spectrum and can be used to trace the skylines.

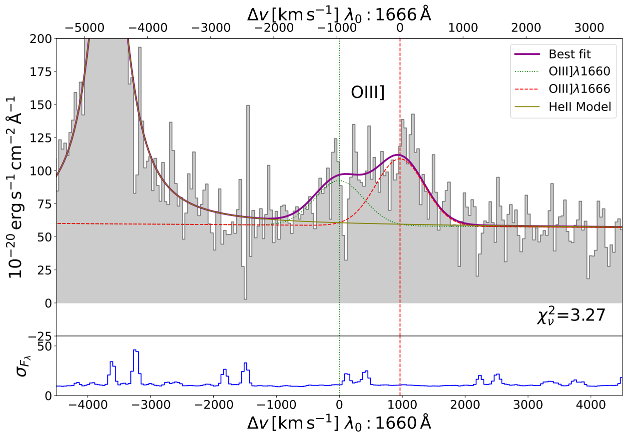

Fig. 6. O III] best-fit model using the MCMC method. The dark magenta line shows the best O III] fit combined with the He II from Sect. 4.2. The emissions of the O III] doublet are shown in dotted green and dashed red curves. The line centers of the systemic emissions expected for the doublet components from the He II implied redshift are shown in vertical dotted green and red lines. The solid olive line shows the He II model that is fixed in the O III] fit. The χ^2_ν of the fit is reported to give a hint of the quality of the fit. *Lower panel*: standard deviation (noise) of the spectrum derived from the variance extension of the data cube that is used as a fitting weight. It is shown in the same units as the spectrum and can be used to trace the skylines.

For C IV, we therefore only focus on the results from two larger spatial regions in Sect. 5.2. It is impossible to fit the N V spatially due to its extremely low S/N even in the master spectrum.

5.1. Spatially resolved Lyα signatures

We first present the morphological and kinematic features of Lyα emission derived from the spatially resolved fitting analysis (Fig. 7). In each panel, we show the measured parameters in 64 spatial bins identified through our binning method in Sect. 3.3. In Fig. 7a, we show the intrinsic Lyα surface brightness (SB) map. It is important to note that this shows the integrated Lyα flux derived from the Gaussian emission model (summation of the two components; see Sect. 3.2), after correction for the H I absorption. The extended emission to the north, encompassing the northern jet hotspot, is due to the large size of the bin (see Fig. F.1, bin 59). The position of the SB peak coincides with the radio core (central green contours). In all panels of Figs. 7 and 8, we overplot this intrinsic Lyα SB as black contours. In Fig. 7b, we present the W_{80} map generated from the unabsorbed Lyα emission. W_{80} is a nonparametric measurement of the velocity width of emission lines (e.g., Liu et al. 2013). We notice the W_{80} peaks close to the southern jet hotspot, which is likely the approaching jet because of its clumpier morphology, which in turn could be caused by Doppler beaming (Parijskij et al. 2014). While we consider that result as tentative, it may be a signature of jet-gas interactions (e.g., Humphrey et al. 2006; Nesvadba et al. 2017a). We present the v_{50} map in Fig. 7c, which is a nonparametric measurement of the velocity shift of the emission profile (e.g., Liu et al. 2013) independent of interpreting the individual Gaussian components added to the fit. The result suggests the existence of blueshifted Lyα emission. However, since the map is based on fitting and estimating the intrinsic, unabsorbed Lyα emission (i.e., it is not fully nonparametric), we do not interpret it further.

Figure 8 shows the column density and velocity shift maps for absorbers #1 and #2, which are the two prominent absorbers detected in every spatial bin suggesting high areal fractions. We note that we show here the velocity shift with respect to the mean velocity of the respective absorber Δv as derived from the from the master spectrum (see Table 2). In Fig. 8a, we identify a column density gradient in absorber #1 from southwest (SW) to northeast (NE), which is roughly in the perpendicular direction to the radio jet axis with an increasing of 1 dex in 24 kpc. We consider this as a robust detection after checking the associated uncertainties in each bin. In Fig. 8b, we identify a small velocity gradient for absorber #1 along the direction of the jet increasing from ~ -50 km s^{-1} in the southeast (SE) to ~ 35 km s^{-1} in the northwest (NW) in 20 kpc. In Sect. 7, we discuss possible explanations for these observations.

We do not observe such gradients or spatial variations in the column density and velocity shift maps of absorber #2 in Figs. 8c and d. We note that the fitting uncertainties for absorber #2 are larger compared to those for absorber #1, such that any small variations would not show up in our analysis. This also demonstrates that our observations only provide us with enough sensitivity to study the spatial properties of H I absorber #1. Hence, we do not show the maps for absorbers #3–8. During the analysis of the spatial properties of the C IV absorbers, we also extract and fit the Lyα spectra from the two spatial apertures (see Sect. 5.2 for details) that partly constrain the high-velocity shift of the H I absorbers at different positions. The results of the fitted parameters are presented in Table G.2. Though the S/N is low and some absorbers are only partially constrained, we do not observe any significant changes in column density for absorber #3−8 in the two regions. We notice that we do not

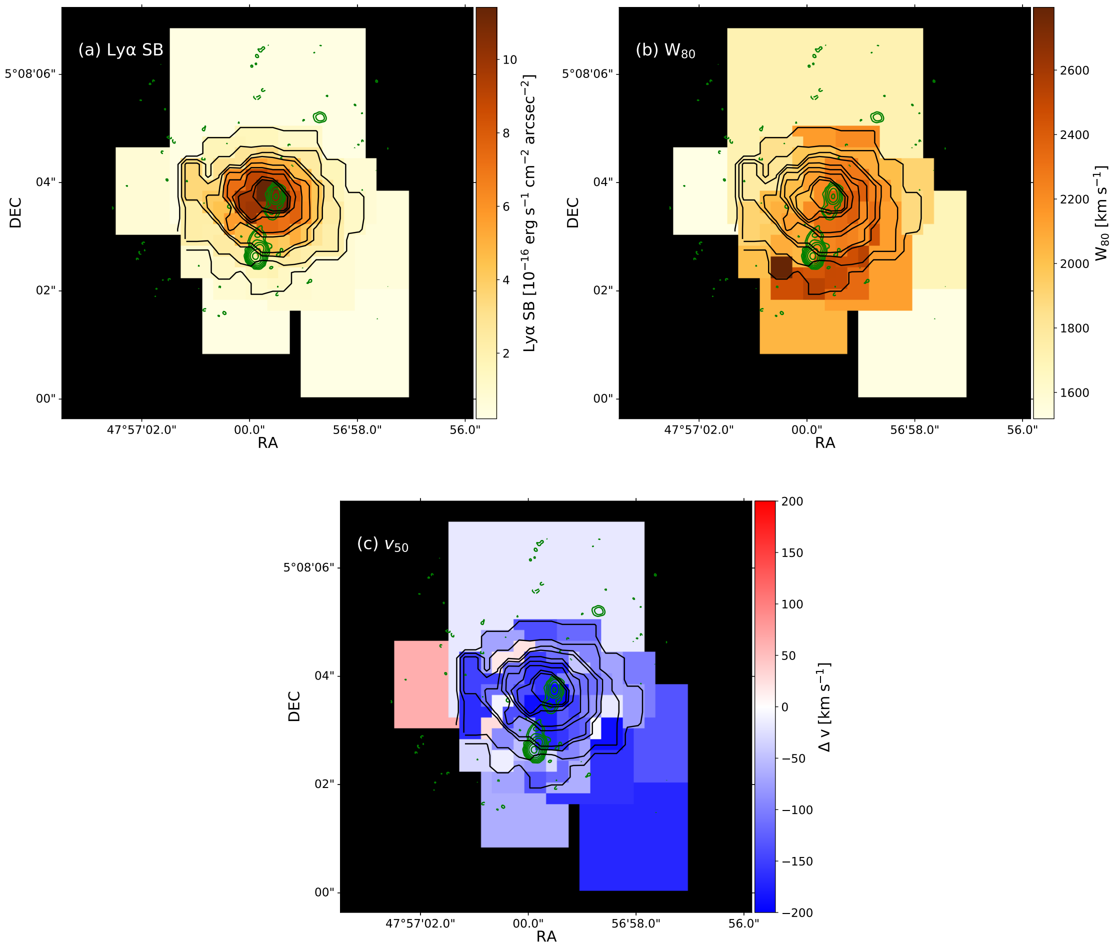

Fig. 7. Spatial mapping results of Lyα emission. The contours are the same in all panels, with the green showing the position of the radio source (see the Fig. 1 caption for details; Parijskij et al. 2013, 2014) and black tracing the Lyα surface brightness resulting from spatial fitting (the levels are given arbitrarily). All these maps are constructed based on the fitting results, i.e., not directly from the data. (*a*) Intrinsic surface brightness map of Lyα emission. (*b*) W_{80} map of Lyα emission (nonparametric measurement of the line width; see text). (*c*) v_{50} map of the fitted Lyα emission profile (nonparametric measurement of the line-of-sight velocity; see text).

observe any strong velocity gradients for any of the absorbers. We therefore exclude the possibility of absorber spatial blending, that is, absorbers identified at the same wavelength position could not be different absorbers in different spatial bins.

In Appendix F, Figs. F.2–F.5, we present the fitting results of 64 individual Lyα spectra from the 64 spatial bins.

5.2. Spatially resolved C IV signatures

We present the spatial analysis of C IV in this section. As mentioned in Sect. 3.3, the S/N of C IV makes it difficult to study its spatial variations in as much detail as Lyα. However, since we observe a column density gradient of H I absorber #1 (Sect. 5.1), it is worthwhile to investigate whether the C IV shows similar features. We manually set two regions from which we extract spectra (Fig. 9): NE where the column density of H I absorber #1 is higher and SW where the column density of H I absorber #1 is lower. When selecting the apertures, we keep the same number of spaxels (30 spaxels or $1.2\,\mathrm{arcsec}^2$) in these two regions and avoid the impact of the jet. Most of the spaxels in these two regions are covered in the master aperture (red circle in Fig. 9) in order to be consistent with the 1D spectrum analysis.

For the spectral fitting, we follow the similar strategy described in Sects. 3.2 and 4.2. The fitting results from these two regions are presented in Table G.1 for emissions and Table G.2 for absorption. In Fig. 10, we show the best-fit models of the two C IV lines. The intrinsic C IV emission shown in the figure indicates that the absorption is indeed needed to better describe the line profile, especially in the NE. The quality of the C IV fits is affected by their low S/N partly due to smaller aperture from which the spectra are extracted and the influence of skylines. To avoid over-fitting, we fix the Doppler parameters, b, and redshifts, z, of all absorbers in the two regions and refer to the column density results as upper limits. The exception is the column density of C IV absorber #1 in the NE region, which has a well-defined probability distribution and is considered a detection (see Appendix G and Fig. G.1 for more details). In Fig. 10, we mark the positions for the un-constrained absorbers in dashed bars with lighter colors to visually distinguish them from absorber #1 in the NE region.

In addition, we extract the Lyα spectra from these two regions and perform the fitting analysis (Fig. 10) with the goal to compare the column density ratio of the C IV and Lyα absorber #1 (results shown in Tables G.1 and G.2). We measure

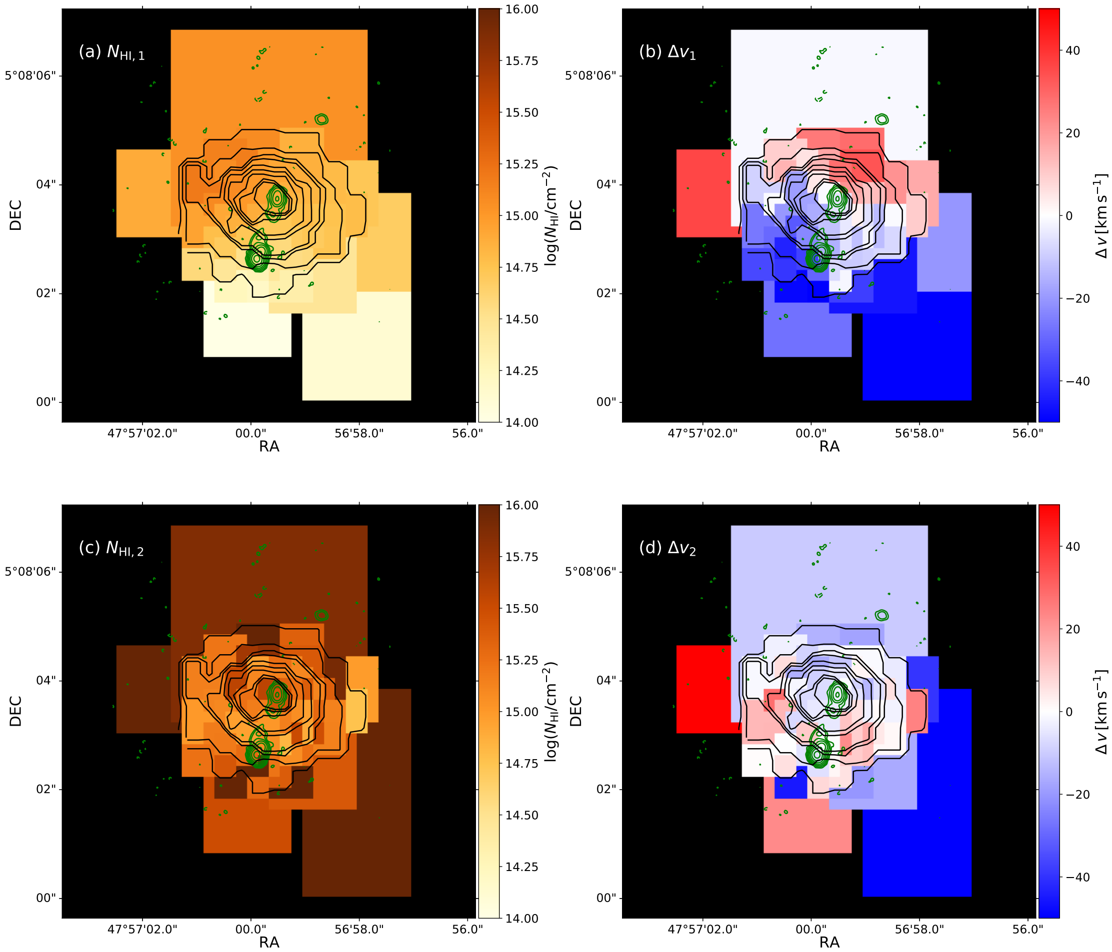

Fig. 8. Column density and velocity shift maps of H I absorber #1 (*panels a* and *b*) and #2 (*panels c* and *d*). The black contours are the same as in Fig. 7. The zero points for the velocity shift maps are chosen individually to be the Δv of each absorber as derived from the master spectrum fitting reported in Table 2. The maps therefore show the velocity shifts relative to the redshift of the respective absorber.

$N_{\mathrm{C\,IV,NE}}/N_{\mathrm{H\,I,NE}} = 0.11 \pm 0.04$, and $N_{\mathrm{C\,IV,SW}}/N_{\mathrm{H\,I,SW}} < 0.04$ and further interpret this result in Sect. 6.3.2.

We also perform the similar analysis for another two regions along the radio jet for completeness (not shown in Fig. 9). The two regions are chosen to be the similar as the previous dark blue and magenta ones but rotated 90° clockwise with respect to their geometric center. The column density variation in C IV absorber #1 is also tentatively identified along this direction as well as the H I–C IV ratio (SE-NW) with NW region having a higher value. Specifically, the C IV absorber #1 is only marginally fitted in the SE region with its result can only be used as upper limit. We also check the velocity shift of the H I absorber #1 in the two regions (SE-NW) along the radio axis and confirm the gradient observed in Fig. 8.

6. Discussion

6.1. Emission line properties

Emission line fluxes, flux ratios and spatial locations of individual kinematic components provide powerful diagnostics of gas properties and ionization source. In this work, we detect five UV lines, namely Lyα, N V, C IV, He II and O III]. Lyα is a resonant line that suffers heavily from scattering, making it difficult for us to trace its intrinsic velocity structures (e.g., Dijkstra 2014). Although we detect a blueshifted broad component, we refrain from assigning it a physical meaning and do not to compare it with the blueshifted components seen in N V and C IV.

6.1.1. Emission line characteristics

We first compare the emission line properties for Lyα and He II detected with MUSE in this work and the [O II] from SINFONI (Nesvadba et al. 2017a). In Fig. 11, all lines are shown within the velocity range where the zero point is set by the systemic redshift derived from the He II fit. For Lyα and He II, their best fits from this work are shown. In addition, we include the fitted line centers of the narrow component of the [O II] doublet (pink dotted lines) and the broad component (pink dot-dash line) (Nesvadba et al. 2017a), respectively. We note that the wavelength calibration for SINFONI is done using the vacuum wavelength while MUSE uses air wavelengths. To eliminate this discrepancy, we apply the equation from Morton (2000) to convert all wavelengths into air wavelengths[6]. We did not correct

[6] $\lambda_{\mathrm{air}} = \lambda_{\mathrm{vac}}/n$, where $n = 1 + 8.34254\times10^{-5} + 2.406147\times10^{-2}/(130 - s^2) + 1.5998\times10^{-4}/(38.9 - s^2)$, $s = 10^4/\lambda_{\mathrm{vac}}$ and λ_{vac} in the unit of Å.

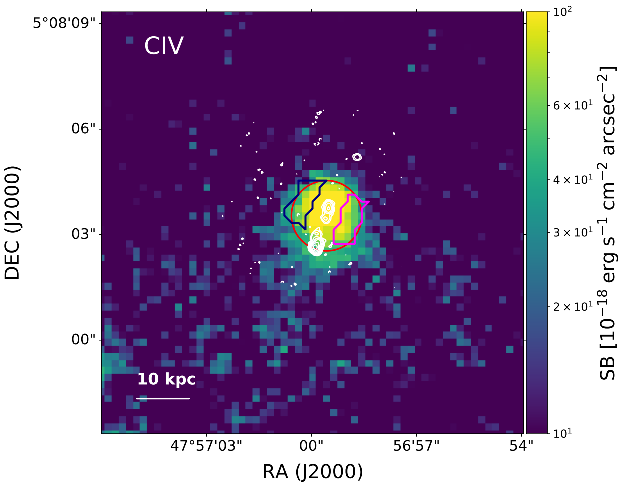

Fig. 9. C IV broadband image clasped between 8400–8600 Å in the observed frame. The white contour traces the radio jet, while the red circle marks the position where the spectrum analyzed in Sect. 4 is extracted (see the caption of Fig. 1). The dark blue and magenta regions show the apertures from which the spectra used to studied the spatial features of C IV are extracted. The spectrum from the dark blue (magenta) region is marked as NE (SW).

the difference in wavelength due to the heliocentric frame used in SINFONI observation, which is $\sim$30 km s^{-1}.

In the He II panel, we show again the three blueshifted models with the line center fixed to the value obtained from C IV fit as in Fig. 4. The velocity of the C IV blueshifted component is indicated by the vertical dashed blue line in He II and [O II] panels. From this figure, we conclude that the broad blueshifted component observed in [O II] ($\Delta v \simeq -240$ km s^{-1}, $FWHM \simeq 1400$ km s^{-1}) is not seen in He II. Though affected by resonant scattering, the blueshifted Lyα component is consistent with the blueshifted component seen in [O II] and they both may trace emission from the same potential outflow. The high-velocity blueshifted component (as seen in C IV), however, is possibly also present in [O II]. We discuss this in Sect. 6.1.2 together with N V and C IV. The marginally detected continuum in Nesvadba et al. (2017a) is consistent with our MUSE observation.

6.1.2. Emission line ratios and sources of ionization

We next investigate the emission line flux ratios for the individual kinematic components that we observe for N V, C IV, and He II in order to determine the ionization mechanism. In Sect. 4, we report the fitted intrinsic emission line fluxes of these three lines. The derived flux ratios are presented in Table 3. For N V and C IV, the flux ratio between their systemic emission line components is $F_{\rm N\,V,sys}/F_{\rm C\,IV,sys} = 0.32 \pm 0.09$ (which is comparable to other HzRGs; e.g., De Breuck et al. 2000). The ratio between the systemic C IV and He II components is $F_{\rm C\,IV,sys}/F_{\rm He\,II} = 0.55 \pm 0.14$.

For the blueshifted components, the velocity shifts (with respect to the zero point set by the systemic He II) of the C IV (-1026 ± 112 km s^{-1}) and N V ($\sim$$-1587$ km s^{-1}) are roughly consistent and we therefore assume that they are tracing the same kinematic component of the gas (more detail on Appendix C.4). The flux ratio between the blueshifted components has a value of $F_{\rm N\,V,b.l.}/F_{\rm C\,IV,b.l.} \simeq 0.7$. We do not clearly observe a blueshifted component in He II. This is a somewhat different situation compared to observations in other HzRGs. For example, in MRC 0943–242 (a HzRG in our MUSE+ALMA sample, Kolwa et al. 2019) a blueshifted component is observed in C IV ($E_{\rm C\,IV} = 64.5$ eV) and He II but not N V. Nevertheless, in order to constrain its flux, we plot three models of the blueshifted He II with velocity shift and FWHM fixed to the values of blueshifted C IV and having flux 0.2, 0.3 and 0.4 of $F_{\rm C\,IV,b.l.}$ (Sect. 4.2, Fig. 4). From this, we can set a lower limit of $F_{\rm C\,IV,b.l.}/F_{\rm He\,II,b.l.} \gtrsim 3.3$.

Feltre et al. (2016) presents emission-line diagnostics at ultraviolet wavelengths of photoionization models of active and inactive galaxies with the aim is to identify new line-ratio diagnostics to discriminate between gas photoionization by AGN and star formation. According to their models (Figs. 5 and 7 in Feltre et al. 2016) the ionization source for the systemic kinematic component that we observe in N V, C IV and He II (Table 3) is consistent with photoionization from an AGN, though the C III] data are unavailable. This is also consistent with the diagnostic from Nakajima et al. (2018), which involves the equivalent width of C IV (EW(C IV$_{\rm sys}$) $\simeq 12$ Å) and $F_{\rm C\,IV}/F_{\rm He\,II}$. As for the ionization source of the blueshifted component, the diagnostic from Feltre et al. (2016) indicate it to be due to star formation only with our derived upper limit of $F_{\rm C\,IV,b.l.}/F_{\rm He\,II,b.l.}$. Using EW(C IV$_{\rm b.l.}$) $\simeq 26$ Å and $F_{\rm C\,IV,b.l.}/F_{\rm He\,II,b.l.} \gtrsim 3.3$ and comparing to Fig. 11 in Nakajima et al. (2018), the diagnostics are consistent with the region where ionization from both AGN and star formation are possible. This is surprising given even extreme star formation processes are unlikely to drive such a high-velocity outflow (see Heckman et al. 2015).

High-velocity shocks (due to the radio jets) may be another possible solution to explain the blueshifted emission line component. Dopita & Sutherland (1995, 1996) modeled the shock ionization process and provided spectral line diagnostics that can be applied to narrow line regions (NLRs) of AGN. De Breuck et al. (2000), Humphrey et al. (2008b) used these models to analyze samples of HzRGs and suggested some limitations of these models. Allen et al. (2008) extended the Dopita & Sutherland (1995, 1996) models to embrace larger parameter ranges. Due to the limited number of available spectral lines for 4C04.11 (e.g., lacking useful diagnostic lines [O III]$\lambda\lambda$4959, 5007, C III]$\lambda\lambda$1906, 1908 and C II]λ2326), we cannot draw strong conclusions on shock ionization scenarios. Nevertheless, with the inferred high $F_{\rm C\,IV,b.l.}/F_{\rm He\,II,b.l.}$ and $F_{\rm N\,V,b.l.}/F_{\rm He\,II,b.l.}$ (Table 3), the blueshifted emission is not inconsistent with being due to shocks. This is also consistent with [O II] if the flux excess seen at $\sim$$-1000$ km s^{-1} (Fig. 11) comes from the same gaseous component with C IV and N V.

We remind the reader that the uncertainties associated with our flux and flux ratio measurements are non-negligible and deeper data are needed to investigate the true nature of the individual gaseous components. Our observations nevertheless indicate that the blueshifted kinematic component observed in N V and C IV traces a metal-enriched (see Sect. 6.3) gaseous outflow within the ISM of 4C04.11 that is distinct in both kinematics and ionization mechanism from the systemic component.

We further investigate the differences between the blueshifted- and systemic components by assessing their respective spatial locations. Usually, the broad component will have compact (often un-resolved) spatial distribution if it is AGN-driven. We compare the spatial locations of these two components from pseudo-narrowband images of C IV focused on its blue wing (8400–8500 Å, $-4464 < \Delta v < -948$ km s^{-1})

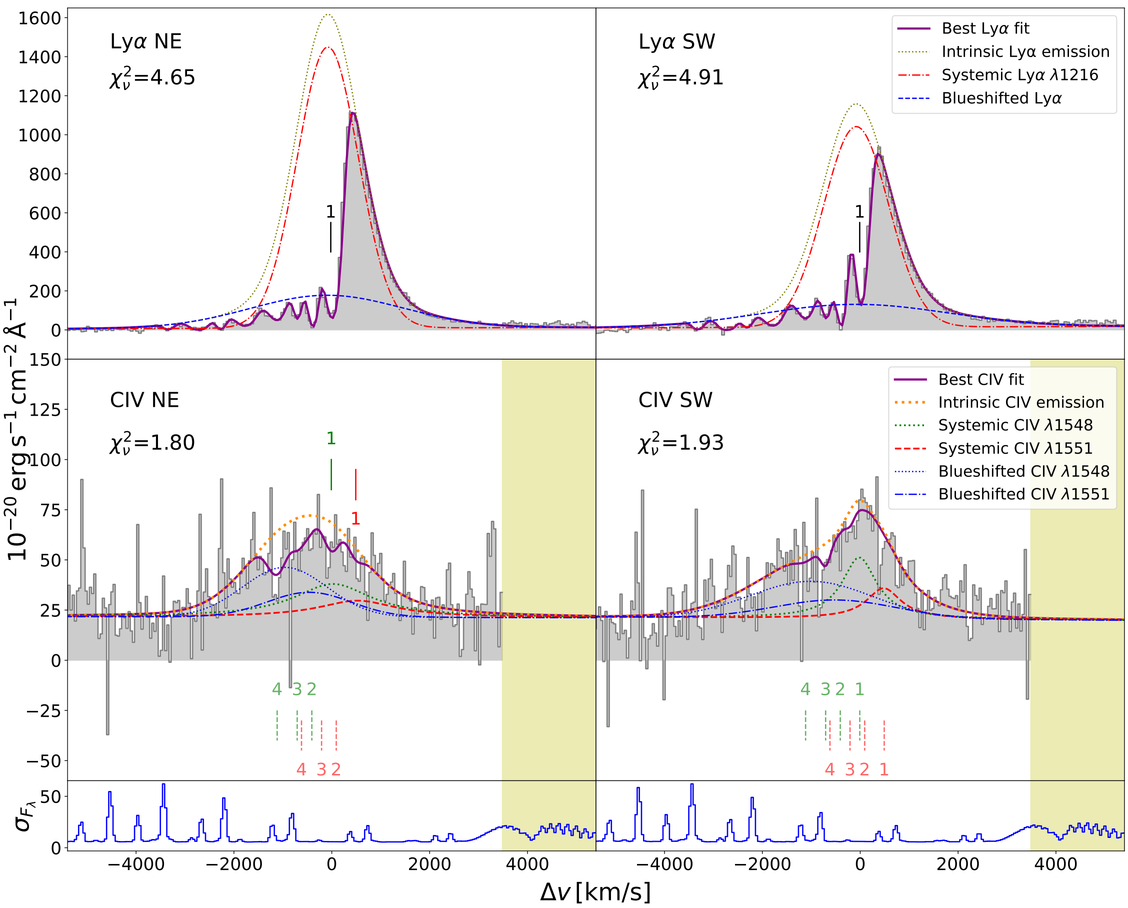

Fig. 10. Spectra and fit of Lyα (*top row*) and C IV (*middle row*) and noise spectra of C IV (*lower row*) extracted from the dark blue (NE) and magenta (SW) regions shown in Fig. 9. The positions of H I absorber #1 are marked with black bars in the top row. The velocity shift is relative to the systemic redshift, z = 4.5077, fitted from He II (Sect. 4.2). The line styles used to show the fitting results are the same ones as that of the master Lyα (Fig. 3) and C IV (Fig. 4). We note that except for C IV absorber #1 detected in the NE region, the positions for the other C IV absorbers are marked in dashed bars, with lighter colors indicating that they are only marginally constrained (see text), which is consistent with the "master C IV" presentation (Fig. 4). The intrinsic C IV emission is also shown in orange dotted lines for the two spectra in the middle row. The panels in the *bottom row* show the standard deviations (noise) of the C IV spectra derived from the variance extension of the data cube, which are used as fitting weights. They are shown in the same units as the data spectra and can be used to show the quality of the spectra and trace the positions of skylines.

and on its red wing (8500–8600 Å, $-948 < \Delta v < 2567\,\mathrm{km\,s^{-1}}$), respectively. The S/N of the N V is too low to preform this check. We do not observe a significant spatial difference as the two components are located around the center of the Lyα SB peak with a extension of ~3 arcsec (~2 for the blue wing), which is larger than the seeing element. The large detected line widths of the blueshifted components (Table 1) could also represent a set of individual clouds that are not spatially nor spectrally resolved in our data leaving the possibility open for the AGN being the primary ionization source.

6.2. H I absorbers

When fitting the absorption features in Sect. 3.2, we work with the assumption where several extended screens of gas are responsible for the absorption troughs. This assumption is justified as we coherently observe the signatures of H I absorbers #1, 2, 3, and 4 across large spatial scales, which indicates large areal fractions. The spatial extent for absorbers #1 and 2 is ~$30 \times 30\,\mathrm{kpc}^2$ (Fig. 8) and ~$16 \times 16\,\mathrm{kpc}^2$ for #3 and 4 whose maps are not shown in this paper due to their low S/N. For clarification, the presence of absorber #3 and 4 (and further) cannot be obviously identified in the tessellation bins 50–64 (see Figs. F.1–F.5) based on which their spatial extent is determined. The screens may be part of a shell similar to the shell models proposed by many theoretical works, for example Verhamme et al. (2006) and Gronke et al. (2015). For absorber #1, with the highest S/N in our data, we furthermore observe a significant column density and velocity gradient (Sect. 5.1), which we discuss separately in Sect. 7. However, our observations are not sensitive enough to probe the spatial (morphological and kinematic) details of absorber #2 (Sect. 7) or any of the higher-velocity absorbers.

As for absorbers #5–8 (which have velocity shifts with respect to the systemic redshift of -1791 ± 9, -2306 ± 10, -2748 ± 13 and $-3348 \pm 15\,\mathrm{km\,s^{-1}}$, respectively), their spatial distributions are difficult to identify since they are located in the blue, low S/N wing of Lyα and are therefore only observed in

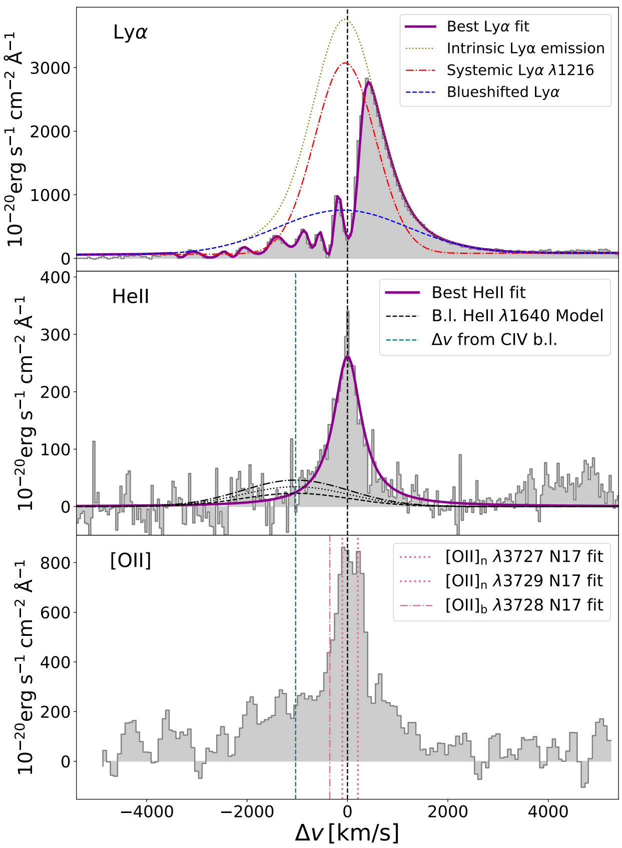

Fig. 11. Comparison between the Lyα, He II, and [O II] rest-frame spectra. The Lyα and He II presented here are the same ones analyzed in Sects. 4.1 and 4.2 in velocity scale. We subtract the continuum from the He II here to better present the low flux region of the emission. The black lines are the same ones as shown in Fig. 4 for the blueshifted He II models, with the dashed, dotted, and dash-dotted lines indicating the line flux of 0.2, 0.3, and 0.4 of the total fitted flux of the blueshifted C IV. The [O II] is taken from SINFONI (Nesvadba et al. 2017a). In each panel, the black dashed lines indicate the zero velocity. In the last two panels, the dashed vertical teal blue lines show the velocity shift of the C IV blueshifted component. For Lyα and He II, the best fit models from this work are shown. We also mark the fitted line centers of the [O II] narrow doublet from Nesvadba et al. (2017a) in pink dotted lines and the broad component line center in a pink dash-dot line.

the high surface brightness regions of Lyα close to the center of the host galaxy. They may have a larger spatial extent but this cannot be constrained without deeper observations. Additionally, we note that there is a large velocity shift difference between H I absorber #4 and #5, ~600 km s^{-1}. Absorbers #5−8 are therefore likely intervening absorbers between the radio galaxy and the observer beyond the galaxy potential well. The reason that many of these intervening absorbers have large b values when compared to related works about Lyα forest absorption (e.g., Rauch 1998; Schaye et al. 2000; Fechner & Reimers 2007) is probably due to the spectral resolution of MUSE not resolving individual components of connect narrower absorbers (e.g., van Ojik et al. 1997; Jarvis et al. 2003).

If the velocity shift for absorbers #2−4 corresponded to a cosmological redshift difference as is probably the case for absorbers #5−8, we can calculate the physical separation between central radio galaxy and the absorber. For absorber #2, which has the smallest shift, the luminosity distance difference between it and the systemic redshift is 84 Mpc, much larger than the virial radius of the host galaxy, $R_{\rm vir} \simeq 175$ kpc (Sect. 3.4). Hence, if the physical distance was the reason for the velocity shifts, all absorbers would be gravitationally unbound to the host galaxy. In contrast, if the velocity shift was caused by the kinematics of an outflowing shell, the absorption troughs can and should be observed on large spatial scales, which they are. Given the velocity offset of absorbers #2, 3, and 4 derived from the master spectrum and their spatial extent (i.e., large areal fraction), we therefore conclude that they are likely outflowing gas shells potentially driven by the AGN.

While the other absorbers (#5−8) are very likely intervening absorbers, we cannot fully exclude from our data that they may represent fast-outflows. For example, Kriss et al. (2018) investigates ultrafast X-ray outflows (UFOs) seen in AGN in absorption and their relation with the associated H I and other lower-ionization ions, such as C IV. These UFOs with $v_{\rm out} \gtrsim 0.1c$, where c is the speed of light, are much more extreme cases of outflows compared to our observations. Absorber #8, if it was an outflow, would have a velocity of $0.01c$. In addition, the H I absorption widths predicted by the UFOs are much wider than our observations ($FWHM \sim 1000$ km s^{-1}), their column densities are lower ($<10^{14}$ cm^{-2}) and the required ionization parameter is higher (e.g., compared to absorption studies in other HzRGs; Kolwa et al. 2019). All this indicates that the UFOs seen in X-ray and Lyα absorption studied by Kriss et al. (2018) trace a different scenario than the absorbers in 4C04.11. Even if there was UFO-associated H I absorption for 4C04.11, it would be located at much shorter wavelengths where the continuum level is too faint to allow them to be detected.

Table 3. Line flux ratios and equivalent width.

	$F_{\rm C\,IV}/F_{\rm He\,II}$	$F_{\rm N\,V}/F_{\rm C\,IV}$	$F_{\rm N\,V}/F_{\rm He\,II}$	EW [Å]
sys.	0.55 ± 0.14	0.32 ± 0.09	0.17 ± 0.02	~12
b.l.	$\gtrsim 3.3$	0.7 ± 0.1	$\gtrsim 2$	~26

Notes. The line flux of C IV and N V are summations of the doublet. The sys. and b.l. indicate that the derived values are for the systemic or blueshifted, respectively. We note that the EW derived should be treated as lower limit as the continuum level may be overestimated.

6.3. Metal absorption

6.3.1. Metal absorbers in the master spectrum

Relative column density ratios between different elements can provide information on the enrichment of the gas assuming an ionization parameter. The underlying assumption for the metal absorbers analyzed here is that they are ionized by the central AGN (e.g., Kolwa et al. 2019). Constraining whether this AGN photoionization is geometrically possible is beyond the scope of this work given the resolution of the data and the limited knowledge of the evolution state and ionization episode of the radio galaxy. Hence, we do not discuss more about the source(s) of ionization for the metal absorbers and proceed with the discussion of the following implication with the assumption of central AGN ionization. One hint on the AGN ionization could be due to the wide ionization cone that covers some fraction of the absorbing gas seen (e.g., Fig. 12). Nevertheless, we remind the reader that the shocks or a hard source of ionization (for example, AGN of meta-galactic background) inferred by the presence of a high column density N V absorber (see blow) could also be possible.

In this work, we identified the absorbers around the systemic redshift of H I, C IV, and N V in the master spectrum, which we sassume belong to the same cloud. The corresponding ratios are $N_{\rm C\,IV,1}/N_{\rm H\,I,1} = 0.12 \pm 0.05$ and $N_{\rm N\,V,1}/N_{\rm H\,I,1} = 1.4 \pm 0.2$. We remind the readers that the $N_{\rm N\,V,1}$ should be treated as a lower limit given that the Doppler parameter associated with it hits the upper boundary (Appendix C.4). Comparing this with CLOUDY (spectral synthesis code, Ferland et al. 2017) models (the same models as Fig. 17 in Kolwa et al. 2019), we can roughly estimate that absorber #1 has (super) solar metallicity ($Z \gtrsim 1\,Z_{\odot}$) independent of a specific assumption for the ionization parameter. The derived $N_{\rm N\,V,1}$ value is consistent with the conclusion. This suggests strongly that absorber #1 has an origin inside the ISM of the radio galaxy. Given the age of the Universe at $z = 4.5077$, it is unlikely that absorber #1 is the infalling material that has been enriched by a previous outflow and is now recycled through a galactic fountain mechanism. The column density, $N_{\rm N\,V} \sim 14.99\,{\rm cm}^{-2}$, is relatively high. As discussed in Kolwa et al. (2019), the secondary nitrogen production is responsible for the nitrogen column density enhancement of the absorber if the gas has (super) solar metallicity (also Hamann & Ferland 1993). Hence, though the CNO cycle for the secondary carbon and nitrogen can produce solar N/C ratio over a large range in metallicities (e.g., Nicholls et al. 2017), $Z \gtrsim 1\,Z_{\odot}$ is needed, which is consistent with our conclusion here. We further discuss the nature of absorber #1 in Sect. 7 combining the metallicity and spatial features observed in H I.

For absorber #2 and #3, their column density results can only be treated as upper limits. The corresponding ratios of H I absorbers are $N_{\rm C\,IV,2}/N_{\rm H\,I,2} \sim 3{\times}10^{-4}$ and $N_{\rm C\,IV,3}/N_{\rm H\,I,3} \sim 0.02$. In addition, absorber #4 has the ratio of $N_{\rm C\,IV,4}/N_{\rm H\,I,4} = 0.25 \pm 0.05$. It is difficult to confine the metallicities of these three absorbers without the data from N V. Nevertheless, the ratios are indicative of the absorbers having sub-solar metallicity according to the CLOUDY models ($Z \lesssim 0.5\,Z_{\odot}$), except for absorber #4, which could have solar metallicity. From the discussion in Sect. 6.2, we consider these three absorbers as outflowing gaseous clouds with the one having the highest velocity shift (absorber #4) being the most recently ejected. Combined with the proposed scenario of absorber #1 in Sect. 7.1, the low metallicity of absorbers #2–#4 can be explained: Absorber #1 was ejected first and carried most of the metal elements produced in the early star formation activities. The timescale between the ejection of absorber #1 and the later ejected clouds (absorbers #2–#4) was then not large enough to enrich the gas again to solar like metallicity. If we take it further that this may explain the latest absorber #4 has higher metallicity than absorber #2 and #3 because it has the longest time to be enriched, though this is impossible to be proved and has large uncertainties.

The reason we do not observe C IV absorber#5–#8 could be that they are located in the low S/N emission wing. Considering the discussion in Sect. 6.2, however, this could be alternatively explained as they are intervening absorbers outside the potential well of the central radio galaxy (IGM) and they consist of cold, un-enriched pristine gas.

6.3.2. Spatial distribution

As derived in Sect. 5.2, the column density ratios between the H I and C IV absorber #1 are 0.11 ± 0.04 and <0.04 for the $N_{\rm C\,IV,NE}/N_{\rm H\,I,NE}$ in the NE and $N_{\rm C\,IV,SW}/N_{\rm H\,I,SW}$ in the SW, respectively. This is considered to be consistent with the observed H I column density in absorber #1. We compare these two ratios with the CLOUDY models and find that, despite the lack of spatial information of N V, the NE cloud may have solar metallicity ($Z_{\rm NE} \gtrsim 0.5\,Z_{\odot}$), while the metallicity of the SW cloud may be sub-solar ($Z_{\rm SW} \lesssim 1.0\,Z_{\odot}$). Readers should bear in mind that the inferred metallicity of absorber #1 in these two regions are derived from low S/N spectra and should be treated with caution.

If we assume these two regions have similar metallicity, this is consistent with the analysis in Sects. 6.3.1 and 7.1 that absorber #1 is an outflowing shell that is enriched homogeneously by star formation activities in the ISM prior to the launch of the outflow.

On the other hand, if we assume the NE region has higher metallicity than the SW region, it suggests a spatially inhomogeneous enrichment. This could indicate merger activities or unevenly dilution due to cosmic accretion of metal-poor gas. Given that the S/N of the two C IV spectra (especially the SW one), we do not further interpret the result.

7. Large-scale characteristics of H I absorber #1

In this section we discuss several possible explanations for the observed properties (areal fraction, kinematics, column density gradient) of the H I absorber #1 (Sect. 5.1). The H I absorbers #1 and 2 are the only two absorbers in our analysis with a high enough S/N to perform the spatial analysis. We identify a significant column density gradient of absorber #1, but not for absorber #2 (Fig. 8) suggesting a relatively uniform distribution within the uncertainties of our fitting analysis. The data quality does not allow us to spatially map any of the higher-velocity absorbers and we briefly discuss their potential nature in Sect. 6.2. We argue that the absorbing gas responsible for absorber #1 is spatially detached from the Lyα emitting gas since we do not observe any similarity between the kinematics of the absorbing and emitting components (Figs. 7b, c, and 8b). The opposite situation may be seen in the blue absorber in TN J1338–1942 (a HzRG in our ALMA-MUSE sample) where the velocity shift maps of the emission and absorption show resemblance (Fig. 4 in Swinbank et al. 2015) and indicate that emitting and absorbing gas are mixed.

Recently, Gronke et al. (2016, 2017) showed simulations of Lyα radiative transfer through a medium where detailed subparsec structures are considered, which is a more realistic model than a continuous shell model. It should be noticed that our spatial mapping of the column density of H I absorber #1 is far from sensitive enough to probe the details in the absorption medium. In addition, Gronke et al. (2017) concluded that the resultant spectral features of their clumpy model are similar to a shell model, that is, the observational features are not affected much by the absorbing medium being either clumpy or a continuous shell. Hence, we only present simple explanations to the reported column density and velocity gradient (Fig. 8) and use the simulation works to assess them to first-order, leaving sophisticated modeling for future works. For example, Peeples et al. (2019) simulated the CGM on a sub-kiloparsec scale and find that the absorbing gas responsible for observed feature around several hundreds of km s^{-1} in velocity shift range may span hundreds of kiloparsecs in space. It is impossible even for the state-of-the-art instrument like MUSE to probe the real morphology of the CGM gas given that we can only observe features in projection.

7.1. Outflowing shell

We first consider the model of an outflowing gas shell to explain the column density and velocity shift gradient we identify for

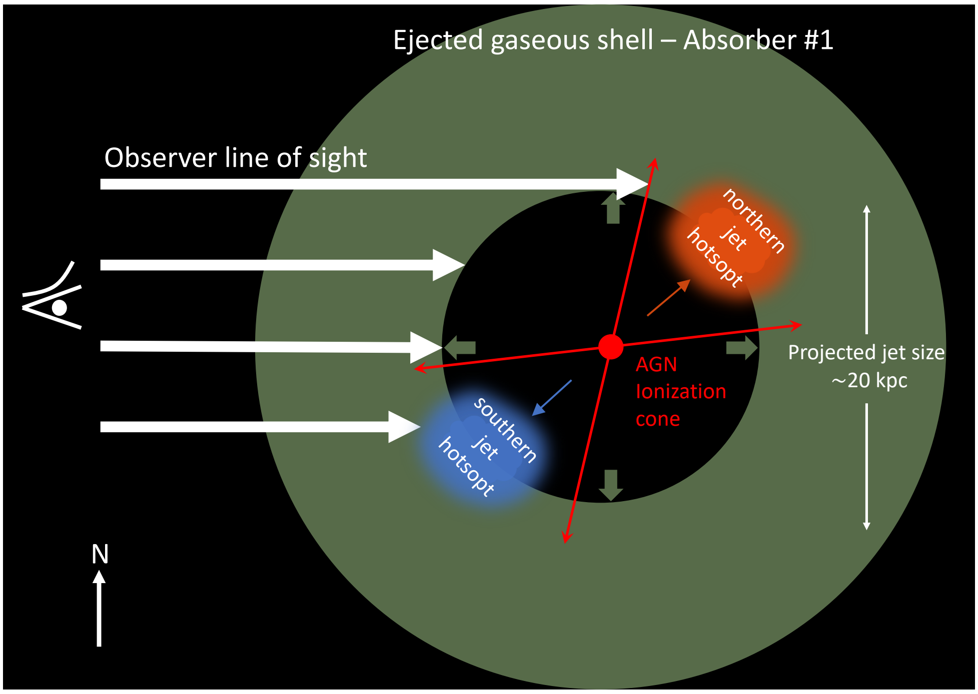

Fig. 12. Schematic view of the proposed outflowing shell model in Sect. 7.1. The large dark green annulus represents the outflowing gaseous shell that could be the absorbing cloud of absorber #1. The blue and orange regions mark the southern (approaching) and northern (receding) jet hotspot interacting with the previous ejected shell, respectively. We note that the morphology of the gaseous shell is not necessarily in a circular shell as shown here, and we do not have information for the shell at the backside of the AGN. The red lines in the annulus center indicate the region of the AGN ionization cone that could have a wider opening angle than the jet beam (see text). The column density gradient we observed in Sect. 5.1 in the S-N (SW-NE, due to the orientation on the sky plane, which is not shown here) direction could simply be explained by the different lengths of the observer line of sight intersecting with the gaseous shell at different spatial locations (see text). This process is shown with the length of white arrows intersecting with the dark green annulus in the figure. For the column density decreasing after passing the midplane, which cannot be explained by the geometry setting, the southern jet (blue region) interaction with the ejected gaseous shell could cause the decreasing of column density through instabilities and/or partially ionizing the gas. Though the rough projection size of the jet is shown, we note that other parts of this sketch are not to scale.

H I absorber #1. We remind the reader that absorber #1 is at $\sim 0\,\mathrm{km\,s^{-1}}$ and covers a large area of the sky (Sects. 4.1 and 5.1) approximately on scales of $30 \times 30\,\mathrm{kpc}^2$. We identify a column density gradient along the SW-NE direction increasing over 1 dex in 24 kpc. We also check Lyα spectra extracted from the two spatial regions along the radio jet in the SE-NW direction (the two regions for completeness study of C IV spatial mapping in Sect. 5.2) where we also marginally identify the column density gradient.

Following Binette et al. (2000, 2006), Krause (2002, 2005), we propose that the absorbing material of absorber #1 is a wind-driven gaseous shell. The wind may have been powered by stellar feedback and/or AGN activity several tens of megayears before the radio jet was launched. The wind traveled isotropically with its speed decreasing from thousands of $\mathrm{km\,s^{-1}}$ within 1 kpc to a few $\mathrm{km\,s^{-1}}$ at 10 s of kpc (may even halt or fall back; Krause 2005; Wagner et al. 2013; Richings & Faucher-Giguère 2018). Tens of megayears after the beginning of the shell expansion, the relativistic jet is launched. The jet that travels at a few tenths of the speed of light catches up with the previously ejected shell in a few megayears (Parijskij et al. 2014), accelerates and disturbs it. The age of the jet could be even smaller ($\sim$1 Myr) in the scenario described here if an earlier galactic wind has cleared the surrounding leading to fewer interactions of the jet traveling inside the wind-driven shell. The velocity gradient along the radio axis we see in Fig. 8b could be a hint for this jet gas interaction. Using polarization measurements, Parijskij et al. (2014) reported that the southern (northern) jet is very likely the approaching (receding) one, which agrees with absorber #1 velocity shift map (the southern part of absorber #1 is the blue-shifted part). In Fig. 12, we show a schematic presentation of the proposed scenario where the SW-NE column density gradient may be explained by the spatially different intersected length between the observational line of sight (thick white arrows on the left of the figure) and the gaseous shell (absorber #1, dark green annulus). This is a similar situation to the sunlight traveling a longer path through the Earth's atmosphere when the altitude of the Sun is low and causing more scattering. For the column density decreasing in the northern half of the shell, the gradient may be explained by this geometry. The southern jet, which we believe is the approaching one, may be responsible for the observed column density keeping decreasing in the southern half of the gaseous shell. The approaching and receding jet-gas interaction hotspots are marked in Fig. 12 as blue and red regions, respectively. As the figure shows, the approaching jet catches and disturbs the gaseous shell probably through Kelvin–Helmholtz instability in its surrounding (e.g., Mukherjee et al. 2020). The interaction will cause a decrease in the particle number density (Mukherjee et al. 2020) in the immediate vicinity of the jet hotspot (or the jet may even ionize a part of the cooled gas). Hence, the combination of the two aforementioned effects will result in the observed column density and velocity gradient.

Though we mark the approximate projected size of the observed jet, readers should bare in mind that the Fig. 12 is not to scale. We note that the red lines mark the regions of the AGN ionization cones as the radio jets are narrow collimated streams (i.e., opening angles; e.g., Drouart et al. 2012; Obied et al. 2016) of the ionization cones are suggested to be wider than the jet beams. Besides, the jet-gas interaction hotspots are smaller regions compared to the gaseous shell; nevertheless, we emphasize them in Fig. 12 with larger symbols.

Several simulation works have shown the possibility of AGN wind expelling medium to kiloparsec scales (e.g., Wagner et al. 2013, for an AGN driven wind accelerating the surrounding medium to $\sim$1000 km s^{-1} within 1 kpc). Oppenheimer et al. (2020) specifically studied the impact of AGN feedback on the CGM. This research shows that feedback can drive out the metal elements, which could explain the metal-enrichment of absorber #1 in our observations. The authors reported that the expulsion of metal elements beyond the virial radius, for example like C IV in our case, takes longer with a timescale of 0.5–2.5 Gyr. Hence, on smaller timescales, such as a few hundred megayears, the CGM can be enriched with the gaseous metal-enriched cloud still within the galactic potential well like the case of 4C04.11. Furthermore, Richings & Faucher-Giguère (2018) showed that swept up gas can efficiently cool within an outflow, which could be one possible origin for the neutral gas that absorber #1 consists of.

In Sect. 6.3 we discussed the enrichment of absorber #1, which is also observed in N V and C IV, suggesting that the absorbing cloud has super solar metallicity. This supports the proposed scenario in which the outflowing shell is launched from within the galaxy where the gas has been enriched through star formation activities. It furthermore suggests that we are observing the redistribution of metals through feedback processes and the enrichment of both the ISM and the CGM. Our previous analysis in Sect. 6.3 is based on the assumption that the metal absorbers (N V and C IV) are ionized by the AGN. This could be possible if the opening angle of the ionization cone is wide enough to cover some fraction of the absorber #1 gaseous shell (like the scenario shown in Fig. 12).

It may be too coincident for absorber #1 to be at $\Delta v \sim 0$ km s^{-1}. Even considering the reported 1σ fitting uncertainty, the range of the velocity shift is still close to 0. We notice that the spectral resolution of MUSE, $\sim$100 km s^{-1}, is much larger than the MCMC reported probability distribution range. Hence, the absorption could have some intrinsic velocity with respect to the systemic redshift of the radio galaxy, which would need to be verified with high-resolution spectroscopy.

7.2. Absorption by large-scale CGM gas

Peeples et al. (2019) showed the simulation of the FOGGIE project (Figuring Out Gas & Galaxies in Enzo), which focuses on the CGM. In their work, the authors presented the absorption characteristics of the CGM gas on scales of hundreds of kiloparsecs with considerable column density for both H I and metals (for example, C IV). An alternative scenario for the characteristics of our absorber #1 is therefore that it consists of gas in the CGM, which extends tens to hundreds of kiloparsecs and has a complex sub-structure beyond the detectability of MUSE. This gaseous cloud is the surrounding medium unrelated to the ejected material by the central radio galaxy. In this scenario, the column density gradient could be due the uneven concentration nature of the CGM gas as shown in Peeples et al. (2019). The tentative velocity gradient may be invoked through a rotation of the large-scale medium. For a system of virial mass on the order of $10^{13}\,M_\odot$, the virial velocity is around 500 km s^{-1} (Sect. 3.4), which is larger than the value we observe. While unlikely, this inconsistency between the observed velocity gradient (-50 km s^{-1} to 35 km s^{-1}, Fig. 8b) of absorber #1 and the virial velocity could be due to a combination of the MUSE spectral resolution and projection effects.

This gaseous halo could be on its way to being accreted onto the central galaxy to feed the SMBH and/or star formation activities. The observed radio jet with a projection length of $\sim$20 kpc (Parijskij et al. 2014) could be well within the giant CGM gas halo and unrelated if the aforementioned scenario is the case. The high column density part in the north may be related be the inner part of inflow, which is denser according to the simulation presented by Mandelker et al. (2020). The spatial extent of this inflow could be up to $\sim$60 kpc in our case, which covers the detected absorber #1 well ($0.5\,R_{\rm vir}$; see Sect. 3.4; Mandelker et al. 2020).

Although this scenario can explain the H I column density and the surrounding medium can be enriched to a small extent, it is difficult to reconcile super solar metallicty with this scenario (Sect. 6.3.1, and especially the high column density of N V). Hence, we consider the model proposed in Sect. 7.1 as the more probable situation.

7.3. Alternative models

Alternatively, the double-peak structure of the Lyα spectrum (which we believe is due to the H I absorber #1) with the trough at $\sim$0 km s^{-1} could be explained by other numerical models.

The absorbing gas could be entrained within the jet and detached from the jet path, which could explain the tentative velocity gradient. After the detachment, the gas will gradually slow down, which could explain its low velocity shift around 0 km s^{-1}. This model, however, has problems to reproduce the observed column density gradient in the direction roughly perpendicular to the radio jet.

The absorbing H I gas we see may be the product of the "positive feedback" from the jet interaction with the ISM/CGM (e.g., Croft et al. 2006; Gaibler et al. 2012; Fragile et al. 2017). In this situation, we could ignore the self-gravity of the gas due to the dark matter dominated potential (Fragile et al. 2017), which could explain the velocity shift of around 0 km s^{-1} of the H I absorber. The jet compresses the CGM gas on its path. The higher H I absorber #1 column density in the NE could be that the line of sight passing longer length in the northern part given the jet orientation (similar to the geometric effect proposed in the outflowing model, Sect. 7.1). This could also in principle explain the observed tentative velocity shift gradient. This explanation again, however, has the shortcoming to reproduce the metal enrichment of absorber #1.

8. Conclusions

In this paper we present MUSE observations of the CGM of a radio galaxy, 4C04.11, at $z = 4.5077$. Particularly, we focus on the absorption in the halo and its spatial properties. The main conclusions of this work are summarized as follows:

1. The Lyα emission halo is detected on scales of 70×30 kpc^2 (more extended low surface brightness regions are not shown in the presented narrowband image in Fig. 1). We model the Lyα profile using a double Gaussian and report on a blueshifted component at ~ -102 km s^{-1} whose nature is still

debatable. The map of the Lyα velocity width (Fig. 7) may indicate signatures of jet-gas interactions.

2. The systemic redshift of 4C04.11 is derived from the brightest nonresonant line, He II, of 4.5077 ± 0.0001. This is consistent with the near-infrared observation of [O II] (Nesvadba et al. 2017a) and a large improvement compared to previous work using Lyα (Kopylov et al. 2006).
3. Metal emission lines, C IV, N V, and O III] are also detected; C IV in particular can be spatially mapped (Fig. 9). This suggests that the CGM is largely metal enriched. Both the C IV and N V lines show blueshifted emission components with consistent velocity shifts ($\Delta v_{\mathrm{C\,IV,b.l.}} = -1026 \pm 112\,\mathrm{km\,s^{-1}}$ and $\Delta v_{\mathrm{N\,V,b.l.}} \sim -1587\,\mathrm{km\,s^{-1}}$). This component may have a different ionization mechanism than the systemic emission and could provide evidence for a star formation and/or AGN-driven outflow (Sect. 6.1).
4. We identify at least eight H I absorbers with a velocity shift range of -3345–$0\,\mathrm{km\,s^{-1}}$. The column density of these eight H I absorbers are around $10^{14.8}\,\mathrm{cm^{-2}}$, and their Doppler parameters, b, have a range of 40–271 $\mathrm{km\,s^{-1}}$ (Table 2). We infer the presence of two C IV absorbers, which are believed to be associated with H I absorbers #1 and #4 and have a column density of $\sim 10^{14}\,\mathrm{cm^{-2}}$. The column densities of C IV absorbers #2 and #3 are only constrained to upper limits (Table 2). The presence of absorber #1 is also inferred in N V with a relatively high column density, $\sim 10^{14.99}\,\mathrm{cm^{-1}}$. This suggests that the first four absorbers are within the potential well of the host galaxy, while absorbers #5–8 are likely intervening absorbers (Sects. 6.2 and 6.3).
5. We spatially map the H I absorbers and identify a column density gradient of absorber #1 in the SW-NE direction (increases 1 dex in 24 kpc; Fig. 8). The velocity map of H I absorber #1 shows a tentative gradient along the radio jet axis, with the blueshifted part in the south. This is spatially coincident with the approaching radio jet (Parijskij et al. 2014). Absorber #1 is also detected in C IV; we can measure its column density in two distinct regions, and we identify a column density gradient similar to that of H I #1, albeit with large uncertainties (Sect. 5.2). We propose and discuss several possible models to explain the observed features. We conclude that absorber #1 likely represents a metal-enriched expelled gaseous shell that is disturbed by the jet that was launched later (Sect. 7.1).
6. Our observations suggest that we are observing the redistribution of metals through feedback processes and the enrichment of both the ISM and the CGM.

This work represents a pilot study and showcases the power of IFS instruments like MUSE for studying the absorbing "invisible" CGM gas and its enrichment and interplay with AGN and star formation activity in and around massive active galaxies in the early Universe. We will perform a similar analysis to our full sample of eight HzRGs with redshift 2.9–4.5, whose SFRs span a wide range (84–626 $M_\odot\,\mathrm{yr^{-1}}$; Falkendal et al. 2019). Although our targets are rare in terms of number density predicted from the galaxy mass function, they are unique representatives for studying the early stellar mass assembly, the feedback process, and the baryon cycle.

Acknowledgements. We thank the anonymous referee for the valuable comments, which improved this manuscript. All of the MUSE data used in this paper are available through the ESO science archive. This work was based on a Master Thesis supervised by Benjamin P. Moster. We thank his support for the thesis work. We thank Dr. Thorsten Tepper García for pointing us to their erratum and sharing the original numerical code of Voigt Hjerting function. DW is supported by through the Emmy Noether Programme of the German Research Foundation. AH was supported by Fundção para a Ciência e a Tecnologia (FCT) through the research grants UIDB/04434/2020 and UIDP/04434/2020, and an FCT-CAPES Transnational Cooperation Project "Parceria Estratégica em Astrofísica Portugal-Brasil". MVM acknowledges support from grant PGC2018-094671-BI00 (MCIU/AEI/FEDER,UE). Her work was done under project No. MDM-2017-0737 Unidad de Excelencia "María de Maeztu" Centro de Astrobiología (CSIC-INTA). This work uses the NASA's Astrophysics Data System and a number of open source software other than the aforementioned ones such as Jupyter notebook (Kluyver et al. 2016); `matplotlib` (Hunter 2007); `SciPy` (Virtanen et al. 2020); `NumPy` (Harris et al. 2020); `Astropy` (Astropy Collaboration 2018); and `LMFIT` (Newville et al. 2016).

References

Adelberger, K. L., Steidel, C. C., Shapley, A. E., & Pettini, M. 2003, ApJ, 584, 45
Allen, M. G., Groves, B. A., Dopita, M. A., Sutherland, R. S., & Kewley, L. J. 2008, ApJS, 178, 20
Arrigoni Battaia, F., Prochaska, J. X., Hennawi, J. F., et al. 2018, MNRAS, 473, 3907
Arrigoni Battaia, F., Hennawi, J. F., Prochaska, J. X., et al. 2019, MNRAS, 482, 3162
Astropy Collaboration (Price-Whelan, A. M., et al.) 2018, AJ, 156, 123
Bacon, R., Accardo, M., Adjali, L., et al. 2010, in Ground-based and Airborne Instrumentation for Astronomy III, eds. I. S. McLean, S. K. Ramsay, & H. Takami (SPIE), Int. Soc. Opt. Photon., 7735, 131
Bacon, R., Vernet, J., Borisova, E., et al. 2014, The Messenger, 157, 13
Bacon, R., Piqueras, L., Conseil, S., Richard, J., & Shepherd, M. 2016, Astrophysics Source Code Library [record ascl:1611.003]
Behroozi, P. S., Wechsler, R. H., & Conroy, C. 2013, ApJ, 770, 57
Behroozi, P., Wechsler, R. H., Hearin, A. P., & Conroy, C. 2019, MNRAS, 488, 3143
Bessell, M. S. 1990, PASP, 102, 1181
Binette, L., Kurk, J. D., Villar-Martín, M., & Röttgering, H. J. A. 2000, A&A, 356, 23
Binette, L., Wilman, R. J., Villar-Martín, M., et al. 2006, A&A, 459, 31
Bolmer, J., Ledoux, C., Wiseman, P., et al. 2019, A&A, 623, A43
Bonnet, H., Abuter, R., Baker, A., et al. 2004, The Messenger, 117, 17
Boquien, M., Burgarella, D., Roehlly, Y., et al. 2019, A&A, 622, A103
Bordoloi, R., Tumlinson, J., Werk, J. K., et al. 2014, ApJ, 796, 136
Borthakur, S., Heckman, T., Tumlinson, J., et al. 2015, ApJ, 813, 46
Cai, Z., Fan, X., Yang, Y., et al. 2017, ApJ, 837, 71
Cai, Z., Cantalupo, S., Prochaska, J. X., et al. 2019, ApJS, 245, 23
Cantalupo, S., Arrigoni-Battaia, F., Prochaska, J. X., Hennawi, J. F., & Madau, P. 2014, Nature, 506, 63
Cappellari, M., & Copin, Y. 2003, MNRAS, 342, 345
Cashman, F. H., Kulkarni, V. P., Kisielius, R., Ferland, G. J., & Bogdanovich, P. 2017, ApJS, 230, 8
Collet, C., Nesvadba, N. P. H., De Breuck, C., et al. 2015, A&A, 579, A89
Collet, C., Nesvadba, N. P. H., De Breuck, C., et al. 2016, A&A, 586, A152
Croft, S., van Breugel, W., de Vries, W., et al. 2006, ApJ, 647, 1040
Davidzon, I., Ilbert, O., Laigle, C., et al. 2017, A&A, 605, A70
De Breuck, C., Röttgering, H., Miley, G., van Breugel, W., & Best, P. 2000, A&A, 362, 519
De Breuck, C., Seymour, N., Stern, D., et al. 2010, ApJ, 725, 36
Dekel, A., Zolotov, A., Tweed, D., et al. 2013, MNRAS, 435, 999
Dijkstra, M. 2014, PASA, 31, e040
Dijkstra, M. 2017, ArXiv e-prints [arXiv:1704.03416]
Dopita, M. A., & Sutherland, R. S. 1995, ApJ, 455, 468
Dopita, M. A., & Sutherland, R. S. 1996, ApJS, 102, 161
Drouart, G., De Breuck, C., Vernet, J., et al. 2012, A&A, 548, A45
Drouart, G., De Breuck, C., Vernet, J., et al. 2014, A&A, 566, A53
Eisenhauer, F., Abuter, R., Bickert, K., et al. 2003, SPIE Conf. Ser., 4841, 1548
Fabian, A. C. 2012, ARA&A, 50, 455
Falkendal, T., De Breuck, C., Lehnert, M. D., et al. 2019, A&A, 621, A27
Falkendal, T., Lehnert, M. D., Vernet, J., De Breuck, C., & Wang, W. 2021, A&A, 645, A120
Fanaroff, B. L., & Riley, J. M. 1974, MNRAS, 167, 31P
Fechner, C., & Reimers, D. 2007, A&A, 461, 847
Feltre, A., Charlot, S., & Gutkin, J. 2016, MNRAS, 456, 3354
Ferland, G. J., Chatzikos, M., Guzmán, F., et al. 2017, Rev. Mex. Astron. Astrofis., 53, 385
Foreman-Mackey, D., Hogg, D. W., Lang, D., & Goodman, J. 2013, PASP, 125, 306
Förster Schreiber, N. M., & Wuyts, S. 2020, ARA&A, 58, 661
Fragile, P. C., Anninos, P., Croft, S., Lacy, M., & Witry, J. W. L. 2017, ApJ, 850, 171

A&A 654, A88 (2021)

Fu, H., Xue, R., Prochaska, J. X., et al. 2021, ApJ, 908, 188
Fumagalli, M., Prochaska, J. X., Kasen, D., et al. 2011, MNRAS, 418, 1796
Gaia Collaboration (Prusti, T., et al.) 2016, A&A, 595, A1
Gaia Collaboration (Brown, A. G. A., et al.) 2018, A&A, 616, A1
Gaibler, V., Khochfar, S., Krause, M., & Silk, J. 2012, MNRAS, 425, 438
Goss, W. M., Parijskij, Y. N., Soboleva, N. S., et al. 1992, AZh, 69, 673
Gower, J. F. R., Scott, P. F., & Wills, D. 1967, Mem. R. Astron. Soc., 71, 49
Gronke, M., Bull, P., & Dijkstra, M. 2015, ApJ, 812, 123
Gronke, M., Dijkstra, M., McCourt, M., & Oh, S. P. 2016, ApJ, 833, L26
Gronke, M., Dijkstra, M., McCourt, M., & Oh, S. P. 2017, A&A, 607, A71
Gullberg, B., De Breuck, C., Lehnert, M. D., et al. 2016, A&A, 586, A124
Haiman, Z., & Rees, M. J. 2001, ApJ, 556, 87
Hamann, F., & Ferland, G. 1993, ApJ, 418, 11
Hanuschik, R. W. 2003, A&A, 407, 1157
Harris, C. R., Millman, K. J., van der Walt, S. J., et al. 2020, Nature, 585, 357
Heckman, T. M., & Best, P. N. 2014, ARA&A, 52, 589
Heckman, T. M., Alexandroff, R. M., Borthakur, S., Overzier, R., & Leitherer, C. 2015, ApJ, 809, 147
Ho, L. C. 2008, ARA&A, 46, 475
Humphrey, A. 2019, MNRAS, 486, 2102
Humphrey, A., Villar-Martín, M., Fosbury, R., Vernet, J., & di Serego Alighieri, S. 2006, MNRAS, 369, 1103
Humphrey, A., Villar-Martín, M., Fosbury, R., et al. 2007, MNRAS, 375, 705
Humphrey, A., Villar-Martín, M., Sánchez, S. F., et al. 2008a, MNRAS, 390, 1505
Humphrey, A., Villar-Martín, M., Vernet, J., et al. 2008b, MNRAS, 383, 11
Humphrey, A., Zeballos, M., Aretxaga, I., et al. 2011, MNRAS, 418, 74
Humphrey, A., Vernet, J., Villar-Martín, M., et al. 2013, ApJ, 768, L3
Hunter, J. D. 2007, Comput. Sci. Eng., 9, 90
Jarvis, M. J., Wilman, R. J., Röttgering, H. J. A., & Binette, L. 2003, MNRAS, 338, 263
Kikuta, S., Imanishi, M., Matsuoka, Y., et al. 2017, ApJ, 841, 128
Kluyver, T., Ragan-Kelley, B., Pérez, F., et al. 2016, in Positioning and Power in Academic Publishing: Players, Agents and Agendas, eds. F. Loizides, & B. Schmidt (IOS Press), 87
Kolwa, S., Vernet, J., De Breuck, C., et al. 2019, A&A, 625, A102
Kopylov, A. I., Goss, W. M., Pariĭskiĭ, Y. N., et al. 2006, Astron. Lett., 32, 433
Kormendy, J., & Ho, L. C. 2013, ARA&A, 51, 511
Kramida, A., Ralchenko, Yu., Reader, J., & NIST ASD Team 2020, NIST Atomic Spectra Database (ver. 5.8), available: https://physics.nist.gov/asd [2021, February 12]. National Institute of Standards and Technology, Gaithersburg, MD
Krause, M. 2002, A&A, 386, L1
Krause, M. 2005, A&A, 436, 845
Kriss, G. A., Lee, J. C., & Danehkar, A. 2018, ApJ, 859, 94
Krogager, J. K. 2018, Astrophysics Source Code Library [record ascl:1408.015]
Le Fevre, O., Deltorn, J. M., Crampton, D., & Dickinson, M. 1996, ApJ, 471, L11
Liu, G., Zakamska, N. L., Greene, J. E., Nesvadba, N. P. H., & Liu, X. 2013, MNRAS, 436, 2576
Mackenzie, R., Pezzulli, G., Cantalupo, S., et al. 2021, MNRAS, 502, 494
Madau, P., & Dickinson, M. 2014, ARA&A, 52, 415
Mainzer, A., Bauer, J., Grav, T., et al. 2011, ApJ, 731, 53
Man, A. W. S., Lehnert, M. D., Vernet, J. D. R., De Breuck, C., & Falkendal, T. 2019, A&A, 624, A81
Mandelker, N., van den Bosch, F. C., Nagai, D., et al. 2020, MNRAS, 498, 2415
McCarthy, P. J. 1993, ARA&A, 31, 639
Miley, G., & De Breuck, C. 2008, A&ARv, 15, 67
Mills, B. Y., Slee, O. B., & Hill, E. R. 1958, Aust. J. Phys., 11, 360
Morrissey, P., Matuszewski, M., Martin, C., et al. 2012, SPIE Conf. Ser., 8446, 844613
Morton, D. C. 2000, ApJS, 130, 403
Mukherjee, D., Bodo, G., Mignone, A., Rossi, P., & Vaidya, B. 2020, MNRAS, 499, 681
Nakajima, K., Schaerer, D., Le Fèvre, O., et al. 2018, A&A, 612, A94
Nesvadba, N. P. H., Lehnert, M. D., Eisenhauer, F., et al. 2006, ApJ, 650, 693
Nesvadba, N. P. H., Lehnert, M. D., De Breuck, C., Gilbert, A., & van Breugel, W. 2007, A&A, 475, 145
Nesvadba, N. P. H., Lehnert, M. D., De Breuck, C., Gilbert, A. M., & van Breugel, W. 2008, A&A, 491, 407
Nesvadba, N. P. H., De Breuck, C., Lehnert, M. D., et al. 2011, A&A, 525, A43
Nesvadba, N. P. H., De Breuck, C., Lehnert, M. D., Best, P. N., & Collet, C. 2017a, A&A, 599, A123
Nesvadba, N. P. H., Drouart, G., De Breuck, C., et al. 2017b, A&A, 600, A121
Nesvadba, N. P. H., Bicknell, G. V., Mukherjee, D., & Wagner, A. Y. 2020, A&A, 639, L13
Newville, M., Stensitzki, T., Allen, D. B., et al. 2016, Astrophysics Source Code Library [record ascl:1606.014]
Nicholls, D. C., Sutherland, R. S., Dopita, M. A., Kewley, L. J., & Groves, B. A. 2017, MNRAS, 466, 4403
Nielsen, N. M., Kacprzak, G. G., Pointon, S. K., et al. 2020, ApJ, 904, 164
Obied, G., Zakamska, N. L., Wylezalek, D., & Liu, G. 2016, MNRAS, 456, 2861
Oppenheimer, B. D., Davies, J. J., Crain, R. A., et al. 2020, MNRAS, 491, 2939
Ouchi, M., Ono, Y., & Shibuya, T. 2020, ARA&A, 58, 617
Parijskij, Y. N., Goss, W. M., Kopylov, A. I., et al. 1996, Bull. Spec. Astrophys. Obs., 40, 5
Parijskij, Y. N., Goss, W. M., Kopylov, A. I., et al. 2000, Astron. Astrophys. Trans., 19, 297
Parijskij, Y. N., Zhelenkova, O. P., Thomasson, P., et al. 2013, in EAS Publications Series, eds. A. J. Castro-Tirado, J. Gorosabel, & I. H. Park, 61, 439
Parijskij, Y. N., Thomasson, P., Kopylov, A. I., et al. 2014, MNRAS, 439, 2314
Peek, J. E. G., Ménard, B., & Corrales, L. 2015, ApJ, 813, 7
Peeples, M. S., Corlies, L., Tumlinson, J., et al. 2019, ApJ, 873, 129
Piqueras, L., Conseil, S., Shepherd, M., et al. 2019, ASP Conf. Ser., 521, 545
Rauch, M. 1998, ARA&A, 36, 267
Reuland, M., van Breugel, W., Röttgering, H., et al. 2003, ApJ, 592, 755
Richings, A. J., & Faucher-Giguère, C.-A. 2018, MNRAS, 478, 3100
Rottgering, H. J. A., Hunstead, R. W., Miley, G. K., van Ojik, R., & Wieringa, M. H. 1995, MNRAS, 277, 389
Schaye, J., Theuns, T., Rauch, M., Efstathiou, G., & Sargent, W. L. W. 2000, MNRAS, 318, 817
Seymour, N., Stern, D., De Breuck, C., et al. 2007, ApJS, 171, 353
Silk, J., & Rees, M. J. 1998, A&A, 331, L1
Silva, M., Humphrey, A., Lagos, P., et al. 2018a, MNRAS, 474, 3649
Silva, M., Humphrey, A., Lagos, P., et al. 2018b, MNRAS, 481, 1401
Skrutskie, M. F., Cutri, R. M., Stiening, R., et al. 2006, AJ, 131, 1163
Snios, B., Siemiginowska, A., Sobolewska, M., et al. 2020, ApJ, 899, 127
Soto, K. T., Lilly, S. J., Bacon, R., Richard, J., & Conseil, S. 2016, MNRAS, 458, 3210
Springel, V., White, S. D. M., Jenkins, A., et al. 2005, Nature, 435, 629
Stern, D., Holden, B., Stanford, S. A., & Spinrad, H. 2003, AJ, 125, 2759
Swinbank, A. M., Vernet, J. D. R., Smail, I., et al. 2015, MNRAS, 449, 1298
Tepper-García, T. 2006, MNRAS, 369, 2025
Tepper-García, T. 2007, MNRAS, 382, 1375
Tumlinson, J., Thom, C., Werk, J. K., et al. 2013, ApJ, 777, 59
Tumlinson, J., Peeples, M. S., & Werk, J. K. 2017, ARA&A, 55, 389
Umehata, H., Fumagalli, M., Smail, I., et al. 2019, Science, 366, 97
van Breugel, W., de Vries, W., Croft, S., et al. 2006, Astron. Nachr., 327, 175
van Ojik, R., Roettgering, H. J. A., Carilli, C. L., et al. 1996, A&A, 313, 25
van Ojik, R., Roettgering, H. J. A., Miley, G. K., & Hunstead, R. W. 1997, A&A, 317, 358
Venemans, B. P., Kurk, J. D., Miley, G. K., et al. 2002, ApJ, 569, L11
Venemans, B. P., Kurk, J. D., Miley, G. K., & Röttgering, H. J. A. 2003, New Astron. Rev., 47, 353
Venemans, B. P., Röttgering, H. J. A., Overzier, R. A., et al. 2004, A&A, 424, L17
Venemans, B. P., Röttgering, H. J. A., Miley, G. K., et al. 2005, A&A, 431, 793
Venemans, B. P., Röttgering, H. J. A., Miley, G. K., et al. 2007, A&A, 461, 823
Verhamme, A., Schaerer, D., & Maselli, A. 2006, A&A, 460, 397
Vernet, J., Fosbury, R. A. E., Villar-Martín, M., et al. 2001, A&A, 366, 7
Vernet, J., Lehnert, M. D., De Breuck, C., et al. 2017, A&A, 602, L6
Villar-Martín, M. 2007, New Astron. Rev., 51, 194
Villar-Martín, M., Vernet, J., di Serego Alighieri, S., et al. 2003, MNRAS, 346, 273
Virtanen, P., Gommers, R., Oliphant, T. E., et al. 2020, Nat. Meth., 17, 261
Wagner, A. Y., Umemura, M., & Bicknell, G. V. 2013, ApJ, 763, L18
Weilbacher, P. M., Monreal-Ibero, A., Verhamme, A., et al. 2018, A&A, 611, A95
Weilbacher, P. M., Palsa, R., Streicher, O., et al. 2020, A&A, 641, A28
Wilman, R. J., Jarvis, M. J., Röttgering, H. J. A., & Binette, L. 2004, MNRAS, 351, 1109
Wisotzki, L., Bacon, R., Blaizot, J., et al. 2016, A&A, 587, A98
Wisotzki, L., Bacon, R., Brinchmann, J., et al. 2018, Nature, 562, 229
Wright, E. L., Eisenhardt, P. R. M., Mainzer, A. K., et al. 2010, AJ, 140, 1868
Wylezalek, D., Galametz, A., Stern, D., et al. 2013, ApJ, 769, 79
Wylezalek, D., Vernet, J., De Breuck, C., et al. 2014, ApJ, 786, 17
Wylezalek, D., Zakamska, N. L., Greene, J. E., et al. 2018, MNRAS, 474, 1499
Yang, G., Boquien, M., Buat, V., et al. 2020, MNRAS, 491, 740

Appendix A: Line fitting procedure

In this work we use both Gaussian (Lyα, C IV and C IV) and Lorentzian (He II and C IV) functions to fit the emission of the spectrum lines. The Gaussian emission model is expressed as

$$F_{\lambda,\mathrm{G}} = \frac{F}{\sigma_\lambda \sqrt{2\pi}} \exp\left[-\frac{1}{2}\left(\frac{\lambda-\lambda_0}{\sigma_\lambda}\right)^2\right], \tag{A.1}$$

and the Lorentzian emission profile is defined as

$$F_{\lambda,\mathrm{L}} = \frac{F}{\pi} \frac{\frac{1}{2}\Gamma_\lambda}{(\lambda-\lambda_0)^2 + \left(\frac{1}{2}\Gamma_\lambda\right)^2}, \tag{A.2}$$

where the F is the integrated emission flux of the line, λ_0 is the line center and λ is the wavelength at which the flux density, $F_{\lambda,\mathrm{G}}$ or $F_{\lambda,\mathrm{L}}$, is calculated. The σ_λ in Eq. A.1 is the line width while the Γ_λ in Eq. A.2 is the Full Width at Half Maximum (FWHM) of the line.

The absorption can be described as $\exp(-\tau_\lambda)$ by the radiation transfer theory. The parameter, optical depth τ_λ, is approximated by the Voigt-Hjerting (Voigt for short) function,

$$\tau_\lambda = \frac{\sqrt{\pi} e^2 f_i \lambda_0^2}{\Delta\lambda_\mathrm{D} m_\mathrm{e} c^2} \times N \times H(a,x), \tag{A.3}$$

where N is the column density, e is the electron charge, m_e is the electron mass, c is the speed of light and f_i is the oscillator strength. In this work, we adopt the atomic data from Cashman et al. (2017) and Kramida et al. (2020). The $\Delta\lambda_\mathrm{D}$ is defined as $\Delta\lambda_\mathrm{D} = \frac{b}{c}\lambda_0$, where b is the Doppler parameter. $H(a,x)$ is the Hjerting function in the following definition:

$$H(a,x) \equiv \frac{a}{\pi} \int_{-\infty}^{+\infty} \frac{\exp\left(-y^2\right)}{(x-y)^2 + a^2} dy. \tag{A.4}$$

In this approximation, $x \equiv \frac{(\lambda-\lambda_0)}{\Delta\lambda_\mathrm{D}}$ and the constant a is defined as

$$a \equiv \frac{\lambda_0^2 \Gamma_i}{4\pi c \Delta\lambda_\mathrm{D}}, \tag{A.5}$$

where Γ_i is the Lorentzian width. We use the approximation of $H(a,x)$ in this work adopted from Tepper-García (2006, 2007) for system whose column density $< 10^{22}\,\mathrm{cm}^{-2}$, which has the form

$$H(a,x) = H_0 - \frac{a}{\sqrt{\pi} x^2} \times \left(H_0 \times H_0 \times \left(4x^4 + 7x^2 + 4 + Q\right) - Q - 1\right), \tag{A.6}$$

where $H_0 = \exp\left(-x^2\right)$ and $Q = 1.5x^{-2}$. The calculated Voigt profile by the aforementioned equations, τ_λ, is then combined with other profiles, which represent different absorbers seen in one emission line using the radiation transfer equation. Then this convolves with the line spread function (LSF) of MUSE to match the observed resolution,

$$CV = e^{-\left(\sum_{i=1}^{n} \tau_{\tau_{\lambda,n}}\right)} \circledast LSF(\lambda), \tag{A.7}$$

where the CV is the acronym of convolved Voigt and n is the number of absorbers. The LSF is described by a Gaussian model with a full width of half maximum ($FWHM$) of 2.65 Å. We note that the LSF varies with observed wavelength, the location on the charge-coupled device and many other factors (Weilbacher et al. 2020). We determine the mean $FWHM$ using the intermediate production in the data reduction process that contains the LSF profile. This is consistent with the MUSE LSF approximated by polynomial in other work (e.g., Weilbacher et al. 2018). This is also the LSF value used in Kolwa et al. (2019), who study the MUSE observations of another HzRG in our sample. The fitting procedure is implemented in Python by the package `LMFIT`. The convolution is realized through the fast-Fourier transform method in the package `SciPy` (Virtanen et al. 2020) following Krogager (2018). The final fitted function is

$$F_\lambda = \left(\sum_{j=1}^{m} F_{\lambda,\mathrm{G\,or\,L}}\right) \times CV, \tag{A.8}$$

where m is the number of emission components (Gaussian or Lorentzian). Both the fits of C IV and Lyα need to include an additional blueshifted emission component (see Sect. 4).

Appendix B: SED fitting

In this appendix, we present the photometric data used for the SED fitting (Table B.1) and the fitting result (Fig. B.1) of 4C04.11. The listed photometric data are given in flux densities in this paper. As stated in Parijskij et al. (2014), the *BVRI* bands used are closer to the Johnson-Kron-Cousins systems (Bessell 1990) with which we convert the magnitudes to flux densities. The *K* band magnitude is calibrated using 2MASS (Two-micron All-Sky Survey; Skrutskie et al. 2006) sources (Parijskij et al. 2014) using which we convert it to flux density. The IRAC 1 is treated as upper limit in this SED fitting as it is contaminated by the Hα line. Since the WISE bands 1 and 2 are closer to IRAC 1 and 2, we only use the high S/N IRAC data. X-ray photometry from (Snios et al. 2020) is converted using the function provided with X-CIGALE (Yang et al. 2020). We also include the detected systemic emission fluxes of Lyα, C IV and He II in this work into the X-CIGALE to better constrain the nebular emission component.

Table B.1. Photometric results used for the SED fitting.

Band	S_ν [mJy]	Ref.
0.5–7 keV	$4.2 \pm 0.8 \times 10^{-7}$	S20
B	$< 6.4 \times 10^{-4}$	P14
V	$< 7.6 \times 10^{-4}$	P14
R	$(5 \pm 1) \times 10^{-3}$	P14
I	$(3.6 \pm 0.4) \times 10^{-3}$	P14
K	$(2.1 \pm 0.2) \times 10^{-2}$	P14
IRAC 1	$< 8.67 \times 10^{-2}$	[1]
IRAC 2	$(7.71 \pm 0.05) \times 10^{-2}$	[1]
WISE 3	< 0.56	[2]
WISE 4	3.04 ± 1.16	[2]

Notes. The X-ray 0.5 – 7.0 keV photometry is reported in (Snios et al. 2020, S20). The *BVRIK* and *K* band photometric results are taken from (Parijskij et al. 2014, P14). [1] The *Spitzer* IRAC 1 and 2 data are from Program ID 70135 (PI: D. Stern, see Wylezalek et al. 2013, 2014, for data reduction and flux measurement). [2] The WISE 3 and 4 are archival ALLWISE data (Wright et al. 2010; Mainzer et al. 2011) (`https://irsa.ipac.caltech.edu/Missions/wise.html`).

The fitted SED model and dust, AGN and unattenuated stellar emission components are shown in Fig. B.1. From this fit,

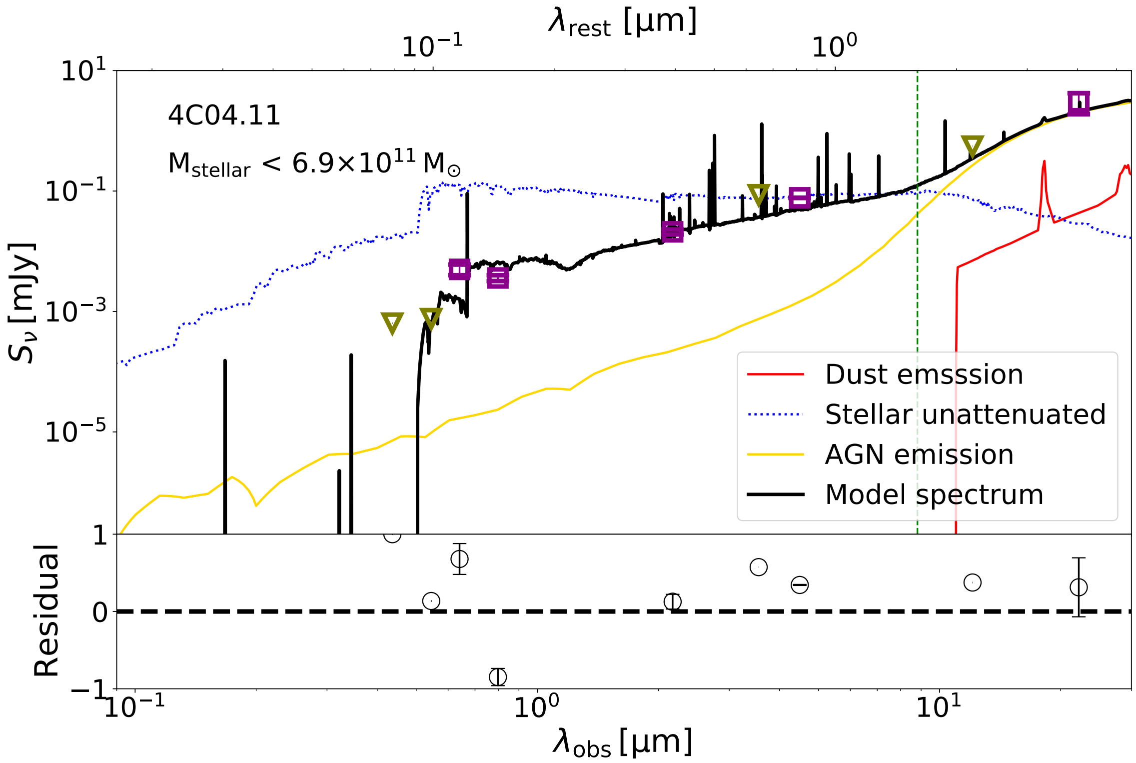

Fig. B.1. SED fitting model and photometric data. In the *upper panel*, we show the fitted SED model spectrum from X-CIGALE with a black curve. In addition, dust and unattenuated stellar and AGN emissions are shown in red, blue dotted, and yellow curves, respectively. The input observed photometry flux densities are marked in dark magenta boxes and olive triangles (upper limits). The X-ray data are not shown as they do not constrain the stellar component. The green vertical dashed line is the position of rest frame 1.6 μm from which the unattenuated stellar flux is adopted for $M_{\rm stellar}$ estimation. In the *lower panel*, we present the relative residuals, $\frac{S_{\nu,\rm obs}-S_{\nu,\rm mod}}{S_{\nu,\rm obs}}$, where $S_{\nu,\rm obs}$ and $S_{\nu,\rm mod}$ are the observed and model flux densities, respectively.

we extract the rest frame 1.6 μm flux for stellar mass estimation (Sect. 3.4). As shown in the figure, the stellar flux is the dominating emission component at this wavelength, that is to say, the flux at this sweet spot will offer relatively accurate stellar mass estimation (Seymour et al. 2007). We should, however, bare in mind that this should be treated as upper limit as (i) the AGN may contribute more flux and (ii) the photometry data point, WISE 3, which constrains the flux at this wavelength more, is an upper limit.

Appendix C: Notes on the master spectra fitting

C.1. Fitting procedure implementation

During the process of implementing the MCMC fitting, we notice that the numerical approximation of the Voigt profile by Tepper-García (2006, 2007) may not behave well at the center, that is, the Voigt function (Eq. A.6) will return a double-peak feature when $x \to 0$. Hence, we manually set

$$\lim_{x\to 0} H(a, x) = 1 - 2a/\sqrt{\pi}$$

(T. Tepper-García, priv. comm.). We also test the possibility using a more sophisticated function, the Faddeeva function, to approximate the Voigt function following Bolmer et al. (2019). It, however, does not perform well to produce the expected result, probably because the resolution of MUSE does not allow such a delicate function to work. Hence, we keep the Tepper-García (2006, 2007) approximation (Eq. A.6), which has proven to be successful on MUSE data (Kolwa et al. 2019).

C.2. Lyα fitting notes

In this appendix, we discuss the details and uncertainties run into during the Lyα fitting. For the continuum with relatively low flux underneath the Lyα, we decide to fit it using a first-order polynomial function and let the slope and intercept as free parameters during the further Gaussian+Voigt fitting. We describe how sensitive the H I absorption fitting results are with respect to different continuum fitting strategies in Appendix D.

As shown in Fig. 3, the Lyα line is asymmetric and highly absorbed. It can be fitted with the systemic redshift determined from He II (Sect. 4.2). To fit this complicated line with Gaussian+Voigt profile with many free parameters, it is challenging without any prior-knowledge (unlike Kolwa et al. 2019, which has a previous high spectral resolution UV spectrum analysis as guidance). Since all absorbers identified here are located at the blue wing (one near the $v = 0\,\rm km\,s^{-1}$) of the Lyα line, we first use only the red wing of Lyα to constrain the unabsorbed, intrinsic emission. Then, we add Voigt profiles to model the H I absorbers following the procedure described in 3.2. However, it is still impossible to fit all eight absorbers simultaneously without the initial values of $N_{\rm H}$ and b confined to an accurate range. Hence, we first start with fitting the first four absorbers with the data input just covering their spectral range and add more absorbers

Table C.1. Boundary constrains for the parameters of Lyα fitting using MCMC method.

Fit parameters	Constraints
Gaussian emission:	
Line center, λ_0 [Å]	$\Delta\lambda = 4$
Line center (b.l.), $\lambda_{0,\,\mathrm{blue}}$ [Å][a]	$\lambda_{\mathrm{in}} - 8.93 \sim \lambda_{\mathrm{in}} - 2.23$
Line flux, F [erg s^{-1} cm^{-2}]	$(90\% - 120\%)F_{\mathrm{in,\,m}}$
Line width, σ [Å][b]	$(80\% - 120\%/150\%)\sigma_{\mathrm{in,\,m}}$
Voigt absorption:	
Column density $\log(N_{\mathrm{H}}/\mathrm{cm}^{-2})$	13 – 20
Doppler parameter b [km s^{-1}]	40 – 400
Absorber redshift z^c	$\Delta z = 0.004$
Absorber redshift z^d	$\Delta z = 0.005$

Notes. The lower index "in" stands for initial. λ_{in} is the observed Lyα wavelength calculated using systemic redshift derived from He II fitting (see Sect. 4.2). The $F_{\mathrm{in,\,m}}$ and $\sigma_{\mathrm{in,\,m}}$ are line flux and width derived from primary fitting of the emission using only the red wing as input. The lower index "m" indicates both the systemic and blueshifted components have the similar boundary setup. The boundaries of the redshift, z, of different absorbers are customized according to their sensitivities to the parameters tested in running the fitting. [(a)]The wavelength range corresponds to $-400 \sim -100$ km s^{-1}. [(b)]120% for the narrow and 150% for the broad component. [(c)]This set of constraints is for absorbers #1-3, 5 and 8. [(d)]This set of constraints is for absorbers #4, 6 and 7.

when satisfied with the previous step. There are at least eight H I absorbers. We decide not to include further ones due to the low S/N and their large velocity shifts indicating them being outside the galactic potential well. As discussed in Sect. 3.2, the primary fit is performed using the least-squares method and is then changed to MCMC later using the results from least-squares as initial inputs for accurate results and uncertainties. The boundary conditions applied to the Lyα fitting are shown in Table C.1. We follow Kolwa et al. (2019) to constrain the H I column density to be within $10^{13} - 10^{20}$ cm^{-2}.

The Lyα blueshifted Gaussian component is at ~ -102 km s^{-1}, which is the boundary manually set. If no constraints are applied in the final fit, both Gaussian emission components would be at ~ 0 km s^{-1}, which would lead to an underestimation of the flux on the blue wing. This is probably due to the red wing being un-absorbed to which the algorithm gives high weight. We limit the line center (< -100 km s^{-1}) of the broad component to be blueshifted to account for the flux excess between absorbers #7 and #8 (Fig. 3).

We note that the Doppler parameters of absorbers #4 and #5 have large values exceeding 200 km s^{-1}, which may indicate that we are observing two or more spectrally unresolved absorbers with similar velocity shifts. This may be a the similar situation as observed for MRC 0200+015 using low- and high-resolution spectrographs (van Ojik et al. 1997; Jarvis et al. 2003). We test this by including two secondary absorbers (#4a and #5a) close to absorbers #4 and #5 when performing the fitting. There is no significant improvement and values of the fitted parameters of absorbers #4, #4a, #5, and #5a are not well constrained, and we therefore do not further regard this option. This issue may be revisited in the future using higher spectral resolution data.

C.3. C IV and He II fitting notes

We describe several strategies used in Sect. 4.2 to fit the C IV and He II lines, which have low S/N. In this appendix, we present

Table C.2. MCMC fitting constrains of C IV + He II and N V.

Fit parameters	Constrains
Emission:	
C IV systemic line center	$\frac{\lambda_{0,\mathrm{C\,IV}}}{\lambda_{0,\mathrm{He\,II}}} = \frac{\lambda_{\mathrm{C\,IV}}}{\lambda_{\mathrm{He\,II}}}$
blueshifted doublet line center[a]	$\frac{\lambda_{0,1}}{\lambda_{0,2}} = \frac{\lambda_1}{\lambda_2}$
doublet line width[a,b]	$\frac{\sigma_1}{\sigma_2} = \frac{\lambda_1}{\lambda_2}$
doublet line flux[a]	$\frac{F_1}{F_2} = \frac{f_1}{f_2}$
Voigt absorption:	
Redshift	$z_1 = z_2$
Doppler parameter	$b_1 = b_2$
Column density	$N_1 = N_2$

Notes. The systemic C IV emission line centers (both of the doublet lines), $\lambda_{0,\mathrm{C\,IV}}$, are constrained to the line center of He II, which is the systemic redshift, i.e., the fitted line center ratio, $\frac{\lambda_{0,\mathrm{C\,IV}}}{\lambda_{0,\mathrm{He\,II}}}$ is set equal to the rest frame line ratio $\frac{\lambda_{\mathrm{C\,IV}}}{\lambda_{\mathrm{He\,II}}}$. The lower index "1" and "2" used in this table indicate the blue and red component of the doublet line, respectively. The blueshifted doublet line center ratio, $\frac{\lambda_{0,1}}{\lambda_{0,2}}$, is only constrained to the ratio in rest frame, $\frac{\lambda_1}{\lambda_2}$, i.e., the velocity shift of blueshifted doublet is leaving free. The line widths of the doublet are set to be equal to each other in velocity space. Hence, the ratio of the line width in wavelength space, as the direct fitting parameter in this work, is proportional to the ratio of doublet line center in rest frame, $\frac{\lambda_1}{\lambda_2}$. The line flux ratio of the doublet, $\frac{F_1}{F_2}$, is set to be equal to the ratio of its oscillator strength, $\frac{f_1}{f_2}$. Using data from Cashman et al. (2017), we fix the $\frac{f_1}{f_2}$ to be approximately 2 for both the C IV and N V doublets. The absorption fit parameters are set to be the same for the doublet. [(a)]The constrains here apply to both N V and C IV. [(b)]The fitted line width of systemic C IV component is Γ (FWHM) in the Lorentzian model. For others, they are the σ for Gaussian model.

details and reasons for the adjustment and discuss some uncertainties faced in running the fitting. In particular, we adjust the fitting procedure described in Sect. 3.2 in the following eight aspects.

First, we fit C IV and He II simultaneously. Because C IV, which is also a doublet, suffers from absorption and may contain several kinematic emission components, it is better to fix the line center of its intrinsic emission with the redshift determined by the He II.

Second, we fixed the continuum level underneath these two lines, which is determined beforehand with emissions lines masked. Third, we excluded the wavelength ranges from the fitting where the contribution of skylines is significant (marked as yellow shaded regions in Fig. 4).

Fourth, we removed the potentially blueshifted broad component of the C IV intrinsic emission, which is probably heavily absorbed. This could be the same emission component we included in the Lyα fitting (Sect. 4.1).

Fifth, to alleviate the removal of this blueshifted component, we adopted a Lorentzian profile instead of a single Gaussian to account for the broad wings of both C IV and He II. The Lorentzian may not be the best physical description of the underlying emission profile, but it is the best solution given the limited S/N to allow for absorption fits in the C IV blue side. Sixth, since the C IV is very broad (Fig. 4), we included an additional set of Gaussian to account for the extreme (> 1000 km s^{-1}) blueshifted component.

Seventh, to account for the absorption, we included four C IV absorbers that we assumed to be the same ones causing the

Lyα absorption (Sect. 4.1). The reason we only included four absorbers instead of all eight is that the positions of absorber #5 and beyond are in the low flux and S/N part of the C IV lines, which also suffers from skyline contamination and cannot be robustly fitted. We notice that we allow the redshift of the absorbers to be free within a limited range ($\Delta z = 0.006$ for absorber #1, $\Delta z = 0.004$ for absorber #4) following Kolwa et al. (2019) who argues that fixing the redshift of absorption caused by different species is un-physical given their different ionization energies.

Finally, we fixed the Doppler parameters and redshifts of absorbers #2 and #3 to the values derived from H I absorbers #2 and #3. We also set the ranges of the column densities to $10^{11.5} - 10^{12}$ cm^{-1} and $10^{12} - 10^{14}$ cm^{-1} for absorbers #2 and #3, respectively. These are implemented due to the large overlapping of these two absorbers (with others), which leads to a failure of fitting without further constrains.

The initial guess for the redshift (He II line center), 4.514, is adopted from Kopylov et al. (2006) and is used only in the least-squares fitting. After the redshift constrained to a relatively satisfied range, we allow it to vary within ±2 Å during the MCMC fitting. The velocity shift of the blueshifted C IV component is left relatively free with a broad range, $-3000 \sim -500$ km s^{-1}. The results from ~ -1500 km s^{-1} to ~ -900 km s^{-1} will all give us satisfied overall fit. This is also indicated by the distribution of $L_{\rm C\,IV,2}$, line center of the blueshifted component, seen in Fig. E.4, which has a long tail toward the lower values. Based on this, we argue in Sect. 4.3 that the blueshifted component of C IV and N V likely result from the same gaseous cloud. The boundaries of the Doppler parameters, b, and column density, $N_{\rm C\,IV}$, are set to $40 - 400$ km s^{-1} and $10^{13} - 10^{16}$ cm^{-2}, respectively (stricter settings for absorber #2 and #3 as mentioned above) following Kolwa et al. (2019). Table C.2 summarizes the constraints used in the C IV and He II fitting. The rules for line center, line width and line flux of the doublet are presented as well as the constraints of the absorption parameters of the doublet.

The major result we interested in from the He II fitting is the systemic redshift. We test the possibility of using a double Gaussian to fit the He II. The result is similar (4.5079 ± 0.0001 and 4.5077 ± 0.0001) to the Lorentzian fit and shows that the algorithm will fit both of the line centered at $\Delta v \sim 0$ km s^{-1}. This further indicates that the S/N of the line is not enough to fit the two Gaussian.

We test the possibilities of using (i) only absorbers #1 and #4 or (ii) absorbers #1, #3, and #4 to fit the C IV, which is under the assumption that absorbers #2 and/or #3 have low metallicity. Both settings (i) and (ii) have similar results for absorbers #1 and #4. Hence, we include all four absorbers and avoid the strong assumption.

C.4. N V *fitting notes*

The position of the N V is at the broad wing of Lyα. The flux excess we see on Fig. 3 above the fitted Lyα model at around 5000 km s^{-1} is due to the contribution of the blueshifted N V component. In addition, the low flux and highly absorbed systemic emission make N V a non-obvious detection.

As described in Sect. 4.3, we fix the best-fit Lyα model from Sect. 4.1 and use a constant continuum when fitting the N V. The reasons we do not apply the same continuum level for Lyα and N V lines are: (i) we test in Appendix D that using a continuum determined from the red wing and free first-order polynomial have similar results for the H I fitting (Appendix D); (ii) the first-order polynomial will slightly overestimate the continuum flux of Lyα red wing whose influence is probably negligible for Lyα, which is a broad line with high flux. For N V, however, which is at longer wavelength than Lyα and has extremely low S/N, the continuum overestimation will affect the fit more. This is indeed the case when the first-order polynomial continuum is applied during the N V fitting, which results in poor constraints.

As we see in Fig. E.6, the line center of the blueshifted component, $L_{\rm N\,V,b}$, and Doppler parameter, b_1, are not fully constrained. For $L_{\rm N\,V,2}$, we set the range $-1600 \sim -500$ km s^{-1} according to C IV blueshifted component. The reason it hits the lower boundary is due to the influence of Lyα red wing. As mentioned in Appendix E.2, the velocity shift down to -1500 km s^{-1} will still give satisfying results for the C IV fit. The main parameter in this fit, $N_{\rm N\,V}$, does not change much if we vary the given boundary of the line center of the blueshifted component. Besides, we test to leave it relatively free and end up with poor fit quality (unphysical result). Therefore, we manually set this lower boundary, which results in a satisfying fit given the low S/N. More importantly, this velocity shift shows the consistence between N V and C IV, which agrees with the hypothesis. For b_1, which hits the upper boundary, we tested fixing it to the value obtained from C IV absorber #1, which results in a poor fit quality as well. This could probably be due to (i) the low S/N of the N V; (ii) the influence of the unresolved H I redshifted absorber(s); (iii) the imperfect sky line subtraction. Hence, we present this fit and remind the readers to be cautious about the $N_{\rm N\,V}$, which should be considered as a lower limit given the well-known $b - N$ degeneracy (Silva et al. 2018a).

Appendix D: Lyα continuum sensitivity test

The Lyα emission of quasars and galaxies at high redshift are highly absorbed by the intervening hydrogen clouds located between observer and source. This so-called Lyα forest (e.g., Adelberger et al. 2003) heavily affects the blue wing of Lyα making it difficult for continuum fitting. For our MUSE observation, the spectral resolution is too low to resolve the narrow intervening absorbers, but we can clearly identify a change between the continuum of the blue and red side of the Lyα, namely the continuum flux is lower in the blue than the red. Several potential methods can be used to fit this continuum. Hence, we run a test to see how significant the change that different continuum fitting strategies may cause the absorption fitting. We use five different methods, which are described below.

In the first method, the continuum is fitted using a first-order polynomial prior to the Gaussian+Voigt fitting and fixed during the following fitting. The wavelength range used in this method for the continuum is 6405 – 6986 Å ($-13\,000 \sim 13\,000$ km s^{-1}) with the emission region masked.

For the second method, the continuum is fitted using a first-order polynomial together with the Gaussian+Voigt fitting. The values of slope and intercept from method 1 are used as initials.

In the third method, the continuum is fitted using a zero order polynomial of the red wing and fixed during the Gaussian+Voigt fitting. The wavelength range used in this method for the continuum is 6880 – 6986 Å ($8\,258 \sim 13\,000$ km s^{-1}). We chose the wavelength range to be at extremely red wing of the Lyα to avoid the contamination of the N V (Sect. 4.3 and Appendix C.4).

For the fourth method, the continuum is fitted using a zero order polynomial of the blue wing and fixed during the Gaussian+Voigt fitting. The wavelength range used in this method for the continuum is 6405 – 6600 Å ($-13\,000 \sim -4\,300$ km s^{-1}).

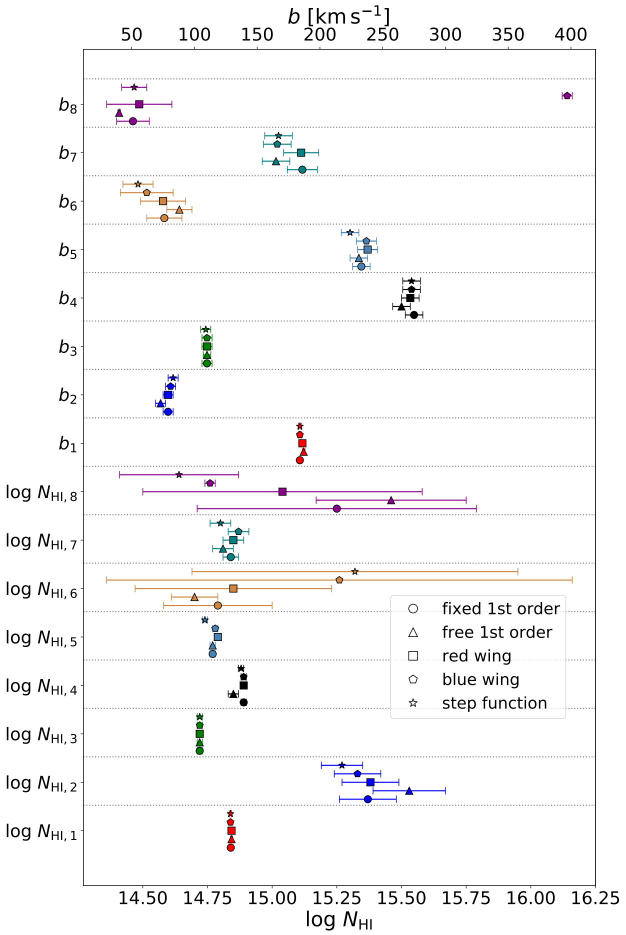

Fig. D.1. MCMC fitted Voigt parameters, $N_{\rm H}$ and b, of the eight H I absorbers from five continuum fitting methods. The subscripts 1–8 represent the indices of the absorbers. The colors represent different parameters (the same color is used for the $N_{\rm H}$ and b of the same absorber), while the mark styles indicate different continuum fitting methods.

As for the fifth method, the continuum is fitted using a step function. The wavelength of the step is fitted together with the Gaussian+Voigt fitting. The left (right) value is set to the one from blue (red) wing zero order polynomial result and fixed during the fit.

The result is shown in Fig. D.1 in which the fitted Voigt parameters using MCMC method, $N_{\rm H\,I}$ and b, of the eight absorbers from different continuum fitting strategies are presented. It is intuitive to identify that most of the fitted values from different continuum methods are consistent, though some have relatively large scatters (e.g., absorbers #6–8), which is understandable given that these absorbers are located at the low S/N tail. Therefore, we decided that the continuum fitting method has a minor effect on the absorption parameters, which is our primary focus in this work. By checking the corner plots produced from these five methods, we find that fitting the first-order polynomial continuum together with the Gaussian+Voigt model (method 2) constrains the probability distribution of the absorption parameters (z, b, and $N_{\rm H\,I}$) best. Hence, we use the method 2 when doing the Lyα fit. Using a first-order polynomial to fit the continuum is a commonly used method (e.g., Kolwa et al. 2019), and giving freedom to the slope and intercept will constrain better the line features.

As for the spatially resolved Lyα analysis, we first fit the continuum level of the spectra in each spatial bin with emission part masked. We then keep the continuum fixed to this level when running the Gaussian+Voigt fitting. Because, for consistence, we use the same model for fitting each of the 64 spectrum (see Sect. 3.3) and some spectra have lower S/N ratios, which may affect the fitting if we add more free parameters (for the continuum).

Appendix E: Auxiliary materials of MCMC fitting

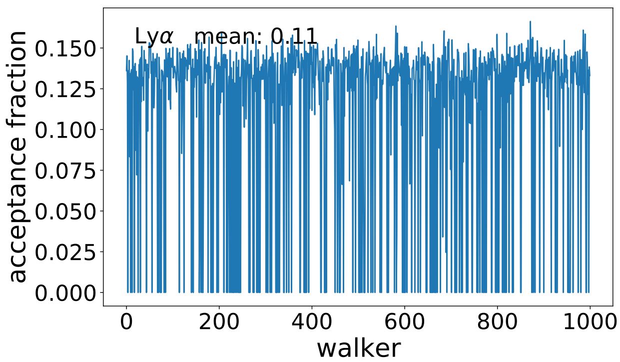

Fig. E.1. Acceptance fraction of each walker used in the Lyα MCMC fitting.

In this appendix, we present some side products of the MCMC fitting, which can be used as auxiliary materials to better understand the fitting quality, namely the corner plot and acceptance fraction plot. The corner plot is a tracer for the probability distributions of the fitted parameters and correlation between each parameters; in other words, we can identify the degeneracy between fitted parameters from the corner plot. The acceptance fraction plot is used to check the acceptance fraction of each walker used in MCMC (see Foreman-Mackey et al. 2013, for details). This can be used as an easy check of the performance of the MCMC run. Although some details are not clear, the acceptance fraction lies in 0.2–0.5 is thought to be an indication of a successful run (Foreman-Mackey et al. 2013).

E.1. Lyα

The acceptance fraction and corner plot of MCMC fitting of master Lyα are shown in Fig. E.1 and E.2, respectively. In Fig. E.1, we can see that a number of walkers are rejected with a mean acceptance fraction of 0.11. This is due to the larger number (32) of free parameters used in the Lyα fitting. In Fig. E.2, we identify several banana shapes of the correlation distribution (e.g., between b_i and $N_{\rm Hi}$). This is a well-known degeneracy in the Voigt fitting (e.g., Silva et al. 2018a) that a combination of larger N value and smaller b value can the overall similar result with a combination of smaller b and larger N.

E.2. C IV and He II

The acceptance fraction and corner plot of MCMC fitting of master C IV He II are shown in Fig. E.3 and E.4, respectively. In Fig. E.3, we can see that the acceptance fraction of all of the

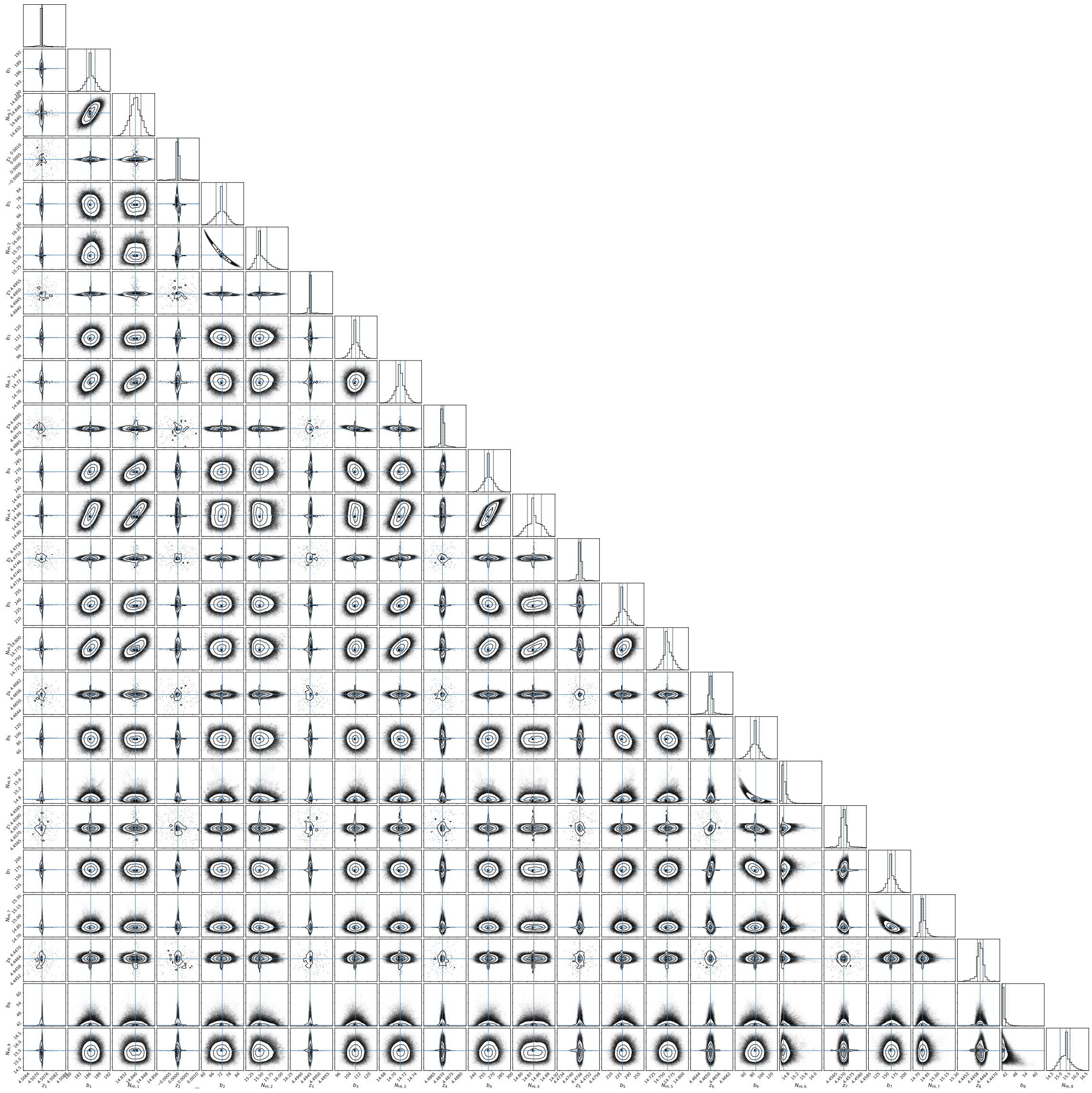

Fig. E.2. Corner plot derived from the MCMC fitting of the Lyα line (see Sect. 4.1). In this figure we only show the correlation between the absorption parameters, namely z_i, b_i, and $N_{\mathrm{C\,IV}i}$, which are the fitted redshifts, Doppler parameters (in units of km s^{-1}), and column densities (logarithmic) of the eight H I absorbers. The black dotted lines in each of the histograms represent 15.8 and 84.2 percentiles, which correspond to the reported uncertainty ranges. The blue solid lines mark the median and reported fit values, respectively.

walkers are in the range of 0.2 – 0.5 with a mean of 0.26. This is evidence indicating the success of the fitting. In Fig. E.4, we see that the probability distributions of $N_{\mathrm{C\,IV2}}$ and $N_{\mathrm{C\,IV3}}$ have tentative peak and un-defined tail to the lower value. This is more severe for absorber #2 given that the lower boundary we apply ($10^{11.5}$ cm^{-2}) is extremely low. Based on the above, we decide to treat the column density of absorber #2 and #3 as upper limit.

E.3. N V

The acceptance fraction and corner plot of the MCMC fitting of the master N V are shown in Fig. E.5 and E.6, respectively. In Fig. E.5, we can see that all walkers are in the range of 0.2–0.5 with a mean of 0.41, which indicates the MCMC fitting of N V is successful. We discuss the uncompleted sampled distribution of $L_{\mathrm{N\,V,b}}$ and b_1 in Appendix C.4.

E.4. O III]

The acceptance fraction and corner plot of the MCMC fitting of master O III] are shown in Fig. E.7 and E.8, respectively. We perform the MCMC fitting for this two-free-parameter model to be consistent with other fittings. In Fig. E.7, we can see that all walkers are above 0.5 with a mean of 0.72, which indicates that the model is probably over-fitted.

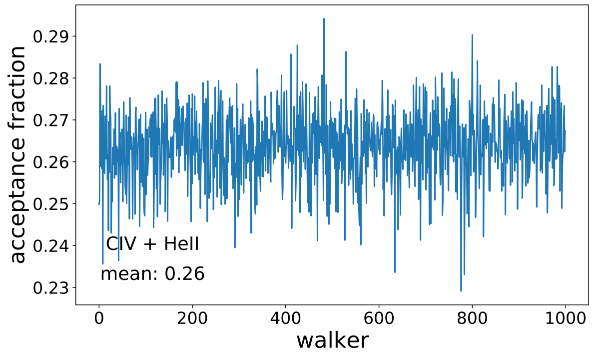

Fig. E.3. Acceptance fraction of each walker used in the C IV and He II MCMC fitting.

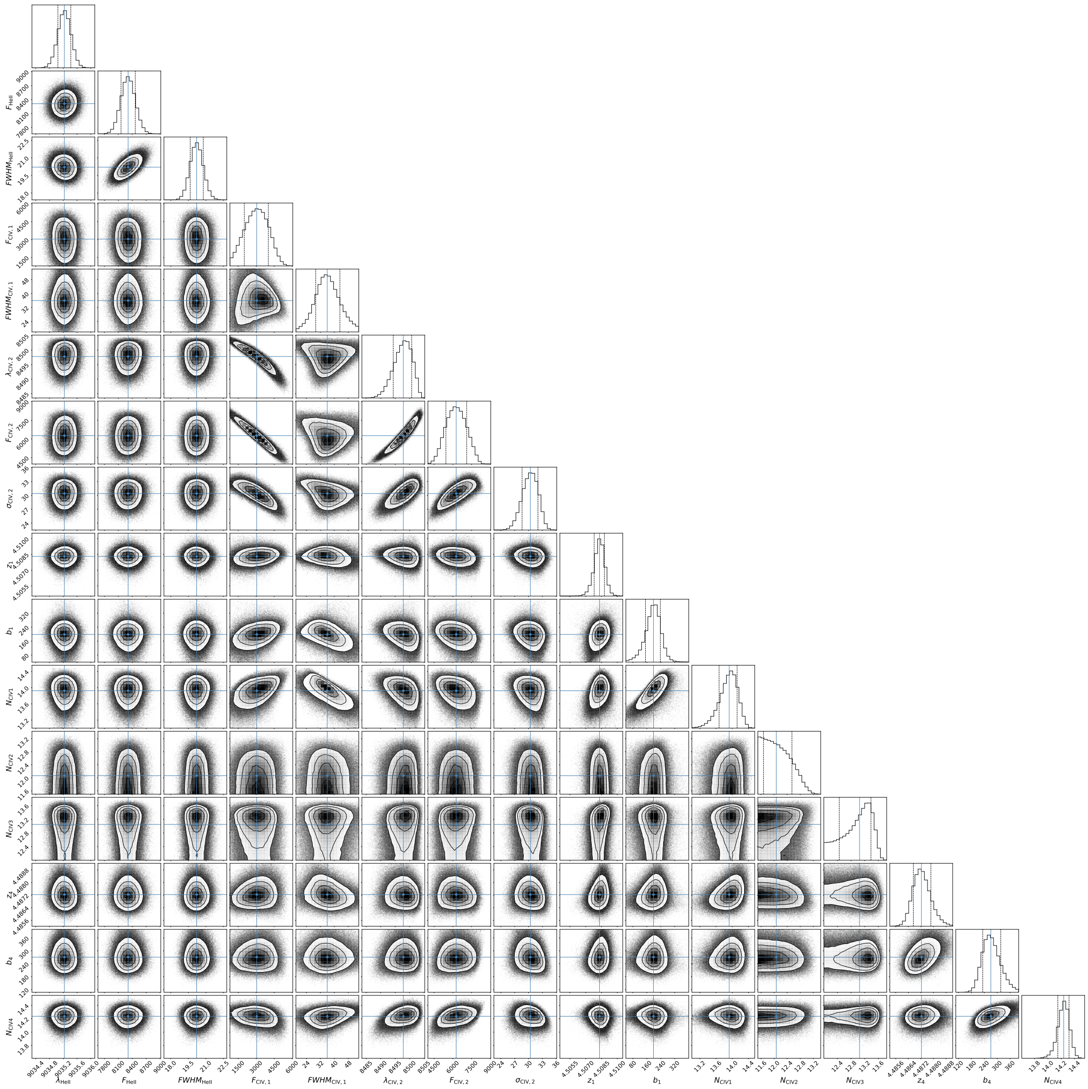

Fig. E.4. Corner plot derived from the MCMC fitting of the C IV and He II (see Sect. 4.2). In this figure we show the correlation between the free parameters in the C IV+He II fit. The $\lambda_{\mathrm{He\,II}}$ and $\lambda_{\mathrm{C\,IV},2}$ are the line centers of the He II and blueshifted C IV (for the 1548 Å line) emissions in Å, respectively. The $F_{\mathrm{He\,II}}$, $F_{\mathrm{C\,IV},1}$, and $F_{\mathrm{C\,IV},2}$ are the integrated line fluxes of He II, systemic C IV, and blueshifted C IV (only for the 1548 Å line) emissions in 10^{-20} erg s^{-1} cm^{-2} Å^{-1}, respectively. The $FWHM_{\mathrm{He\,II}}$, $FWHM_{\mathrm{C\,IV}}$, and $\sigma_{\mathrm{C\,IV},2}$ are the line widths of He II, systemic C IV, and blueshifted C IV (for the 1548 Å line) emissions in Å. z_i, b_i, and $N_{\mathrm{C\,IV}i}$, which are the fitted redshifts, Doppler parameters (in units of km s^{-1}), and column densities (logarithmic) of the four absorbers. The black dotted lines in each of the histograms represent 15.8 and 84.2 percentiles, which correspond to the reported uncertainty ranges. The blue solid lines mark the median and reported fit values, respectively.

A&A 654, A88 (2021)

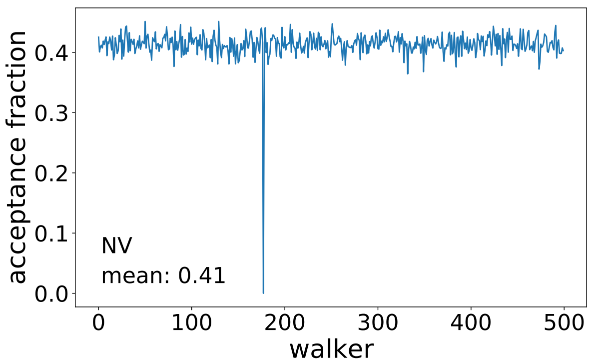

Fig. E.5. Acceptance fraction of each walker used in the N V MCMC fitting.

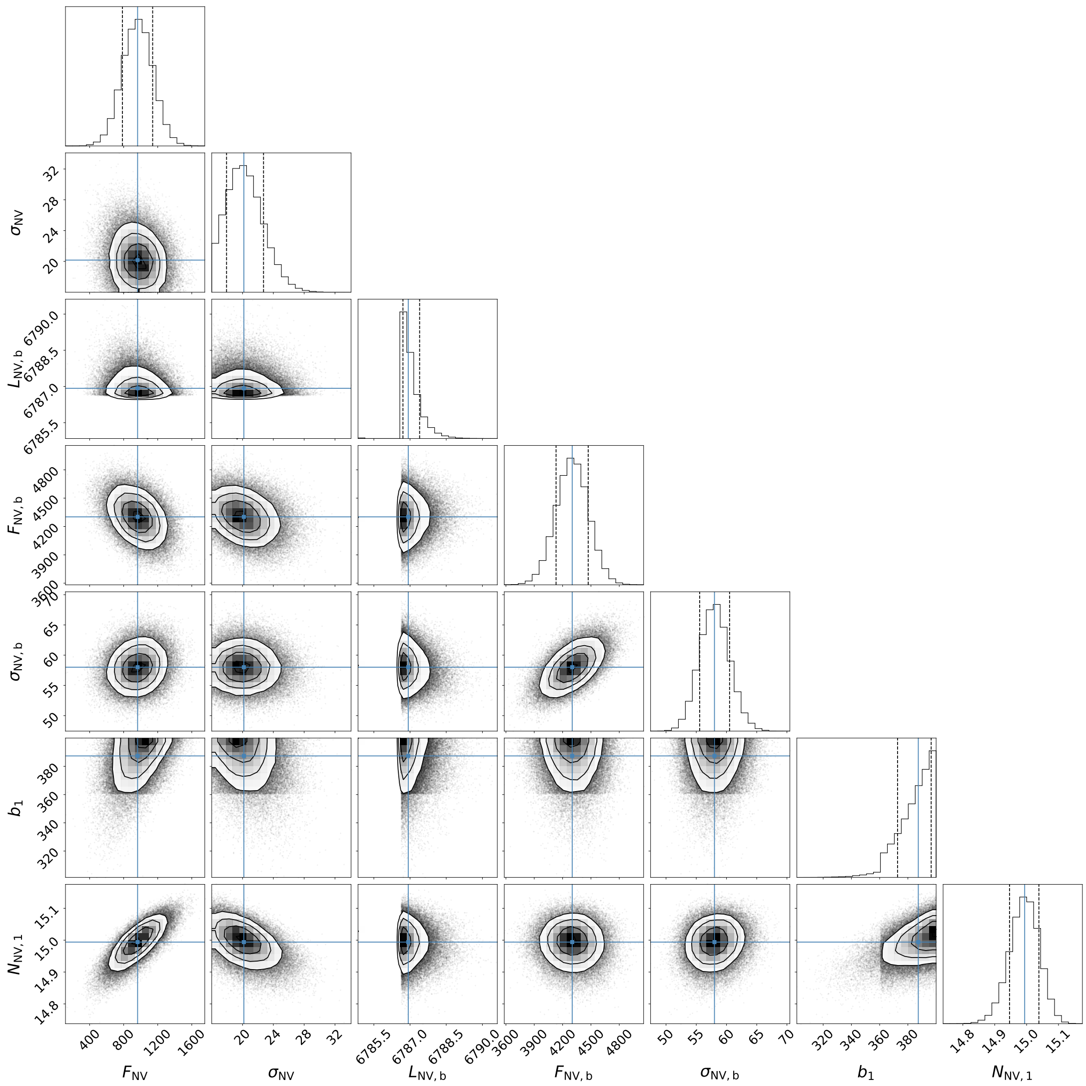

Fig. E.6. Corner plot derived from the MCMC fitting of the N V (Sect. 4.2). In this figure we show the integrated line flux ($F_{\rm N\,V}$ in 10^{-20} erg s^{-1} cm^{-2} Å^{-1}) and the Gaussian line width ($\sigma_{\rm N\,V}$, in Å) of the systemic N V emission; the line center ($L_{\rm N\,V,b}$ in Å), integrated line flux ($F_{{\rm N\,V},b}$), and Gaussian line width ($\sigma_{{\rm N\,V},b}$) of the blueshifted N V component (for the 1238 Å line); and the Doppler parameter (b_1) and column density ($N_{\rm N\,V}$, 1) of absorber #1. The black dotted lines in each of the histograms represent 15.8 and 84.2 percentiles, which correspond to the reported uncertainty ranges. The blue solid lines mark the median and reported fit values, respectively.

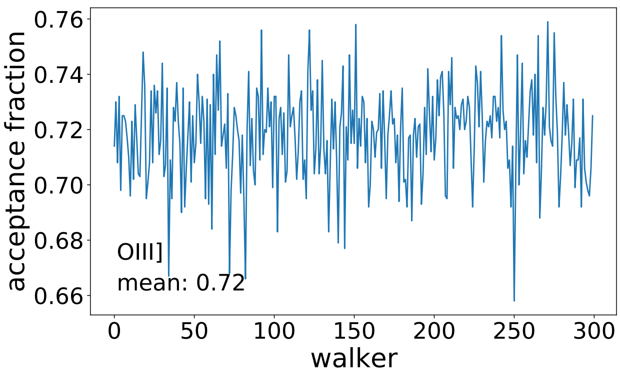

Fig. E.7. Acceptance fraction of each walker used in O III] MCMC fitting.

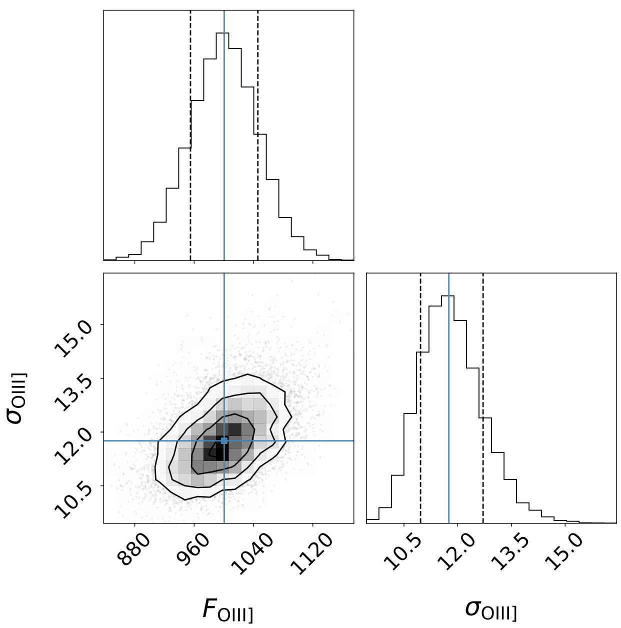

Fig. E.8. Corner plot derived from the MCMC fitting of the O III] (Sect. 4.4). The $F_{\rm O\,III]}$ and $\sigma_{\rm O\,III]}$ are the integrated line flux and line width of the 1660.81 Å doublet line, respectively. The black dotted lines in each of the histograms represent 15.8 and 84.2 percentiles, which correspond to the reported uncertainty range. The blue solid lines mark the median and reported fit values, respectively.

Appendix F: Individual Lyα spectra fitting

In this appendix, we present the Lyα fitting results from each individual bins described in Sects. 3.3 and 5.1 in Fig. F.2 to F.5. The spatial region (bin) from which each of the presented spectrum is extracted is shown in Fig. F.1. The spatial bins are numbered (and color-coded) and are the same as those marked in Figs. F.2 to F.5 in order to trace their spatial location. The details of the tessellation is described in Sect. 3.3.

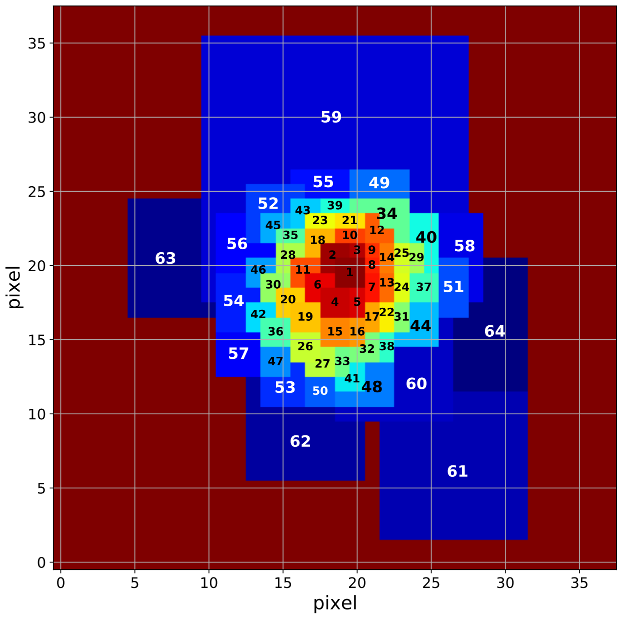

Fig. F.1. Spatial binning results from Sect. 3.3. The colors represents different bins. The bin numbers correspond to the numbers marked in Figs. F.2–F.5. The black or white colors of the bin number are given to better distinguish it from the color of the bin.

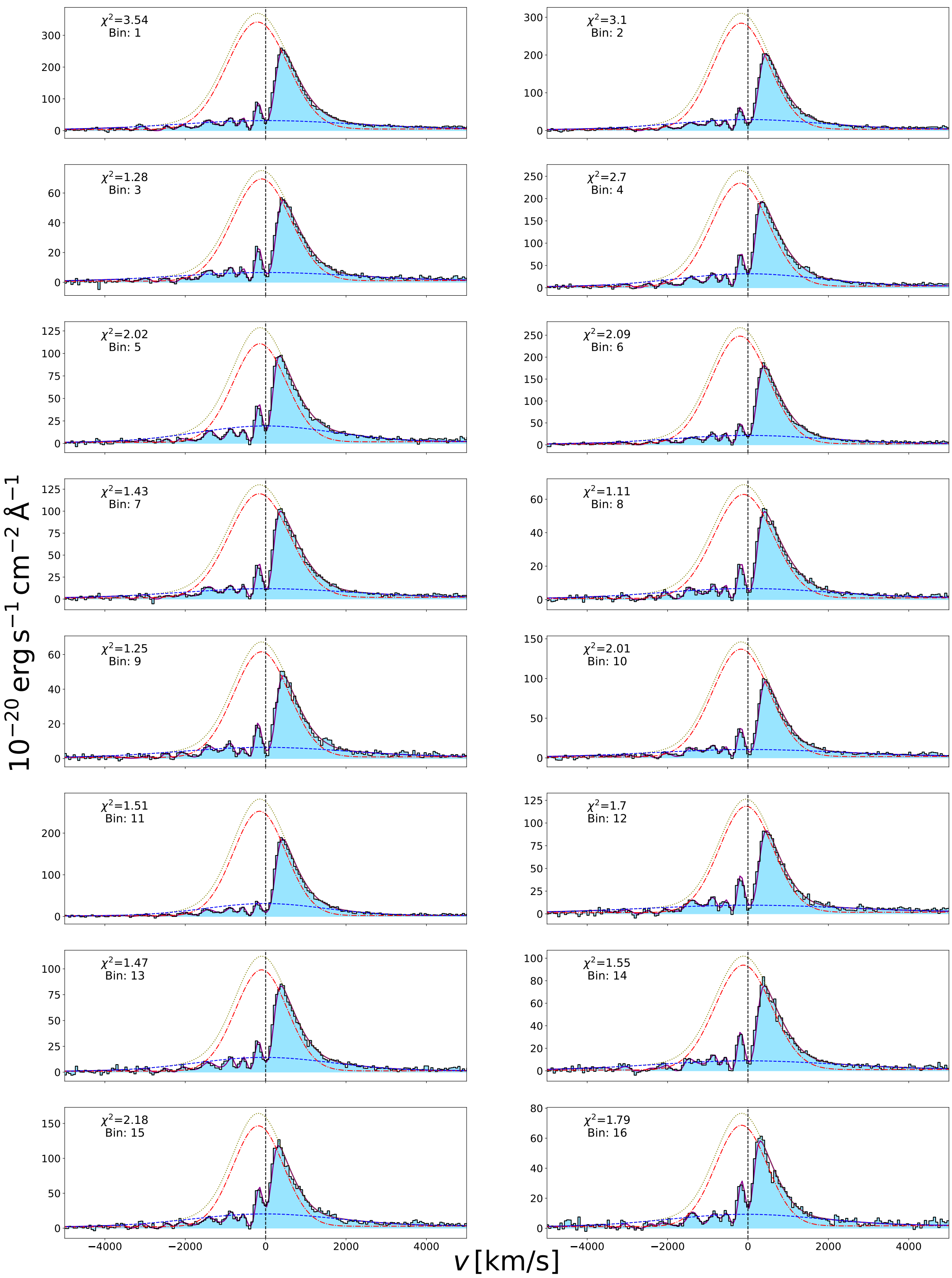

Fig. F.2. Spectra extracted from the 64 spatial bins (see Sect. 3.3) and Gaussian+Voigt fitting results. In each panel, the thick dark magenta line indicates the best fit model. The dot-dash red line and dashed blue line denote the narrow and broad emission components, respectively. The dotted olive lines are the summation of the two emissions. The χ^2_ν calculated from each fit is shown as an indicator of the fit quality. We note that each spectrum is summed from the spatial bin, each of which contains a different number of spaxels. Hence, the fluxes of the spectra shown here are not to be compared directly.

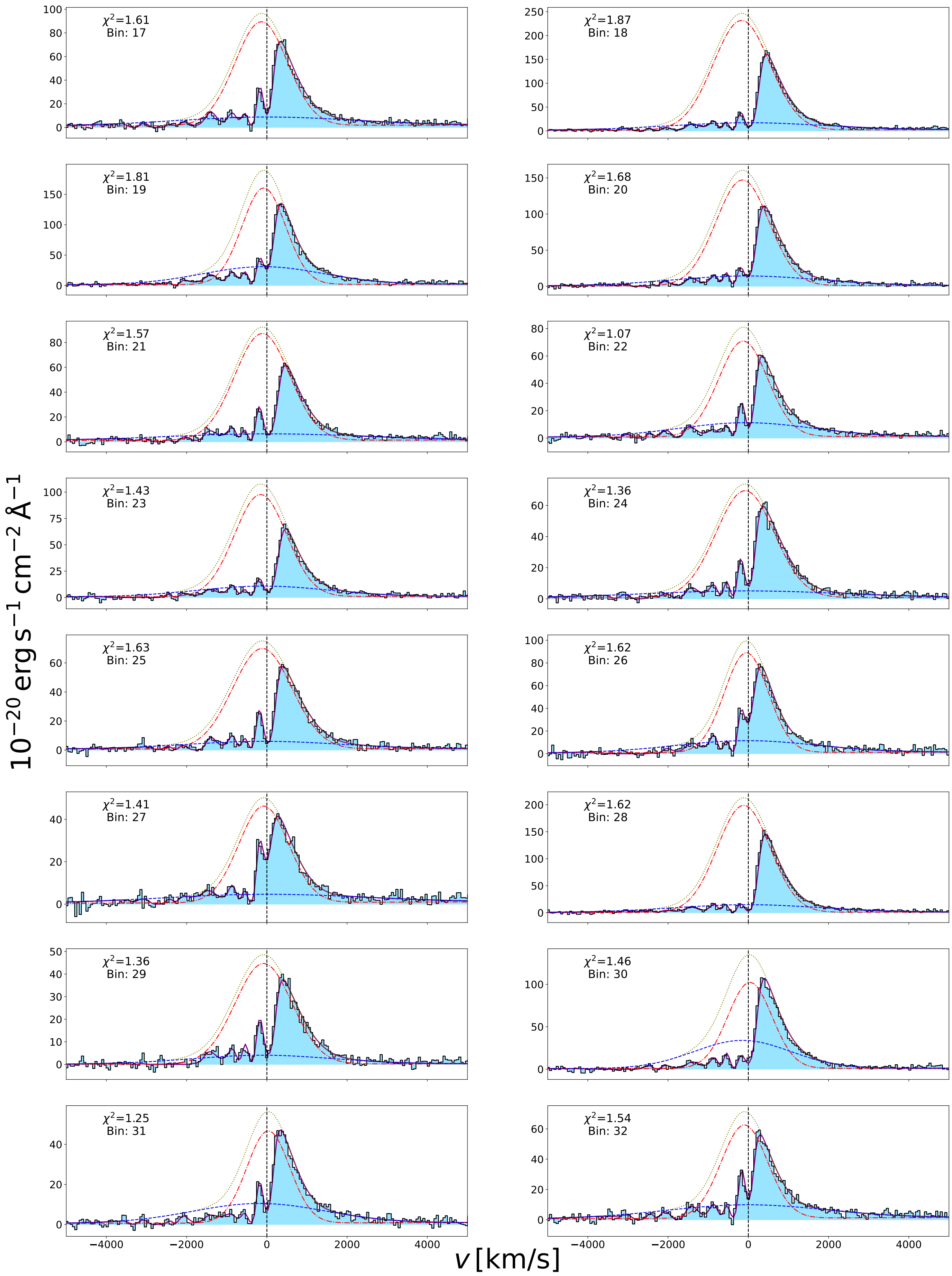

Fig. F.3. Figure F.2 continued.

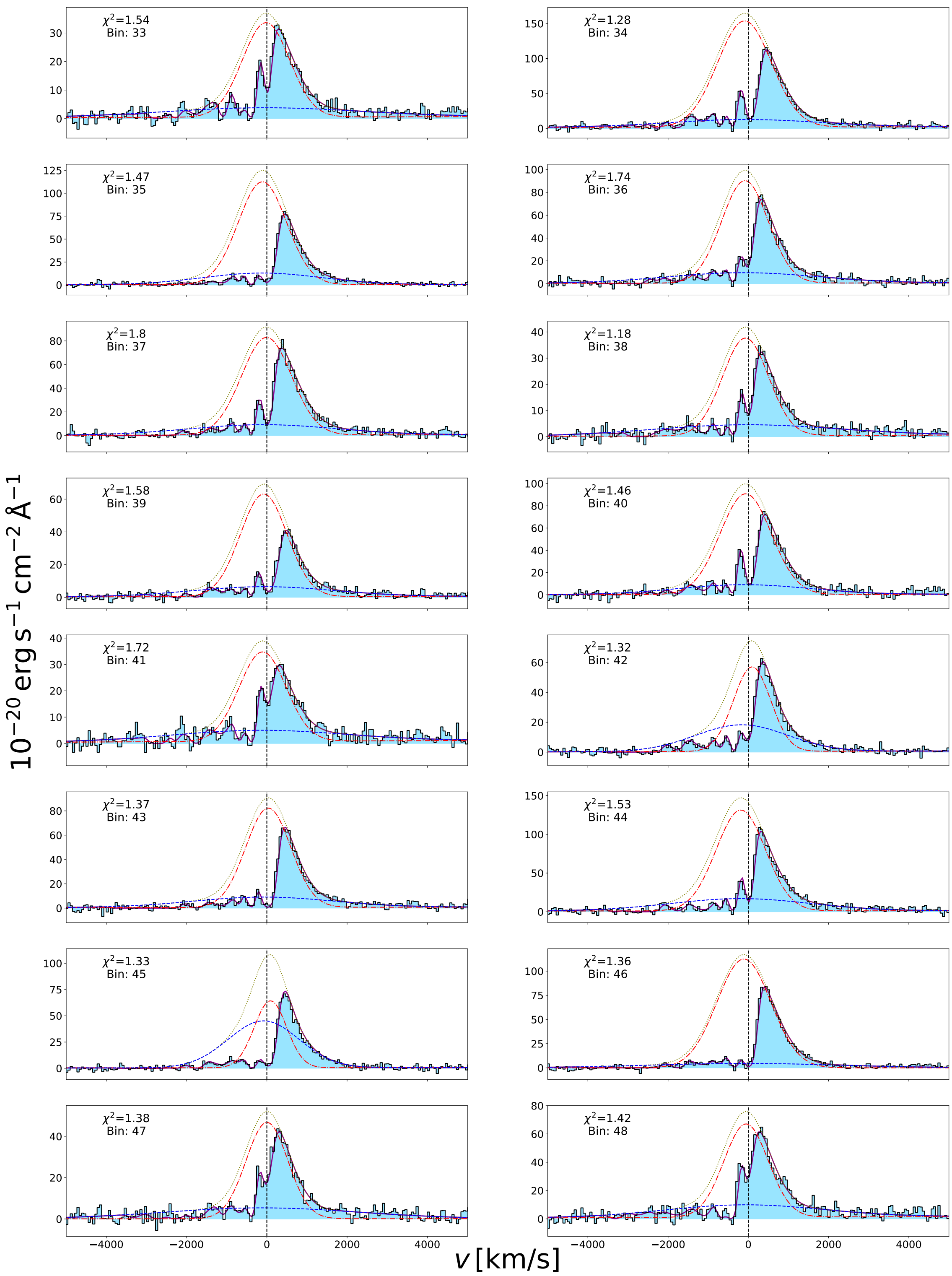

Fig. F.4. Figure F.3 continued.

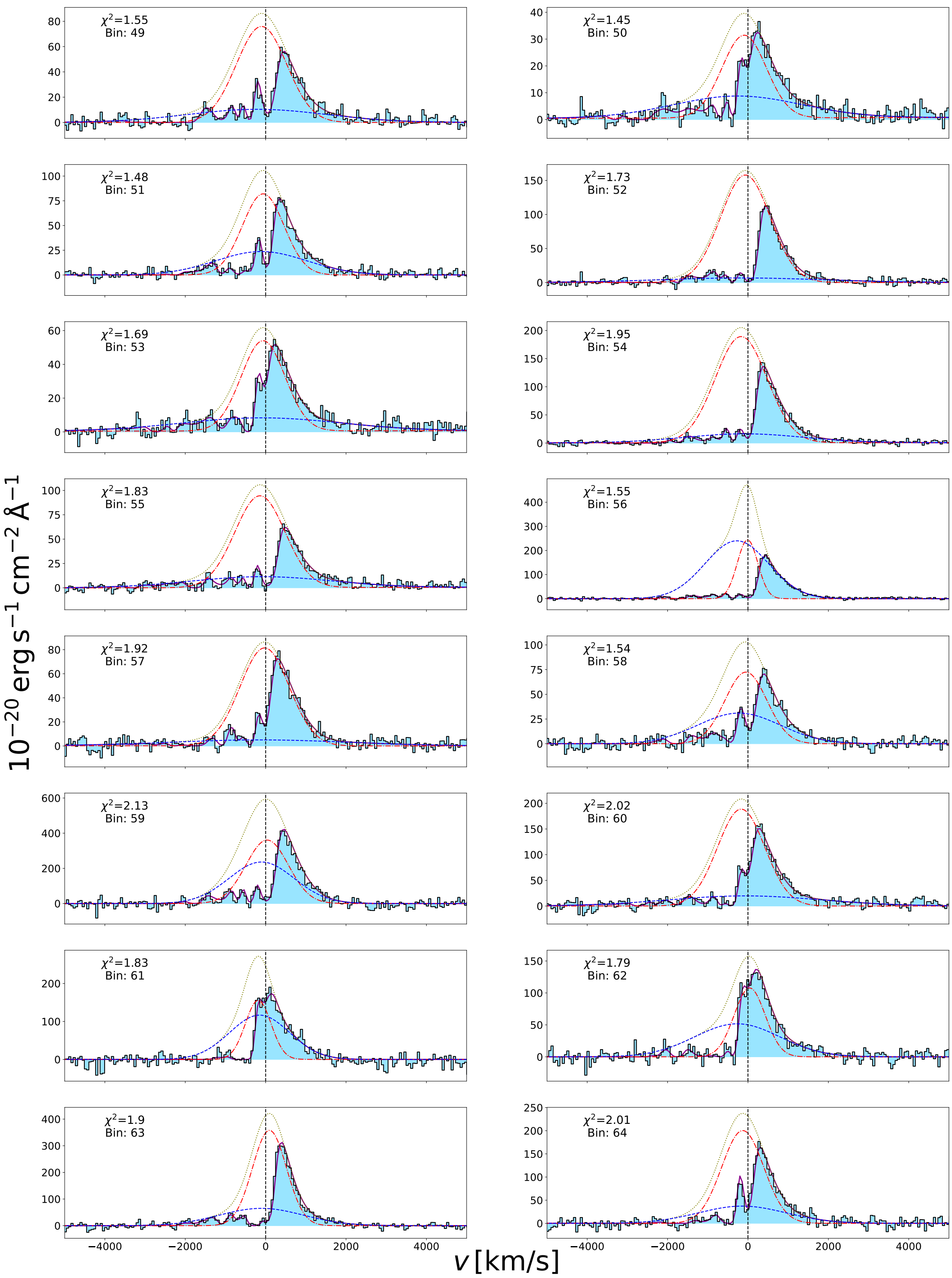

Fig. F.5. Figure F.4 continued.

Appendix G: C IV spatial mapping

In this appendix we present the parameters derived from the C IV spatial fitting (see Sect. 5.2). The fittings are done for He II and C IV simultaneously with the similar procedure described in Sects. 3.2 and 5.2. The emission results for both He II and C IV from NE and SW are presented in Table G.1. In Table G.2, we show the absorption fitting results of the 4 C IV absorbers from these two regions. For comparison, we also show the emission and absorption fitting results of the Lyα lines from these two regions in the corresponding tables. Due to the low S/N of the two C IV spectra and in order to avoid overfitting, we fix the z and b of the absorbers in the fit and use the derived column densities as upper limit. The exception is the column density of absorber #1 of the NE spectrum, which has a well distributed probability extracted from the corner plot. The distribution is presented in Fig. G.1 in blue with a well defined peak. We also show the distribution of the same absorber from the SW spectrum for comparison in this figure in orange. We note that the z and b for the absorbers in both of the NE and SW C IV spectra are fixed to the corresponding values derived from master Lyα during the fitting. It will cause unsuccessful fitting if we use the fitted values from NE and SW Lyα to fix the corresponding C IV fits. We argue that the adopted choice is reasonable because (i) large parts of the NE and SW regions are covered by the master aperture; (ii) the master Lyα has high S/N.

Table G.1. Best fitted emission results of the 1D aperture-extracted spectrum from the NE and SW regions using the MCMC method.

Ion	Line center (rest) λ_0 [Å]	Line center (obs.) λ [Å]	Line flux F [10^{-17} erg s^{-1} cm^{-2}]	Line width $FWHM$ [km s^{-1}]
NE				
Lyα	1215.67	6693.75 ± 0.24	50.51 ± 1.25	1474 ± 21
Lyα (b.l.)	1215.67	~ 6693.20	14.68 ± 0.91	3669 ± 150
C IV	1548.20	8527.65 ± 0.46	1.43 ± 0.35	1933 ± 342
C IV (b.l.)	1548.20	8499.69 ± 4.29	1.52 ± 0.31	2027 ± 297
C IV	1550.77	8541.86 ± 0.46	0.71 ± 0.17	1930 ± 342
C IV (b.l.)	1550.77	8513.85 ± 4.30	0.76 ± 0.15	2024 ± 296
He II	1640.47	9035.94 ± 0.48	2.39 ± 0.11	651 ± 43
SW				
Lyα	1215.67	6693.72 ± 0.20	38.34 ± 0.69	1569 ± 17
Lyα (b.l.)	1215.67	~ 6693.23	12.58 ± 0.46	4522 ± 122
C IV	1548.20	8526.41 ± 0.46	1.17 ± 0.50	857 ± 254
C IV (b.l.)	1548.20	8498.50 ± 9.11	1.63 ± 0.46	2935 ± 484
C IV	1550.77	8540.62 ± 0.46	0.58 ± 0.25	856 ± 253
C IV (b.l.)	1550.77	8512.66 ± 9.13	0.82 ± 0.23	2930 ± 484
He II	1640.47	9034.63 ± 0.49	2.24 ± 0.11	646 ± 50

Notes. The notations used are the same as in Table 1 (see table notes there).

Table G.2. Best absorption fitting results of the 1D aperture-extracted spectrum from the NE and SW regions using the MCMC method.

Abs. #	Ion	Redshift z	Absorber wav. λ [Å]	Velocity Δv [$\mathrm{km\,s^{-1}}$]	Column density $\log(N/\mathrm{cm^{-2}})$	Doppler b [$\mathrm{km\,s^{-1}}$]
NE						
1	Lyα	4.5073 ± 0.0001	6695.08 ± 0.06	-21 ± 3	14.99 ± 0.01	199 ± 3
	C IV	–	8526.70	–	14.02 ± 0.17	–
2	Lyα	4.5001 ± 0.0001	6686.31 ± 0.07	-414 ± 3	15.1 ± 0.1	97 ± 10
	C IV	–	8515.37	–	<12.43	–
3	Lyα	4.4946 ± 0.0001	6679.64 ± 0.10	-712 ± 4	14.72 ± 0.02	105 ± 10
	C IV	–	8506.86	–	<13.04	–
4	Lyα	4.4872 ± 0.0001	6670.62 ± 0.15	-1116 ± 7	14.97 ± 0.02	284 ± 18
	C IV	–	8495.20	–	<14.4	–
5	Lyα	4.4750 ± 0.0002	6655.77 ± 0.22	-1781 ± 10	14.81 ± 0.02	241 ± 20
6	Lyα	4.4657 ± 0.0002	6644.45 ± 0.21	-2288 ± 10	<15.81	~ 54
7	Lyα	~ 4.4572	~ 6634.20	~ -2747	<15.05	~ 158
8	Lyα	~ 4.4457	~ 6620.21	~ -3373	<14.91	~ 75
SW						
1	Lyα	4.5075 ± 0.0001	6695.31 ± 0.03	-6 ± 3	14.74 ± 0.01	156 ± 2
	C IV	–	8526.70	–	<13.4	–
2	Lyα	4.5002 ± 0.0001	6686.47 ± 0.06	-427 ± 10	15.16 ± 0.11	89 ± 7
	C IV	–	8515.37	–	<12.4	–
3	Lyα	4.4947 ± 0.0001	6679.74 ± 0.08	-750 ± 26	14.70 ± 0.02	110 ± 9
	C IV	–	8506.86	–	< 13.7	–
4	Lyα	4.4871 ± 0.0001	6670.60 ± 0.13	-1150 ± 19	14.86 ± 0.02	260 ± 13
	C IV	–	8495.21	–	<13.6	–
5	Lyα	4.4747 ± 0.0002	6655.45 ± 0.18	-1790 ± 10	14.76 ± 0.02	220 ± 15
6	Lyα	~ 4.4648	~ 6643.34	~ -2341	<14.59	~ 94
7	Lyα	~ 4.4572	~ 6634.10	~ -2754	<15.67	~ 103
8	Lyα	~ 4.4462	~ 6620.82	~ -3347	<15.60	~ 60

Notes. The notations used are the same as in Table 2 (see table notes there). Due to the low S/N of the C IV spectra extracted from these two regions, the column density results of C IV absorbers are treated as upper limits with z and b fixed to the fitted H I values, correspondingly. The exception is the column density of absorber #1 in the NE, which has a well distributed probability (see Fig. G.1).

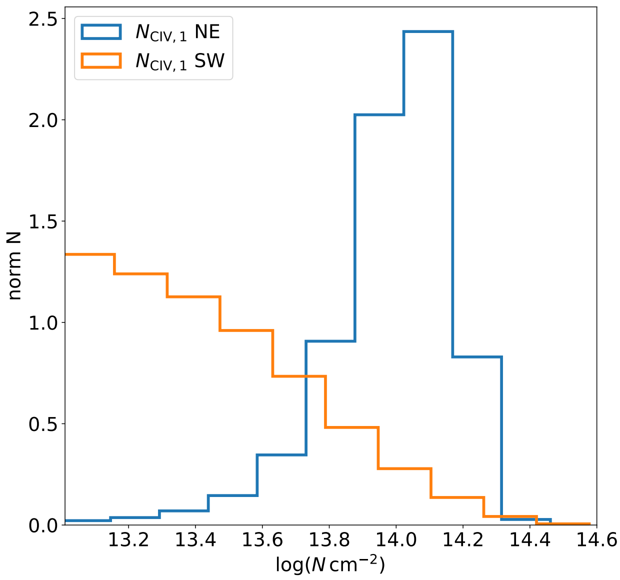

Fig. G.1. Probability distributions of the C IV absorber #1 column density extracted from the corner plots. The blue and orange histograms represent the results of the NE and SW spectra, respectively.

3

3D tomography of the giant Lyα nebulae of z≈3-5 radio-loud AGN

Authors:
Wuji Wang, Dominika Wylezalek, Joël Vernet,
Carlos De Breuck, Bitten Gullberg, et al.

Published in *A&A 680, A70 (2023)*.

Wuji Wang is the principal author of this article. The method was developed by Wuji Wang. Wuji Wang, Dr. Vernet, Dr. De Breuck, and Dr. Wylezalek had the idea for the paper. Wuji Wang performed data process, calculations and analysis of the observations. Wuji Wang produced all the figures and tables and wrote the manuscript. All authors collaborated with corrections and suggestions to the manuscript, and Wuji Wang performed the last improvements during the review process. Dr. Kolwa made suggestions to the English writing.

A&A 680, A70 (2023)
https://doi.org/10.1051/0004-6361/202346415

Astronomy & Astrophysics

3D tomography of the giant Lyα nebulae of $z \approx 3$–5 radio-loud AGN

Wuji Wang (王无忌)[1], Dominika Wylezalek[1], Joël Vernet[2], Carlos De Breuck[2], Bitten Gullberg[3,4], Mark Swinbank[5], Montserrat Villar Martín[6], Matthew D. Lehnert[7], Guillaume Drouart[8], Fabrizio Arrigoni Battaia[9], Andrew Humphrey[10], Gaël Noirot[11], Sthabile Kolwa[12], Nick Seymour[8], and Patricio Lagos[10]

[1] Astronomisches Rechen-Institut, Zentrum für Astronomie der Universität Heidelberg, Mönchhofstr. 12-14, 69120 Heidelberg, Germany
e-mail: wuji.wang@uni-heidelberg.de; wuji.wang_astro@outlook.com
[2] European Southern Observatory, Karl-Schwarzschild-Str. 2, 85748 Garching, Germany
[3] Cosmic Dawn Center, Copenhagen, Denmark
[4] DTU Space, Technical University of Denmark, Elektronvej 327, 2800 Lyngby, Denmark
[5] Centre for Extragalactic Astronomy, Department of Physics, Durham University, South Road, Durham DH1 3LE, UK
[6] Centro de Astrobiología, CSIC-INTA, Ctra. de Torrejón a Ajalvir, km 4, 28850 Torrejón de Ardoz, Madrid, Spain
[7] Univ. Lyon, Univ. Lyon1, ENS de Lyon, CNRS, Centre de Recherche Astrophysique de Lyon UMR5574, 69230 Saint-Genis-Laval, France
[8] International Centre for Radio Astronomy Research, Curtin University, 1 Turner Avenue, Bentley, WA 6102, Australia
[9] Max-Planck-Institut fur Astrophysik, Karl-Schwarzschild-Str 1, 85748 Garching bei München, Germany
[10] Instituto de Astrofísica e Ciências do Espaço, Universidade do Porto, CAUP, Rua das Estrelas, 4150-762 Porto, Portugal
[11] Institute for Computational Astrophysics and Department of Astronomy & Physics, Saint Mary's University, 923 Robie Street, Halifax, NS B3H 3C3, Canada
[12] Physics Department, University of Johannesburg, 5 Kingsway Ave, Rossmore, Johannesburg 2092, South Africa

Received 14 March 2023 / Accepted 26 September 2023

ABSTRACT

Lyα emission nebulae are ubiquitous around high-redshift galaxies and are tracers of the gaseous environment on scales out to $\gtrsim$100 pkpc (proper kiloparsec). High-redshift radio galaxies (HzRGs, type-2 radio-loud quasars) host large-scale nebulae observed in the ionised gas differ from those seen in other types of high-redshift quasars. In this work, we exploit MUSE observations of Lyα nebulae around eight HzRGs ($2.92 < z < 4.51$). All of the HzRGs have large-scale Lyα emission nebulae with seven of them extended over 100 pkpc at the observed surface brightness limit (~ 2–20×10^{-19} erg s^{-1} cm^{-2} arcsec^{-2}). Because the emission line profiles are significantly affected by neutral hydrogen absorbers across the entire nebulae extent, we performed an absorption correction to infer maps of the intrinsic Lyα surface brightness, central velocity, and velocity width, all at the last scattering surface of the observed Lyα photons. We find the following: (i) that the intrinsic surface brightness radial profiles of our sample can be described by an inner exponential profile and a power law in the low luminosity extended part; (ii) our HzRGs have a higher surface brightness and more asymmetric nebulae than both radio-loud and radio-quiet type-1 quasars; (iii) intrinsic nebula kinematics of four HzRGs show evidence of jet-driven outflows but we find no general trends for the whole sample; (iv) a relation between the maximum spatial extent of the Lyα nebula and the projected distance between the active galactic nuclei (AGN) and the centroids of the Lyα nebula; and (v) an alignment between radio jet position angles and the Lyα nebula morphology. All of these findings support a scenario in which the orientation of the AGN has an impact on the observed nebular morphologies and resonant scattering may affect the shape of the surface brightness profiles, nebular kinematics, and relations between the observed Lyα morphologies. Furthermore, we find evidence showing that the outskirts of the ionised gas nebulae may be 'contaminated' by Lyα photons from nearby emission halos and that the radio jet affects the morphology and kinematics of the nebulae. Overall, this work provides results that allow us to compare Lyα nebulae around various classes of quasars at and beyond cosmic noon ($z \sim 3$).

Key words. galaxies: active – galaxies: evolution – galaxies: high-redshift – galaxies: halos – galaxies: jets

1. Introduction

Being the most abundant element in the Universe, hydrogen (especially the cold gas, i.e. neutral hydrogen atoms and hydrogen molecules, H_2) is the building block of the baryonic Universe. Studying H_2 directly is difficult due to lack of prominent transition lines. It is often probed using low-J CO transitions as a proxy that unfortunately results in added uncertainties, for example in the conversion factor (e.g. Bolatto et al. 2013). In contrast, neutral atomic hydrogen can be easily ionised ($E_{\mathrm{H}^0} = 13.6$ eV) and cascade with line emissions being produced. The H I Ly$\alpha\lambda$1216 (Lyα hereafter) line is the most prominent one among them. For high-redshift galaxies, it is a commonly targeted emission line that can easily be observed in the optical to near-infrared bands (e.g. Hu & McMahon 1996; Cowie & Hu 1998; Shimasaku et al. 2006; Dawson et al. 2007; Leclercq et al. 2017; Wisotzki et al. 2018; Umehata et al. 2019; Ono et al. 2021; Ouchi et al. 2020, and reference therein). Lyα emission can be detected on a range of spatial scales, for example at interstellar medium (ISM) to circumgalactic medium (CGM, Tumlinson et al. 2017) scales and even beyond the viral radius of the central object out to intergalactic medium (IGM) scales (e.g. Cantalupo et al. 2014; Cai et al. 2019; Ouchi et al. 2020). However, it is non-trivial to identify the origin of Lyα emission (e.g. due to the resonant nature of Lyα emission and various potential ionising sources acting at once), which is essential to understanding the physics of the emitting gas observed on different scales and around various types of objects (Dijkstra 2019; Ouchi et al. 2020). This is further complicated when active galactic nuclei (AGN) are present.

Active galaxies hosting AGN, especially the ones with quasar level activities (bolometric luminosity, $L_{\rm bol} \gtrsim 10^{45}\,{\rm erg\,s^{-1}}$), at a high redshift are known to host Lyα nebulae on scales of a few 100 kpc (e.g. Heckman et al. 1991a; Basu-Zych & Scharf 2004; Weidinger et al. 2004, 2005; Dey et al. 2005; Prescott et al. 2015; Cantalupo et al. 2014; Arrigoni Battaia et al. 2016, 2019; Borisova et al. 2016; Cai et al. 2019). The central powerful AGN act as a main ionising mechanism for the surrounding gas, which is responsible for the detection of these extended Lyα nebulae (as predicted by theoretical works, e.g. Costa et al. 2022). In addition, the diffuse emission from galaxies near the AGN host can also contribute to the overall profile observed of the central target (e.g. Byrohl et al. 2021). In some of the giant nebulae, it is natural to find various mechanisms functioning at different scales and positions (e.g. Vernet et al. 2017). Therefore, despite leaving internal physics entangled, Lyα acts as a simpler tool for detecting a gaseous environment throughout cosmic time.

Before wide field integral field spectrographs (IFS) became available, narrow-band imaging and long slit spectroscopy provided effective methods to detect diffuse Lyα nebulae (e.g. Steidel et al. 2000; Francis et al. 2001; Matsuda et al. 2004; Saito et al. 2006; Yang et al. 2009, 2010; Cantalupo et al. 2012, 2014; Hennawi & Prochaska 2013; Prescott et al. 2015; Arrigoni Battaia et al. 2016). However, these observations have been limited by uncertainties in the systemic redshift measurements and limited spatial coverage, respectively. Integral field unit (IFU) observations – for example with the Multi-Unit Spectroscopic Explorer (MUSE/VLT) and Keck Cosmic Web Imager (KCWI/Keck) – allow us to measure the extent of the nebulae together with the information of their dynamics. Numerous works of Lyα nebulae around quasars report (tens of kiloparsecs to over 100 kpc) extended emission across a large range of redshifts ($z \sim 2$ to $z \sim 6.3$) and quasar types (e.g. radio-quiet and radio-loud type-1, radio-quiet type-2, and extremely red quasars, Christensen et al. 2006; Borisova et al. 2016; Arrigoni Battaia et al. 2019; Cai et al. 2019; Farina et al. 2019; den Brok et al. 2020; Fossati et al. 2021; Mackenzie et al. 2021; Lau et al. 2022; Vayner et al. 2023; Zhang et al. 2023). This diversity in nebula properties suggest a range of driving mechanisms, dependencies on orientation, and demonstrate that well-selected samples are needed. Despite the effort that has been made regarding this topic, a link between the aforementioned types and type-2 radio-loud quasars on a CGM scale is missing.

Among the high-redshift quasar population, high-redshift radio galaxies (HzRGs) are a unique sample despite being smaller in number (see Miley & De Breuck 2008, as a review). They host type-2 quasars and have powerful radio jets. They have been shown to reside in dense protocluster environments (Venemans et al. 2007; Wylezalek et al. 2013, 2014; Noirot et al. 2016, 2018), which may evolve to modern galaxy clusters. HzRGs were among the first sources where giant Lyα nebulae were discovered ($\sim 10^{44}\,{\rm erg\,s^{-1}}$, $\gtrsim$100 kpc, e.g. Hippelein & Meisenheimer 1993; van Ojik et al. 1996, 1997; Reuland et al. 2003; Villar-Martín et al. 2006, 2007b) and observed with the previous generation of IFU instruments (e.g. Adam et al. 1997). The Lyα nebulae of HzRGs have been found to have two distinctive parts, namely the high surface brightness kinematically disturbed inner part and the quiescent low surface brightness extended outer nebula (e.g. Villar-Martín et al. 2002, 2003, 2007a). The spatial separation of these two parts seem to be consistent with the extent of the radio jets (e.g. Villar-Martín et al. 2003), suggesting that the jet plays a role in disturbing the inner part. Specifically, there is evidence that the Lyα nebulae around HzRGs are related to jet-driven outflows (Humphrey et al. 2006), while some of the quiescent gas may be related to infalling material (Humphrey et al. 2007). AGN photoionisation is likely the main mechanism of exciting these nebulae (e.g. Villar-Martín et al. 2002, 2003; Morais et al. 2017), but ionisation by fast shocks might also play a role (e.g. Bicknell et al. 2000; Morais et al. 2017). Polarisation measurements show that some of the Lyα emission in HzRGs is scattered (Humphrey et al. 2013). Despite these works, however, a comparison of the nebulae of HzRGs and other quasar samples has yet to be performed, which is the motivation of this work.

The Lyα nebulae of HzRGs are known to be partially absorbed by neutral hydrogen (H I absorbers, e.g. Rottgering et al. 1995; van Ojik et al. 1997; Jarvis et al. 2003; Wilman et al. 2004; Humphrey et al. 2008; Kolwa et al. 2019). The absorbing gas is found to be extended on galaxy-wides scales and likely related to outflowing gas from the host galaxy (e.g. Binette et al. 2000; Swinbank et al. 2015; Silva et al. 2018a; Wang et al. 2021b). The correction of this absorption is only possible through spectral observation. Without careful treatment, a considerable amount (a factor of $\gtrsim$5) of flux would be missed, and inaccurate conclusions would be drawn. Alternatively, some absorption trough features might potentially be explained by radiative transfer effects (Dijkstra 2014; Gronke et al. 2015, 2016; Gronke & Dijkstra 2016). Although it is interesting to compare the different treatments of the observed Lyα spectra, it is beyond the scope of this work.

There was also clear observational evidence that the morphology of the continuum and line emission regions of HzRGs are aligned with the jet direction (e.g. Chambers et al. 1987; Pentericci et al. 1999; Miley et al. 2004; Zirm et al. 2005; Duncan et al. 2023) on a relatively smaller scale (several kiloparsecs to tens of kiloparsecs). Molecular gas detected around HzRGs was reported to be distributed along the jet within and outside the hot spot, which may suggest several scenarios (e.g. jet-driven outflow, jet-induced gas cooling, and a jet propagating into a dense molecular gas medium, Emonts et al. 2014; Gullberg et al. 2016; Falkendal et al. 2021). On a megaparsec scale, West (1991) found that the radio jet often points towards nearby galaxies. Eales (1992) proposed a model explaining the alignment effect, suggesting that the high-redshift radio emission is often detected when the jet travels close to the major axis of surrounding asymmetrically distributed gas. With the advanced IFS observation and hundreds of kiloparsec gas tracers of Lyα, we were able to probe the intrinsic (i.e. corrected for absorption) gaseous nebula around HzRGs for this work, test its distribution with respect to the radio jets, and seek evidence following these pioneering works.

For this paper, we utilised the power of MUSE IFU to fully map the Lyα emission nebulae of a sample of HzRGs over a redshift range of 2.92−4.51 and initiated a comparison with type-1 quasars and study of CGM-scale environments. We introduce our sample of HzRGs, the MUSE observations, and data reduction in Sect. 2. We present how we measured the maximum extent of the nebulae in Sect. 3.1 and summarise the spectral fitting procedure in Sect. 3.2. We then present the results

Table 1. Details of the MUSE observation of the HzRG sample.

HzRG	Redshift z (†)	UT date (dd/mm/yyyy)	Program ID	Mode	Exp. time total hours	Seeing arcsec (*)
MRC 0943-242	2.9230	21/02/2014	60.A-9100(A)	WFM-NOAO-E	5.21	0.65 [a]
–	–	15/12/2015-18/01/2016	096.B-0752(A)	–	–	–
MRC 0316-257	3.1238	15/01-17/01/2015	094.B-0699(A)	WFM-NOAO-N	4.24	0.61 [b]
TN J0205+2242	3.5060	03/12-08/12/2015	096.B-0752(B)	WFM-NOAO-N	4.24	0.73
TN J0121+1320	3.5190	06/10/2015	096.B-0752(C)	WFM-NOAO-N	5.30	0.83
–	–	08/08-28/08/2016	097.B-0323(C)	–	–	–
4C+03.24	3.5828	17/06-18/06/2017	60.A-9100(G)	WFM-AO-N	1.25	0.63
4C+19.71	3.5892	08/06-02/09/2016	097.B-0323(B)	WFM-NOAO-N	5.83	1.03
TN J1338-1942	4.0959	30/04-06/05/2014	60.A-9100(B)	WFM-NOAO-N	8.93	0.77 [a]
–	–	30/06/2014	60.A-9318(A)	–	–	–
4C+04.11	4.5077	03-15/12/2015	096.B-0752(F)	WFM-NOAO-N	4.24	0.88

Notes. (†)The redshifts are determined from the He IIλ1640Å or [C I](1-0) emission line (Kolwa et al. 2023). For MRC0316-257 which is not included in Kolwa et al. (2023), we reported its z_{sys} in this paper based on He II fit from our MUSE data (Appendix E). (*)The seeing reported here is determined from the fitted 2D Moffat FWHM (full width at half maximum) of a star in the white-light image (5000−9000 Å) produced from the combined cube. We note that the stars used are red in colour, i.e. the image quality in the Lyα wavelength should in general be worse than the reported seeing (e.g. larger by 10 to 20%). (a)The seeing is determined from a star in the overlapping region of the two pointings. (b)There is no available star in the FoV. The seeing is determined from the fit of the most point-like source.

of surface brightness, kinematics, and morphology in Sect. 4 followed by a discussion in Sect. 5. Finally, we conclude in Sect. 6. In this paper, we assume a flat ΛCDM cosmology with H_0 = 70 km s^{-1} Mpc^{-1} and Ω_m = 0.3. Following this cosmology, 1 arcsec ≃ 6.6–7.7 pkpc for our sample redshifts. Throughout the paper, pkpc stands for proper kiloparsec and ckpc represents comoving kiloparsec, ckpc = $(1+z)$pkpc. In this paper, we use 'intrinsic' to refer to the absorption-corrected Lyα emission.

2. HzRGs sample, observations, and data processing

2.1. MUSE HzRGs sample

2.1.1. Sample selection

The 8 HzRGs at $2.92 < z < 4.51$ (Table 1) that we investigate in this paper were selected to (i) be at $z > 2.9$ for Lyα to be covered by MUSE ; (ii) have a known extended bright Lyα (>10″) emission nebula; and (iii) be at Dec < 25° to be observable by ground-based telescopes in the southern hemisphere. This sample also has a wealth of high quality supporting data obtained by our team, including deep *Spitzer*/IRAC and *Spitzer*/MIPS 24 µm imaging, and *Herschel*/SPIRE detections (Seymour et al. 2007; De Breuck et al. 2010). ALMA Band 3 or 4 data are also available for the sample targeting dust continuum and molecular lines (Falkendal et al. 2019; Kolwa et al. 2023). Being identified as radio galaxies, the radio observations (e.g. VLA, Carilli et al. 1997) provide information on the jet morphology and polarisation. Based on these supporting data sets, we have estimates of the total stellar mass of the host galaxies (several 10^{11} $M_\odot$ for all targets, De Breuck et al. 2010) and the star formation rates ranging from uppers limit of <84 $M_\odot$ yr^{-1} to constraints of 626 $M_\odot$ yr^{-1} (Falkendal et al. 2019).

2.1.2. AGN bolometric luminosity estimation

To put the HzRGs into context with other quasar species, we plan to link our Lyα nebulae to literature works based on AGN bolometric luminosity. There are different methods for estimating the bolometric luminosity of AGN, $L_{\rm bol,\,AGN}$, for example through scaling of the far-IR AGN-heated dust luminosity (e.g. Drouart et al. 2014), scaling the IR flux density (e.g. $f_{3.45\,\mu m}$ which is used for type-1 quasars, Lau et al. 2022) and through [O III] emission (which can be affected by star formation and/or shocks Reyes et al. 2008; Allen et al. 2008). However, there is a large uncertainty between the values derived through these different methods which makes it non-trivial to directly compare the $L_{\rm bol,\,AGN}$ of type-1s and type-2s. For instance, the estimates for type-2 AGN are affected by obscuration by the dusty torus assuming the AGN unification model (e.g. Antonucci 1993). Accounting for this by applying an extinction correction factor would lead to a large uncertainty (e.g. Drouart et al. 2012) if we were to use the same method for type-1s to estimate the $L_{\rm bol,\,AGN}$ for our sample. We report that the $L_{\rm bol,\,AGN}$ estimated for our sample using those different methods varies from $10^{45.9}$ to $10^{48.5}$ erg s^{-1}. Given this large uncertainty, we find it is unreasonable to draw further conclusions from the comparison of $L_{\rm bol,\,AGN}$ between type-1s and our HzRGs. However, it is worthwhile to report this estimation procedure and the resulted inconsistency under different assumptions. A systematic study of the $L_{\rm bol,\,AGN}$ is beyond the scope of this work and may be done more thoroughly through multi-wavelength approach.

2.1.3. Jet kinematics

To distinguish between the approaching and receding sides of the jet, we use the kinematics information from [O III] as a proxy which is often used for studying quasar outflow (e.g. Veilleux et al. 2005; Zakamska et al. 2016; Nesvadba et al. 2017a,b; Vayner et al. 2021). 5 out of 8 of our sample targets have been observed by SINFONI from which the [O III] velocity shifts are available (Nesvadba et al. 2007, 2008, 2017a). For MRC0943-242 and TN J1338-1942, we use the radio hot spot polarisation information as indicator where the more depolarised indicates the far side (receding) of the jet (Carilli et al. 1997; Pentericci et al. 2000). These are also consistent with the tentative [O II] velocity gradient of TN J1338-1942 found in Nesvadba et al. (2017a; also He II kinematics in Kolwa et al. 2023) and MRC0943-242 He IIλ1640 Å (He II) kinematics in

Kolwa et al. (2019). For 4C+04.11, Parijskij et al. (2014) gives the jet kinematics based on high-resolution radio polarisation. We note here that the reported approaching and receding directions based on the current observations should be treated with caution. The polarisation of the radio lobes could especially be affected by the intervening ionised structures. We also quantified the size of the jets by calculating the angular distance between the jet hot spots on either side to the AGN position (presented in Appendix D).

2.2. MUSE observations

In this work, we analyse data from MUSE integral field spectrograph (Bacon et al. 2010, 2014) mounted on the ESO Very Large Telescopes (VLT) Yepun (UT4). All observations were carried out in Wide-Field Mode (WFM) offering a 1×1 arcmin^2 field of view and spatial sampling of 0.2 arcsec pixel^{-1}. MUSE provides two sets of wavelength coverage: a nominal range (N, 480−930 nm) and an extended range (E, 465−930 nm) without using of the adaptive optics (AO). For observations carried in AO mode, the wavelength coverage of 582−597 nm is excluded due to the Na Notch filter. The MUSE spectrograph has the spectral sampling of 0.125 nm pixel^{-1} and resolving power of 1750−3750 for 465−930 nm which corresponds to $\Delta v \sim 171$−90 km s^{-1}.

The observations of our sample were carried mostly in service mode under the program IDs 094.B-0699, 096.B-0752 and 097.B-0323 (PI: J. Vernet). For MRC 0943-242, we also include the data of MUSE commissioning observation under the program ID 60.A-9100(A) (e.g. Gullberg et al. 2016). The extended wavelength coverage was employed for MRC 0943-242, the lowest redshift sample target, to cover its Lyα emission ($L_{\mathrm{Ly}\alpha,\mathrm{obs}}$ = 4769 Å). We use the MUSE commissioning and science verification data of TN J1338-1942 under the program IDs 60.A9100(B) and 60.A-9318(A) (e.g. Swinbank et al. 2015). For 4C+03.24, we adopt the data released from the MUSE WFM-AO commissioning observations under the program ID 60.A-9100(G). The information of the observations of our sample, in the order of redshift, is summarised in Table 1. For each object, observations consist of 1 (4C+03.24) to 6 (TN J 1338-1942) observing blocks (OBs). Within each OB, the 2 or 3 exposures of 20−30 min were slightly dithered (with a <1″ amplitude pattern) and rotated by 90 degrees from each other.

2.3. Data processing

The reduction of the raw MUSE data are carried out following the standard procedure using the MUSE pipeline (Weilbacher et al. 2020, version 2.8.4) executed by EsoRex (ESO Recipe Execution Tool; ESO CPL Development Team 2015). For studying the extended Lyα nebulae to the faintest edge, we reduce the data following the optimised procedure developed in our pilot study of 4C+04.11 (Wang et al. 2021b). We first reduce each exposure individually with the standard pipeline doing the sky-line subtraction and then using ZAP (Zurich Atmosphere Purge, Soto et al. 2016) to remove the sky-line residuals (see below details regarding the ZAP execution). We then combine all exposures to the final data cube using MPDAF `Cubelist.combine` (MUSE Python Data Analysis Framework Bacon et al. 2016). We correct the astrometry of the final combined cubes using star positions from the available *Gaia* EDR3 catalogue (Early Data Release 3, Gaia Collaboration 2021). Two sources had no *Gaia* star within the MUSE field-of-view (FoV). For TN J0121+1320 we use the SDSS DR16 (16th Data Release, Ahumada et al. 2020) catalogue instead. For MRC 0316-257, we use *Gaia* EDR3 to first correct the astrometry of the HST/ACS $F814W$ image and then matched the MUSE cube to the HST image.

Using ZAP directly for sky-line residual removal without applying masks may remove faint narrow Lyα line emission at the outskirt of our sample. Since the Lyα nebulae in our sample extend much further beyond the continuum emission regime of the host galaxy and become narrower in line width (e.g. Villar-Martín et al. 2003; Humphrey et al. 2007) such that they are mistakenly treated as sky-line residuals and removed. To alleviate this problem (Soto et al. 2016), for each source, we (i) generate a first version of the combined data cube without masks in the ZAP step; (ii) construct a Lyα mask that covers most line-emission region[1]; (iii) re-run ZAP using this Lyα mask on individual cubes for each exposures; (iv) combine the newly obtained individual cubes to the final version data cube with MPDAF.

We also correct for small residual (mostly) negative background level offsets probably due to a slight over-subtraction of the sky continuum in previous steps. To do so, we (i) extract a median spectrum from an $r \simeq 10''$ circular aperture around the radio galaxy masking all continuum sources falling in the aperture; (ii) mask the Lyα line emission wavelength range and strong sky-lines ($>10^{16}$ erg s^{-1} cm^{-2} Å^{-1} arcsec^{-2}, Hanuschik 2003) for this median spectrum; (iii) fit a 6th-order polynomial to this masked spectrum; (iv) subtract this solution from the whole cube.

Finally, to correct for the known underestimation of the variance in the standard pipeline reduction (see Weilbacher et al. 2020), variance scaling is implemented as described in Wang et al. (2021b). Specifically, we scale the variance extension propagated by the pipeline based on the scale factor calculated in source-free regions using the variance estimated from the data extension.

3. Data analysis

3.1. Lyα nebulae extent and tessellation

To systematically study the Lyα nebulae of our HzRGs sample, we first need to determine all the voxels (volume pixel) containing usable Ly-alpha signal (Sect. 3.1.1) and bin the data to a sufficient signal-to-noise ratio (S/N) using a tessellation technique (Sect. 3.1.2) before fitting the emission feature described in Sect. 3.2.

3.1.1. Maximum extent of the nebulae

To select the Lyα signal with optimised sensitivity and capture the very low surface brightness structures of the nebulae, we used our own version of the adaptive smoothing algorithm described in Martin et al. (2014; see also Vernet et al. 2017, for an application to one of the sources in our sample). We first smooth the data cube in the wavelength direction by averaging n_λ neighbouring pixels. Then for each wavelength plane, the algorithm iteratively smoothes spatially with a growing gaussian kernel selecting pixels passing a given S/N threshold ($T_{\mathrm{S/N}}$) and leaving to the next iterations only spaxels below this S/N threshold, until a maximum smoothing radius is reached ($\sigma_{\max}$). The spaxels not selected by the end of the iterative process are

[1] We note that this mask is only used in this process to eliminate the impact of the Lyα signal on ZAP. The detection map for determining the maximum extent of the Lyα nebula is described in Sect. 3.1.1.

masked out. To further clean the smoothed data cube from spurious noise features and make sure that a proper line fitting can be made, we mask spatial positions selected by the adaptive smoothing algorithm in less than n_c consecutive wavelength bin.

To determine the optimal combination of the four parameters (n_λ, $T_{S/N}$, σ_{max} and n_c), we explore a range of possible combinations and select the set that is most sensitive to the extended low-surface brightness emission while at the same time minimising the number of detached 'island-like' structures (see Appendix A.1 for details). We note that the maximum nebulae extents selected by this method are similar to the results from previous studies of individual targets by different procedure (TNJ1338–1942 from Swinbank et al. 2015) or pure manual selection (MRC0316-257 in Vernet et al. 2017). We then manually clean up this map for the few remaining isolated island-like regions with further checking spectra extracted from these regions. This clean-up is accompanied by signal checking through spectrum extraction and only affects low S/N regions (Appendix A.1). Thus, the bulk of the detection map remains unchanged. This resulting detection map defines the pixels that we consider as part of the nebula and that we use in the analysis in this paper (see also Appendix A.1).

3.1.2. Tessellation procedure

In order to increase the S/N to a level that allows fitting of the Lyα line, especially close to the detection limit at the periphery of the nebulae, we tessellate the Lyα detection map. To construct the tessellation map, we firstly use a S/N map based on a narrow-band image (~15 Å wide) extracted around the Lyα emission peak. We implement a two-step Voronoi binning (Cappellari & Copin 2003) procedure which optimises the performance for both high S/N and low S/N regions by tessellating individually on these two parts. Specifically, the two-step procedure uses different target S/N for inner and outer regions. In this way, we can avoid large size tiles at the low S/N (outer) regions which may unnecessarily smear spatial resolution by imposing too high target S/N. We then combine the tessellated regions from the two-step process into one map. We emphasise that the tessellation is a trade-off between spatial resolution and S/N. The main goal of the work is to study the extend Lyα nebulae to the detection limit. This can only be achieved by sacrificing the spatial information. The details of this tessellation process are described in Appendix A.2, and in A.3 we present the resulting the maps.

3.2. Spectral fitting

3.2.1. Lyα absorption modelling

In this work we treat the Lyα emission system of HzRGs as an idealised case where several assumptions have been made prior to the analysis: (i) the radio galaxies reside in giant reservoirs of neutral hydrogen (~100s kpc); (ii) the neutral hydrogen is rather diffuse with large covering factor; (iii) the geometry of the giant reservoirs is unknown but can be highly asymmetrical due to the influence of the radio jet. Under these assumptions, it is natural that we observe absorption effecting the Lyα profiles. Indeed, such absorption troughs are observed in our Lyα spectra (see Fig. 1) that need to be accounted for when drawing conclusions about the intrinsic emission line flux and higher moment measurements. Specifically, high resolution spectrocopy using the UltraViolet and Echelle Spectrograph (UVES) on the VLT exists for seven out of eight of the targets in our sample (Jarvis et al. 2003; Wilman et al. 2004, Ritter et al., in prep.). These spectra with ~30 higher resolution than MUSE display sharp edges which is fully consistent with a well-defined absorption profile rather than radiative transfer effects. We note that the term 'radiative transfer' used in the paper refers to the process where Lyα photons are scattered in frequency (wavelength) but are still captured in the spectrum (i.e. not 'lost' in the observer's line of sight). In our assumptions, contrary to this, the photons are 'lost' either due to being scattered outside our line of sight or being absorbed by dust and remitted at longer wavelength. We therefore adopt the technique used in our pilot study (Wang et al. 2021b, and equations therein) and fit the spectra using a combination of Gaussian emission line profiles and Voigt absorption troughs (e.g. Tepper-García 2006, 2007; Krogager 2018). This procedure has also been implemented successfully in the literature for fitting the Lyα line emission in HzRGs (e.g. Swinbank et al. 2015; Silva et al. 2018b; Kolwa et al. 2019).

The known degeneracy between the H I column density and Doppler parameter in our fits (e.g. Silva et al. 2018a) does not affect the reconstructed intrinsic emission which is the focus of this work. We show the 'Master Lyα spectrum' extracted from a central 1″ aperture in Fig. 1a which presents how the intrinsic profile compares to the observed spectrum (see Sect. 4.1 for details).

We emphasise that the term 'intrinsic Lyα emission' throughout the work refers to the nebula Lyα emission corrected for intervening absorbers. The absorption troughs seen on the spectra (Fig. 1a) are due to the Lyα emission being absorbed by these neutral hydrogen gas clouds or shells along the line of sight. Under the aforementioned assumptions, a natural consequence is that the absorbers must be distributed across the whole projected extension of the nebula. The fact that we mostly observe these features continuously across the extent of the nebulae in most HzRGs indeed indicates they are coherent intergalactic-scale structures. This can be found in Figs. 2–4 where similar absorption features are seen in the selected spectra at larger distance (10s of kpc) away from AGN. Similar maps of the remaining sources are shown in Appendix C which are the ones have been previously published (Swinbank et al. 2015; Gullberg et al. 2016; Vernet et al. 2017; Falkendal et al. 2021; Wang et al. 2021b). Our approach is a common interpretation in studies of HzRGs. Conversely, such absorbers are not often seen in the Lyα nebulae of other quasars. This reinforces the interpretation that strong (radio-mode) feedback on intergalactic scales is needed to create such 'shells' of H I material. The use of a Gaussian as underlying intrinsic emission profile is supported both by observational and modelling works (e.g. Arrigoni Battaia et al. 2019; Chang et al. 2023). This could be a result of prior radiative transfer effects of Lyα (e.g. local scattering or scattering from the broad line region of the AGN Verhamme et al. 2006; Gronke & Dijkstra 2016; Gronke et al. 2016; Li et al. 2022). The radiative transfer modelling requires assumptions about the composition and geometry (and kinematics) of the gas near the AGN which is not the focus of this paper. Hence, we just assume the Gaussian shape of the Lyα (which could be due to the radiative transfer effects) and correct for the absorption along the line of sight to reconstruct the intrinsic emission on CGM scales. Incorporating radiative transfer calculations into the study of HzRGs Lyα nebulae is beyond the scope of this current work. Further developments of theoretical works are required (e.g. adding jet and resolving shells in simulations), and our dataset would be well suited for such studies. We therefore stress that the presented results are only valid for the stated

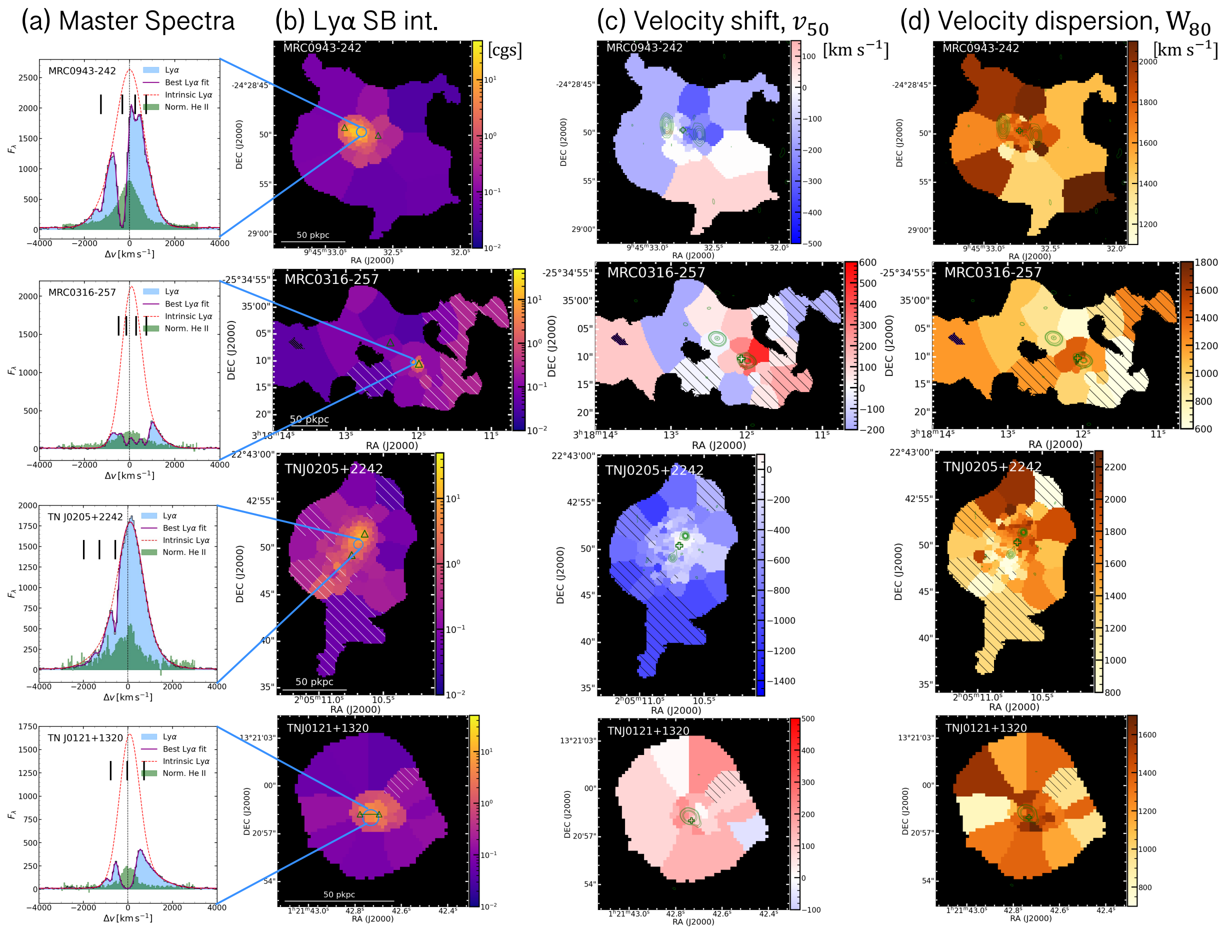

Fig. 1. Mapping results of our MUSE HzRGs sample. (a) Master Lyα spectrum (blue shaded histogram) extracted from a $r = 0.5$ arcsec aperture at the AGN position with best fit (solid dark magenta line). Red dashed curve shows the intrinsic Lyα from fitting, i.e. corrected for absorption. The vertical black bars above the emission line mark the positions of the H I absorbers. The yellow shaded region (if any) indicates the 5 wavelength pixel range excluded in the fitting due to the contamination from the 5577 Å sky-line. The flux density unit, F_λ, is 10^{-20} erg s^{-1} cm^{-2} Å^{-1}. We also show the scaled He IIλ1640 Å spectrum extracted from the same position in green histogram. We scale the peak flux density of He II to 0.3−0.7 (varied for different targets) of the maximum peak flux density of observed Lyα spectrum in −1000 to 1000 km s^{-1}. The $\Delta v = 0$ km s^{-1} is the systemic redshift based on He II or [C I] (Table 1, Kolwa et al. 2023). (b) Intrinsic Lyα surface brightness map. The flux in each tile is the integrated flux of the line emission corrected for absorption, i.e. total flux of the one or two Gaussians, see Sect. 3.2. The light blue circle shows the aperture where the Master spectrum is extracted from. Green triangles mark the positions of the radio lobes. We place a green bar linking the triangles on TN J0121+1320 to indicate the unresolved state of its radio emission. The length of the bar represents the linear size of the 3σ contour along the east-west direction. The white hatched regions are the ones where the flux uncertainty is higher than 50% of the fitted intrinsic flux. The white bar indicates the 50 pkpc at the redshift of the radio galaxy. The unit of the surface brightness is 10^{-16} erg s^{-1} cm^{-2} arcsec^{-2}. We apply the same colour scale for all targets. (c) v_{50} map of the intrinsic Lyα nebula. The zero velocity used for each target is determined by the systemic redshift (Table 1). Green contours show the morphology of the radio jet in arbitrary values. The green cross mark the AGN position (Table 2). (d) W_{80} map of the intrinsic Lyα nebula. The black hatched regions on (c, d) are the same as (b). The purple hatched regions (in 4C+03.24 and TN J1338-1942) are manually excluded due to contamination from either foreground star or known companion (Arrow galaxy in the filed of MRC0316-257, see Vernet et al. 2017). We note that the colour scales for panels c and d are customised. The purple hatched area (if any) indicates the manually excluded region affected by foreground star or known Lyα emitter.

assumptions that absorption rather than radiative transfer is primarily responsible for the line profiles. We discuss the limitation of this treatment in Sect. 5.1.

We note that the O V]$\lambda\lambda$1213.8, 1218.2 (O V]) line underneath the Lyα can affect the obtained flux especially in the nuclear region where the ionisation parameter (and metallicity) is higher (Humphrey 2019). In our pilot study (Wang et al. 2021b) of 4C+04.11, we found the contribution from O V] is negligible. Hence, we do not further include O V] in our line fitting. We leave the inspection to future work when data of metal lines (e.g. N V$\lambda\lambda$1238, 1243 which is found to be related with O V]) and high resolution spectra are analysed.

3.2.2. Fitting procedure

To reconstruct the intrinsic Lyα emission across the nebula, we fit each spectrum in each tessellation bin (see Sect. 3.1.2) following the procedure described in Sect. 3.2.1. We take into account the physical connection between neighbouring tiles by using the fit results of a previous connected bin as the starting parameters

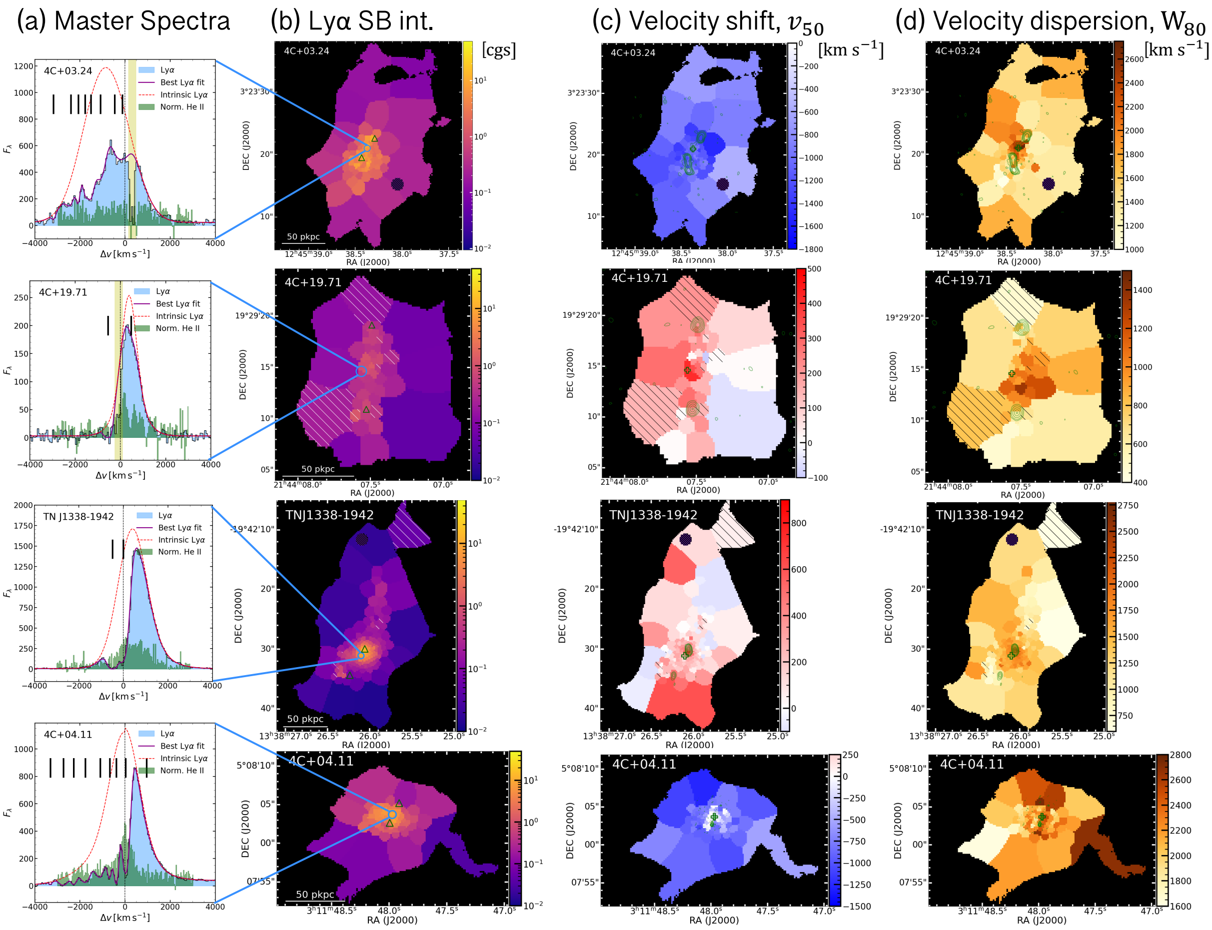

Fig. 1. continued.

for the next bin (see Appendix A for details on the ordering). We determine the number of absorbers based on the Master spectrum where the S/N is the highest (Fig. 1a). We then use that same number of absorbers across the nebula, where the centroid, column density and Doppler parameter of absorbers are fitted in a given range (Appendix B). This assumption is supported by the profile shapes at the largest spatial extents (see Figs. 2–4 and also Appendix C). We note that the number of absorbers selected here may be incomplete but this has minor effects on the results of this paper: (i) the absorbers that impact most the intrinsic flux (i.e. spatially extended ∼10″ and having higher column density and/or larger Doppler parameter) are included; (ii) absorbers that seem to be 'superfluous' at the wings have only minor effects on the reconstructed flux where S/N is low (Fig. 2–4). Future work using high spectral resolution data will address these issues also taking into account that some of these absorbers have counterparts in metal lines covered by the MUSE data (e.g. N V$\lambda\lambda$1238, 1243 and C IV$\lambda\lambda$1548, 1551 Kolwa et al. 2019; Wang et al. 2021b). We perform the fit in each bin using both one and two Gaussian emission line components and we choose the solution that minimises the reduced χ^2. The fit is done using a least-squares method followed by a Markov chain Monte Carlo (MCMC, using the python package `emcee`, Foreman-Mackey et al. 2013) sampling. The uncertainties we report are either the direct output of the 1σ error by the MCMC or the propagated 1σ error. A detailed description of the fitting procedure is provided in Appendix B. We reiterate that we do not report any further parameters on the absorption features which will be analysed in future work in combination with higher spectral resolution data (e.g. Jarvis et al. 2003; Wilman et al. 2004; Kolwa et al. 2019, Ritter et al., in prep.). We present the results of this procedure for all of our sources in Fig. 1.

4. Results

4.1. Intrinsic mapping

In this section, we present the intrinsic maps (i.e. corrected for absorption) constructed following the fitting procedure described in Sect. 3.2. For each sources we show the Master spectrum together with its best fit in Fig. 1a as an example (Sect. 3.2.1). We also show the non-resonant He II spectrum extracted in the same aperture (green histogram, not continuum subtracted) which is used for systemic redshift ($\Delta v = 0\,\mathrm{km\,s^{-1}}$, Table 1) determination. We note that there is no He II detected at the AGN position for 4C+03.24 (Sect. 4.2.4). In addition, to illustrate how fitting procedure works spatially (Sect. 3.2.2), the selected exemplar individual fits are shown in Figs. 2–4 (also see Appendix C).

The intrinsic Lyα surface brightness maps are shown in Fig. 1b on the same flux scale. Regions with larger fitting

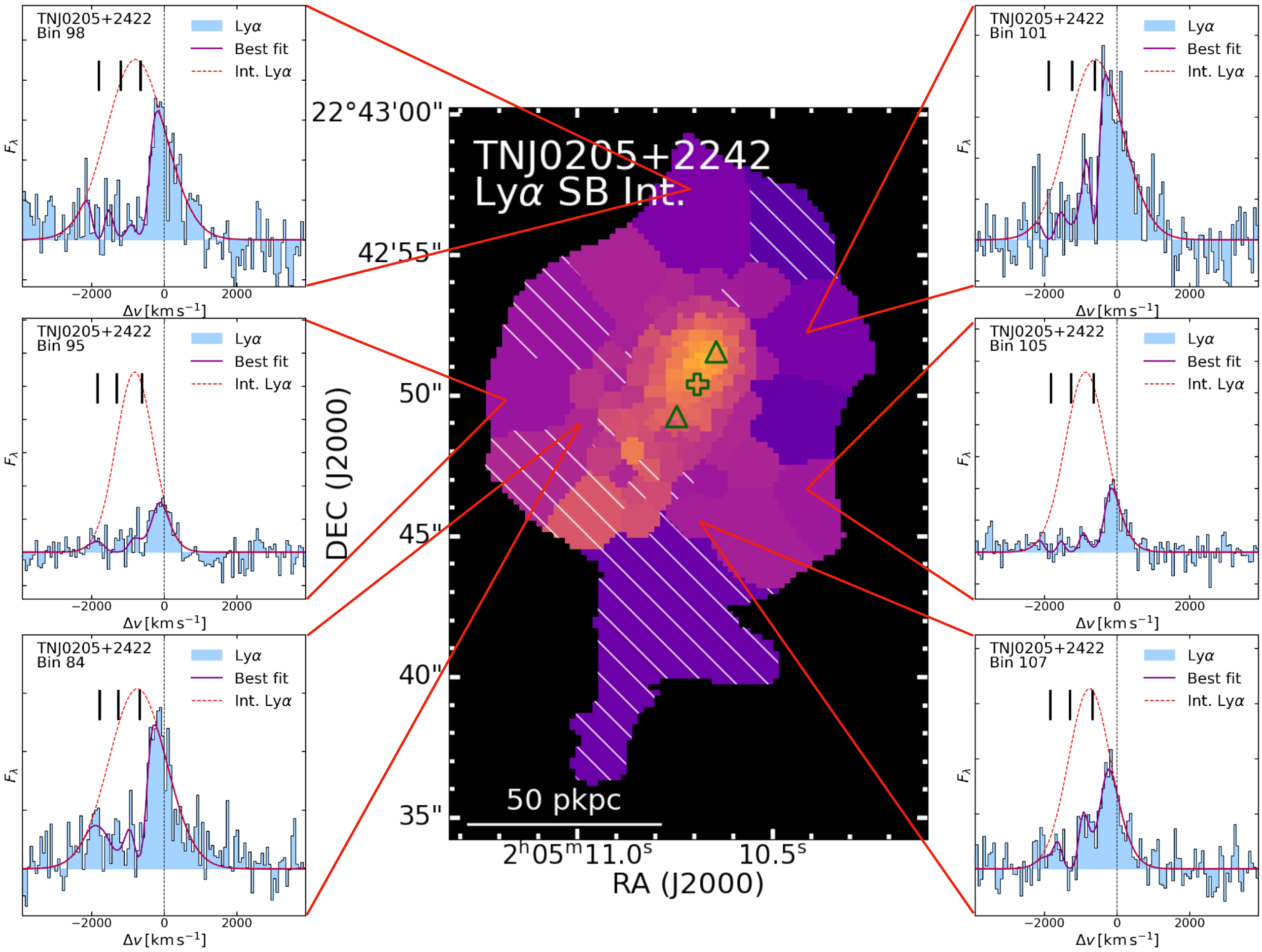

Fig. 2. Example for the intrinsic mapping of the Lyα nebula of TNJ0205+2242. The central panel shows the intrinsic surface brightness map of TNJ0205+2242 which is the same as Fig. 1b. The green cross and triangles mark the position of the AGN and jet lobes, respectively. In each of the side panel, we show the spectrum (blue shade histogram in normalised flux unit) extracted from the individual spatial bin whose number is labelled at the top left, and the best fit (dark magenta curve) and recovered intrinsic Lyα (dashed red line). The black vertical bars indicate the positions of the H I absorbers.

uncertainties ($\gtrsim$ 50%) that should be treated with caution are indicated by the overlaid hatched tiles. We report the total intrinsic Lyα luminosities ($L_{\mathrm{Ly}\alpha,\mathrm{int}}$) of the nebulae in Table 2 and their maximum linear extent, $d_{\max}$, in Table 3. Down to the surface brightness limit (Table 2), seven of our nebulae are extended over 100 pkpc with the largest being ~347 pkpc (MRC0316-257). TNJ0121+1320 is the only target with nebula < 100 pkpc (~72 pkpc). The total intrinsic surface brightness ($L_{\mathrm{Ly}\alpha,\mathrm{int}}$) of the nebulae ranges from 2 to 29×10^{44} erg s^{-1}.

To characterise the kinematic information of the intrinsic nebulae that are fitted with one or two Gaussians, we use a set of non-parametric emission line measurements (see e.g. Liu et al. 2013) derived from the cumulative line flux as a function of velocity $\Phi(v)$ defined as:

$$\Phi(v) = \int_{-\infty}^{v} f(v')\mathrm{d}v' \tag{1}$$

where $f(v')$ is the flux density at v'. The often used v_{50} is the velocity where the cumulative flux reaches 50% of the total integrated value, $\Phi(v_{50}) = 0.5\Phi(\infty)$. The v_{05}, v_{10}, v_{90} and v_{95} are defined similarly. The line width measurement, W_{80}, defined in this context is $W_{80} = v_{90} - v_{10}$. In case of single Gaussian fits, W_{80} is directly related to the FWHM and v_{50} is the Gaussian centroid.

The non-parametric velocity shift (v_{50}) and line width (W_{80}) of the nebulae are shown respectively in panels c and d of Fig. 1. The v_{50} maps do not show clear trend on larger scale (i.e. beyond the jet hot spots) for the whole sample. This is foreseeable given that (i) Lyα is a resonant line which is sensitive to scattering (i.e. it will not necessarily show the bulk velocity of the gas), and we only observe the last scattering surface; (ii) the size of the tile far from the centre is larger which could smear out potential velocity structures; (iii) the line emissions on several 10s of pkpc could trace the inflowing gas (or other gas components not governed by the host galaxy and/or kinematically related to the quasar outflow, e.g. Vernet et al. 2017). Within the extent of the radio jets, 3 targets (MRC0943-242, MRC0316-257 and TN J1338-1942) show tentative velocity gradients consistent with the jet kinematics (Sect. 2.1.3). For the line width maps, W_{80}, 3 targets (4C+03.24, 4C+19.71 and TN J1338-1942) show a trend with the line being broader near the centre and becoming narrower outwards. There are some tiles on the periphery of the nebulae,

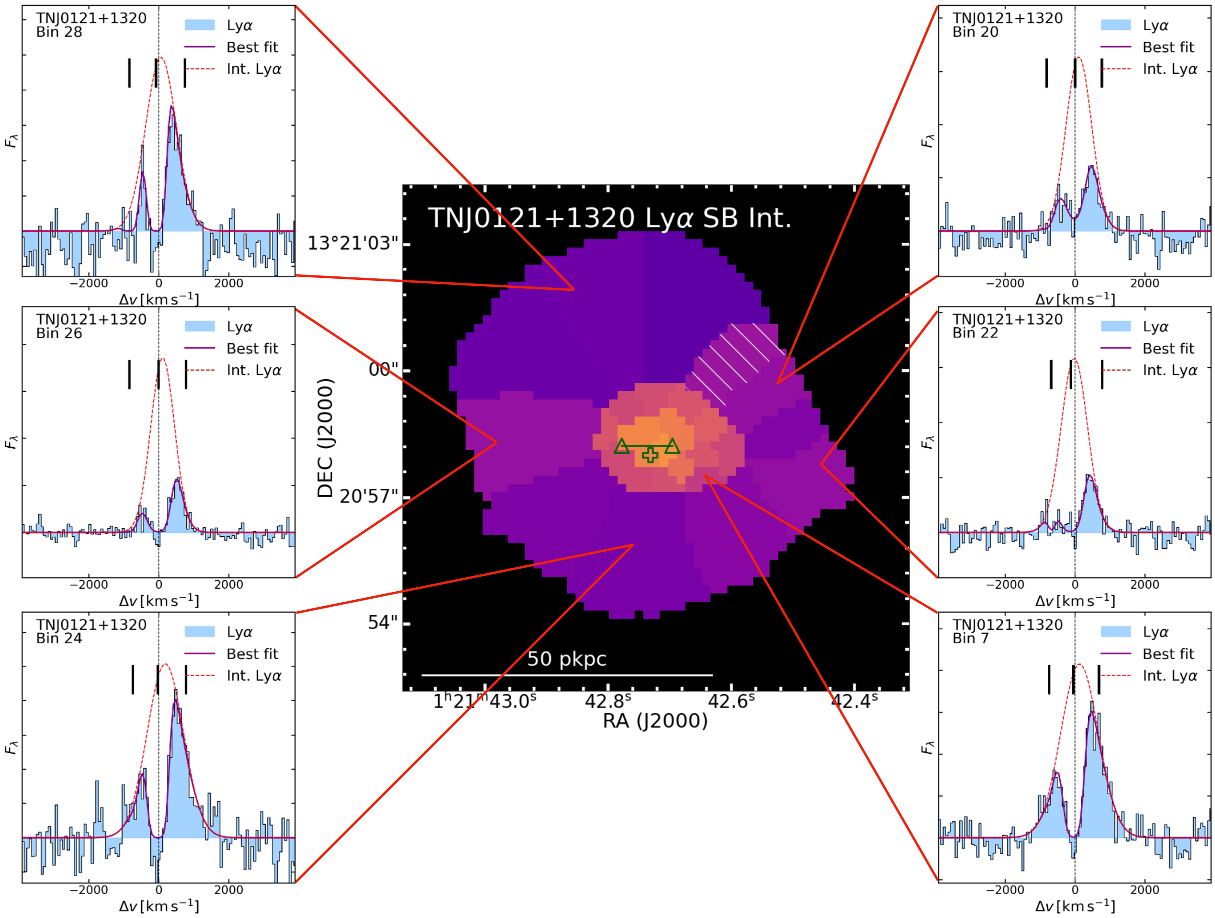

Fig. 3. Similar to Fig. 2, but for TNJ0121+1320.

for example the south-west tile of 4C+04.11, displaying larger W_{80} values ($\gtrsim$2500 km s^{-2}). Except 4C+19.71, all targets show a line width of ~800–2500 km s^{-1}. For 4C+19.71, due to the strong 5577 Å sky-line located close with the observed Lyα peak wavelength, its line width should be treated as lower limit ($\gtrsim$600km s^{-1}) especially for the tiles in the outskirts of the nebula.

We note that the non-parametric measurements used in this mapping are based on intrinsic (= absorption-corrected) line profiles which are determined through model fitting, same as Wang et al. (2021b). In Appendix C, we present the maps of observed surface brightness and flux ratio as supplementary material.

4.2. Radial profiles

4.2.1. Circularly averaged surface brightness radial profiles

In this section, we present the surface brightness radial profile of the eight Lyα nebulae. In order to compare our HzRGs to other quasar samples, we extract the surface brightness profile centred around the AGN in circular annuli. The annuli over which the profiles extracted are shown in Fig. D.1. We compute the surface brightness in each annulus as the mean of the surface brightness of each contributing spaxel weighted by the fraction of the spaxel area covered by the annulus. Table D.2 lists the extracted intrinsic profile values.

Figure 5 shows the radial profiles after correction for cosmological dimming and in comoving units for observed (upper panel) and intrinsic (lower panel, corrected for absorption) maps. The dashed lines in the upper panel represent the comparison quasar samples or single targets (an extremly red quasar and 2 radio-loud quasars from Lau et al. 2022; Vayner et al. 2023, respectively). The selected quasars are all observed by advanced IFU instruments (MUSE or KCWI) and cover a large range of redshift and physical properties. They are luminous radio-quiet quasars at z ~ 3.2 quasar from Borisova et al. (2016; profiles from Marino et al. 2019), luminous type-1 quasars at z ~ 3.17 from Arrigoni Battaia et al. (2019), luminous quasars at z ~ 2.3 from Cai et al. (2019), high redshift quasars at z ~ 6.28 from Farina et al. (2019) and luminous quasars at z ~ 3.8 from Fossati et al. (2021). The quasar nebulae do not show so many absorption features as in our HzRGs and the studies were preformed without absorption corrections (Sect. 5.1). Nevertheless, since the comparison quasar samples are not corrected for absorption, we do not show them all again in our intrinsic profile (lower) panel. The two exceptions are Farina et al. (2019, hereafter F19) and Vayner et al. (2023; 7C 1354+2552, V22 7C). Those two are on the higher surface brightness end of the comparison samples, and we examine them quantitatively along with both the intrinsic and observed HzRGs profiles. We note that Vayner et al. (2023) fitted the Lyα absorbers from the spatially integrated 1D spectrum and found ~$10^{13.5}$ cm^{-2} for

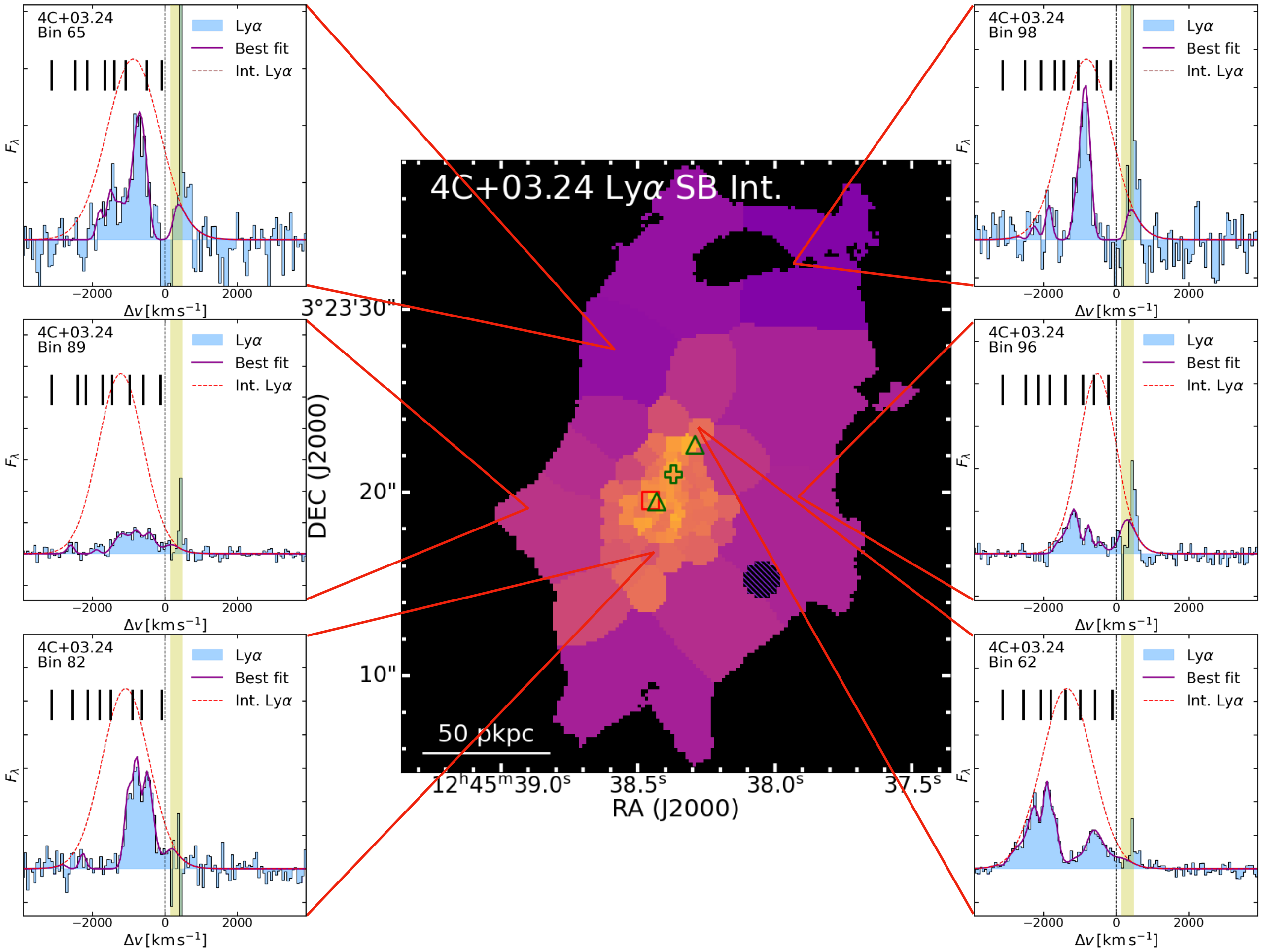

Fig. 4. Similar to Fig. 2, but for 4C+03.24. The red box marks the secondary southern K-band continuum emission peak (van Breugel et al. 1998, Sect. 4.2.4). The yellow shaded regions show the wavelength range excluded due to the 5577 Å sky-line.

Table 2. HzRGs MUSE sample properties.

HzRG	RA (J2000) [†] hh:mm:ss	Dec (J2000) [†] dd:mm:ss	SB limit [*] 10^{-19} cgs	$L_{\mathrm{Ly}\alpha,\,\mathrm{int}}$ [‡] 10^{44} erg s^{-1}	$L_{\mathrm{Ly}\alpha,\,\mathrm{obs}}$ [§] 10^{44} erg s^{-1}
MRC 0943-242	09:45:32.73	−24:28:49.65 [a]	17.0	4.7±0.1	2.39±0.03
MRC 0316-257	03:18:12.07	−25:35:10.22 [b]	2.62	7.3±1.2	1.04±0.04
TN J0205+2242	02:05:10.69	+22:42:50.4 [a],[c]	13.3	8.3±0.4	3.82±0.06
TN J0121+1320	01:21:42.73	+13:20:58.0 [a]	5.64	2.0±0.1	0.55±0.01
4C+03.24	12:45:38.37	+03:23:21.0 [d]	11.5	28.8±0.8	5.43±0.20
4C+19.71	21:44:07.56	+19:29:14.6 [a]	4.77	4.3±0.3	1.48±0.22
TN J1338–1942	13:38:26.10	−19:42:31.1 [e]	4.34	12.3±0.3	5.89±0.10
4C+04.11	03:11:47.97	+05:08:03.74 [f]	9.84	20.0±0.7	2.89±0.07

Notes. [†]Position of the AGN and/or host galaxy. [*]The surface brightness limit is the 2σ limit extracted from continuum-source- and Lyα-free regions in a narrow band image. The narrow band image is collapsed from v_{05} to v_{95} (see Sect. 4.1). The cgs unit is erg s^{-1} cm^{-2} arcsec^{-2}. [‡]Intrinsic Lyα luminosity (i.e. corrected for absorption) of the nebula. It is integrated over the entire area selected in Sect. 3.1 and multiplied with the luminosity distance using the cosmological parameters (Sect. 1). [§]Observed Lyα luminosity of the nebula integrated over the entire area from v_{05} to v_{95} (see text).

References. [a]*Spitzer* (Seymour et al. 2007; De Breuck et al. 2010). [b]*Chandra* Obs. ID 5734 (PI:Pentericci). *Chandra* Source Catalogue (Evans et al. 2010). [c]Radio (De Breuck et al. 2002). [d]Radio (van Ojik et al. 1996). [e]Radio (De Breuck et al. 1999). [f]Radio (Parijskij et al. 2014).

Table 3. HzRGs nebulae properties.

HzRG	$e_{\rm weight}$ $^{(\dagger)}$	$e_{\rm weight,\,obs}$ $^{(\dagger)}$	$e_{\rm unweight}$ $^{(\dagger)}$	$\lvert\theta_{\rm w.} - {\rm PA_{radio}}\rvert$ $^{(*)}$ deg	$\lvert\theta_{\rm unw.} - {\rm PA_{radio}}\rvert$ $^{(*)}$ deg	$d_{\rm AGN-neb}$ $^{(\ddagger)}$ pkpc	$d_{\rm max}$ $^{(\S)}$ pkpc
MRC 0943-242	0.73±0.01	0.76	0.62	4.7±1.8	7.2	3.4±0.1	164
MRC 0316-257	0.28±0.38	0.96	0.87	28±54	20.8	13.5±0.2	347
TN J0205+2242	0.91±0.01	0.79	0.75	2.1±2.3	8.6	9.0±0.1	170
TN J0121+1320	0.66±0.05	0.74	0.48	10.5±8.7	72.1	3.1±0.1	72
4C+03.24	0.79±0.01	0.72	0.82	8.1±1.2	2.0	9.9±0.1	248
4C+19.71	0.85±0.02	0.83	0.51	20.1±9.1	29.3	6.7±0.1	143
TN J1338–1942	0.94±0.01	0.87	0.90	1.3±1.4	1.2	15.3±0.1	265
4C+04.11	0.76±0.01	0.20	0.59	81.4±1.3	45.3	5.7±0.1	163

Notes. $^{(\dagger)}$Intrinsic flux-weighted ($e_{\rm weight}$), observed flux-weighted ($e_{\rm weight,\,obs}$) and unweighted elliptical asymmetric measurements. The flux-weighted ellipticity is sensitive to the morphology of the high surface brightness part of the nebula. The unweighted ellipticity quantifies the morphology of the whole nebula. We note that for $e \rightarrow 0$, the nebula is closer to round shape and vice versa. $^{(*)}$Absolute difference between flux-weighted (unweighted) nebula position angle, $\theta_{\rm weight}$ ($\theta_{\rm unweight}$), and radio axis position angle, ${\rm PA_{radio}}$. $^{(\ddagger)}$Offset between the intrinsic flux-weighted centroid of Lyα nebula and AGN position. $^{(\S)}$Maximum linear extent spanned by the Lyα nebula.

the column densities. For F19, there is not much evidence of absorption. Therefore, the comparison is legitimate. The best fit profiles to the observed Lyα nebulae of radio loud quasars in Arrigoni Battaia et al. (2019) are included in both panels of Fig. 5 which can be used as a reference between the two panels.

Except for the extremely red quasar from Lau et al. (2022; which is also highly obscured), type-1 radial profiles are dominated by direct emission from bright AGN point source in the inner regions (~50 ckpc or ~10 pkpc). Hence, due to point spread function (PSF) subtraction, the inner-most radius covered in the comparison samples is limited to ~50 ckpc in most cases (except Vayner et al. 2023). At larger radii, the contamination by the PSF should be negligible. Of the three single target profiles, V22 7C (7C 1354+2552 from Vayner et al. 2023) has the highest surface brightness. At a radius of ~50 ckpc, the intrinsic surface brightness of our HzRG sample has a factor of 0.5−7 compared with V22 7C (7 of our targets are brighter). This source then shows a faster drop off compared with HzRGs. At the faint end corresponding to ~300 ckpc (except TN J0121+1320), the HzRGs have a factor of 7−100 higher surface brightness than V22 7C. The profile of Farina et al. (2019) shows the highest surface brightness among the comparison samples. At ~50 ckpc, the intrinsic HzRG profiles are still a factor of 1.1 − 15 (or 4 − 40 at ~400 ckpc, except TN J0121+1320) brighter than the 75th percentile of Farina et al. (2019). These indicate that our eight observed HzRG have some of the brightest known Lyα nebulae (Sect. 2.1). We note that the jet compression is also known to result in high Lyα nebula luminosity (e.g. Heckman et al. 1991a,b). Compared to quasars with similarly deep observations (i.e. avoiding the surface brightness detection limit), our HzRG sample generally maintains a high surface brightness out to larger radii (5 out of 8 >500 ckpc). We note again that the detected extent of our nebulae will have similar range even if adopting other detection methods than the ones in this paper (Sect. 3.1). For example, Gullberg et al. (2016) reported the similar extend Lyα nebula in MRC0943-242 with less exposure time. Vernet et al. (2017) detected the nebula of MRC0316-257 >700 ckpc based on visual detection. Swinbank et al. (2015) found the > > 500 ckpc nebula of TN J1338-1942 with (or even without) a simpler binning algorithm. Hence, we are sure that the detection of the ≳500 ckpc nebulae in our sample based on our method is robust. However, we do caution that this sample is not representative since they are selected to have bright and extended Lyα emission. The profiles of MRC0943-242, MRC 0316-257 and TN J1338-1942 show a flattening at $r_{\rm AGN} > 200$ ckpc. For the comparison samples, their profiles drop off monotonically and drop below detection limit at radii smaller than our HzRGs. The lowest surface brightness of HzRG intrinsic profiles is ~$1{\times}10^{-15}$ erg s^{-1} cm^{-2} arcsec^{-2} (MRC0316-257, corrected for cosmological dimming) which is higher than the faint end of the quasar samples by a factor of 5 − 40 (not at similar comoving distances). These indicate that we are observing some of the most extend Lyα nebulae, in two cases (MRC0316-257 and TN J1338-1942) even extending beyond the field of view of MUSE. By simply comparing our intrinsic profiles to the exponential and power law fits of Arrigoni Battaia et al. (2019), we find that the inner part of HzRGs profiles are exponential-like (especially MRC0943-242 and TN J1338-1942) while extended parts show power law decline. We note, however, that the exponential part is affected by seeing smearing.

If we do not correct for the Lyα absorption and instead measure at the observed radial profiles (Fig. 5 upper panel), 5 of the HzRGs are still brighter than the comparison samples, but by a lower factor of ~2–4 (~2–6) at radii of ~400 (~50) ckpc compared to the 75th percentile of Farina et al. (2019). Comparing the results from intrinsic and observed profiles, this suggest that the quasar samples may miss a non-negligible amount of flux (≳5) due to uncorrected for absorption.

The radial surface brightness profiles of the comparison samples are extracted from a fixed velocity or wavelength range, for example ±2000 km s^{-1} in Cai et al. (2019), 30 Å in Arrigoni Battaia et al. (2019) and ±500 km s^{-1} in Farina et al. (2019). Considering the redshift difference between these samples, the integration range adopted are consistent. For our study, particularly for the observed radial profile, our extraction is based on the v_{05} and v_{95} which are determined based on intrinsic fitting (Sect. 4.1). In this way, we can minimise the uncertainties coming from the observed line width difference, for example between the emission lines in the vicinity of the host and outskirts of the nebula. Our velocity range (v_{05} and v_{95}) used is basically the value of W_{90} which has the range of ~800−2700 km s^{-1} for all tiles of all targets. Nevertheless, we conduct a check by extracting observed circular radial profiles through integration of 30 Å around the systemic redshift of our targets for comparison. The results vary by ~ ± 10% in each annulus to the profiles in Fig. 5 (from v_{05} and v_{95}), especially for emissions at >50 ckpc where the line width is narrower comparing to the centre. The

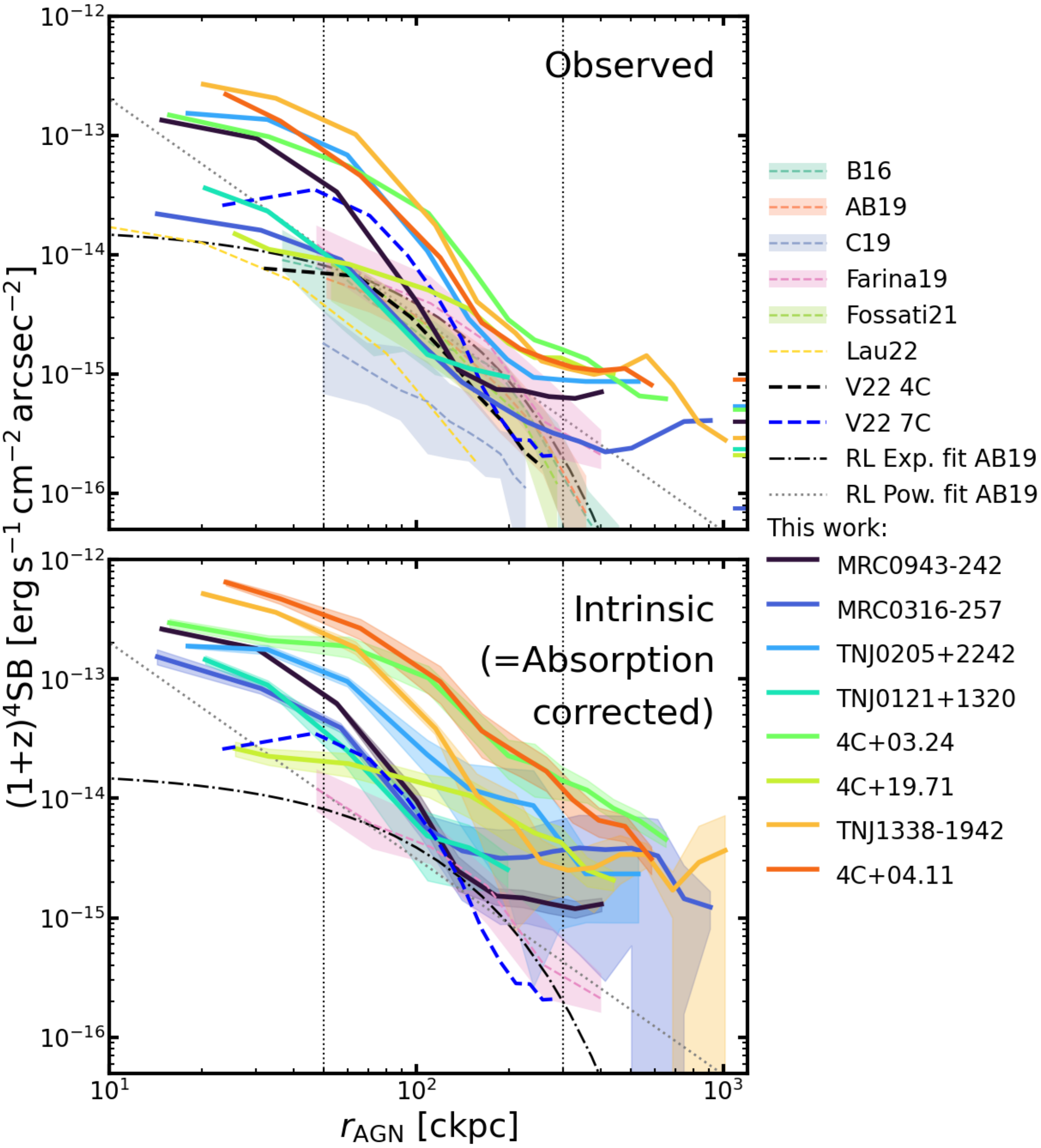

Fig. 5. Radial profiles of the Lyα nebulae extracted in circular annuli (Fig. D.1). For better comparison, we show the radial profile in comoving kpc (ckpc) and take the cosmological dimming into account by a factor of $(1+z)^4$, where z is the redshift of the target. The black dot-dashed curve and grey dotted line in both panels are the best fitted exponential and power law profiles of the Arrigoni Battaia et al. (2019) radio loud sample, respectively. The two vertical dotted lines mark the 50 and 300 ckpc, respectively. Upper panel: Radial profile of observed surface brightness map in thicker solid lines. In this panel, we also include the radial profiles of other quasar samples (dashed lines) for comparison: B16 – Borisova et al. (2016), AB19 – Arrigoni Battaia et al. (2019), C19 – Cai et al. (2019), Farina19 – Farina et al. (2019), Fossati21 – Fossati et al. (2021), L22 – Lau et al. (2022) and V22 – Vayner et al. (2023; two sources, 4C09.17 and 7C 1354+2552). When it is available, we show the range spanned by the 25th and 75th of the comparison sample radial profile as the shaded region around median profile in the same colour. The horizontal bars at the right-most indicate the observed surface brightness limits (scaled by area from Table 2) for each target in the same colour. Lower panel: Intrinsic radial profile in thicker solid lines. The shaded regions around each profiles indicates the uncertainty range of the surface brightness from fitting. In this panel, we show again the same profiles of F19 and V22 7C as in the upper panel for comparison. Our HzRGs are extended further with higher surface brightnesses (or flattening in some sources) at larger radii (~300 ckpc) compared to other samples.

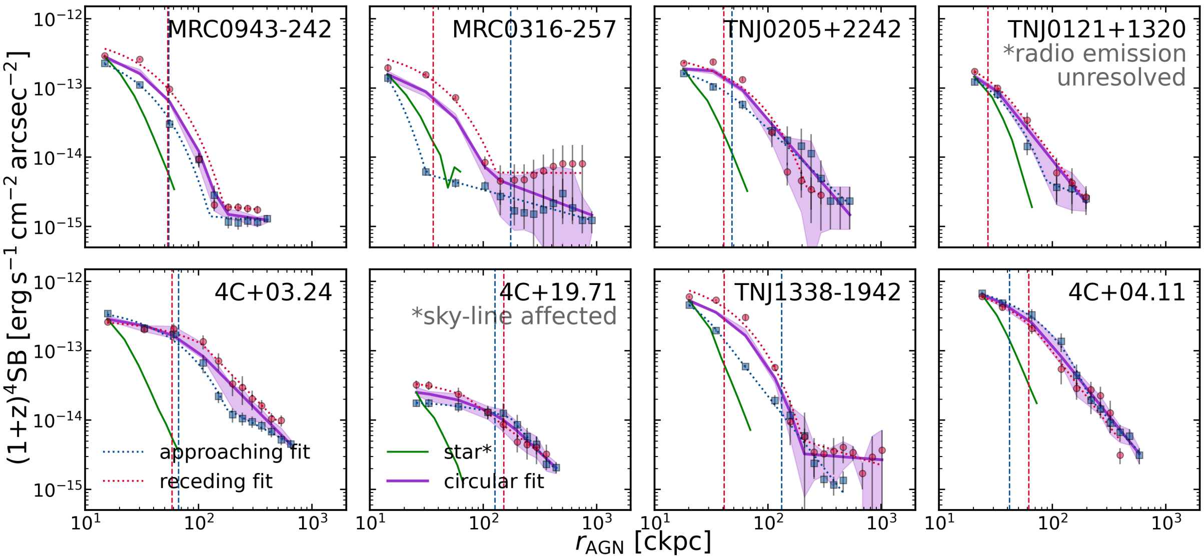

Fig. 6. Surface brightness radial profiles for approaching (blue squares) and receding (red circles) directions along the jet axis. The dotted curves in corresponding colours show the exponential+power law fits for the two directional profiles. We also include the fits for the circularly averaged profile in solid magenta lines. In each panel, the magenta shaded region mark again the same uncertainty range for the intrinsic surface brightness profile as Fig. 5. The solid green curve is the normalised radial profile of a star extracted up to 2″ (the one in the FoV of MRC0316-257 is extracted from a round galaxy due to no available star) showing the PSF (Table 1). The vertical dashed lines indicate the distances of the jet hot spots in corresponding colours. The profile along the receding side of the jet is brighter than along approaching side for most sources within the extent of the jets except 4C+03.24 and 4C+04.11. This may indicate different gas density distribution (see Sect. 4.2.2). We also identify flatting of the profile at $\gtrsim$ 100 ckpc for MRC0943-242, MRC0316-257 and TNJ1338-1942 which may related to nearby companions (see Sect. 5.4).

30 Å extracted profile could be 40% less than the $v_{05} - v_{95}$ extraction in the centre regions (wider line width) for high-redshift targets where the fixed wavelength range in observed frame corresponds to a narrower rest frame range. Hence, to alleviate this problem brought by the difference in line width and redshift range spanned by our sample, we keep the v_{05}-to-v_{95} extraction. As for the intrinsic radial profile, it is redundant to integrate from a narrower range when we can have the direct fit results for the integrated Lyα line. We show the flux ratio between the intrinsic and observed maps in the same velocity range in Appendix C which can be used as a proxy for scaling between the two profiles. Therefore, the different wavelength (velocity) ranges used when extracting radial profiles for our study and comparison quasar samples will not bring additional discrepancy besides the relatively large surface brightness value in our sample.

4.2.2. Directional surface brightness profiles

Since the shapes of our Lyα nebulae are asymmetric (Sect. 4.3), the radial profiles extracted in Sect. 4.2.1 smear out direction-dependent features. For instance, several HzRG Lyα nebulae display features aligned with their radio jets, such as having higher line width and elongated morphology along the jet axis (e.g. van Ojik et al. 1997; Villar-Martín et al. 2003; Miley et al. 2004; Zirm et al. 2005; Humphrey et al. 2007; Morais et al. 2017). Hence, in this section, we study the radial profile of the intrinsic Lyα emission along the direction of the radio jet which could exert a kinematical and/or electromagnetic influence on the surrounding gas. Due to the limited S/N, we split our nebulae into two half parts (approaching and receding, Appendix D) along the jet direction and extract the surface brightness profile in each direction using the same annuli as Sect. 4.2.1. Figure 6 shows these directional profiles. We also show the position of the jet hot spot for the receding (red) and approaching (blue) side with vertical dashed lines[2]. Qualitatively speaking, the surface brightness on the receding side is higher than on the approaching side within the radio jet extent for most of our sources (except 4C+03.24 and 4C+04.11). In three sources, the receding jet hot spot is closer to the AGN: MRC0316-257, TN J0205+2242 and TN J1338-1942. This result was first reported by McCarthy et al. (1991) where the authors found that the line emission is brighter in HzGRs on the side with shorter radio jet. They interpreted this as a large-scale asymmetry in the density of gas on either side of the nucleus: the denser gas absorbs more ionising radiation resulting in brighter emission lines, while the radio jet is more contained as it travels more slowly through the denser medium.

4.2.3. Fitting the surface brightness profiles

To quantify the shape of the profiles, we fit the circularly averaged intrinsic profile and two directional intrinsic profiles with a piecewise function split into an exponential for the inner part and power law for the outer part. This can be mathematically represented by

$$\mathrm{SB}(r) = \begin{cases} C_{\rm e}\exp(-r/r_{\rm h}) & r \leq r_{\rm b} \\ C_{\rm p}r^{\alpha} & r > r_{\rm b} \end{cases}, \quad (2)$$

where $r_{\rm h}$ is the scale length of the exponential profile, $r_{\rm b}$ is the distance at which the inner and outer profiles separate and $C_{\rm e}$ and $C_{\rm p}$ are normalisation parameters for exponential and power law profiles, respectively ($C_{\rm p} = C_{\rm e}\exp(-r_{\rm b}/r_{\rm h})/r_{\rm b}^{\alpha}$). The determination of the piecewise function is motivated by previous studies

[2] We note that the radio emission of TN J0121+1320 is unresolved. The 'jet size' represented by the vertical lines are linear size of the 3σ contour along the east-west elongation of the radio map.

of quasar Lyα nebula (e.g. Arrigoni Battaia et al. 2019; Cai et al. 2019; den Brok et al. 2020) which fit the profile by either power law or exponential. We also test to fit our profiles use only one of the two functions. The single profile, however, cannot fit some targets well. For example, the reduced χ^2 are high (>20) for MRC0943-242, MRC0316-257 and TN J1338-1942 with the single-function fit. We therefore fit all of the profiles with the piecewise function for consistency. Figure 6 shows the fits and Table D.3 presents the fitted parameters.

For most of our targets, the two directional surface brightness profiles are similar to the circularly averaged profile. One exception is the approaching side of MRC0316-257 which has ~1 dex lower than the receding side. This could be an extreme case of uneven Lyα emitting which may trace the different gas distribution. In Fig. 6, we also show the distance of the jet hot spots on both directions (Appendix D). There is no correlation between the distance of the jet hot spot and r_b (nor r_h). As Sect. 4.2.1 described, our HzRGs are high in surface brightness (large C_e); the reasons for this include (i) our sample is composed of HzRGs with bright Lyα emission, (ii) our profiles are absorption corrected, (iii) the quasar surface brightness is extracted from a fixed wavelength range (Sect. 4.2.1). The exponential shape is also seen in other quasar samples, for example Arrigoni Battaia et al. (2019), Farina et al. (2019), den Brok et al. (2020) and Lau et al. (2022). The r_h values derived for our sample are mostly <20 pkpc (Table D.3) which is consistent with the quasars. This suggests a similarity between the central (high surface brightness) part of HzRGs to other quasars (type-1 radio-loud and radio-quiet, type-2 radio-quiet), despite the high surface brightness in our sample. We note that the PSF-subtraction of quasar samples and resolution effects will impact the inner part to the profile. We further discuss the power law declining (flattening) part of our nebula in Sect. 5 combining the information from nebular morphology (Sect. 4.3).

4.2.4. Radial profiles of kinematic tracers

It is of interest to study how the nebula kinematics changes radially which may offer evidence of outflow and/or inflow (e.g. Humphrey et al. 2007; Swinbank et al. 2015; Vernet et al. 2017). We stress that it is beyond the scope of this work to separate different Lyα kinematics emission components (e.g. systemic and outflow) which will be inspected through high resolution spectroscopic data. Hence, we adopt the v_{50} and W_{80} parameters to measure the overall kinematics of the line emitting gas (Sect. 4.1). We caution that the kinematics derived in this way may be biased, for example if there are several gas components with different kinematics but on similar flux levels.

In Fig. 7, we show the directional radial profiles of v_{50} (Fig. 1c) and W_{80} (Fig. 1d), respectively. The profiles are extracted in a similar way as the directional surface brightness in Sect. 4.2.2 by splitting the map into two halves (approaching and receding). The v_{50} (W_{80}) value shown at each radius is averaged in the corresponding annulus. Within the extent of the radio jet hot spots (vertical dashed lines), MRC0943-242, MRC0316-257, TN J0205+2242 and TN J1338+1942 show evidence of jet-driven outflows (e.g. Nesvadba et al. 2008, 2017a) if we ignore the absolute v_{50} value but focus on the relative gradient. That is to say the velocity shift at the approaching side is higher than the receding side. For these four targets, we overplot a solid green line to show the fit of the velocity radial profile within the radio jet extent in Fig. 7. The same velocity gradient is also identified in He II for MRC0943-242 (Kolwa et al. 2019), MRC0316-257 (Appendix E) and TN J1338+1942 (Swinbank et al. 2015). There is no other evidence from the v_{50} of ordered gas bulk motion for the overall sample. This further suggests that Lyα is an unreliable tracer of kinematics at least on 10s to 100s pkpc scale in HzRGs. We note that the tessellation implemented, especially for tiles with larger size (~5 arcsec^2) which are usually located in the low S/N region away from the host galaxy, may smear out potential kinematic features. One possible consequence of combining different kinematic components is broadening of the line width. This may be the case for the receding side of MRC0316-257 and both sides of TNJ0121+1320 and 4C+04.11. In general, the W_{80} does not show an increasing trend towards larger $r_{\rm AGN}$. However, if the line width decreases intrinsically away from the AGN, this will counteract the broadening which makes it difficult to check the impact of smearing. Therefore, we mark the regions with $r_{\rm AGN} > 5''$ on the kinematic radial profile using grey shade to flag the possible high uncertainty in Fig. 7.

If we assume that the bulk of the gas resides in the potential well of the radio galaxy, we expect to see the Lyα emission gas centred around systemic velocity, at least in the vicinity of the AGN. Offsets of the v_{50} levels at $r_{\rm AGN} \sim 0$ ckpc from 0 km s^{-1} (based on systemic redshift, Table 1) are identified for most of our targets which may be due to the aforementioned bias from different kinematic components and scattering of Lyα photons. The most noticeable case is 4C+03.24 which has an offset of ~900 km s^{-1}. We note that its systemic redshift (Table 1) is based on [C I](1–0) emission (Kolwa et al. 2023) due to lack of He II from the AGN position in the MUSE data (Fig. 1a). This offset can be eased if we use the redshift of Hβ, $z_{\rm H\beta} \simeq 3.566$, reported by Nesvadba et al. (2017b) as zero velocity. It is marked in black dashed horizontal line in the v_{50} panel of 4C+03.24 in Fig. 7. This corresponds to -1100 km s^{-1} with respective to the systemic velocity shift used in this paper. We caution that, however, the Hβ was not exclusively extracted at the AGN position (radio core). There is also a known jet-gas interaction in the south of the AGN (see bend of the radio jet contours in Fig. 1b and also van Ojik et al. 1996). From the K-band image (van Breugel et al. 1998), we can find a second continuum emission peak in the south. The position of this emission peak is marked by the red square in Fig. 4. Given these pieces of evidence, we propose that there is a companion galaxy at $z_{\rm H\beta} \simeq 3.566$ in the south of our radio galaxy (z = 3.5828). If there is (or was) an interaction between these two galaxies, the companion may have deprived gas from the AGN resulting in a gas poor AGN host (no detection of He II and less molecular gas detected at the AGN position, Kolwa et al. 2023). The companion then becomes sufficiently massive and gas-rich to deflect the jet. Therefore, the Lyα nebula of 4C+03.24 may trace the CGM of the companion galaxy. Scheduled JWST data (Wang et al. 2021a) will offer a clearer view of this particular situation.

For the W_{80} radial profiles in Fig. 7, we can first identify that most of the HzRGs have high W_{80} even at larger radii (~1500 km s^{-1}). The exception is 4C+19.71 whose measurement is affected by sky-line residuals (Sect. 4.1). The W_{80} reported here is similar to FWHM (especially at large radii, >100 ckpc or $\gtrsim$22 pkpc) where most of our fit are done with a single Gaussian (Sect. 3.2). In 4C+03.24, 4C+19.71 and TN J1338-1942, we can see a clear radial decrease of W_{80} along both directions. This may be related to results found in Villar-Martín et al. (2003) who observed a Lyα FWHM drop off at distance beyond the extent of the radio jets in a sample of HzRGs (including MRC0943-242) using deep Keck long slit spectroscopy. In our study, however, we firstly do not find such a decrease in all targets. The grey shaded regions ($r_{\rm AGN} > 5''$) should be treated with caution. We note that the FWHM in Villar-Martín et al. (2003) was

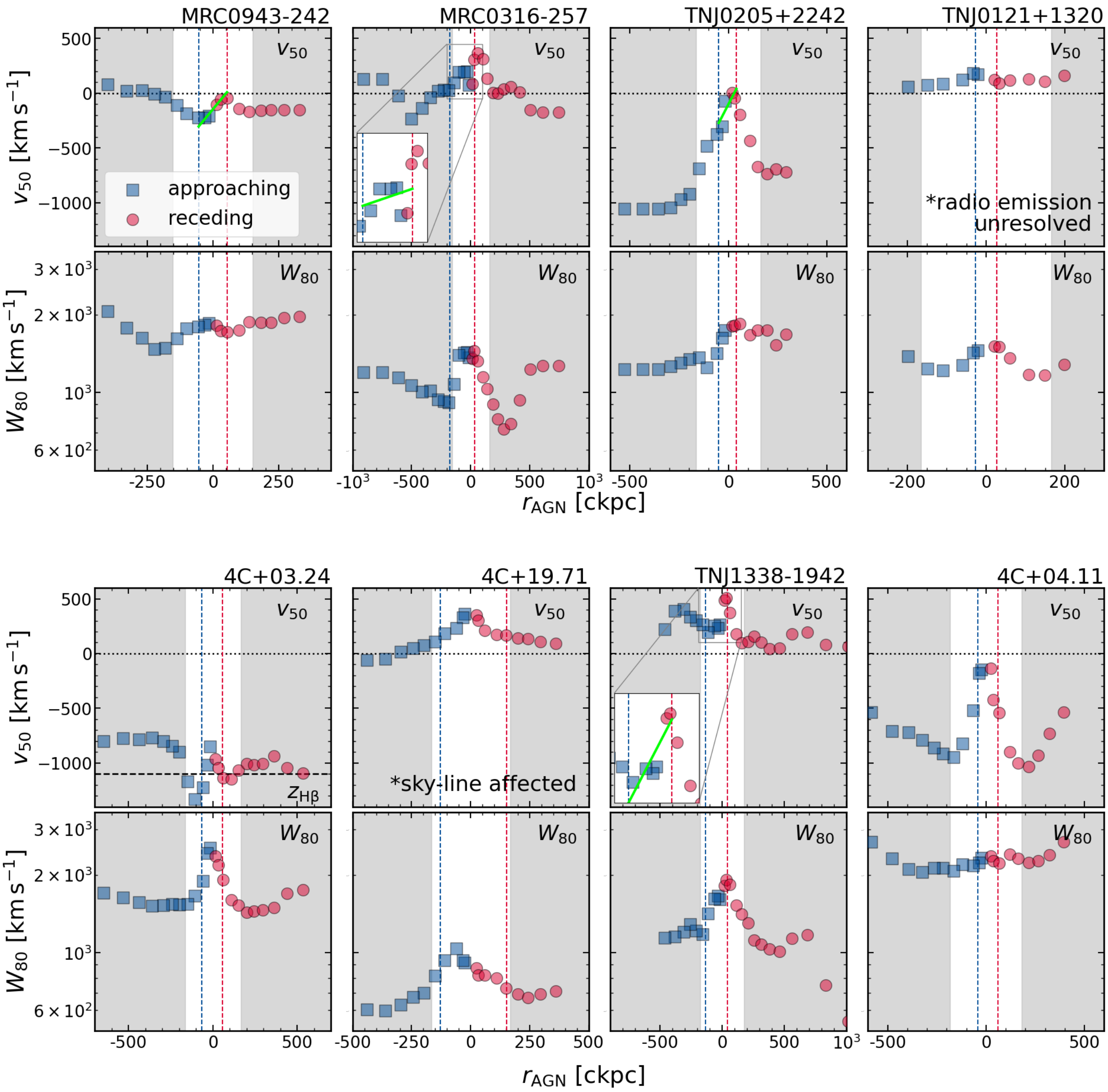

Fig. 7. Directional v_{50} and W_{80} profiles for approaching (blue squares) and receding (red circles) sides along the jet axis extracted from the intrinsic maps (i.e. corrected for absorption, Fig. 1cd). The vertical dashed lines indicate the distances of the jet hot spots (blue for approaching, red for receding, Appendix D). We note that the radio emission of TN J0121+1320 is unresolved. The grey shaded regions are >5 arcsec from the host galaxy. The data points in the shaded regions should be treated with caution given the large tile size may smear kinematic structures. The horizontal black dotted line in the v_{50} panel marks the 0 km s^{-1} derived from systemic redshift. The dashed horizontal black line in the v_{50} panel of 4C+03.24 indicates the velocity shift of Hβ redshift ($z_{\rm H\beta} \simeq 3.566$, -1100 km s^{-1} with respect to the systemic redshift; Nesvadba et al. 2017b) with respect to its systemic used in this paper (Table 1, see text). We note that the range of the x-axis is customised for each target and that the W_{80} is shown in logarithmic scale. We show a zoom-in view of the central part of the v_{50} profiles of MRC 0316-257 and TN J1338-1942 in the insets. For MRC 0943-242, MRC 0316-257, TN J0205+2242 and TN J1338-1942, we mark the fit to the v_{50} profiles within the jet hot spots (vertical lines) in green lines to guide the eye of the evidence of nebula velocity gradient following jet kinematics. In general, there is no clear evidence of a trend in bulk motion identified for the whole sample. For some targets (4C+03.24, 4C+19.71 and TN J1338-1942), W_{80} decreases with increasing radial distance which may indicate that the jet is disturbing the gas.

derived without correction for absorption. Since we see a high spatial coverage of absorbers (Figs. 2–4), the correction indeed helps with recovering the close-to-intrinsic gas kinematics at large radii. In Fig. D.2, we show the position-velocity diagram extracted based on our observed and intrinsic surface brightness maps along the jet as a direct comparison with the long slit spectroscopic study. Although it resembles the detection of Villar-Martín et al. (2003) at first glance, we note that this is due to the tessellation and the contrast between high surface brightness and low surface brightness part.

By considering both the radial profiles from v_{50} and W_{80}, we can generally find that the profiles within the jet extents have behave differently compared to the profiles outside the jet extent. This again suggests the jet is disturbing or entraining the Lyα emitting gas. There are unclear signs of kinematics other than outflows or inflows seen mostly at larger radial distance ~300 ckpc. For example, MRC0943-242 stays relatively flat (for both v_{50} and W_{80}), while MRC0316-257 has a decrease in W_{80} followed by an increase beyond the jet extent on the receding side. We reiterate that in this analysis we do not distinguish between (potential) different kinematics components by using v_{50} and W_{80} to quantify the overall velocity shift and line width. This may bring bias of the measured values. Additionally, the measured kinematics farther from the AGN are averaged from larger annulus (e.g. projected area of $\sim 4 \times 10^4$ pkpc^2 at ~60 pkpc or ~300 ckpc) which will bring another bias. We point out again that we use grey shade to mark the data >5″ from the centre which has larger tile size. Nevertheless, we note that the detected W_{80} of $\sim 10^3$ km s^{-1} (and abrupt velocity shift) at large radii (~300 ckpc) in some of the profiles could be caused by the fact that the detected Lyα emission is dominated by emission halos of nearby companions (e.g. Byrohl et al. 2021).

4.3. Morphology of the nebulae

The nebula morphology is related to the ionising sources, gas dynamics and galaxy environment (Byrohl et al. 2021; Costa et al. 2022; Nelson et al. 2016). Especially when the Lyα nebulae (in our sample) can probe the CGM gas beyond 100 pkpc. By visual inspection, we observe that the shape of our Lyα nebulae are asymmetric (e.g. Fig. 1). In this section, we study quantitatively the nebula morphology. We first focus on the whole nebula by introducing the morphology quantification measurements (ellipticity, nebula orientation and offset between nebula centroid and AGN position) in Sect. 4.3.1 and compare with other samples in Sect. 4.3.2. Then, in Sect. 4.3.3, we study how the nebula asymmetry changes with radial distance for individual targets. We also report the detected morphology correlations between different measurements (i.e. offset between AGN and nebula centroid position, nebula ellipticity and nebula linear size) in Sect. 4.3.4. These shed light on how the central quasar and nearby companions can affect the observed nebula morphology. Finally, in Sect. 4.3.5, we show the non-random oration of jet axis and its relation with the elongated direction of nebula which hints at the CGM gas distribution.

4.3.1. Morphology quantification measurements

To quantify the asymmetry, we introduce a set of morphology measurements. Arrigoni Battaia et al. (2019) used flux-weighted asymmetry measurements for the Lyα nebulae which is sensitive to the high surface brightness part. In other works (e.g. den Brok et al. 2020), an unweighted asymmetry measurement was adopted for better studying the extended structure of the nebulae (sensitive to the morphology of the whole nebula). To better characterise the morphology of our HzRGs and perform comparison with other samples, we analyse the asymmetry with both the flux-weighted and flux-unweighted methods.

First, we follow Arrigoni Battaia et al. (2019) and calculate the flux-weighted asymmetry, $\alpha_{\rm weight}$ (see Arrigoni Battaia et al. 2019, for the definition). This quantifies the asymmetry of the nebula in two perpendicular directions. Together with the asymmetry measurement, we also obtain the flux-weighted position angle $\theta_{\rm weight}$, which we use as an indicator for the elongation direction of the nebula after converting it to the same reference system as the radio jet axis (i.e. angle measured east from north). The flux-weighted nebula centroid (centre of the nebula) is also computed. We note that the intrinsic flux and its uncertainty are used as weight to measure these three parameters and to calculate the corresponding uncertainties, respectively. We also derive the asymmetry measurement weighted by observed flux for comparison. Second, to compare with flux-unweighted asymmetry reported for other quasar samples (e.g. Borisova et al. 2016; den Brok et al. 2020), we calculate the $\alpha_{\rm unweight}$ following den Brok et al. (2020). In this context, we also derive $\theta_{\rm unweight}$ (flux-unweighted position angle) to examine the jet-nebula relation with respect to the entire nebula. Figure 8 visualises the weighted (nebula centroids and $\theta_{\rm weight}$) and unweighted ($\theta_{\rm unweight}$) parameters on the eight nebulae.

In Lau et al. (2022), the authors compared morphology of different quasar samples. Following their comparison, we convert the aforementioned asymmetry measurement (for both flux-weighted and unweighted), α, to an intuitive elliptical asymmetry measurement (or ellipticity) $e = \sqrt{1-\alpha^2}$. For $e_{\rm weight} \to 0$, the nebula is closer to round shape and vice versa. Table 3 reports the morphological parameters of our sample. Since the absolute flux-weighted centroid position and $\theta_{\rm weight}$ (and $\theta_{\rm unweight}$) are irrelevant, we report the projected distance between the nebula centroid and the AGN position ($d_{\rm AGN-neb}$) and the difference in angles between $\theta_{\rm weight}$ (and $\theta_{\rm unweight}$) and the jet position angle ($|\theta_{\rm weight} - {\rm PA}_{\rm radio}|$ and $|\theta_{\rm unweight} - {\rm PA}_{\rm radio}|$), respectively. The jet position angle (PA$_{\rm radio}$) is shown in Fig. 8 and listed in Appendix D.

4.3.2. Comparison of nebula asymmetry with other quasar samples

Figure 9 presents the ellipticity measurements as a function of their nebula Lyα luminosity for our targets and other quasars (Borisova et al. 2016; Arrigoni Battaia et al. 2019; Cai et al. 2019; Mackenzie et al. 2021; den Brok et al. 2020; Sanderson et al. 2021; Lau et al. 2022). We note that the $L_{\rm Ly\alpha}$ for comparison samples are not corrected for absorption. Part of the comparison samples are also used in Sect. 4.2.1 for surface brightness radial profile analysis. We point out the newly included ones here: faint $z \sim 3.0$ type-1 from Mackenzie et al. (2021) and type-2 AGN at $z \sim 3.4$ from den Brok et al. (2020) and $z \sim 3.2$ from Sanderson et al. (2021). The reason why they are not included in radial profile analysis is that they do not add new information.

The HzRGs from our sample are measured to be asymmetric for their high surface brightness emission region (median $e_{\rm weight} \approx 0.78$). Compared to the Arrigoni Battaia et al. (2019) and Cai et al. (2019) samples, our HzRGs are consistent in asymmetry measurements and on the higher end of their distribution (type-1 median $e_{\rm weight} \approx 0.72$, dashed horizontal in Fig. 9a). The $e_{\rm weight}$ of radio-loud type-1s from (Arrigoni Battaia et al. 2019) have a median of 0.69 which is even lower than the value of all type-1 targets (Arrigoni Battaia et al. 2019; Cai et al. 2019). This indicates that the radio emission in type-1 does not disturb the gaseous nebula as in our HzRGs at least along the plane of the sky. This further suggests that orientation is a critical factor (Sect. 5.3). By comparing the intrinsic flux-weighted and observed flux-weighted elliptical asymmetry measurements, we find the $e_{\rm weight}$ can vary significantly (e.g. MRC 0316-257 and 4C+04.11). For MRC0316-257, we can already identify its asymmetric morphology through visual checking (Fig. 1). There is also a large error bar associated with the intrinsic flux-weighted ellipticity. Hence, the morphology of MRC0316-

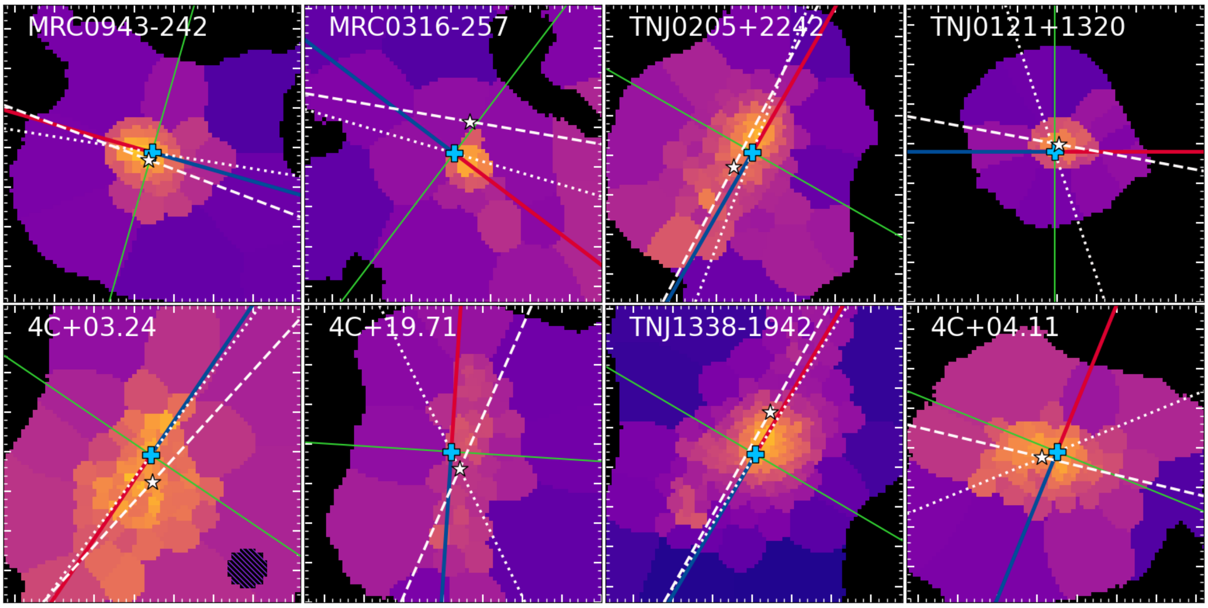

Fig. 8. Zoom-in intrinsic surface brightness maps (Fig. 1b) of the HzRGs sample to 15×15 arcsec^2 (or $\sim 110 \times 110$ pkpc^2) around the central AGN (blue cross). In each panel, the blue+red and green solid lines indicate the direction of, and perpendicular to, the radio jet. The blue (red) colour represents the direction of the approaching (receding) jet. The white dashed line shows the flux-weighted position angle of the nebula ($\theta_{\rm weight}$). The white dotted line shows the unweighted position angle of the nebula ($\theta_{\rm unweight}$). The white star indicates the intrinsic flux-weighted centroid of the Lyα nebula. The flux weighted measurement is sensitive to the morphology of the high surface brightness part of the nebula. The unweighted measurement quantifies the morphology of the whole nebula. We find that nebula is elongated along the jet axis for most of HzRGs.

257 is more towards the asymmetric end. The large difference between its intrinsic and observed $e_{\rm weight}$ could be due to the absorption correction elevates the flux difference between the high and low S/N regions thus gives more weight to the central nebula. As for 4C+04.11, this could be due to the potential over-correction of the absorption in the low S/N regions given we use nine absorbers across the nebula (Sect. 3.2, 5.1). However, we point again that the absorption is necessary to reconstruct the intrinsic flux given that the absorption features across the nebula were observed (e.g. Swinbank et al. 2015; Wang et al. 2021b).

Our HzRGs have a median $e_{\rm unweight} \approx 0.70$ which is lower than the measurement of type-2s and relatively consistent with the type-1s (median $e_{\rm unweight} \approx 0.80$ and $\approx$0.69, respectively, Borisova et al. 2016; den Brok et al. 2020; Sanderson et al. 2021; Mackenzie et al. 2021). The ellipicity of the comparison type-2s is calculated from five sources which may not be representative. We note that there is a large scatter in the $e_{\rm unweight}$ measured for our sample with four clustered around the type-2s and other four below the median $e_{\rm unweight}$ of type-1s. This result could be biased by the implemented analysis methods (i.e. detection map and tessellation, Sect. 3.1): (i) the construction of the detection map may smooth out the nebula asymmetry at larger radii (lower S/N); (ii) the tessellation results in lager bin sizes along the direction perpendicular to the radio jet (lower surface brightness and S/N, Sect. 5.5) which shapes the nebula morphology to be more round. This brings more effects of the quantification of the entire nebula. Hence, the HzRGs nebulae will likely have larger $e_{\rm unweight}$ (i.e. more asymmetric) than the quantified value. In spite of that, we can conclude that at least half of our sample, together with the type-2s, distribute at the most asymmetric end in terms of the whole nebula. The rest has the possibility to be skewed to higher $e_{\rm unweight}$. Our HzRGs have diverse properties and are not necessarily representative for the entire HzRGs population. Inspection for individual targets is required.

As for the $L_{\rm Ly\alpha}$, our HzRGs host the most luminous Lyα nebula compared with other quasar types. This is due to the following: (i) sample selection[3]; (ii) absorption correction; and (iii) quasar PSF subtraction of comparison samples (Sect 4.2.3).

We further compare our HzRGs to the ERQ from Lau et al. (2022). In Fig. 9, both the $e_{\rm weight}$ (0.44) and $e_{\rm unweight}$ (0.69) of L22 are lower than the measurements from HzRGs. Its $L_{\rm Ly\alpha}$ is also lower than our HzRGs by $\sim$2 orders of magnitude. This confirms that the nebula of this EQR is type-1 like but highly obscured (e.g. Lau et al. 2022). Since it is the only source of this type, we do not further discuss it.

4.3.3. Asymmetry radial profile

To further quantify the morphology of individual nebula as a function of distance from the AGN, we follow den Brok et al. (2020) and decompose our HzRGs intrinsic surface brightness using Fourier coefficients, $a_k(r)$ and $b_k(r)$:

$$\mathrm{SB}_{\rm Ly\alpha}(r,\theta) = \sum_{k=0}^{\infty} [a_k(r)\cdot\cos(k\theta) + b_k(r)\cdot\sin(k\theta)]\,, \tag{3}$$

where $\mathrm{SB}_{\rm Ly\alpha}(r,\theta)$ is the surface brightness at given polar coordinate (r,θ). The coefficients $a_k(r)$ and $b_k(r)$ are defined as:

$$a_k(r) = \frac{1}{2\pi}\int_0^{2\pi} \mathrm{SB}_{\rm Ly\alpha}(r,\theta)\cdot\cos(k\theta)\mathrm{d}\theta$$

$$b_k(r) = \frac{1}{2\pi}\int_0^{2\pi} \mathrm{SB}_{\rm Ly\alpha}(r,\theta)\cdot\sin(k\theta)\mathrm{d}\theta. \tag{4}$$

[3] We can see that even the absorption uncorrected observed $L_{\rm Ly\alpha}$, smaller symbols in Fig. 9, is on the higher end (Sect. 2.1.1).

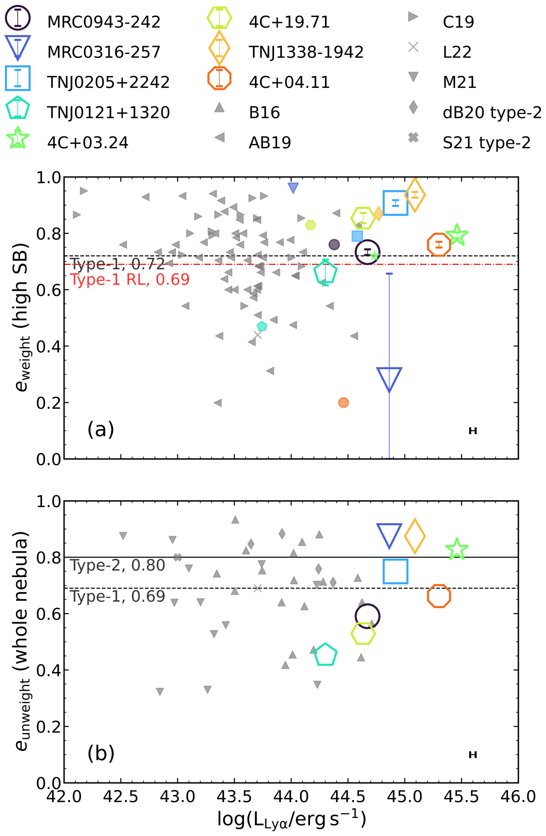

Fig. 9. Relation between Lyα nebula luminosity and asymmetry measurement. (a) Flux-weighted Lyα nebula elliptical asymmetry measurement versus nebula luminosity, $L_{\rm Ly\alpha}$. We show the intrinsic flux-weighted ellipticity ($e_{\rm weight}$) in larger open symbols for our targets versus their intrinsic Lyα luminosity. We also show the observed flux-weighted ellipticity $e_{\rm weight,obs}$ for our targets versus their observed Lyα luminosity in smaller filler symbols. The small grey symbols are data of comparison targets (AB19 – Arrigoni Battaia et al. 2019, C19 – Cai et al. 2019 and L22 – Lau et al. 2022). We mark the median flux-weighted (not corrected for absorption) ellipticity, 0.72, of type-1s with the horizontal dashed line. We also show the median $e_{\rm weight}$, 0.69, of radio-loud type-1 quasars from Arrigoni Battaia et al. (2019) in red horizontal dash-dotted line. (b) Flux-unweighted Lyα nebula elliptical asymmetry measurement versus $L_{\rm Ly\alpha}$. The larger symbol are measurements for our HzRGs while the grey symbols are comparison targets (type-1s: B16 – Borisova et al. 2016, L22 – Lau et al. 2022 and M21 – Mackenzie et al. 2021; type-2s: dB20 – den Brok et al. 2020 and S21 – Sanderson et al. 2021). We mark the median $e_{\rm unweight}$ for type-1s (0.69) and type-2s (0.80) in solid and dashed horizontal lines, separately. The $e_{\rm weight}$ is sensitive to the morphology of the high surface brightness part of the nebula while the $e_{\rm unweight}$ quantifies the morphology of the whole nebula. We note that for $e \to 0$, the nebula is closer to round shape and vice versa. At the bottom right, we show the median uncertainty of the intrinsic $L_{\rm Ly\alpha}$ for our sample in logarithmic scale, 0.04. The ellipticity for our sample are higher compared to the other quasars for both high surface brightness part and whole nebula. There is no clear evidence that the nebula ellipticity correlates with luminosity.

The detailed description can be found in den Brok et al. (2020). Then we combine $a_k(r)$ and $b_k(r)$:

$$c_k(r) = \sqrt{a_k(r)^2 + b_k(r)^2}. \quad (5)$$

We measure the radial dependence of the asymmetry (i.e. how much it deviate from a circular shape) of the nebulae by using the ratio between kth and 0th modes, $c_k(r)/c_0(r)$. In practise, only the first three modes are used since the higher mode coefficients are much smaller (den Brok et al. 2020). Figure 10 shows the radial profiles of this asymmetry measurement (represented by $(c_1/c_0)^2 + (c_2/c_0)^2$ on the y-axis) for our HzRGs. The larger the value, the more asymmetric the morphology shift from circular shape at a given radial distance. We also include type-2 measurements from den Brok et al. (2020; 4 quasars) and Sanderson et al. (2021) as comparison. The type-1 sample from Borisova et al. (2016; which is quantified in den Brok et al. 2020) is also shown. Our HzRGs generally show an increase of the asymmetry as a function of radial distance (some have a smaller secondary peak at $\lesssim$ 50 ckpc) and a steep rise to >1.5 (7 out of 8) at ~250 ckpc. The most noticeable exception is MRC0316-257 which has a secondary peak (~0.8) at ~50 ckpc (~14 pkpc). This flux-weighted measurement confirms the large difference we observed in the high surface brightness part of the directional profiles of MRC0316-257 in Fig. 6. As we already stated in Sect. 4.2, the detected extent of our HzRGs ($\gtrsim$400 ckpc) are larger than the comparison quasars (~300 ckpc). If we limit the comparison to the largest extent (~250 ckpc) reached by the type-1s from (Borisova et al. 2016), we find that our HzRGs are similar in radial asymmetry measurements. Specifically, both have a relatively flat profile to ~200 ckpc which followed by a shallow rise to the value of ~0.5. However, in Sect. 4.3.2 (Fig. 9) we find that the HzRGs ellipticity is larger than type-1s. Together with the radial asymmetry profile in this section, we can conclude that the asymmetry of the nebulae associated with HzRGs and type-1s are different due to structures at larger radial distance (>250 ckpc) from AGN. This is also suggested by den Brok et al. (2020). Although we caution the large W_{80} at large distance in Sect. 4.2.4 and mark the region with r > 5 arcsec in grey in Fig. 7, we can still find that most targets have at least $W_{80} \sim 10^3$ km s^{-1}. This may indicate that these structures are likely disturbed and not 'quiescent' gas in the Cosmic Web (Sect. 5). From the comparison with type-2s (den Brok et al. 2020; Sanderson et al. 2021, which also have a steep rise), we find that the radial asymmetry of our HzRGs rises at larger radial distance ($\gtrsim$250 ckpc) and reaches higher asymmetry value (>1.5 compared with ~1.4 of type-2s). At least one of the radial asymmetry measurement (Cdfs 15, with the furthest extent $r_{\rm AGN} \sim$ 300 ckpc) from den Brok et al. (2020) shows an indication of continuous rising up to the detection limit (1 hour integration with MUSE); we cannot rule out the possibility that this target may show a similar trend as the HzRGs with deeper observations.

4.3.4. Morphological correlations

In Fig. 11, we compare the $e_{\rm weight}$ (ellipticity that is sensitive to high surface brightness nebula) and $d_{\rm max}$ (maximum nebula extent) against $d_{\rm AGN-neb}$ (offset between AGN and nebula flux-weighted centroid). For a consistent comparison for the unweighted measurements, we should use the unweighted offset (centroid) and the unweighted ellipticity. We note that the calculation of unweighted ellipticities, $e_{\rm unweight}$, assumes that the centre of nebula corresponds to the AGN position (den Brok et al. 2020). It would involve large uncertainties if we calculated the flux-unweighted nebula centroids (i.e. the geometric centre of the nebula) which are entirely depended on the spaxel distribution from our detection maps (Sect. 3.1.1). Hence, we report only the correlation between flux-weighted ellipticity and offset, and

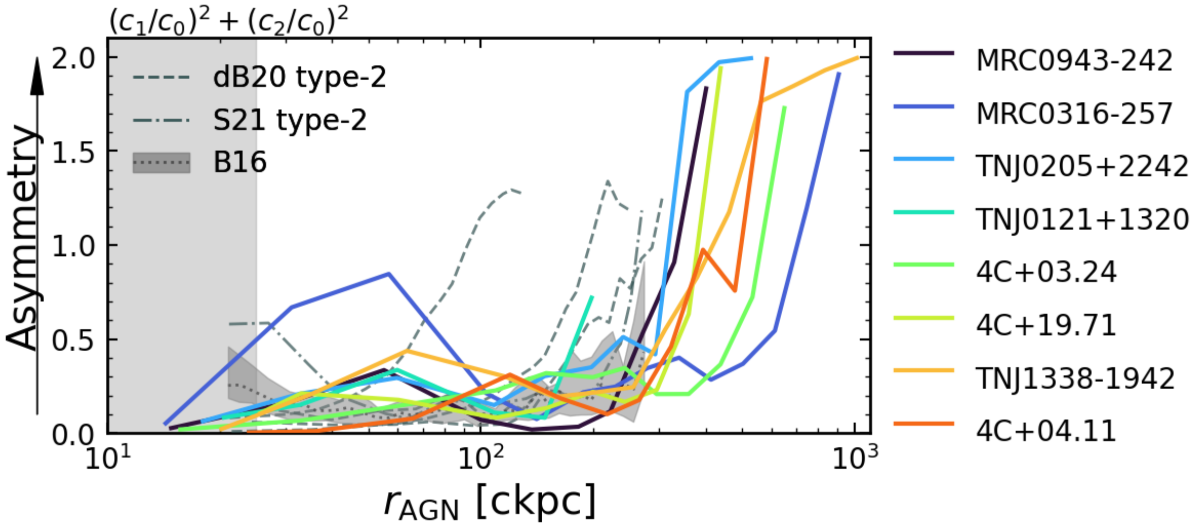

Fig. 10. Radial profiles of the surface brightness Fourier decomposition (asymmetry measurement). The c_0, c_1 and c_2 are the 0th, 1st and 2nd modes Fourier decomposition coefficients of the surface brightness radial profile, respectively (see den Brok et al. 2020, for definition). The $(c_1/c_0)^2 + (c_2/c_0)^2$ is a measurement of nebula asymmetry along the radial distance from the AGN. Our HzRGs are shown in solid colour lines. $r_{\rm AGN}$ is the radial distance measured from the central AGN. For comparison, we include the same measurements for the 4 nebulae of type-2 quasars from den Brok et al. (2020; grey dashed lines) and the type-2 from Sanderson et al. (2021; grey dot-dashed line). We also include the type-1 measurements from Borisova et al. (2016; dotted line represents the median and shaded region marks the 25th and 75th percentile, quantified by den Brok et al. 2020). The vertical shaded region is the 0.75 arcsec (∼25 ckpc) range affected by median seeing of our sample (the radial distance where the type-1 PSF is affected is ∼50 ckpc, see den Brok et al. 2020). The morphologies for most of the HzRGs nebulae are round (symmetric) ≲100 ckpc and become asymmetric at larger radial distances ∼100 ckpc (see text).

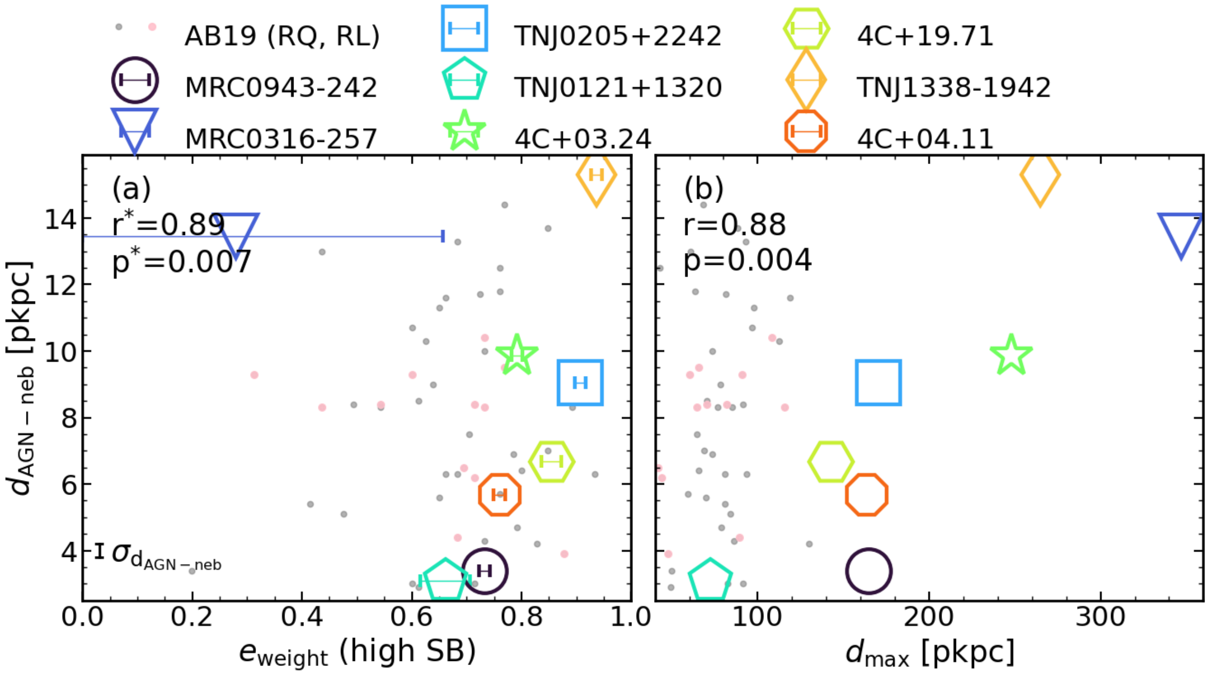

Fig. 11. (a) Intrinsic flux-weighted ellipticity (sensitive to the morphology of the high surface brightness part of the nebula), $e_{\rm weight}$, versus distance offset between nebular centroid and AGN position, $d_{\rm AGN-neb}$. The typical uncertainty of $d_{\rm AGN-neb}$ ($\sigma_{d_{\rm AGN-neb}}$ = 0.4 pkpc, Table 3) is shown at bottom left. (b) Maximum Lyα nebula linear extent, $d_{\rm max}$, versus $d_{\rm AGN-neb}$. In both panels, we give the Spearman correlation measurements for our sample at the top left (the star superscript indicates the correlation is calculated excluding MRC 0316-257 in panel a). We also include the data from Arrigoni Battaia et al. (2019) in both panels in grey (radio quiet) and pink (radio loud) dots. We note that the Arrigoni Battaia et al. (2019) sample shown in this figure is incomplete to concentrate on the relation for our targets. There are positive correlations detected for $e_{\rm weight}$–$d_{\rm AGN-neb}$ and $d_{\rm max}$–$d_{\rm AGN-neb}$.

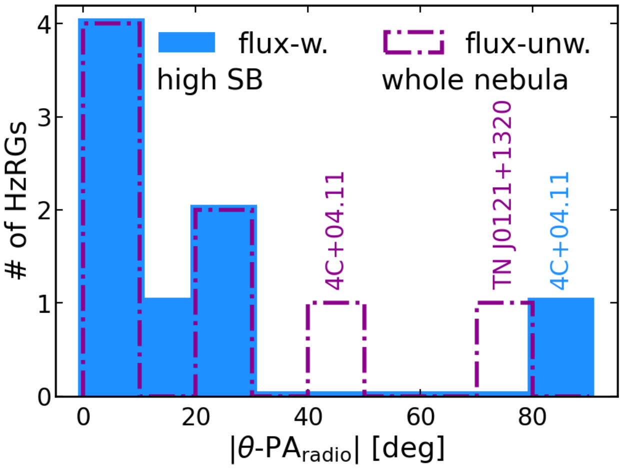

Fig. 12. Distribution of the angle difference between nebular position angle and radio jet position angle, $|\theta - \mathrm{PA_{radio}}|$. The blue histogram shows the number distribution of flux-weighted angle difference, $|\theta_{\rm weight} - \mathrm{PA_{radio}}|$ (sensitive to high surface brightness nebula morphology). The magenta histogram represents the unweighted measurements, $|\theta_{\rm unweight} - \mathrm{PA_{radio}}|$ (quantifying the morphology of the whole nebula). The values are presented in Table 3. We mark the obvious outliers in the two distributions in corresponding colours. This shows that most of our HzRGs have their Lyα nebula elongated along the jet axis.

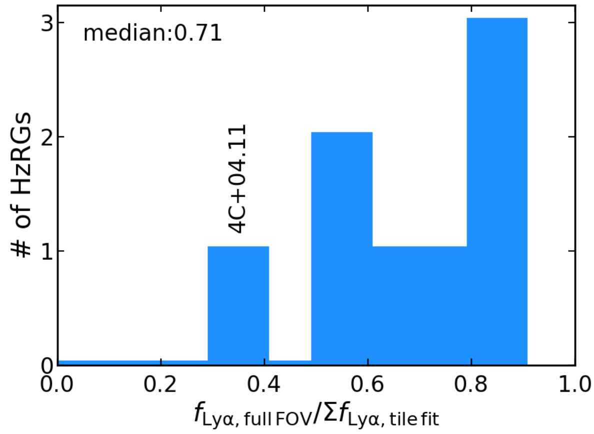

Fig. 13. Distribution of $f_{\rm Ly\alpha,full\,FOV}/\Sigma f_{\rm Ly\alpha,tile\,fit}$ for our HzRGs. The $f_{\rm Ly\alpha,full\,FOV}$ is the intrinsic Lyα flux resulted from fitting the spectrum summed over the entire FOV. The $\Sigma f_{\rm Ly\alpha,tile\,fit}$ is the summation of the intrinsic Lyα flux in each tessellation bin (Fig. 1b). The smaller the value, the more likely the Lyα photon is being double-counted when correcting for absorption. 4C+04.11 is the one with the smallest ratio which may also indicate over-correction (Appendix B).

use it as a proxy of the nebula even though they are more sensitive to the high surface brightness part.

The (r-value, p-value) of Spearman's correlation coefficients are (0.89, 0.007) and (0.88, 0.004) for the $e_{\rm weight}$ versus $d_{\rm AGN-neb}$ and $d_{\rm max}$ versus $d_{\rm AGN-neb}$ relations. We note that due to the large uncertainties of $e_{\rm weight}$ for MRC0316-257, we exclude it from the correlation measurement. From the r-values and p-values, we can conclude that $e_{\rm weight}$ and $d_{\rm max}$ are both correlated with $d_{\rm AGN-neb}$. This suggests that the more asymmetric and more extended nebulae have larger offsets between AGN position and nebular centroid. We also include the Arrigoni Battaia et al. (2019) sample for comparison. The (r-values, p-values) of the $e_{\rm weight} - d_{\rm AGN-neb}$ relation for the Arrigoni Battaia et al. (2019) whole sample and radio-loud targets are (0.3, 0.02) and (0.3, 0.4), respectively, implying no strong correlations. The (r-values, p-values) of the $d_{\rm max} - d_{\rm AGN-neb}$ relation for the Arrigoni Battaia et al. (2019) sample and the radio-loud targets are (0.4, 0.003) and (0.4, 0.1), respectively, suggesting a moderate correlation in their whole sample but not in their radio-loud target. This indicates that the radio-loud type-1s are different from our radio-loud type-2s HzRGs. We revisit these correlations in Sect. 5.

4.3.5. Jet-nebula position angle distribution

We present the distribution of the $|\theta - \mathrm{PA_{radio}}|$ (Sect. 4.3.1, Table 3) in Fig. 12. Both the flux-weighted and unweighted measurements are shown which are sensitive to high-surface brightness parts and the entire nebulae, respectively. Figure 12 shows that most HzRGs have $|\theta - \mathrm{PA_{radio}}| < 30°$. A similar result was reported by Heckman et al. (1991b). This observation is consistent with the scenario proposed by Heckman et al. (1991b,a) that the compression of the gas by the radio jet results in brighter emission along the jet. We discuss the indications behind the alignments further in Sect. 5.5. The exception is 4C+04.11 which has both large $|\theta_{\rm weight} - \mathrm{PA_{radio}}|$ (81.4°) and $|\theta_{\rm unweight} - \mathrm{PA_{radio}}|$ (45.3°), indicating different conditions that in the other targets (such as inflows, Sect. 5.6). In TN J0121+1320 we find a flux-unweighted angle difference of 72.1°. Given its round Lyα nebula morphology and compact radio emission, there is a large uncertainty in angle difference measurement and we do not discuss this source separately. If we assume the observed angle difference is equally distributed from 0−90°, the probability for us to find 7 (or 6) targets in a sample of 8 with $|\theta - \mathrm{PA_{radio}}| < 30°$ is only 0.2% (1.7%) using bimodal distribution.

5. Discussion

5.1. Absorption correction and radiative transfer

We stress that the analysis of our sampled Lyα nebulae in this paper is under the idealised assumptions stated in Sect. 3.2.1. Specifically, we interpret the trough features in the Lyα spectra as absorption features by the neutral hydrogen gas surrounding the radio galaxy. In this section, we discuss the limitations and possible caveats of this treatment for reconstructing the intrinsic Lyα flux along with the possible effects brought by radiative transfer.

Under our assumptions, the absorbing gas is located in between the observer and the last scattering surface of Lyα photons along the line of sight. The intrinsic Lyα flux reconstructed under our treatment is thus assumed to be the one after radiative transfer processes have shaped the Lyα nebula, and is approximated by a Gaussian profile. We also assume the absorbed Lyα photons in the absorbers to be 'lost' rather than continuing their resonant scattering path within the nebula; this may happen when photons are absorbed by dust and re-emitted as infrared thermal emission, or preferentially scattered away from the line of sight due to a particular geometry (see Sect. 3.2.1). The latter may occur because photons originating from the backside of the galaxy have a higher chance to be absorbed by dust when transiting the host galaxy (Liu et al. 2013). These absorbers can be interpreted as intervening low column density gaseous shells (e.g. van Ojik et al. 1997; Swinbank et al. 2015;

Kolwa et al. 2019). The fact that most of the absorbers are located in the blue wing of the Lyα profile as well as the fact the trough of the main absorber is often seen across several tens of kpc scales supports this idea (see Fig. 1a, and TNJ0205+2242 in Fig. 2, see also TNJ1338-1942 in Fig. C.4 and e.g. Wang et al. 2021b).

The situation may be different when we encounter embedded absorbers which are supposed to be closer to the source of Lyα photons (i.e. central AGN in our case). This leaves the trough (or 'main absorber') at around the systemic redshift of the AGN as predicted by radiative transfer studies (e.g. Verhamme et al. 2006). Even though the scales probed in those simulations are different (CGM scale versus sub-kpc), this might be the case in some of our targets, for example MRC0943-242 and TNJ0121+1320 (Figs. 3 and C.1). Therefore, one consequence of our absorption treatment (with 'lost' photons) is that we may double-count Lyα photons that are resonantly scattered to the wing and/or other directions by redundantly adding more when correcting for absorption. We implemented a simple test for checking the double-counting effect, which takes advantage of the IFU nature where slit or spaxel loss effects are compensated by photons resonantly scattered in the neighbouring spaxels. Specifically, we summed all individual spectra into one and reconstruct the intrinsic flux for this single spectrum ($f_{\mathrm{Ly\alpha,full\,FOV}}$); this value removes the IFU information, but should be a good measure of the total value emanating from the nebula in the observer's direction. This is then compared to the sum of individually constructed intrinsic flux in each tile (Fig. 1b, $\Sigma f_{\mathrm{Ly\alpha,tile\,fit}}$). Figure 13 shows the result, where a value of 1.0 is expected if our treatment is fully accurate. Instead, we observe a median value of 0.71 for our sample, indicating that there may be double-counting of photons. However, several effects may also contribute to this. First, our assumption of a Gaussian shape for the intrinsic profile may not be accurate, as prior radiative transfer effects may have created troughs and boosted the line wings (Verhamme et al. 2006). A future paper presenting high spectral resolution UVES observations of our sample will help to better model the profiles (Ritter et al., in prep.). Second, the assumption that all absorbers extend across the entire nebula may also be oversimplified. While many absorbers are indeed seen on 10s (or 100s) of kpc scales for our targets (Figs. 2–4 and also Appendix C), there may be exceptions.

The Lyα nebula properties of the type-1 (and radio-quiet type-2) sources in the comparison samples are derived without correcting for absorption. They are still good comparison samples given that not many absorption features are detected in them (e.g. Arrigoni Battaia et al. 2019). This fact alone is already an indication that there may be an environmental differences between the nebulae of HzRGs and other quasars. Alternatively, this difference may related to intrinsic differences between different AGN types.

Overall, it is likely that both the absorption and radiative transfer effect are working together shaping the Lyα profile. Our analysis assumes that the absorption correction is the dominant factor.

5.2. Lyα nebula and AGN unification model

The unification model of AGN (e.g. Antonucci 1993) proposed that the fundamental difference between type-1 and type-2 is due to the different orientation of the obscuring dusty torus (ionisation cone). Specifically, the ionisation cone of type-1s is more aligned with the observed line of sight than in type-2s.

Within this unification model, we assume that the power of AGN is on a similar level for type-1s and type-2s and that their gaseous nebulae therefore have similar distributions and masses. If we further assume that the ionising photons are primarily produced by the AGN, then the nebulae should have similar morphologies and luminosities. In this picture, the Lyα nebulae are elongated along the direction of the ionisation cone and have a 'rugby-ball' shape. For type-1s, the ionisation cone would be pointing towards the observer resulting in a rounder nebula morphology. For type-2s, the ionisation cone would aligned along the plane of the sky resulting in the observed elliptical morphology. Evidence for such a scenario was indeed reported in He et al. (2018) using ionised gas nebulae but for local AGN and on small scales (sub-kiloparsec to kiloparsec).

Using both the e_{weight} (sensitive to the high surface brightness nebula) and e_{unweight} (whole nebula) quantifying the ellipticity of the nebula, we find that the HzRGs (and other radio quiet type-2s) are more asymmetric than the type-1s in Sect. 4.3.1. This observation agrees with the AGN orientation unification model. The orientation of type-1s probably still vary in a range which causes the large range of the ellipticities. The AGN luminosity and dark matter halo mass (gas distribution) can also play an important role in shaping the observed morphology (Fig. 9).

With the jet axis indicating the direction of the ionisation cone (Drouart et al. 2012) and the alignment between the jet axis and the Lyα nebula (at least in the high surface brightness part where the photons of AGN are presumably dominating the ionisation, Sect. 4.3.5 and Fig. 12), we argue that the AGN orientation between type-1s and type-2s (HzRGs) can explain the observed morphological difference. The evidence for this claim comes mostly from the observed ellipticity distribution (Fig. 9): the e_{weight} (median 0.69, Sect. 4.3.2) for radio-loud type-1s (Arrigoni Battaia et al. 2019) are lower than our HzRGs (median 0.78), which is consistent with the jet (ionisation cone) pointing more towards observers in type-1s. By checking the available radio maps of these radio-loud type-1s (e.g. Fig. B1 in Arrigoni Battaia et al. 2019), we indeed find that they have compact radio morphology (i.e. not the two-side jet like HzRGs) suggesting that the jets are aligned more perpendicular to the plane of the sky. We note that TNJ0121+1320 also has a compact radio morphology (i.e. not having two-side jet) and the lowest e_{weight} (0.66) and e_{unweight} (0.48) in our sample (more consistent with type-1 results, see Fig. 1 and 9) which again fits the unification model.

A similar explanation was also suggested by den Brok et al. (2020) based on Lyα nebula studies of type-2 quasars (also included as comparison sample in this paper). den Brok et al. (2020) suggested that the orientation difference based on unification model can explain the nebula morphology at radial distance $\gtrsim$ 40 pkpc. Using the same radial asymmetry measurement in Fig. 10 (Sect. 4.3.3), we also find large nebula asymmetries at $\gtrsim$40 pkpc (~200 ckpc) in our HzRGs following den Brok et al. (2020) type-2s. den Brok et al. (2020) found more symmetrical morphologies for their type-2s at small radial distances <30 pkpc that are more similar to type-1s. den Brok et al. (2020) suggested that additional ionising sources other than the AGN (e.g. star forming processes) may contribute to this observation and smear out the differences between type-1 and type-2 at such small radii. As for our HzRGs, the jet-gas interaction at $\lesssim 20-30$ pkpc (~100 ckpc) could be a reason for the observed high e_{weight} shown in Fig. 9a (compared to type-1s) and the reason of the small rise (showing higher asymmetry compared to type-2s) in the radial asymmetry measurement at ~60 ckpc in Fig. 10.

5.3. The role of Lyα resonant scattering

As presented in Sect. 4.1 and 4.3, Lyα nebulae around our HzRGs are extended in size ($\gtrsim$150 pkpc) and are asymmetric in shape. Interestingly, there is a correlation between the maximum nebula extent $d_{\rm max}$ ($e_{\rm weight}$: ellipticity measurement that is sensitive to high surface brightness nebula) and the offset between AGN position and nebulae's flux-weighted centroid $d_{\rm AGN-neb}$ (Sect. 4.3.4). This correlation may also reflect our findings regarding the surface brightness and kinematic radial profiles in Sect. 4.2.1 and 4.2.2, such as the exponential shape of the surface brightness in the inner nebula and high W_{80} value. The resonant nature of Lyα photons may be related to this observation.

Villar-Martin et al. (1996) first proposed the idea of resonant scattering being related to the observed extended nebula emission around HzRGs. In simulations, Costa et al. (2022) found that the scattering of Lyα photons, regardless of the powering source, could result in an offset between the luminosity centroid of the nebula and the quasar position ($d_{\rm AGN-neb}$). This offset can vary depending on the line of sight and can reach $\sim$15 pkpc. Such offsets are consistent with what we find (Table 3). The authors also found that scattering can shape the nebula into a more asymmetric morphology ($e_{\rm weight} \rightarrow 1$). This depends on the gas distribution of neutral hydrogen and observed line of sight as described in Costa et al. (2022). Given the common case that gas density is the highest on galaxy scales, and that we target type-2 AGN, we expect the Lyα photons to scatter out to larger projected distances rather than travelling directly towards the observer. Such a scenario may explain our observed correlation in Fig. 11 between $e_{\rm weight}$ and $d_{\rm AGN-neb}$. Specifically, when the scattering is more efficient, we may observe the nebula to be more asymmetric and more extended, at least in the high surface brightness regime.

Resonant scattering has the potential to shape the observed inner parts of the radial profiles (surface brightness and kinematics) and the morphology correlations. The inner part (luminous) of the surface brightness radial profiles have an exponential shape (Sect. 4.2.1). This gradual change in surface brightness and profile slope at smaller radii is suggested to be due to scattering (Costa et al. 2022). The high W_{80} values out to radius of $\sim$50 pkpc (or $\sim$230 ckpc, Sect. 4.2.4) could also be related with efficient scattering (Fig. B1 in Costa et al. 2022). The velocity shift of the nebulae can also be complicated due to scattering at the similar radial distance (Fig. B1 in Costa et al. 2022) which is the case of our v_{50} (Fig. 1c, Sect. 4.1). As shown by the stellar radial profiles (Fig. 6), the impact of seeing cannot be fully responsible for the exponential shape at smaller radii. For the observed kinematics, the jet (which is not included in the simulations) may also play a role here. We overlay the jet hot spot distances on the radial profiles (Figs. 6 and 7). Qualitatively, the v_{50} and W_{80} show different behaviours within and outside the extent of the jet hot spots at least for some targets (e.g. MRC0316-257). We note that the distances marked by the vertical lines are measured from the brightest radio emission positions, that is, the full extent of jet is even larger (Appendix D). The decrease of W_{80} at large radii ($\gtrsim$100 pkpc) observed in some targets (e.g. TN J1338-1942) is, beyond the scope of the Costa et al. (2022) simulations but could be related to the (unvirialised) cosmic web.

In the framework where scattering significantly impacting the observed Lyα properties, Costa et al. (2022) furthermore predicts that Lyα nebulae of edge-on AGN should have lower surface brightness, larger $d_{\rm AGN-neb}$, more asymmetric shape and flatter surface brightness profiles in the centre. Most of the predictions agree with our observations except for lower surface brightnesses, which could be due to our selection criteria and/or jet impact. We note that the analysis of Costa et al. (2022) has been done without correcting for absorption which is reason of the discrepancy.

The orientation (Sect. 5.2) may be the reason for the moderate $d_{\rm max} - d_{\rm AGN-neb}$ relation seen in the sample of (Arrigoni Battaia et al. 2019; i.e. the orientation spans a large range within the sample). The larger the viewing angle (i.e. the more edge-on we are observing the AGN, assuming unification model, Antonucci 1993), the more extended the nebula is expected to be, because both sides of the nebula will be observed. The nebula is expected to become more asymmetric and have larger $d_{\rm AGN-neb}$ as Costa et al. (2022) predicted. The study of type-2 quasars (e.g. den Brok et al. 2020; Sanderson et al. 2021) also found that the difference in nebula morphology when comparing to type-1s is related to AGN orientation. Interestingly, for our HzRGs, we do find a relatively strong correlation between $d_{\rm max}$ and $d_{\rm AGN-neb}$ despite the expectation that most HzRG are observed under similar, large viewing angles, (i.e. close to edge-on). All of our targets have clear two-sided radio lobe morphology (except TN J0121+1320) and none of them shows clear signs of broad-line emission or significant contamination by a bright point-like source in the centre (see also Drouart et al. 2012, and Sect. 2.1.3).

5.4. Large-scale environment: Nearby Lyα emission halos

Byrohl et al. (2021) studied Lyα emission halos and their relation with environmental factors using TNG50 simulation. They found a flattening in the Lyα halo surface brightness radial profile at large radial distances ($\gtrsim$ 30 pkpc). The authors attributed this to the contribution of scattered photons from nearby halos (companions). In Sect. 4.2 (and 4.2.3), we show that the profiles of three of our targets (MRC0943-242, MRC0316-257 and TN J1338-1942) also have an obvious flattening at large radii (Fig. 6). Coincidentally, these targets are known to live in dense environments (on Mpc scale, e.g. Venemans et al. 2007). All of this indicates that our nebulae are 'contaminated' by Lyα halos associated with nearby companions (e.g. Gullberg et al. 2016). In addition, the observed surface brightness radial profile of MRC0316-257 (Fig. 5) at large radii, shows a decline followed of a rise, and is a factor of five brighter than the 2σ surface brightness limit (16 for the intrinsic) which indicate an extra source of Lyα photons. The filamentary Lyα emitting comic structures are observed on Mpc scales (e.g. Umehata et al. 2019; Bacon et al. 2021). Bacon et al. (2021) discussed the possibility that the diffuse Ly-alpha emission is powered by low mass galaxies not directly detectable in the deep (140 hours) MUSE observation.

These results provide additional evidence that the detected nebula connects with the emission halo of companions. If this is the case, we should revisit the $d_{\rm max} - d_{\rm AGN-neb}$ in Sect. 4.3.4. When a quasar resides in a dense environment, its apparent size will likely be impacted by neighbouring Lyα nebulae. This 'contamination' from nearby companions will likely be more related to the large-scale structure and independent of the orientation of the central (quasar) halo. In other words, the hidden parameters behind the $d_{\rm max} - d_{\rm AGN-neb}$ ($e_{\rm weight} - d_{\rm AGN-neb}$, Sect. 4.3.4, Fig. 11) relations may be related to the distribution of the companion emission halos. Contamination from neighbouring halos will result in the centroid of the nebula being offset from the AGN position and cause a more asymmetric nebula morphology.

The nearby companions can be the disturbing sources resulting in the ~1000 km, s^{-1} line width seen at ~100 pkpc (W_{80}, Fig. 7).

The radial asymmetry profiles of our targets have a larger value than type-1s and type-2s (Fig. 10) at larger radii, which is unlikely to be entirely due to the AGN orientation (Sect. 4.3.3). This can now be explained by the impact and contamination of nearby companions at 100s of pkcp. We point out that the type-2 from Sanderson et al. (2021) has a projected size of 173 pkpc, a nebula centre offsets from the AGN of ~17 pkpc and high ellipticity (0.8). This source is also found to have nearby companions (~60 pkpc). The difference of the radial asymmetry profiles (Fig. 10) and surface brightness profiles between this source and our HzRGs may be related to the jet (or large-scale gas distribution, Sect. 5.5).

The stellar masses of the galaxies studied in Byrohl et al. (2021) are in the range of $8.5 < \log_{10}(M_\star/M_\odot) < 10$ which is approximately 1 – 2 orders of magnitude lower than the stellar masses of our HzRGs, implying lower dark matter halo masses, as well. Such lower masses may explain the difference in the level of Lyα surface brightness where the flattening of the profiles is observed: in the simulations by Byrohl et al. (2021) the flattening happens at a surface brightness level of $\sim 10^{-20}$ erg s^{-1} cm^{-2} arcsec^{-2} (e.g. their Fig. 7) while we observe it to happen at a level of $\sim 10^{-18}$ erg s^{-1} cm^{-2} arcsec^{-2}). The dark matter halo mass difference can also explain the different radial distance at which the companion emission dominates (~30 pkpc in Byrohl et al. 2021, versus ~40 pkpc, Table D.3). We note that we use the r_b, the radius at which surface brightness radial profile changes from exponential to power law (Sect. 4.2.3), as the distance where nearby halos start to significantly impact the surface brightness.

The ≳100 pkpc extents of the Lyα and the dense environments of HzRGs (Wylezalek et al. 2013) suggest that nearby halos may contribute to our observations (Byrohl et al. 2021). However, this also suggests that our CGM study is 'contaminated' by sources other than the radio galaxy. For this paper, we exclude obvious emission of clearly detected companions (e.g. 'Arrow galaxy' Vernet et al. 2017). A systematic census of the companion galaxies in the MUSE HzRG fields will be reported in a future paper.

5.5. Gas distribution on large scales

So far, we have focussed our discussion on morphological measurements sensitive to the high-surface brightness part of the Lyα nebulae and plausible explanation of environmental effect on ~100 pkpc scales. It is likely that the jet shapes the nebula in the vicinity of the quasar to align with the jet axis (skewed distribution of $|\theta_{\rm weight} - {\rm PA}_{\rm radio}|$ towards values <30°, Fig. 12) through interaction with the gaseous medium. Beyond the extent of the jets, we use $|\theta_{\rm unweight} - {\rm PA}_{\rm radio}|$ (which is equally sensitive to the whole nebula) to inspect the relation between the jet axis and halo asymmetry.

While it is unlikely that the jet plays a major role shaping the morphology of the large-scale halo, Eales (1992) suggested that the observed direction of the radio jet is the result of an inhomogeneous gas density. When a jet is launched along the direction of higher gas density (e.g. $n_{\rm H} \sim 10^{-2}$ cm^{-3}), the jet 'working surface' (hot spots) will leading to brighter radio emission. Such a scenario would introduce a bias in observing jets preferably along directions of higher densities in flux-limited samples and we might expect a correlation between the morphology of a large-scale halo and radio jet axis. Our observations presented in Figs. 11 and 12 is in agreement with such a scenario.

The detection of molecular gas in HzRGs along the jet axis but beyond hot spots provides further evidence (<20°, which suggests the jet runs into filament of cold gas Emonts et al. 2014). If this direction indeed traces a filament of the cosmic web (e.g. West 1991; Umehata et al. 2019; Bacon et al. 2021) with a higher density of companion galaxies, then this is also in agreement with the discussion presented in Sect. 5.4. Humphrey et al. (2007) found evidence of infalling CGM gas on to the HzRGs which bridges the radio galaxy and to the large-scale (IGM) gas. If the CGM gas is being accreted onto the central HzRGs through these higher density distributions, it would reflect the scenario proposed by Humphrey et al. (2007).

5.6. Evidence of capturing inflow from the cosmic web

The relatively large $|\theta - {\rm PA}_{\rm radio}|$ (81.4° and 45.3° for weighted and un-weighted, respectively) detected in 4C+04.11 is inconsistent with other targets (see Fig. 12). This suggests that the nebula of 4C+04.11 is elongated in the east-west direction on both small (<20 pkpc, scope of jet) and large scales (≳ 20 pkpc, Sect. 4.3.1 and 5.4). The tile with the largest distance from AGN position (# 74, Fig. A.9) has a filamentary like structure. There is no known evidence that 4C+04.11 resides at the centre of a dense cluster-like environment (e.g. Kikuta et al. 2017) which makes it unlikely that the asymmetry is caused by contamination of nearby halos as discussed in Sect. 5.4.

High velocity shocks (≳100 km s^{-1}, Allen et al. 2008) can heat the gas which will then cool by radiating UV photons. Shocks could be caused by inflows and power the observed Lyα emission. We estimated the dark matter halo of 4C+04.11 is of the order of $M_{\rm DM} \sim 10^{13}\,M_\odot$ from it stellar mass, $M_\star \sim 10^{11}\,M_\odot$ with an empirical $M_\star - M_{\rm DM}$ relation (Wang et al. 2021b). The surface brightness measured in the farthest tile #74 is $\sim 1.2 \times 10^{-17}$ erg s^{-1} cm^{-2} arcsec^{-2} which is similar to (or slightly higher than) the simulated value from Rosdahl & Blaizot (2012). We converted our measurement to $z = 3$ which is redshift reported in the simulation. Our measurement and the simulation are consistent given that dark matter halo of 4C+04.11 is likely more massive than the one in the simulation ($M_{\rm DM} \sim 10^{12}\,M_\odot$).

Given the estimated dark matter halo mass, the virial radius and virial velocity can then be calculated as $r_{\rm vir} \sim 100$ kpc and $v_{\rm vir} \simeq 580$ km s^{-1}. From the centre of the tile #74, we can derive its distance to the central AGN as ~60 kpc. We note that this is the projected distance averaged for spaxels in the tile. The actual distance of the filament could be farther. Even though it is closer, Nelson et al. (2016) simulated gas accretion into $10^{12}\,M_\odot$ halos at $z = 2$ and found that the accretion flow structure can remain filamentary within $r_{\rm vir}$ ($\sim 0.5 r_{\rm vir}$). The projected v_{50} (velocity offset) of tile #74 is −536 km s^{-1} which is consistent with $v_{\rm vir}$. Thus, our measurements for the projected distance of the tile and its velocity offset are consistent with a scenario where the Lyα emission in tile #74 may be tracing shock driven by inflows. If the distance we observe is indeed $< r_{\rm vir}$, then the post-virial accretion could be more complicated with multi gas phase components and fragmentation involved (e.g. Cornuault et al. 2018). The broad line width of 4C+04.11 at large radii (Fig. 7) may indicate the disturbed nature of the presumed accretion flow.

The discussion in this section based on the $|\theta - {\rm PA}_{\rm radio}|$ and morphology of bin #74 of 4C+04.11. While the angle difference is a clear outlier in the sample, the tile shape may depend on the implemented method for nebula extent (Sect. 3.1.1). However, we checked the Lyα narrow band image (6690 Å to 6707 Å) directly collapsed from the data cube and confirm the indication of emission from this region. As for the nearby potential emission (north to bin #74, Fig. A.9), we confirm by spectral extraction that there is no S/N> 3 detection. Even if the Lyα emission is detected in this additional region, it would still be consistent with the accretion scenario. Complex filamentary structures are seen in simulations (see Rosdahl & Blaizot 2012, and their Fig. 7) for accretion in higher mass dark matter halo. Nevertheless, we caution that this analysis only considers one possibility. As the data are near the detection limit, deeper observation are needed before more conclusive results can be derived.

6. Conclusions

In this paper, we study the intrinsic Lyα nebulae around a sample of eight high-redshift radio galaxies using optical IFU observations obtained with MUSE. We link our observations to results from the literature for other quasars (mainly type-1 quasars) at similar redshifts.

We have developed a new method to measure the maximum extent of the nebulae with an improved sensitivity to low surface brightness emission. We have also developed a new method to tessellate the Lyα maps (Sect. 3.1). We have detected the Lyα emission at scales $\gtrsim$100 pkpc from the central AGN, down to an observed surface brightness of $\sim$2−20 $\times$ 10^{-19} erg s^{-1} cm^{-2} arcsec^{-2}.

We summarise our results as follows: The Lyα emission line profiles of all sources are affected by multiple and deep absorption troughs out to the edge of the nebulae. We have corrected for this H I absorption (Sect. 3.2) and constructed maps of the intrinsic Lyα (Sect. 4.1) emission and also measured the kinematic properties of the spatially resolved Lyα emission.

We first investigated radial dependencies of the surface brightness, velocity shift, and velocity width of our sample. We found that circularly averaged profiles of the intrinsic (absorption-corrected) Lyα surface brightness are brighter and more extended than type-1 quasar samples (Sect. 4.2.1). We did not find major differences when we investigated the radial profiles along the approaching and receding direction of the radio jets, respectively (Sect. 4.2.2). The surface brightness radial profiles can generally be described by an exponential drop-off for the inner high surface brightness part and a power law for the more extended part (Sect. 4.2.3). We did not find evidence of ordered gas bulk motion from the v_{50} radial profile (Sect. 4.2.4). For four targets, the v_{50} profiles at radii within the jet hot-spot range show a similar gradient as the jet-driven outflow (Fig. 7). The W_{80} profiles show relatively large values ($\gtrsim$1500 km s^{-1}, Fig. 7, Sect. 4.2.4) at all radii and three targets show that a decrease beyond the distance of jet hot spots is indicative of jet-gas interactions.

We quantitatively studied the morphology of the HzRG nebulae (for both observed and intrinsic emission) and compared our results to other quasar samples (uncorrected for absorption, Sect. 4.3). We found that our nebulae are, in general, more asymmetric than nebulae of type-1 quasars and that they are more similar to type-2 quasars (Sect. 4.3.2), although, our sampled sources differ in their measure of asymmetry as a function of the radius (Sect. 4.3.3). Furthermore, we found that the more asymmetric and larger the nebulae are, the greater the offset between the centroid of the nebulae and AGN positions ($d_{\rm max} - d_{\rm AGN-neb}$ and $e_{\rm weight} - d_{\rm AGN-neb}$ in Sect. 4.3.4, Fig. 11).

Lyα is a complicated emission line that can be heavily affected by absorption and resonant scattering which, as we demonstrated, needs to be accounted for. Assuming type-1 and type-2 quasars have similar intrinsic shapes for their nebulae, the difference of the nebulae asymmetry morphology between our sample and other quasars can be explained using the AGN unification model where the orientation of the ionisation cone is the fundamental parameter (Sect. 5.2). Resonant scattering of the Lyα emission can result in the observed $d_{\rm max} - d_{\rm AGN-neb}$ and $e_{\rm weight} - d_{\rm AGN-neb}$ relation in our sample and partially explain the shape of the radial profile and the kinematic profiles (Sect. 5.3). We also found evidence in our HzRGs that the extended nebulae are affected by Lyα emissions from nearby companions (Sect. 5.4) and that CGM gas has a higher density distribution along a specific direction, which is coincident with the direction of the radio jet (Sect. 5.5). There is also a possibility that, in our observations, we captured inflows from the cosmic web (Sect. 5.6).

In this paper we have shown that measurements of Lyα nebulae around high-redshift AGN can act as a probe of the environment of AGN and their host galaxies. We have found fundamental differences between the extended ionised nebulae of different types of quasars at cosmic noon and beyond. Due to its resonant nature, it is a challenge to use Lyα as a tracer of gas kinematics especially out to the $\sim$100 pkpc scales. Nevertheless, Lyα line observations offer some insight into the state of CGM gas at a time when it is simultaneously being impacted by more than one physical mechanism (e.g. quasar outflow, jet-gas interaction, and cosmic inflow). These kinds of observations will be particularly useful for future simulation works. The MUSE data only reveal the tip of the iceberg. In upcoming papers, the H I absorbers will be reported together with the high-resolution spectroscopy data. In addition, all of the UV emission lines covered by MUSE will be studied in detail and this will provide crucial information on the ionisation, metallicity, and AGN feedback in the quasar nebulae. Furthermore, scheduled JWST observations will be available for four HzRGs in our sample and this will provide unprecedented details of the AGN and host galaxy connection on scales of $\lesssim$1 kpc ($\sim$0.05″).

Acknowledgements. We would like to thank Bjorn Emonts and Zheng Cai for valuable discussion which improved this work. This work uses the NASA's Astrophysics Data System and a number of open source software other than the aforementioned ones such as Jupyter notebook (Kluyver et al. 2016); `matplotlib` (Hunter 2007); `SciPy` (Virtanen et al. 2020); `NumPy` (Harris et al. 2020); `Astropy` (Astropy Collaboration 2018); and `LMFIT` (Newville et al. 2016). B.G. acknowledges support from the Carlsberg Foundation Research Grant CF20-0644 'Physical pRoperties of the InterStellar Medium in Luminous Infrared Galaxies at High redshifT: PRISM- LIGHT'. M.V.M. acknowledges support from grant PID2021-124665NB-I00 by the Spanish Ministry of Science and Innovation/State Agency of Research MCIN/AEI/ 10.13039/501100011033 and by "ERDF A way of making Europe". G.N. acknowledges funding support from the Natural Sciences and Engineering Research Council (NSERC) of Canada through a Discovery Grant and Discovery Accelerator Supplement, and from the Canadian Space Agency through grant 18JWST-GTO1. P.L. (contract DL57/2016/CP1364/CT0010) is supported by national funds through Fundação para a Ciência e Tecnologia (FCT) and the Centro de Astrofísica da Universidade do Porto (CAUP).

References

Adam, G., Rocca-Volmerange, B., Gerard, S., Ferruit, P., & Bacon, R. 1997, A&A, 326, 501
Ahumada, R., Prieto, C. A., Almeida, A., et al. 2020, ApJS, 249, 3
Allen, M. G., Groves, B. A., Dopita, M. A., Sutherland, R. S., & Kewley, L. J. 2008, ApJS, 178, 20
Andrae, R., Schulze-Hartung, T., & Melchior, P. 2010, ArXiv e-prints [arXiv:1012.3754]
Antonucci, R. 1993, ARA&A, 31, 473
Arrigoni Battaia, F., Hennawi, J. F., Cantalupo, S., & Prochaska, J. X. 2016, ApJ, 829, 3
Arrigoni Battaia, F., Hennawi, J. F., Prochaska, J. X., et al. 2019, MNRAS, 482, 3162

Astropy Collaboration (Price-Whelan, A. M., et al.) 2018, AJ, 156, 123
Bacon, R., Accardo, M., Adjali, L., et al. 2010, SPIE, 7735, 131
Bacon, R., Vernet, J., Borisova, E., et al. 2014, The Messenger, 157, 13
Bacon, R., Piqueras, L., Conseil, S., Richard, J., & Shepherd, M. 2016, Astrophysics Source Code Library [record ascl:1611.003]
Bacon, R., Mary, D., Garel, T., et al. 2021, A&A, 647, A107
Basu-Zych, A., & Scharf, C. 2004, ApJ, 615, L85
Best, P. N., Röttgering, H. J. A., & Longair, M. S. 2000, MNRAS, 311, 23
Bicknell, G. V., Sutherland, R. S., van Breugel, W. J. M., et al. 2000, ApJ, 540, 678
Binette, L., Kurk, J. D., Villar-Martín, M., & Röttgering, H. J. A. 2000, A&A, 356, 23
Bolatto, A. D., Wolfire, M., & Leroy, A. K. 2013, ARA&A, 51, 207
Borisova, E., Cantalupo, S., Lilly, S. J., et al. 2016, ApJ, 831, 39
Byrohl, C., Nelson, D., Behrens, C., et al. 2021, MNRAS, 506, 5129
Cai, Z., Cantalupo, S., Prochaska, J. X., et al. 2019, ApJS, 245, 23
Cantalupo, S., Lilly, S. J., & Haehnelt, M. G. 2012, MNRAS, 425, 1992
Cantalupo, S., Arrigoni-Battaia, F., Prochaska, J. X., Hennawi, J. F., & Madau, P. 2014, Nature, 506, 63
Cappellari, M., & Copin, Y. 2003, MNRAS, 342, 345
Carilli, C. L., Röttgering, H. J. A., van Ojik, R., Miley, G. K., & van Breugel, W. J. M. 1997, ApJS, 109, 1
Chambers, K. C., Miley, G. K., & van Breugel, W. 1987, Nature, 329, 604
Chang, S.-J., Yang, Y., Seon, K.-I., Zabludoff, A., & Lee, H.-W. 2023, ApJ, 945, 100
Christensen, L., Jahnke, K., Wisotzki, L., & Sánchez, S. F. 2006, A&A, 459, 717
Cigan, P. 2019, Astrophysics Source Code Library [record ascl:1909.002]
Cornuault, N., Lehnert, M. D., Boulanger, F., & Guillard, P. 2018, A&A, 610, A75
Costa, T., Arrigoni Battaia, F., Farina, E. P., et al. 2022, MNRAS, 517, 1767
Cowie, L. L., & Hu, E. M. 1998, AJ, 115, 1319
Dawson, S., Rhoads, J. E., Malhotra, S., et al. 2007, ApJ, 671, 1227
De Breuck, C., van Breugel, W., Minniti, D., et al. 1999, A&A, 352, L51
De Breuck, C., van Breugel, W., Stanford, S. A., et al. 2002, AJ, 123, 637
De Breuck, C., Seymour, N., Stern, D., et al. 2010, ApJ, 725, 36
den Brok, J. S., Cantalupo, S., Mackenzie, R., et al. 2020, MNRAS, 495, 1874
Dey, A., Bian, C., Soifer, B. T., et al. 2005, ApJ, 629, 654
Dijkstra, M. 2014, PASA, 31, e040
Dijkstra, M. 2019, in Correction to: Physics of Lyα Radiative Transfer, eds. A. Verhamme, P. North, S. Cantalupo, & H. Atek (Berlin, Heidelberg: Springer)
Drouart, G., De Breuck, C., Vernet, J., et al. 2012, A&A, 548, A45
Drouart, G., De Breuck, C., Vernet, J., et al. 2014, A&A, 566, A53
Duncan, K. J., Windhorst, R. A., Koekemoer, A. M., et al. 2023, MNRAS, 522, 4548
Eales, S. A. 1992, ApJ, 397, 49
Emonts, B. H. C., Norris, R. P., Feain, I., et al. 2014, MNRAS, 438, 2898
ESO CPL Development Team 2015, Astrophysics Source Code Library [record ascl:1504.003]
Evans, I. N., Primini, F. A., Glotfelty, K. J., et al. 2010, ApJS, 189, 37
Falkendal, T., De Breuck, C., Lehnert, M. D., et al. 2019, A&A, 621, A27
Falkendal, T., Lehnert, M. D., Vernet, J., De Breuck, C., & Wang, W. 2021, A&A, 645, A120
Farina, E. P., Arrigoni-Battaia, F., Costa, T., et al. 2019, ApJ, 887, 196
Foreman-Mackey, D., Hogg, D. W., Lang, D., & Goodman, J. 2013, PASP, 125, 306
Fossati, M., Fumagalli, M., Lofthouse, E. K., et al. 2021, MNRAS, 503, 3044
Francis, P. J., Williger, G. M., Collins, N. R., et al. 2001, ApJ, 554, 1001
Gaia Collaboration (Brown, A. G. A., et al.) 2021, A&A, 649, A1
Gronke, M., & Dijkstra, M. 2016, ApJ, 826, 14
Gronke, M., Bull, P., & Dijkstra, M. 2015, ApJ, 812, 123
Gronke, M., Dijkstra, M., McCourt, M., & Oh, S. P. 2016, ApJ, 833, L26
Gullberg, B., De Breuck, C., Lehnert, M. D., et al. 2016, A&A, 586, A124
Hanuschik, R. W. 2003, A&A, 407, 1157
Harris, C. R., Millman, K. J., van der Walt, S. J., et al. 2020, Nature, 585, 357
Harwood, J. J., Hardcastle, M. J., Croston, J. H., & Goodger, J. L. 2013, MNRAS, 435, 3353
He, Z., Sun, A.-L., Zakamska, N. L., et al. 2018, MNRAS, 478, 3614
Heckman, T. M., Lehnert, M. D., Miley, G. K., & van Breugel, W. 1991a, ApJ, 381, 373
Heckman, T. M., Lehnert, M. D., van Breugel, W., & Miley, G. K. 1991b, ApJ, 370, 78
Hennawi, J. F., & Prochaska, J. X. 2013, ApJ, 766, 58
Hippelein, H., & Meisenheimer, K. 1993, Nature, 362, 224
Hu, E. M., & McMahon, R. G. 1996, Nature, 382, 231
Humphrey, A. 2019, MNRAS, 486, 2102
Humphrey, A., Villar-Martín, M., Fosbury, R., Vernet, J., & di Serego Alighieri, S. 2006, MNRAS, 369, 1103
Humphrey, A., Villar-Martín, M., Fosbury, R., et al. 2007, MNRAS, 375, 705
Humphrey, A., Villar-Martín, M., Sánchez, S. F., et al. 2008, MNRAS, 390, 1505
Humphrey, A., Vernet, J., Villar-Martín, M., et al. 2013, ApJ, 768, L3
Hunter, J. D. 2007, Comput. Sci. Eng., 9, 90
Jarvis, M. J., Wilman, R. J., Röttgering, H. J. A., & Binette, L. 2003, MNRAS, 338, 263
Kikuta, S., Imanishi, M., Matsuoka, Y., et al. 2017, ApJ, 841, 128
Kluyver, T., Ragan-Kelley, B., Pérez, F., et al. 2016, in Positioning and Power in Academic Publishing: Players, Agents and Agendas, eds. F. Loizides, & B. Schmidt (IOS Press), 87
Kolwa, S., Vernet, J., De Breuck, C., et al. 2019, A&A, 625, A102
Kolwa, S., De Breuck, C., Vernet, J., et al. 2023, MNRAS, 525, 5831
Krogager, J.-K. 2018, ArXiv e-prints [arXiv:1803.01187]
Lau, M. W., Hamann, F., Gillette, J., et al. 2022, MNRAS, 515, 1624
Leclercq, F., Bacon, R., Wisotzki, L., et al. 2017, A&A, 608, A8
Li, Z., Steidel, C. C., Gronke, M., Chen, Y., & Matsuda, Y. 2022, MNRAS, 513, 3414
Liu, G., Zakamska, N. L., Greene, J. E., Nesvadba, N. P. H., & Liu, X. 2013, MNRAS, 436, 2576
Mackenzie, R., Pezzulli, G., Cantalupo, S., et al. 2021, MNRAS, 502, 494
Marino, R. A., Cantalupo, S., Pezzulli, G., et al. 2019, ApJ, 880, 47
Martin, D. C., Chang, D., Matuszewski, M., et al. 2014, ApJ, 786, 107
Matsuda, Y., Yamada, T., Hayashino, T., et al. 2004, AJ, 128, 569
McCarthy, P. J. 1993, ARA&A, 31, 639
McCarthy, P. J., van Breugel, W., & Kapahi, V. K. 1991, ApJ, 371, 478
Miley, G., & De Breuck, C. 2008, A&ARv, 15, 67
Miley, G. K., Overzier, R. A., Tsvetanov, Z. I., et al. 2004, Nature, 427, 47
Morais, S. G., Humphrey, A., Villar-Martín, M., et al. 2017, MNRAS, 465, 2698
Nelson, D., Genel, S., Pillepich, A., et al. 2016, MNRAS, 460, 2881
Nesvadba, N. P. H., Lehnert, M. D., De Breuck, C., Gilbert, A., & van Breugel, W. 2007, A&A, 475, 145
Nesvadba, N. P. H., Lehnert, M. D., De Breuck, C., Gilbert, A. M., & van Breugel, W. 2008, A&A, 491, 407
Nesvadba, N. P. H., De Breuck, C., Lehnert, M. D., Best, P. N., & Collet, C. 2017a, A&A, 599, A123
Nesvadba, N. P. H., Drouart, G., De Breuck, C., et al. 2017b, A&A, 600, A121
Newville, M., Stensitzki, T., Allen, D. B., et al. 2016, Astrophysics Source Code Library [record ascl:1606.014]
Noirot, G., Vernet, J., De Breuck, C., et al. 2016, ApJ, 830, 90
Noirot, G., Stern, D., Mei, S., et al. 2018, ApJ, 859, 38
Ono, Y., Itoh, R., Shibuya, T., et al. 2021, ApJ, 911, 78
Ouchi, M., Ono, Y., & Shibuya, T. 2020, ARA&A, 58, 617
Parijskij, Y. N., Thomasson, P., Kopylov, A. I., et al. 2014, MNRAS, 439, 2314
Pentericci, L., Röttgering, H. J. A., Miley, G. K., et al. 1999, A&A, 341, 329
Pentericci, L., Van Reeven, W., Carilli, C. L., Röttgering, H. J. A., & Miley, G. K. 2000, A&AS, 145, 121
Prescott, M. K. M., Martin, C. L., & Dey, A. 2015, ApJ, 799, 62
Rauch, M. 1998, ARA&A, 36, 267
Reuland, M., van Breugel, W., Röttgering, H., et al. 2003, ApJ, 592, 755
Reyes, R., Zakamska, N. L., Strauss, M. A., et al. 2008, AJ, 136, 2373
Rosdahl, J., & Blaizot, J. 2012, MNRAS, 423, 344
Rottgering, H. J. A., Hunstead, R. W., Miley, G. K., van Ojik, R., & Wieringa, M. H. 1995, MNRAS, 277, 389
Saito, T., Shimasaku, K., Okamura, S., et al. 2006, ApJ, 648, 54
Sanderson, K. N., Prescott, M. K. M., Christensen, L., Fynbo, J., & Møller, P. 2021, ApJ, 923, 252
Seymour, N., Stern, D., De Breuck, C., et al. 2007, ApJS, 171, 353
Shimasaku, K., Kashikawa, N., Doi, M., et al. 2006, PASJ, 58, 313
Silva, M., Humphrey, A., Lagos, P., et al. 2018a, MNRAS, 481, 1401
Silva, M., Humphrey, A., Lagos, P., et al. 2018b, MNRAS, 474, 3649
Soto, K. T., Lilly, S. J., Bacon, R., Richard, J., & Conseil, S. 2016, MNRAS, 458, 3210
Steidel, C. C., Adelberger, K. L., Shapley, A. E., et al. 2000, ApJ, 532, 170
Swinbank, A. M., Vernet, J. D. R., Smail, I., et al. 2015, MNRAS, 449, 1298
Tepper-García, T. 2006, MNRAS, 369, 2025
Tepper-García, T. 2007, MNRAS, 382, 1375
Tumlinson, J., Peeples, M. S., & Werk, J. K. 2017, ARA&A, 55, 389
Umehata, H., Fumagalli, M., Smail, I., et al. 2019, Science, 366, 97
van Breugel, W. J. M., Stanford, S. A., Spinrad, H., Stern, D., & Graham, J. R. 1998, ApJ, 502, 614
van Ojik, R., Roettgering, H. J. A., Carilli, C. L., et al. 1996, A&A, 313, 25
van Ojik, R., Roettgering, H. J. A., Miley, G. K., & Hunstead, R. W. 1997, A&A, 317, 358
Vayner, A., Zakamska, N. L., Riffel, R. A., et al. 2021, MNRAS, 504, 4445
Vayner, A., Zakamska, N. L., Sabhlok, S., et al. 2023, MNRAS, 519, 961
Veilleux, S., Cecil, G., & Bland-Hawthorn, J. 2005, ARA&A, 43, 769
Venemans, B. P., Röttgering, H. J. A., Miley, G. K., et al. 2007, A&A, 461, 823

Verhamme, A., Schaerer, D., & Maselli, A. 2006, A&A, 460, 397
Vernet, J., Lehnert, M. D., De Breuck, C., et al. 2017, A&A, 602, L6
Villar-Martin, M., Binette, L., & Fosbury, R. A. E. 1996, A&A, 312, 751
Villar-Martín, M., Vernet, J., di Serego Alighieri, S., et al. 2002, MNRAS, 336, 436
Villar-Martín, M., Vernet, J., di Serego Alighieri, S., et al. 2003, MNRAS, 346, 273
Villar-Martín, M., Sánchez, S. F., De Breuck, C., et al. 2006, MNRAS, 366, L1
Villar-Martín, M., Humphrey, A., De Breuck, C., et al. 2007a, MNRAS, 375, 1299
Villar-Martín, M., Sánchez, S. F., Humphrey, A., et al. 2007b, MNRAS, 378, 416
Virtanen, P., Gommers, R., Oliphant, T. E., et al. 2020, Nat. Methods, 17, 261
Wang, W., De Breuck, C. A., Lehnert, M. D., et al. 2021a, JWST Proposal. Cycle 1, 1970
Wang, W., Wylezalek, D., De Breuck, C., et al. 2021b, A&A, 654, A88
Weidinger, M., Møller, P., & Fynbo, J. P. U. 2004, Nature, 430, 999
Weidinger, M., Møller, P., Fynbo, J. P. U., & Thomsen, B. 2005, A&A, 436, 825
Weilbacher, P. M., Palsa, R., Streicher, O., et al. 2020, A&A, 641, A28
West, M. J. 1991, ApJ, 379, 19
Wilman, R. J., Jarvis, M. J., Röttgering, H. J. A., & Binette, L. 2004, MNRAS, 351, 1109
Wisotzki, L., Bacon, R., Brinchmann, J., et al. 2018, Nature, 562, 229
Wylezalek, D., Galametz, A., Stern, D., et al. 2013, ApJ, 769, 79
Wylezalek, D., Vernet, J., De Breuck, C., et al. 2014, ApJ, 786, 17
Yang, Y., Zabludoff, A., Tremonti, C., Eisenstein, D., & Davé, R. 2009, ApJ, 693, 1579
Yang, Y., Zabludoff, A., Eisenstein, D., & Davé, R. 2010, ApJ, 719, 1654
Zakamska, N. L., Hamann, F., Pâris, I., et al. 2016, MNRAS, 459, 3144
Zhang, S., Cai, Z., Xu, D., et al. 2023, ApJ, 952, 124
Zirm, A. W., Overzier, R. A., Miley, G. K., et al. 2005, ApJ, 630, 68

Appendix A: Detection map and tessellation procedures

A.1. Procedure of detection map for nebulae extent

Table A.1. Optimal detection map parameters combination.

HzRG	$T_{S/N}$	n_λ	$2.355\sigma_{\max}$[†]	n_c
MRC 0943-242	3.5	4	25	2
MRC 0316-257	3.5	5	30	3
TN J0205+2242	3.5	5	25	2
TN J0121+1320	2.5	3	35	4
4C+03.24	3.5	5	20	2
4C+19.71	3.5	2	30	3
TN J1338-1942	3.5	2	30	2
4C+04.11	3.5	4	25	2

Notes. [†]Maximum Gaussian kernel scale in FWHM. The unit is in pixel unit.

The basic idea for detection map is to use the 3D information of the MUSE data cube to determine the maximum spatial extent of the Lyα emission. Smoothing technique is the key process in this procedure to guarantee the faint structures are captured. To assist with conveying the procedure, the process is shown schematically in Fig. A.1. In this procedure, we can select the faint end of the emission nebula to the surface brightness detection limit.

Before the generation of detection map, we do a step of continuum subtraction for each spectra spatially centred around the AGN and spectrally around their Lyα wavelength range ($-5000 - 5000\,\mathrm{km\,s^{-1}}$ or $-6000 - 6000\,\mathrm{km\,s^{-1}}$ for 4C+03.24 which has broader line width) with the emission line masked. If there are sky-lines, emission or absorption features from foreground targets in the unmasked range, we do further masking. Continuum from the host galaxy, central AGN and foreground objects need to be subtracted to minimise their contamination. In this way, we exclusively focus on the line-emission nebula. The choice of flat or linear continuum do not have significant impact on the Lyα fitting (Wang et al. 2021b). Hence to better account for the slope from foreground stars, we subtract a first-order polynomial from the cube.

The 3D adaptive smoothing follows the Martin et al. (2014) procedure with adaptation (e.g. Vernet et al. 2017). As described in Sect. 3.1.1, it smooths each of the image planes of the continuum-subtracted cube adaptively with a Gaussian kernel over a wavelength range of $\sim$ 15 Å around the Lyα emission. For the image slice at each wavelength, the algorithm first takes average of adjacent n_λ number of slices around this image slice along the wavelength dimension (Fig. A.1a). Then it adaptively smooths the averaged image with a Gaussian kernel starting from the smallest kernel size, $\sigma_0 = 3/2.355$ pix, until the maximum, $\sigma_{\max}$, is reached (Fig. A.1b). Specifically at each step, the algorithm smooths the spaxels that are not passing the pre-set S/N threshold, $T_{\mathrm{S/N}}$. In the end, the algorithm set the voxels, after being maximally smoothed, that not pass the $T_{\mathrm{S/N}}$ to 0 as no-signal containing (i.e. the voxels that potentially contain Lyα signals have positive value). In this way, we preliminarily detect where we have Lyα in the cube (Fig. A.1c).

To generate a detection map working on the spatial dimensions and guarantee line fitting, we perform a further check along the wavelength dimension for the smoothed cube. Specifically, if the smoothed spectrum at one spatial location (x, y) has n_c numbers of consecutive wavelength pixels preserved (i.e. have positive values), then we flag this spatial location (x, y) as signal-contained (see Fig. A.1d as an example). The others that do not pass this check are discarded. In this way, we can construct the detection map (Fig. A.1e).

The question left is to find a combination of the four parameters ($T_{\mathrm{S/N}}$, n_λ, $\sigma_{\max}$ and n_c) which returns an optimised detection map. For this, we generate a series of detection maps for each targets with different combination of the four parameters. Then we choose the one that optimises the spatial selection (i.e. captures large-scale extent while avoid island-like structures). The best combination of the four parameters for each targets are presented in Table A.1. We check the detection maps constructed using different sets of parameters around our optimal combination (Table A.1) and find that the bulk ($\sim$ 80%) of the selected spaxels remains the same. If using a stricter set of parameters (e.g. higher $T_{\mathrm{S/N}}$ and/or n_λ), we would miss the low S/N part of the nebula by comparing with previous individual target studies (Swinbank et al. 2015; Vernet et al. 2017). If using a more relaxed set, the peripheral regions, mostly disconnected to the bulk of the nebula, with pure noise (after checking spectrum) would likely be selected. Thus, we are assured that the constructed detection map represented the observation to the detection limit and the method is robust against objectiveness. After constructing the map with the best parameter combination, we perform a final manual selection to exclude island-like regions ($\gtrsim$ 1 arcsec^2 in size) which are detached from the main nebulae ($> 1''$) and could be due to noise or companion. A further check of the spectra extracted from these regions is also conducted. Around 50% of the island regions only contain noise. The ones with potential Lyα signal detected are presented in Appendix A.3 (Fig. A.3 and A.4). Since these are detached from the extended nebula around the quasar, we do not include them in this analysis but point out they may trace companion emissions. We note that we refer to the smoothed cube obtained in this way (using $T_{S/N}$, n_λ and $\sigma_{\max}$ in Table A.1) as 'optimally smoothed cube'. The smoothed cube are only used in constructing the detection map and not being further used in other analysis. In Appendix A.3 (Fig. A.2-A.9a), we present the smoothed nebula image extracted from the optimally smoothed cube.

A.2. Tessellation procedure

The Lyα nebulae are irregular in morphology (e.g. Swinbank et al. 2015; Vernet et al. 2017), affected by absorption and having high S/N gradient from centre to outskirt and multiple dynamical components. Hence, neither the simple adoption of Voronoi tessellation (Cappellari & Copin 2003) nor the tessellation method from Swinbank et al. (2015) (which was invented for studying TN J1338-1942 and has also been applied to 4C+04.11 but only works for the central part, see Wang et al. 2021b) can be adopted without adaptation. We describe here the tessellation used in this work.

The Swinbank et al. (2015) tessellation is not optimal for some of our target with significantly irregular nebula shape (e.g. MRC0316-257) since it works with rectangular binning. Hence, we decide to adopt the Voronoi binning (Cappellari & Copin 2003), which is a sophisticate adaptive spatial binning algorithm implemented by various studies of IFU data, for this work. Directly performing Voronoi binning on the image will return detached regions (i.e. regions of spaxels belong to the same tile but are physically separated), as the images are S/N limited for the outer nebulae. The solution could be (i) turning off Weighted Voronoi Tessellation or Centroidal Voronoi Tessellation (see Cappellari & Copin 2003, for details); or (ii) perform-

Wang, W., et al.: A&A 680, A70 (2023)

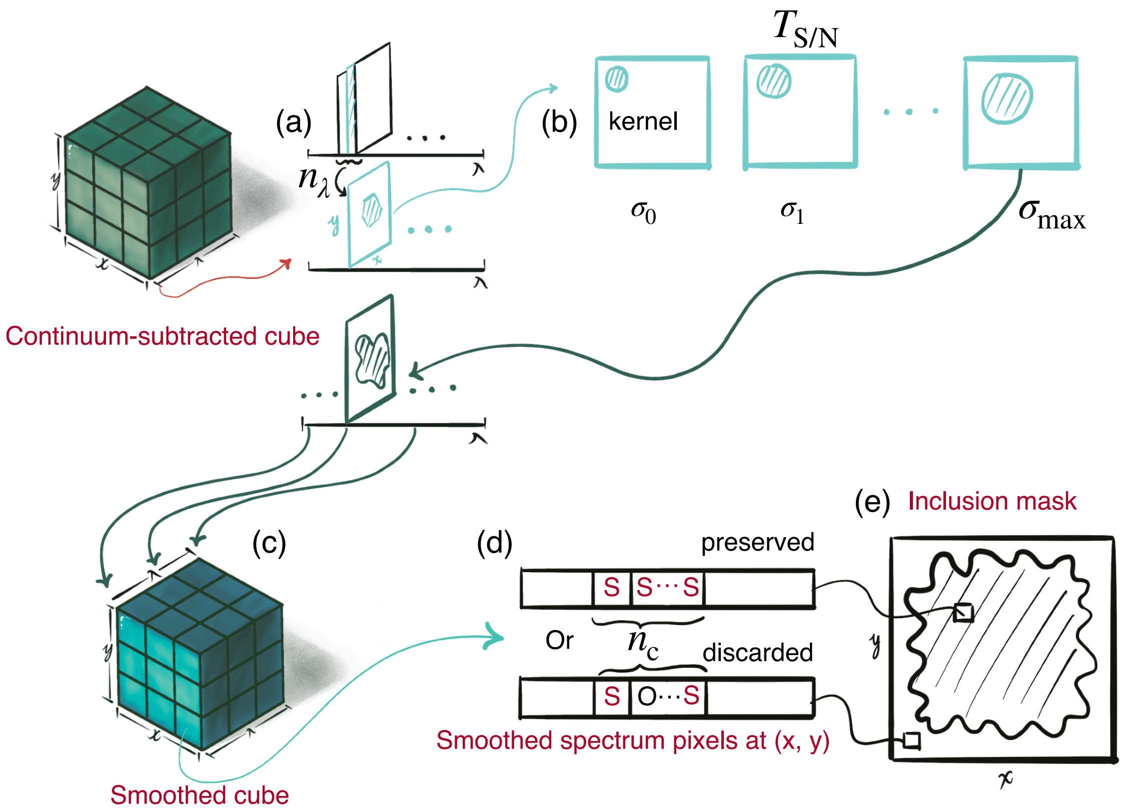

Fig. A.1. Schematic presentation of the detection map construction. **(a)** Average n_λ number of images around each of the image slices (cyan) from the continuum-subtracted cube (dark green cube). **(b)** Spatially smooth each of the averaged image with Gaussian kernel. The algorithm will increase the kernel size ($\sigma_0 < \sigma_1$) to smooth the spaxels that not passing the $T_{S/N}$, S/N threshold, at each steps until the maximum, σ_{max}, has been reached. **(c)** Combine the adaptively smoothed images into the smoothed cube (lighter green cube). **(d)** Check the smoothed spectrum (long black rectangular box) at location (x, y). The position is preserved when there are n_c consecutive number of pixels selected with signal detection (red 'S') in previous steps. **(f)** Construct the detection map.

ing a twofold Voronoi binning by using a S/N cut for doing separate binning for high and low S/N parts (M. Cappellari private communication). Solution (i) will return wedge shape tiles which is a known result (Cappellari & Copin 2003). It is, however, not desirable for our case since it smears out the radial structures which is one of the key interest of this work. Therefore, we adapt solution (ii); the twofold Voronoi binning for our sample.

Firstly, we apply the detection map (Sect. 3.1.1 and Appendix A.1) to the continuum-subtracted un-smoothed cube to preserve only the Lyα signal detected spaxels for tessellation. To avoid complication and keep consistency for the whole sample, we perform the tessellation on a single narrow band image for each target. Since the Lyα spectra may have different observed peaks at different spatial locations, we choose the wavelength range, over which the narrow band image for tessellation will be produced (averaged by the number of wavelength pixels), to enclose as much of line emissions as possible and avoid adding pure noise. This range is ~ 10Å wide. We note that for 4C+19.71, we select two wavelength ranges at both the blue and red sides of 5577 Å(sky-line), which is at roughly the systemic redshift of Lyα. In this way, we construct the S/N map from the narrow band image.

Secondly, a Gaussian smooth is performed to the S/N map to minimise the impact of randomly located spaxels dominated by noise (i.e. further avoid detached region problem). We use a Gaussian kernel with $\sigma_s = 3$ in pixel unit. Then, we apply a S/N cut of 3 to the S/N map to select the high S/N regions for the first Voronoi binning.

Thirdly, for the selected S/N > 3 part, we reassign spaxels with S/N>6 to S/N=6 and perform the Voronoi binning with a target $(S/N)_{vorbin,1st}$ = 15 (12 for 4C+03.24, see later). The reason for the S/N reassignment is to control the minimum size of the tiles to avoid single spaxel tile and account for the seeing effect. Because the Lyα nebulae studied here have high S/N gradient from centre to outskirt, performing Voronoi binning with a high S/N threshold (avoid single spaxel bin in the high S/N region) will result in tiles with large size for the low S/N part which is an overkill for the fitting and smears out resolution information. After reassigning S/N>6 spaxel and using $(S/N)_{vorbin,1st}$ =15, the minimum number of spaxels for one tile is 6 (= 3×2 pix^2 or 0.6× 0.4 arcsec^2) which is roughly half of the seeing disc. This is a compromise for being consistency for the whole sample and also physically connects the neighbour tiles which is useful for the implemented fitting procedure (Sec. 3). As for 4C+03.24 which was observed in the AO mode, we lower its $(S/N)_{vorbin,1st}$ =12 to have a minimum number of spaxels for one tile is 4 (= 2×2 pix^2 or 0.4 × 0.4 arcsec^2).

Finally, for the S/N≤3 spaxels left in the first step, we apply a Voronoi binning with $(S/N)_{vorbin,2nd}$ =8 (11 for 4C+19.71 due to the impact of sky-line).

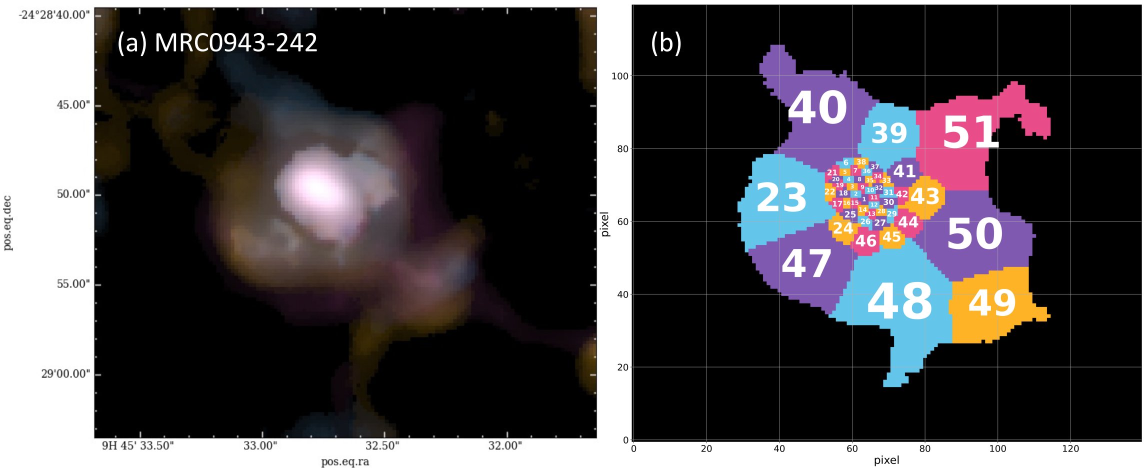

Fig. A.2. Smoothed nebula image (a) and tessellation map (b) of MRC0943-242. (a) The purple, yellow and blue colours represent median pseudo-narrow band Lyα images collapsed arbitrarily from red part, middle and blue part, respectively, of the smoothed cubes.

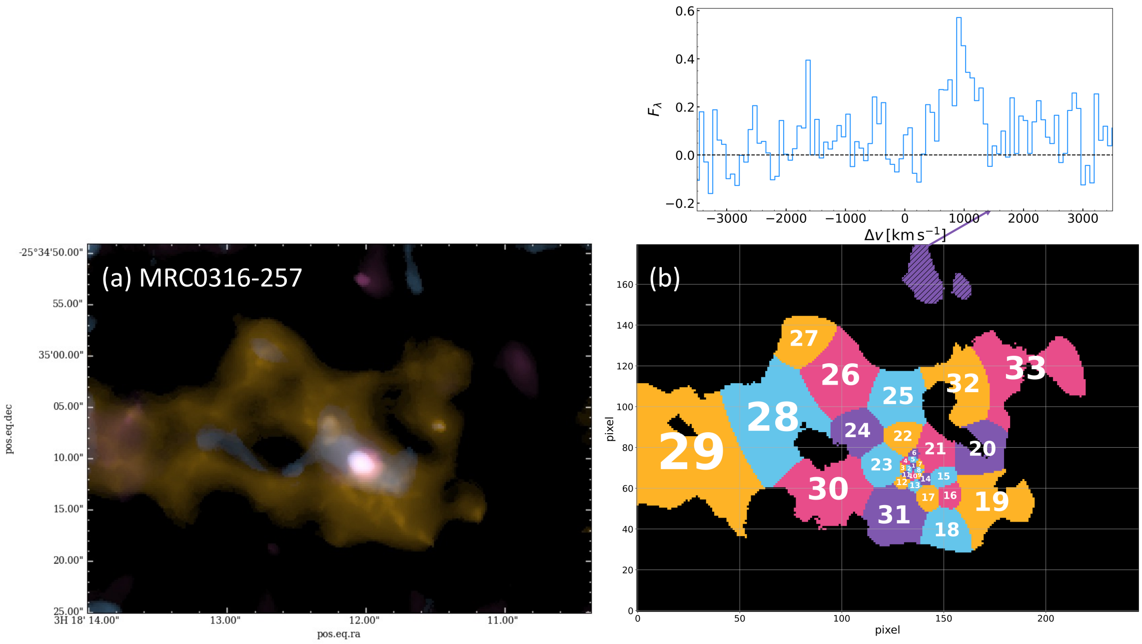

Fig. A.3. Smoothed nebula image (a) and tessellation map (b) of MRC0316-257. The inset spectrum is extracted from the detached regions (hatched) which is selected having Lyα emissions but left out from the analysis following Sect. 3.1.1. (a) The colour-composed image is created in a manner similar to that of Figure A.2a.

In this way, we obtain the tessellation maps where each tile has S/N> 5. We note that the S/N stated here is calculated based on the narrow band image (see above) collapsed $\sim$ 14 wavelength elements (may vary for different targets) and averaged by the number of wavelength elements. This narrow band image is chosen to enclose as much of the Lyα emission as possible which is a compensation for the different emission peak due to kinematics. Hence, a S/N> 5 in each tile selected in this way is feasible for further fitting as there will be other signal contained wavelength pixels outside the range given the broadness of the emission line. For targets where the extent of the nebula is overlapped with bright foreground stars (TN J1338-1942 and 4C+03.24), we manually assign a $d = 1$ arcsec circular mask at the position of the star to minimise its impact. For MRC0316-257, we mask the region where a known Lyα emitting galaxies at the similar redshift overlaps in spatial location with the nebula (see Vernet et al. 2017, Arrow galaxy). These manually masked regions are marked by purple hatches in Fig. 1bcd. The tessellation maps are shown in Appendix A.3. Through the tessellation, we reach $\sim 2\sigma$ surface brightness limit (as reported in Table 2) in the faintest tile.

For the convenience of the spatial fitting (Sect. 3.2.2 and Appendix B), we run an automatic re-numbering algorithm to make physically attached tiles to be as consecutive in number as possible. In each tile, the spatial spectra from every spaxel are then extracted and summed according to the tessellation from the

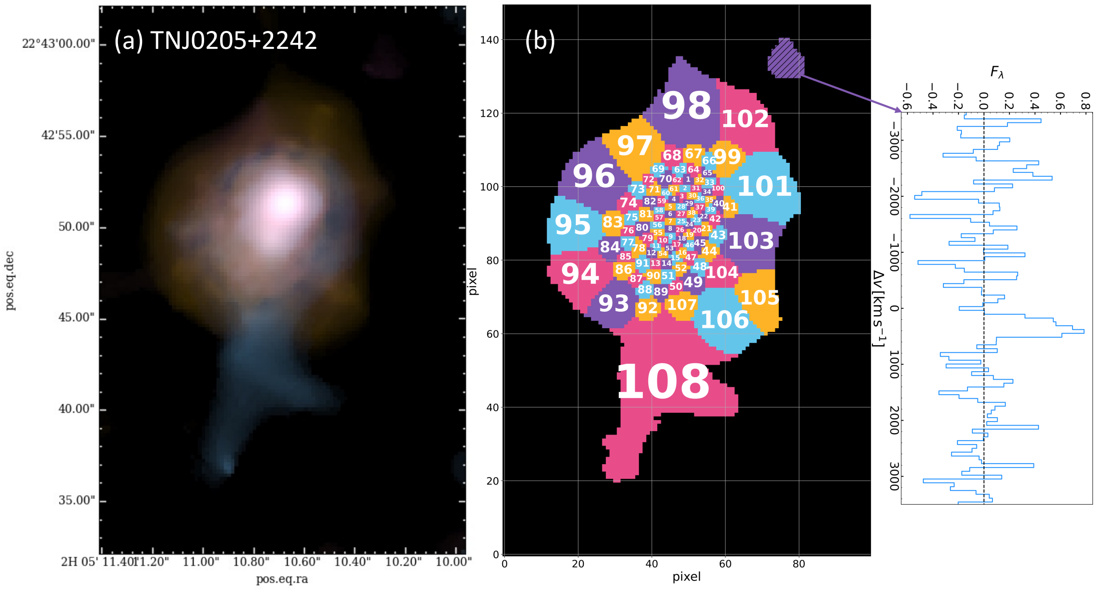

Fig. A.4. Smoothed nebula image (a) and tessellation map (b) of TN J0205+2242. The inset spectrum is extracted from the detached region (hatched) which is selected having Lyα emissions but left out from the analysis following Sect. 3.1.1. (a) The colour-composed image is created in a manner similar to that of Figure A.2a.

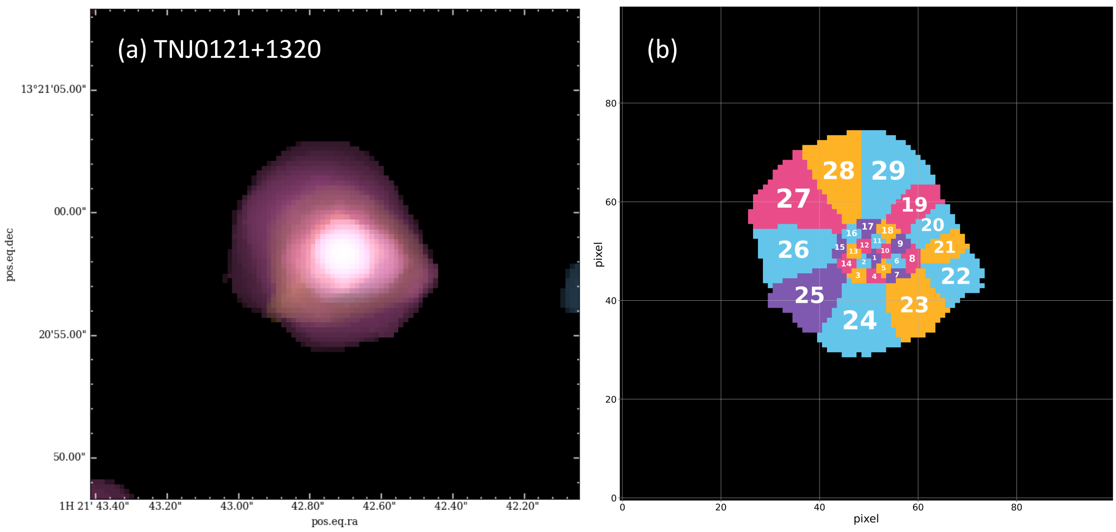

Fig. A.5. Smoothed nebula image (a) and tessellation map (b) of TN J0121+1320. (a) The colour-composed image is created in a manner similar to that of Figure A.2a.

original cube (i.e. the one produced by the reduction, Sect. 2.3, without further continuum subtraction).

A.3. Smooth nebula images and tessellation maps

In this Appendix, we present the smoothed nebula images (produced based on the optimally smoothed cube, Fig. A.2–A.9a) and the tessellation maps (Fig. A.2–A.9b) constructed following Appendix A.1 (Sect. 3.1.1) and A.2 (Sect. 3.1.2), respectively. The false-colour smooth images are generated using multicolourfits (Cigan 2019). Each colour represents a pseudo-narrow band Lyα image constructed from the optimally smoothed cube (Appendix A.1) in arbitrary wavelength range with the goal to show different kinematic structures. Blue, yellow and red are relatively from blue wing, middle and red wing of the Lyα emission, respectively. We note that the smoothed nebula images are only used as representation and demonstration of how the algorithm in Appendix A.1 works. They are not included in the analysis of this work. For MRC0316-257 and TN J0205+2242, we detected line emissions around their Lyα wavelength at isolated regions from the main nebula. We did not include these regions in to account due to its possible origin from companion galaxies, but show the spectra and region where they are extracted in Figs. A.3 and A.4.

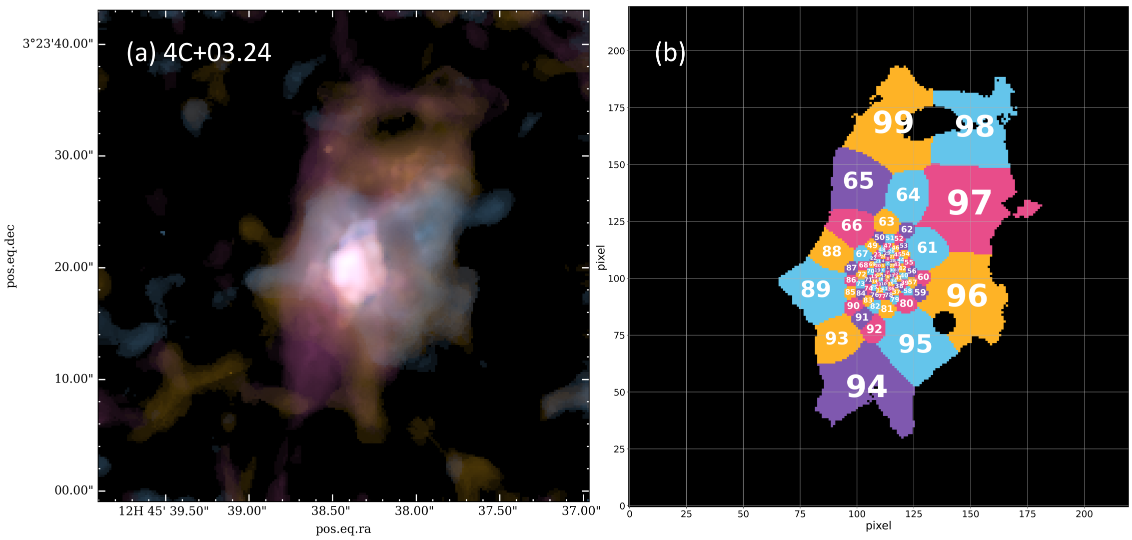

Fig. A.6. Smoothed nebula image (a) and tessellation map (b) of 4C+03.24. (a) The colour-composed image is created in a manner similar to that of Figure A.2a.

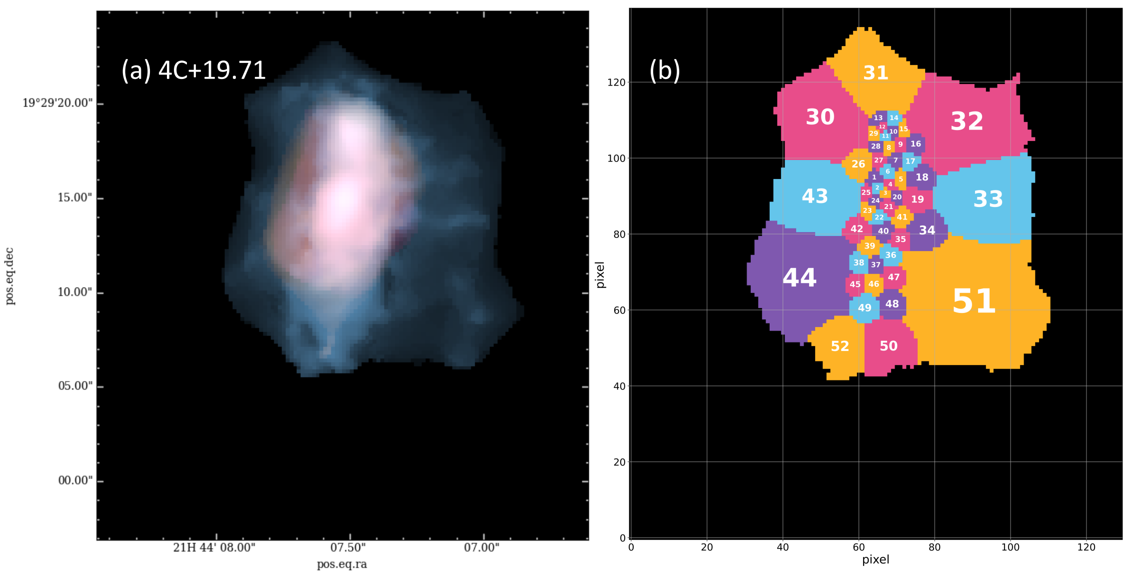

Fig. A.7. Smoothed nebula image (a) and tessellation map (b) of 4C+19.71. (a) The colour-composed image is created in a manner similar to that of Figure A.2a.

Wang, W., et al.: A&A 680, A70 (2023)

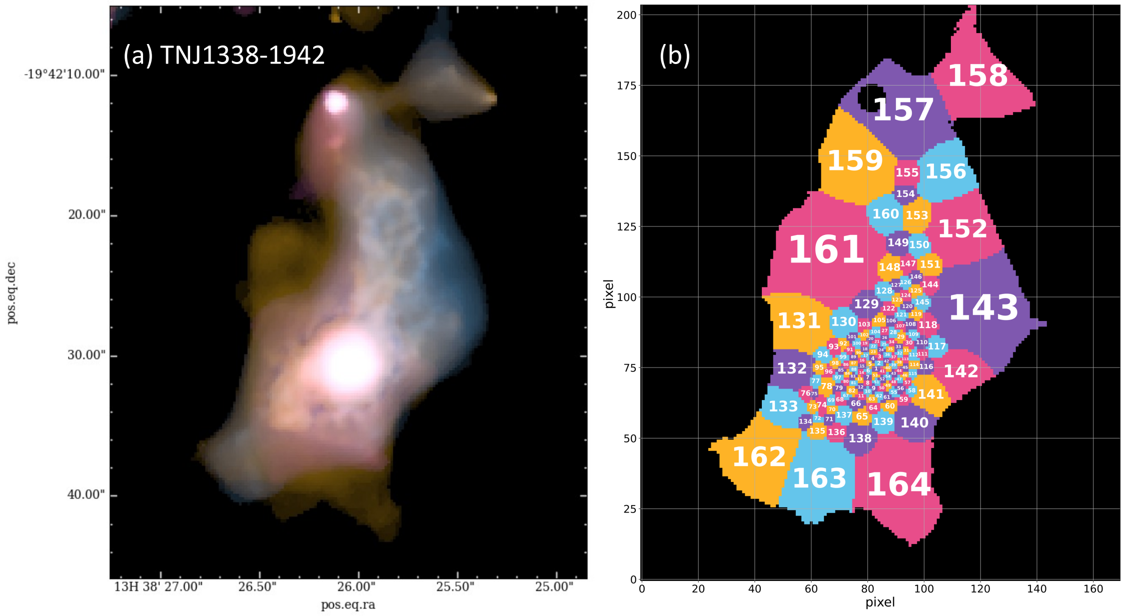

Fig. A.8. Smoothed nebula image (a) and tessellation map (b) of TN J1338-1942. (a) The colour-composed image is created in a manner similar to that of Figure A.2a.

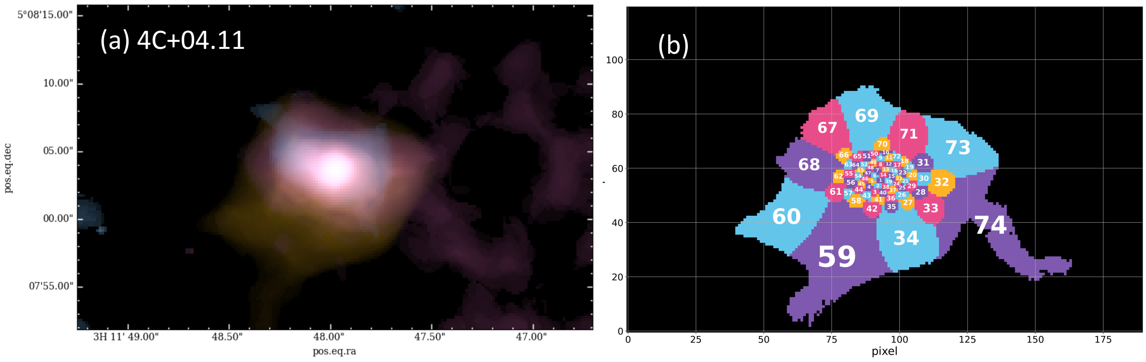

Fig. A.9. Smoothed nebula image (a) and tessellation map (b) of 4C+04.11. (a) The colour-composed image is created in a manner similar to that of Figure A.2a.

Appendix B: Fitting procedure

To minimise the uncertainties introduced by fitting the spectra in neighbour bin independently, and impact from foreground targets and the UV continuum, we have developed the following spatial fitting procedure after extracting spectra from the tessellation in Appendix A.2. In this way, we can link the fitting between adjacent bins to avoid un-physical jump in parameters:

To estimate the UV continuum , we firstly extract a narrow band image between the rest-frame N vλ1240 and O I + Si IIλ1305 from the data cube leaving a rest-frame 10 Å buffer at each end of the central wavelength of the emission line to avoid line emission contamination. This step is implemented to select which tessellated bins are affected by the continuum such that we can model it in the fitting. Hence, this wavelength range is chosen because it is a line-free region closet to Lyα which could be a relatively accurate estimation of the UV continuum emission of the radio galaxy: since the blue wing of Lyα is suffered from absorption. We use this continuum image and the tessellation map (Sect. 3.1.2) to determine which tiles have continuum emissions.

To determine the initial value of the spatial fitting, we secondly extract the 1D Lyα master spectrum from a $d = 1$ arcsec (25 spaxels) at the position of the AGN centre (Table 2) and fit it with Gaussian + Voigt model (Sect. 3.2.1, Fig.1a). In this way, the initial information of the absorbers (number, column density and positions) are determined. We note that for this fit a 0th-order polynomial for continuum and two Gaussian for both the systemic emission and broad (or blueshifted or redshifted) components are used.

To minimise the impact of undesired features, we thridly mask the strong 5577 Å sky-line, which affects 4C+03.24 and 4C+19.71 most, by 5 spectral resolution units. We also mask the foreground or background objects line emission wavelength range (none of them overlapped with the Lyα of the radio galaxy to our current knowledge) and replace with the noise from the cube variance extension (for example of the reported objects in the vincity of Lyα nebula see, e.g. Falkendal et al. 2021).

To get a the first spatial fit, we fourthly fit the spatial spectra from each tiles in the order determined in Appendix A.2 with the Least-square method. In the fitting, we pass the results from the previous tile fit to the next as initials to minimise the potential randomness introduced by fitting each spectra freely without any constrain. We note that (i) the constrains from the previous fit may be relaxed more if the ratio of the integrated observed fluxes between the tiles are significant ($\sim$ 50%) and/or the distance ratio is large (>1.1)[4] and/or the area of the tile is large ($> 9\pi$ arcsec^2); (ii) the Doppler parameter, b, (Tepper-García 2006) is set to a broad range (Kolwa et al. 2019; Wang et al. 2021b, $40 < b < 400\,\mathrm{km\,s^{-1}}$) because of the $b-N$ degeneracy (e.g. Silva et al. 2018b). We only constrain the range of column density, $N_{\mathrm{H\,I}}$. The continuum model is included in the fitting with a 0th-order-polynomial for tiles overlapped with continuum detected region determined in first step. A fixed step function with the step at the wavelength of the systemic Lyα is used for the highest redshift target, 4C+04.11, due to the heavily absorbed continuum on the blue-side which may be due to Lyα forest, e.g. Rauch (1998).

Due to the scattering nature of Lyα and presence of broad (outflow) components, it is important to select which region contains more than one emission component to better study the broader wing. We fit the set of spatial spectra two times: (i) first using 1-Gaussian only for the emission and (ii) then using 2-Gaussian for all spectra. In this way, we can do a simple χ^2 ratio selection between the 2-Gaussian versus the 1-Gaussian fitting results and select the tiles favour 2-Gaussian fit with a threshold of $\sim 0.80-0.98$ (depends on different targets). We point that the χ^2 value is not a robust measurement of the fitting quality (e.g. Andrae et al. 2010). For a quick test in our case, however, it is good enough to the first order. We note that for 4C+03.24, we stay with the 1-Gaussian fit for all tiles due to the complicated spatial variance of spectral shapes. We note that this selection is not crucial in this work since we do not distinguish and separately interpret different velocity components in the analysis. The purpose for this step is to consistently ensure that the non-single-Gaussian line shape is considered without missing flux.

Fifthly, we fit the spatial spectra with 2-Gaussian models for the tiles determined in the last step and 1-Gaussian for the others. The results from the previous steps are passed to the next as initial guesses. To keep consistence, we choose to use the same number of absorbers for the whole map due to the difficulties in determining where one absorber disappears. This is a good assumption to first order given that we observe most absorbers on large extent. For example in Fig. 4, we see the tiles at the nebula edge are also affected by absorbers. The column density of the absorbers is a free parameter during the fit. Given the degeneracy between the column density and Doppler parameter, b (Silva et al. 2018a), we leave the constraint of b to a broad range following Kolwa et al. (2019) (40 to $400\,\mathrm{km\,s^{-1}}$). The centroid (redshift) of the absorbers are also allowed to vary ($\Delta z \approx \pm 0.001$) except for 4C+04.11[5]. For spectra extracted from inner tiles ($\lesssim 10''$, with high S/N), we constrain their column densities to vary within a $\sim$ 2 dex range from the initial input. We ease the column density constrain for the absorbers from outer tiles with distance to AGN $\gtrsim 10''$ such that they can be given low column density ($\sim 10^{13}\,\mathrm{cm^{-2}}$). In this way, the absorbers at low S/N regions can have negligible impact (< 0.1 %) on the reconstructed flux. We use the same number of absorbers reported in previous works for some of our targets (MRC 0943-242, TN J0121+1320, TN J1338-1942 Wilman et al. 2004; Swinbank et al. 2015). Otherwise, we use the number determined in the first step of 1D spectra fitting. For TN J0121+1320, we use 3 absorbers instead of 2 as in Wilman et al. (2004). For 4C+04.11, we use 9 absorbers (instead of 7 as in Wang et al. (2021b)) with 7 of them fixed to the redshifts determined in 1D spectra fit.

Finally, we run MCMC sampling (Foreman-Mackey et al. 2013) using the results from last step as initials and with larger boundaries to probe the probability distribution of the fitted parameters and uncertainties.

We point out one caveat that the low S/N (especially for the tiles at the edge) will affect the reconstructed intrinsic Lyα flux. We implemented a test where we artificially decrease the S/N of the master spectrum and do the absorption correction fit. It shows that the reconstructed intrinsic flux can vary by a factor of ~ 2 when the S/N decreases by one dex (e.g. ~ 100 to ~ 10). This result is based on the fact that we have a relatively good initial guess for the fit. We note that in the aforementioned fitting procedure the fitting parameters are constrained by the neighbouring tiles to have them physically linked. There may still be the chance that the low S/N will affect the fitted flux leading to

[4] Distance ratio, $\frac{r_1+r_2}{d_{1,2}}$, is the ratio between the sum of the radii, $r_1 + r_2$, of the two tiles (estimated by $r = \sqrt{A/\pi}$, where A is the area of the tile) and the distance between the geometric centre of the two tiles, $d_{1,2}$.

[5] For this case, we follow the procedure in Wang et al. (2021b) and fix the positions of five absorbers on the blue low S/N wing to the value determined from the Master spectrum.

over-correction. This may be the case for 4C+04.11 (Fig. 13). We present the flux ratio maps between intrinsic and observed in Appendix C which indicate this possibility ($\sim$ 50 for the tiles at the edge).

Appendix C: Supplementary maps

We show the intrinsic Lyα maps with selected spectra for MRC0943-242, MRC0316-257, 4C+19.71, TNJ1338-1942 and 4C+04.11 in Fig. C.1, C.2, C.3, C.4 and C.5, respectively. The spatial study of the Lyα nebulae for these sources with MUSE were published previously (e.g. Gullberg et al. 2016; Vernet et al. 2017; Falkendal et al. 2021; Swinbank et al. 2015; Wang et al. 2021b). In this paper, we performed a consistent analysis for the full sample with the new method of correcting for absorption. With the individual spectra mostly showing the tiles at larger distance away from the AGN, we can find that the absorption features are observed nearly across the entire nebula.

To better show the difference before and after absorption correction, we present the observed surface brightness maps and flux ratio maps between the intrinsic flux and observed flux. For the observed flux in each tiles, we use the flux integrated from v_{05} to v_{95} and show in Fig. C.6a for each target. For consistency, the v_{05} (and v_{95}) is determined based on the intrinsic line since the v_{05} (and v_{95}) of the observed lines in low S/N regions are affected by noise more. To ensure the intrinsic and observed surface brightness are comparable as in Fig. C.6b, we take the ratio between the intrinsic and observed flux all integrated between v_{05} and v_{95}. Generally, the tiles at the outskirt of the nebulae having larger ratios (> 10). The observed nebular properties derived in the main text are based on the $v_{05}-v_{95}$ observed maps obtained here.

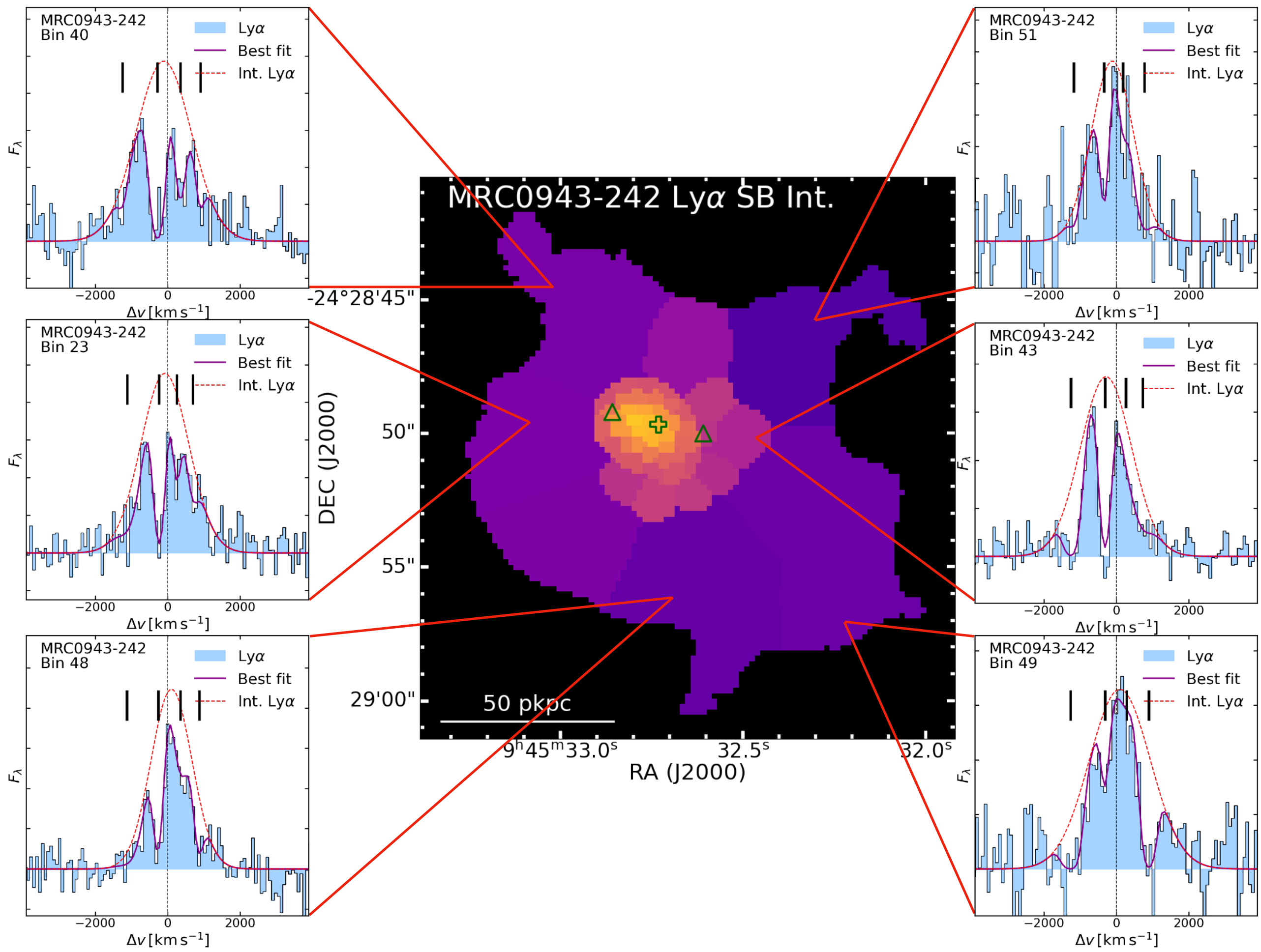

Fig. C.1. Similar to Fig. 2–4, but for MRC0943-242.

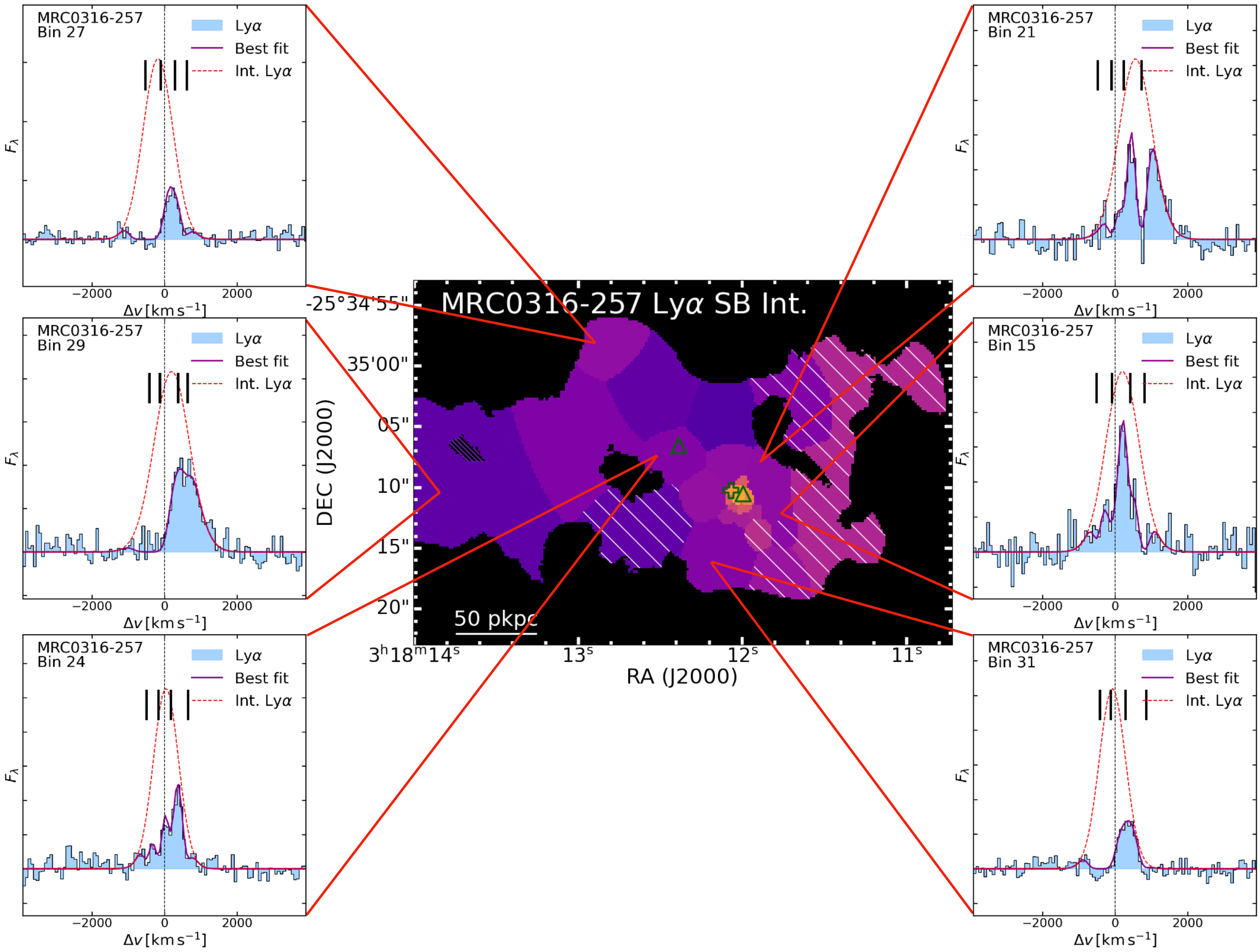

Fig. C.2. Similar to Fig. 2–4, but for MRC0316-257.

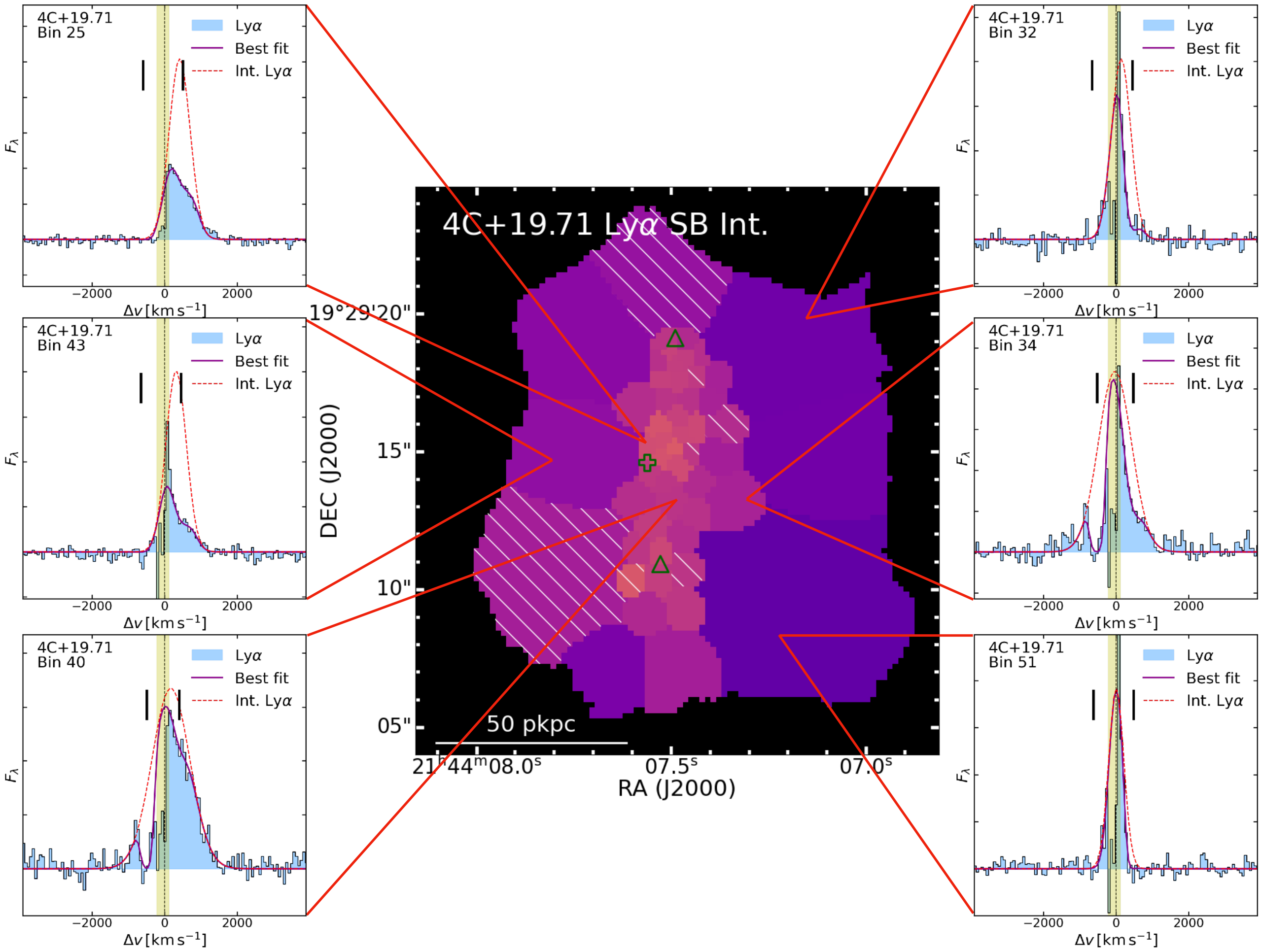

Fig. C.3. Similar to Fig. 2–4, but for 4C+19.71.

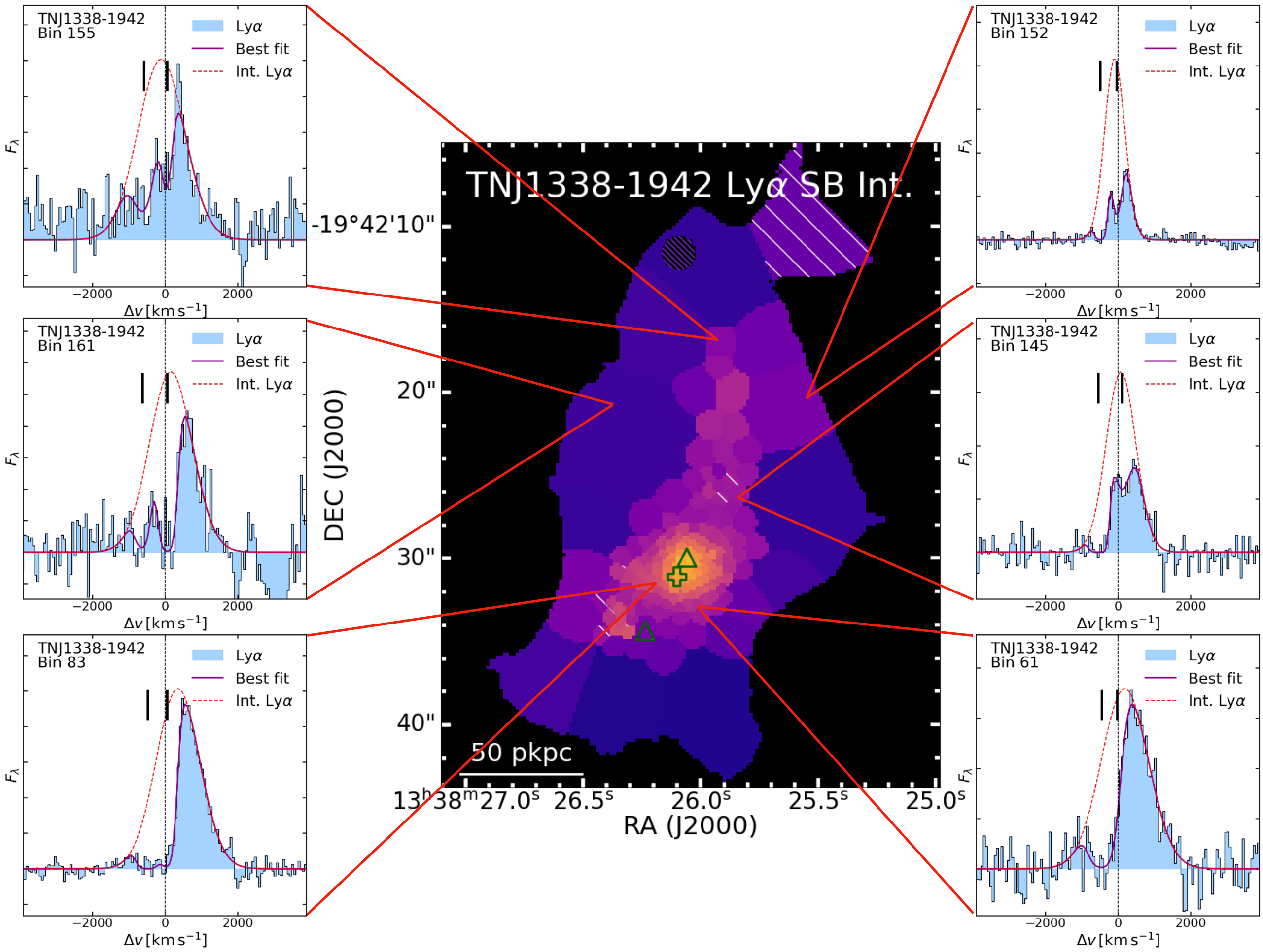

Fig. C.4. Similar to Fig. 2–4, but for TNJ1338-1942.

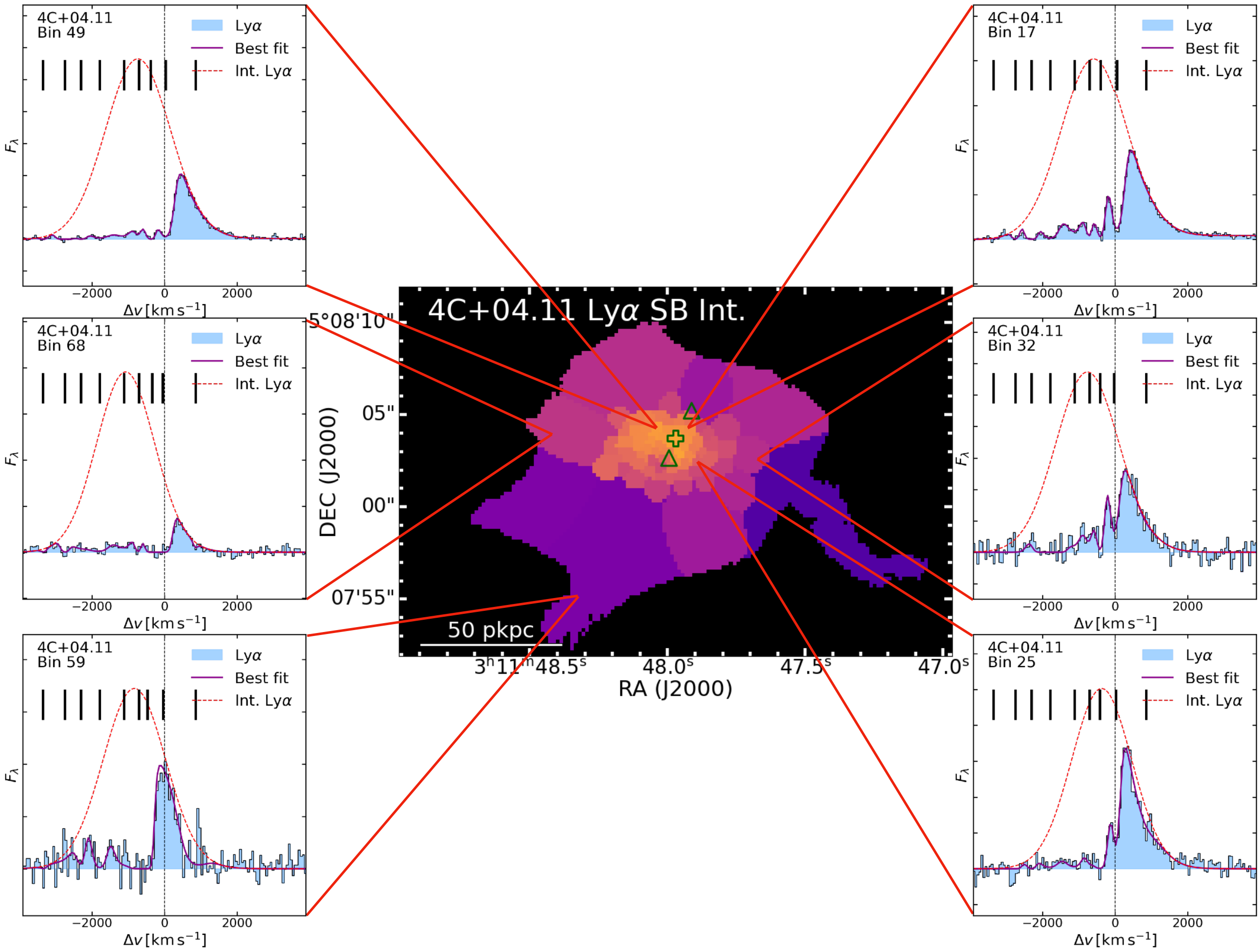

Fig. C.5. Similar to Fig. 2–4, but for 4C+04.11.

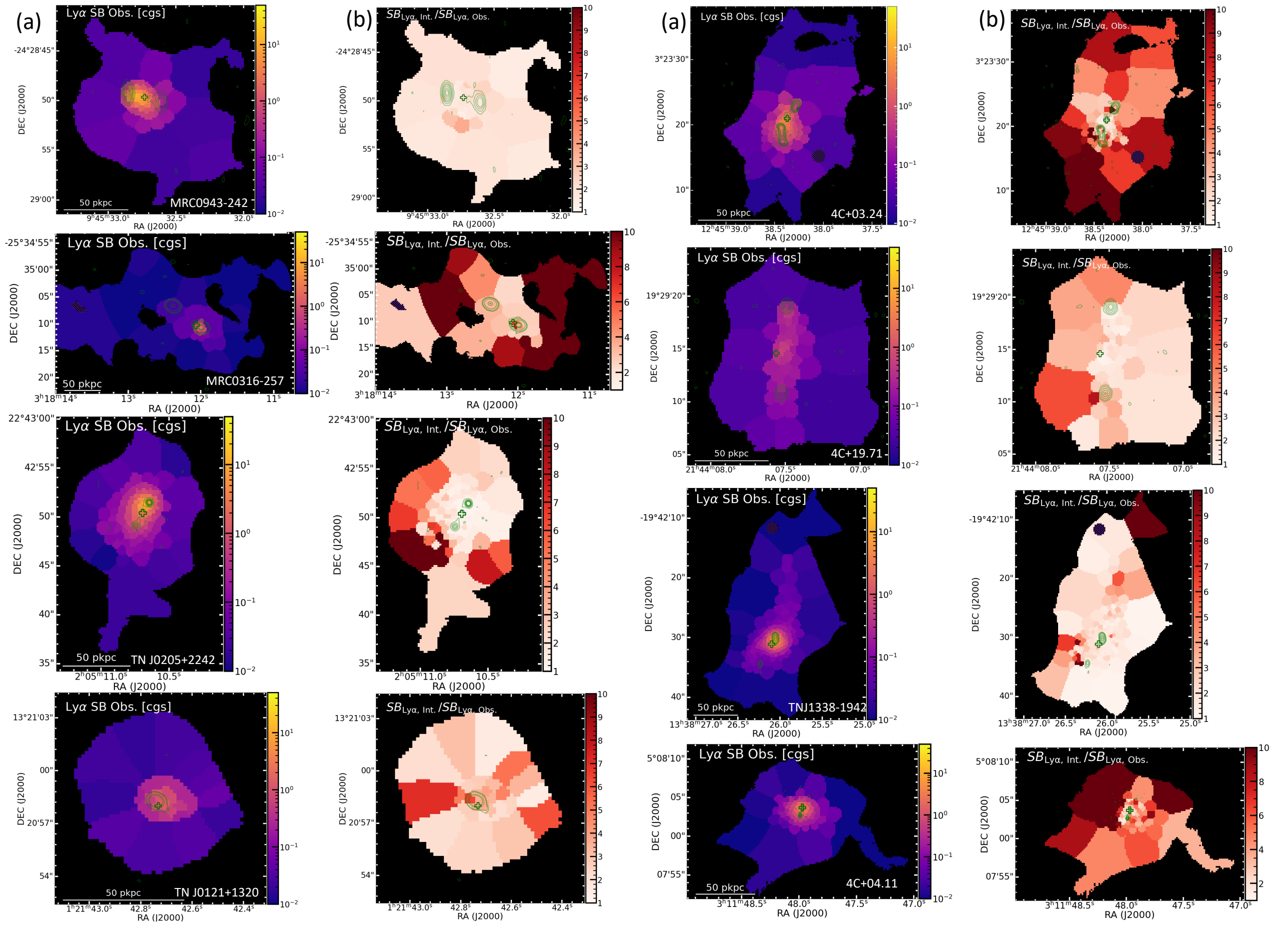

Fig. C.6. (a) Observed surface brightness maps in the unit of 10^{-16} erg s^{-1} cm^{-2} arcsec^{-2}. (b) Flux ratio maps of intrinsic and observed surface brightness. The green cross and contours are the same as Fig. 1 for individual targets, respectively.

Appendix D: Supplements of nebula radial profile and morphology analysis

Table D.1. Position angle and hot spot distance of the radio jet.

HzRG	$\mathrm{PA_{radio}}^{\dagger}$ deg	$r_{\mathrm{app.}}{}^{*}$ arcsec	$r_{\mathrm{rec.}}{}^{*}$ arcsec
MRC 0943-242	74	1.79	1.76
MRC 0316-257	53	5.56	1.15
TN J0205+2242	150	1.47	1.24
TN J0121+1320	90	0.82[a]	0.82[a]
4C+03.24	146	2.00[b]	1.75[b]
4C+19.71	176	3.82	4.58
TN J1338-1942	150	3.78	1.18
4C+04.11	158	1.15[c]	1.70[c]

Notes. [†]Jet position angle. This is measured east from north. We note that we do not quantify the uncertainties which could be ±1 deg. [*]Distance between the hot spot and the AGN position. $r_{\mathrm{app.}}$ and $r_{\mathrm{rec.}}$ are distance for approaching and receding hot spot, respectively. [a]The radio emission of TN J0121+1320 is spatially unresolved. The 'hot spot' distance is represented by the distance from the host galaxy position to the either side of 3σ contour of the radio image along the east-west direction. [b]Approaching hot spot is A1 and receding hot spot is B1 (named after van Ojik et al. 1996). [c]Approaching hot spot is knot8 and receding hot spot is knot1 (named after Parijskij et al. 2014).

In this appendix, we show the supplementary information accompanied with studying nebulae radial profiles and morphology.

We present the annuli used in Sect. 4.2.1 in Fig. D.1. For each targets, the smallest one aperture has the radius equals to 0.75 of its seeing. The radii are in logarithmic steps from centre to outskirt, and the values extract from the annuli are presented in Table D.2.

For the directional radial surface brightness profile analysed in Sect. 4.2.2, it is extracted in half annuli along approaching and receding directions (Fig. 8) with the same step as Fig. D.1.

The position angle of the radio axis is obtained from the two jet hot-spot positions (e.g. van Ojik et al. 1996; Carilli et al. 1997; Pentericci et al. 2000; Parijskij et al. 2014, and unpublished radio maps) and presented in Table D.1. For TN J0121+1320 which has a compact radio emission, we assign an east-west jet position angle to it. We also present the distance of the radio hot spot from the AGN position in Table D.1. This is the value shown in Fig. 6 and 7 (after converted to ckpc). The hot spot is determined to be located at position of the brightest radio emission. 4C+03.24 and 4C+04.11 show multiple radio flux peaks in their radio data. We calculate the jet position angle and hot spot distance based on A1 and B1 knots for 4C+03.24 (named after van Ojik et al. 1996) and knots 1 and 8 for 4C+04.11 (named after Parijskij et al. 2014). We note that the radio jet of TN J0121+1320 is unresolved. Hence, we use the farthest distance reached by the jet (i.e. 3σ contour of the radio image) along the jet direction as a proxy.

We show the exponential and power law fitted parameters (Sect. 4.2.3) of the circularly averaged and directional surface brightness profiles in Table D.3. In Fig. D.2, we show the position-velocity diagram of the observed and intrinsic cubes along the jet direction. This can be used as a direct comparison with Villar-Martín et al. (2003). On each target, we also mark the largest extent of the radio lobes in both directions in horizontal dashed lines. This is determined as the distance from the AGN position along the direction of the jet position angle to the farthest position reached by the $3 sigma$ radio flux contour. We note that the broader line width observed visually is due to the contrast between the high and low surface brightness parts. We find in some cases (e.g. 4C+04.11 and TN J1338-1942) that there is a sharp surface brightness drop at the distance of the radio jet boundary. A discontinuity in the line width and surface brightness of the Lyα nebulae across the extent of the radio source has been previously reported in Villar-Martín et al. (2003). The changes is not as sharp as shown in D.2. The sharpness seen in the intrinsic panels is due to tessellation as it is the transition from high to low surface brightness part. Hence, we assure that these are not all artificial effect due to our analysis methods.

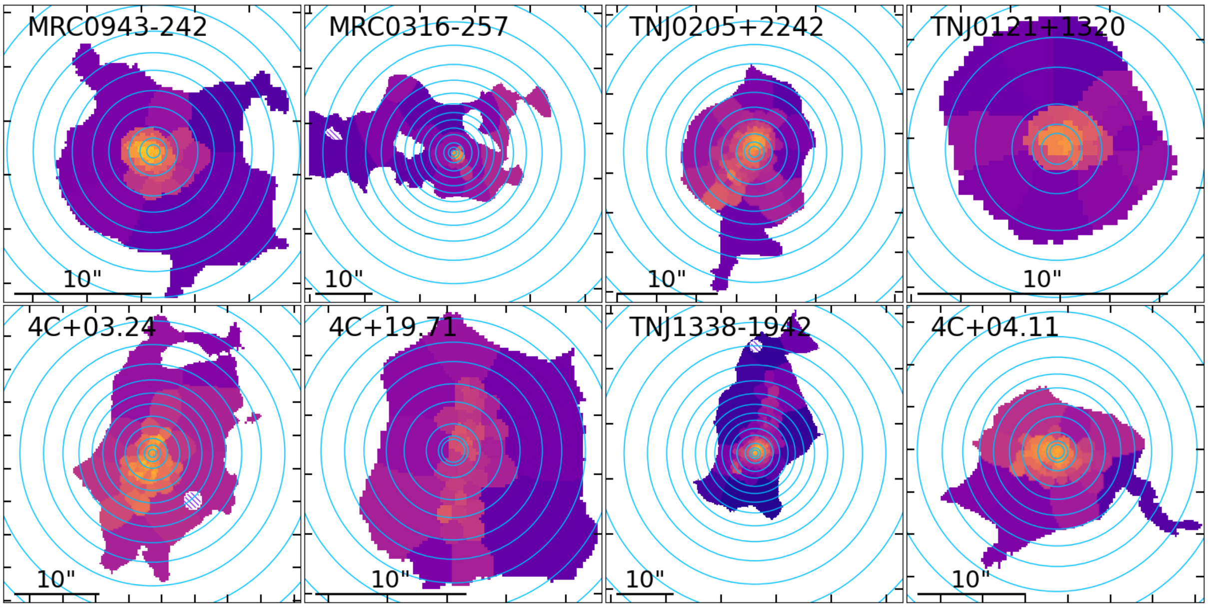

Fig. D.1. Circular apertures for radial profile (Sect. 4.2.1) extraction on top of intrinsic surface brightness maps (Fig. 1a) of the HzRGs sample. In each panel, the blue concentric annuli show the apertures where the radial profile is extracted. The annuli are centred around the host galaxy (central AGN) position (Table 2). The radii of the annuli in each panel are the same in the unit of arcsec for consistence except the smallest radius which is set to be 0.75× seeing for each target. The black bar at the bottom left corner of each panel indicate the 10 arcsec scale.

Table D.2. Intrinsic surface brightness from circular aperture

R [arcsec]	MRC0943-242	MRC0316-257	TN J0205+2242	TN J0121+1320	4C+03.24	4C+19.71	TN J1338-1942	4C+04.11
	$(1+z)^4$SB [10^{-16} erg s^{-1} cm^{-2} arcsec^{-2}]							
0.0-r_s†	2621.4	1534.1	1886.6	1452.9	2955.1	261.9	5177.9	6464.6
r_s† -1.0	1792.0	833.8	1764.7	889.7	2102.8	224.9	3617.2	4686.2
1.0-1.8	623.3	390.1	953.4	250.2	1884.4	195.4	1829.5	2659.6
1.8-3.3	95.3	60.9	232.4	48.5	1020.3	130.1	385.0	950.4
3.3-4.5	24.6	36.4	120.3	38.6	465.3	105.4	106.4	367.7
4.5-6.0	15.2	31.5	97.2	25.4	227.4	68.3	58.4	229.6
6.0-7.3	14.7	32.2	87.1	0.0	194.8	51.3	29.2	168.9
7.3-8.9	13.1	35.9	45.0	0.0	142.9	43.0	25.0	97.6
8.9-10.8	11.9	38.5	23.3	0.0	117.3	25.1	26.3	65.5
10.8-13.2	13.0	37.2	23.3	0.0	82.8	20.7	33.9	58.3
13.2-16.0	0.0	38.3	23.3	0.0	65.0	0.0	33.9	31.2
16.0-19.5	0.0	33.0	0.0	0.0	45.5	0.0	17.0	0.0
19.5-23.8	0.0	14.5	0.0	0.0	0.0	0.0	29.2	0.0
23.8-28.9	0.0	12.3	0.0	0.0	0.0	0.0	36.6	0.0

Notes. $^\dagger r_s$ = 0.75× seeing which is specified for each target Table 1. The median seeing is 0.75 arcsec. Intrinsic surface brightness values extracted from circular annuli following Fig. D.1. To be consistent, the first column gives the radii of each annulus in the unit of arcsec instead of ckpc. The reported surface brightness values are corrected for cosmological dimming.

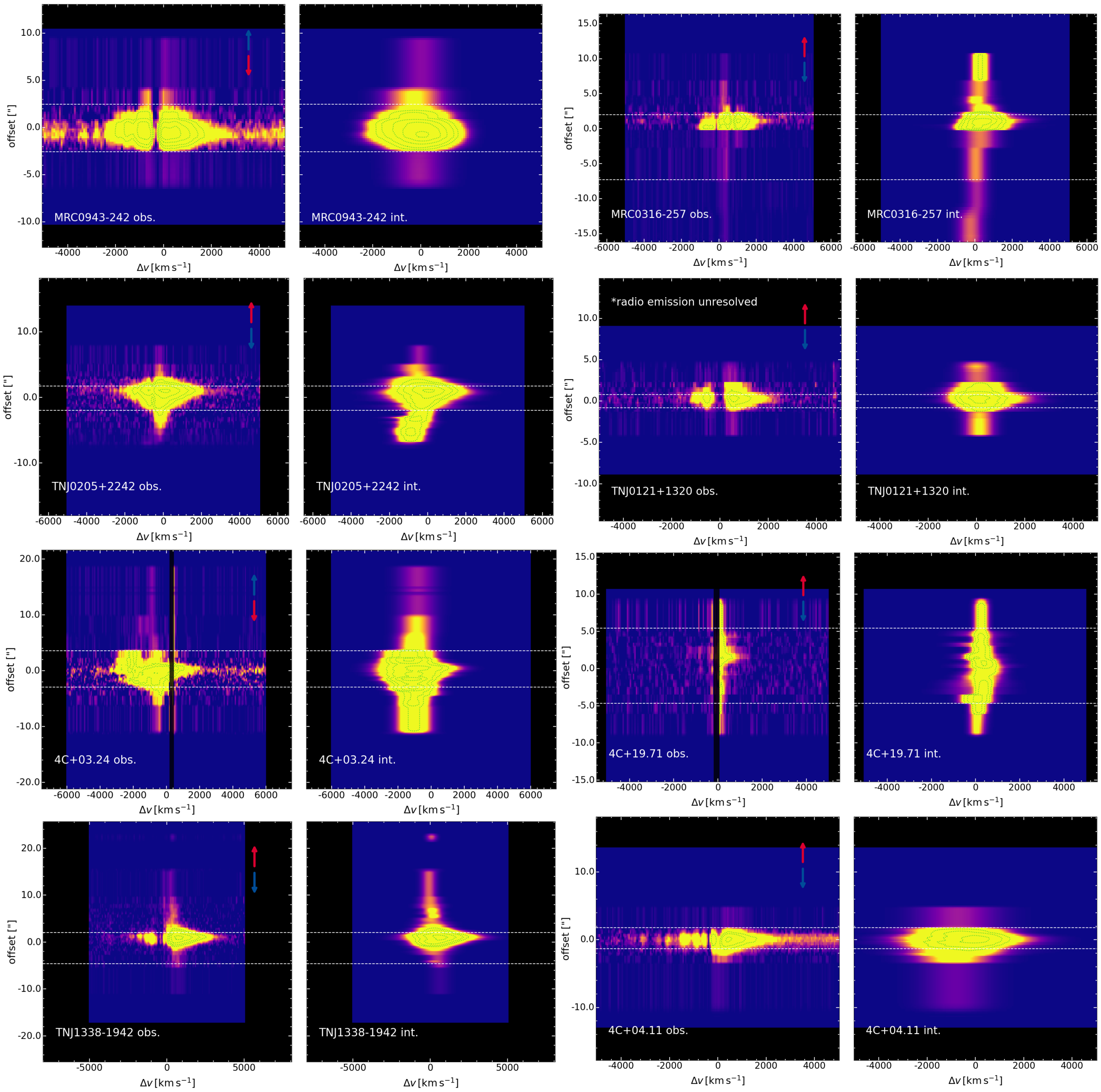

Fig. D.2. Lyα position-velocity diagrams (i.e. 2D spectra) of our sample targets extracted along the radio jet axis. For each target, the left panel shows the diagram constructed from tessellated observed cube (not continuum-subtracted for the host galaxy) and the right panel shows the diagram from absorption-corrected intrinsic cube. The zero offset is set to the position of the central AGN (Table 2). The direction of approaching and receding sides of the jet (see Sect. 2.1.3) are marked in the left panel by the blue and red arrows, respectively. The white horizontal dashed lines represent the furthest extent of the jet. The dotted green contours are given in arbitrary steps which are used to guide the eye for the high brightness part. The vertical black shaded regions in the observed position-velocity diagrams of 4C+03.24 and 4C+19.71 indicate the wavelength ranges affected by the 5577 Å sky-line.

Table D.3. Fit parameters of surface brightness profiles.

HzRG	r_h † pkpc	C_e * 10^{-16} cgs	r_b ‡ pkpc	α §
MRC 0943-242	6.9±0.2	20.7±1.0	39.8±1.5	-0.24±0.18
" " app.	5.6±0.2	18.4±1.1	32.0±1.3	-0.13±0.15
" " rec.	7.5±0.2	25.8±1.0	42.9±1.3	-0.15±0.19
MRC 0316-257	7.0±0.6	8.9±1.2	27.3±3.2	-0.62±0.24
" " app.	1.3±0.3	69.0±70.0	7.7±1.0	-0.46±0.07
" " rec.	7.5±3.3	14.2±15.7	31.6±14.4	-0.01±0.49
TN J0205+2242	48.9±30.4	5.7±0.4	10.9±21.4	-1.90±0.58
" " app.	8.8±2.0	6.2±0.7	13.4±10.8	-1.52±0.26
" " rec.	10.8±3.1	8.3±0.3	48.7±0.7	-0.97±0.14
TN J0121+1320	9.8±1.9	5.6±1.2	6.2±10.0	-2.05±0.71
" " app.	4.4±1.0	8.9±2.3	19.6±6.6	-0.67±0.76
" " rec.	5.1±1.3	10.2±2.1	10.9±9.3	-2.16±0.75
4C+03.24	17.6±1.8	7.9±0.6	20.0±14.9	-1.64±0.21
" " app.	11.2±0.9	10.3±0.9	38.5±4.2	-0.87±0.18
" " rec.	27.7±2.0	6.5±0.4	23.4±10.8	-1.67±0.18
4C+19.71	29.5±7.2	0.8±0.1	23.1±9.7	-1.20±0.16
" " app.	63.6±20.3	0.4±0.1	38.1±7.8	-1.88±0.37
" " rec.	23.3±24.5	1.0±0.2	15.1±15.3	-1.24±0.35
TN J1338-1942	7.3±0.3	13.6±0.7	41.0±2.7	-0.12±0.26
" " app.	3.6±7.0	20.7±8.8	7.5±1.7	-2.10±0.07
" " rec.	7.3±8.0	19.0±5.1	40.0±14.7	-0.52±0.77
4C+04.11	8.2±1.5	11.8±1.3	15.2±11.7	-2.04±0.24
" " app.	9.9±1.0	11.0±0.9	38.9±12.0	-1.77±0.37
" " rec.	7.5±1.6	11.6±1.6	16.0±8.3	-2.14±0.28

Notes. See Section 4.2.3 for the fitting equations (Eq. 2): †Scale length of the exponential profile. *Normalisation parameter of the exponential profile. The cgs unit is erg s^{-1} cm^{-2} $arcsec^{-2}$. ‡Distance where inner exponential profile changes to power law profile. §Power law index.

Appendix E: MRC0316-257 systemic redshift

For MRC0316-257, two velocity components of the He II emission are detected in our MUSE observation which are also separated spatially. The one detected at the position of the X-ray emission peak from *Chandra* observation (Table 2) is believed to be the systemic one while the one at north-west position that is coincident with UV continuum emission peak may trace jet-gas interaction. We show the UV continuum map of MRC0316-257 and the fits of the two He II spectra in Fig. E.1. We note that the UV continuum map is constructed from the MUSE cube using the wavelength in observed frame between N Vλ1240 and O I+Si IIλ1305 which is a emission-line-free region of HzRGs (McCarthy 1993). The bright continuum emission object east of the central AGN position peak is a foreground galaxy (Vernet et al. 2017). We report here that the systemic redshift detected is $z_{\rm sys} = 3.1238 \pm 0.0002$ and the redshift of the component at the UV continuum peak is $z_{\rm red} = 3.1323 \pm 0.0002$ which is redshifted of $v = 620\,{\rm km\,s^{-1}}$ from the systemic one. The velocity gradient of the He II agrees with the Lyα v_{50} (Fig. 1c) and [O III]λ5007 (Nesvadba et al. 2008) within the scope of the jet. The UV continuum at this position may suggest the younger stellar population distribution. Combine with the jet kinematics, we may seeing jet induced star forming activities. However, there is also the possibility that the UV continuum could be produced by the inverse Compton processes. The redshifted He II near the west radio lobe could then be due to the ionisation emission from the shock region exerting on the un-shocked gas. This is supported by the relatively narrow with of the redshift He II (FWHM $\sim 600\,{\rm km\,s^{-1}} < 1000\,{\rm km\,s^{-1}}$) which could indicate that is has not been impacted by shocks (Best et al. 2000; Allen et al. 2008). We note that a detailed verification for this scenario is beyond the scope of this paper which involves spectral ageing inspection of the radio jet hot-spot (e.g. Harwood et al. 2013). Hence, we simply point these possibilities and leave them to future study with multi-wavelength observations combined.

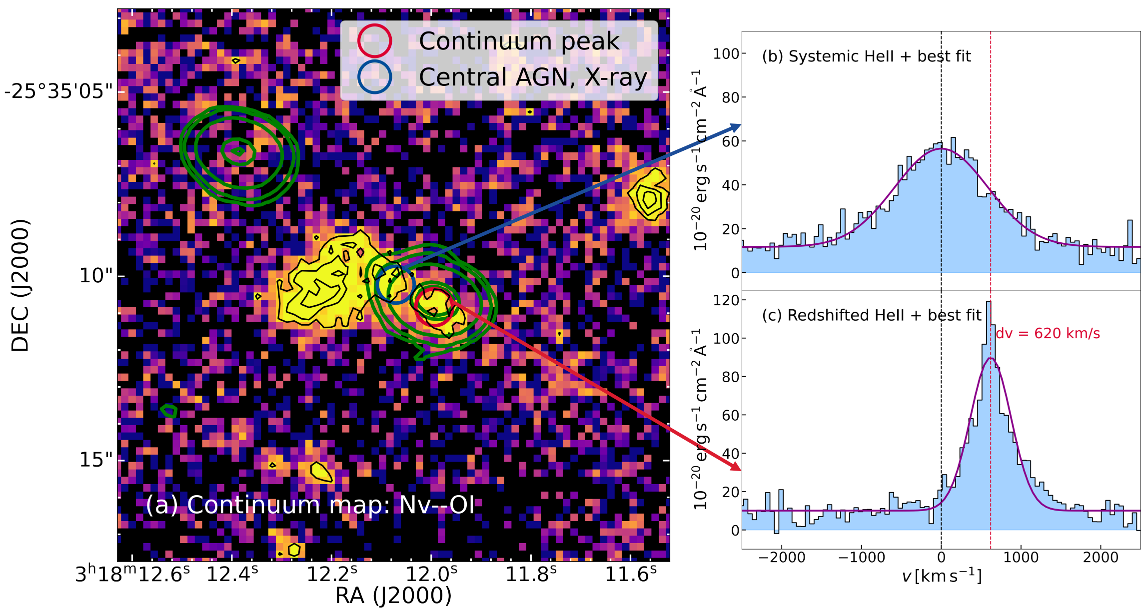

Fig. E.1. UV continuum map around MRC0316-257 (a) and He II spectra from the X-ray position (central AGN, b) and UV continuum peak position (c). The UV continuum map is collapsed between the observed wavelength of N Vλ1240 and O I+Si IIλ1305. The green contours show the radio jet in the same format as Fig. 1cd. The black contours in the step of [3σ, 5σ, 7σ, ...] trace the UV continuum emission, where σ is the background standard deviation. Blue and red circular regions indicate the $r = 0.5$ arcsec apertures where the systemic and redshifted He II spectra are extract, respectively. The right panels (b, c) show the He II spectra (histogram) along with their best Gaussian fitting (dark magenta line) results. The velocity zero (vertical black dotted line) in both panels is the systemic redshift. In the panel(c), we also mark the velocity shift (vertical red dotted line) of the redshifted He II emission with respect to the systemic one.

4

JWST discovers an AGN ionization cone but only weak radiatively driven feedback in a powerful $z \approx 3.5$ radio-loud AGN

Authors:
Wuji Wang, Dominika Wylezalek, Carlos De Breuck, Joël Vernet, David S. N. Rupke, et al.

Published in *A&A 683, A169 (2024)*.

Wuji Wang is the principal author of this article. The software package used was developed by Prof. Rupke and Dr. Vayner. Wuji Wang, Dr. Wylezalek, Dr. De Breuck, and Dr. Vernet had the idea for the paper. Wuji Wang performed data process with the assistance from Dr. Vayner. Wuji Wang conducted calculations and analysis of the observations. Wuji Wang produced all the figures and tables and wrote the manuscript. All authors collaborated with corrections and suggestions to the manuscript, and Wuji Wang performed the last improvements during the review process. Prof. Rupke improved English writing of this article.

A&A, 683, A169 (2024)
https://doi.org/10.1051/0004-6361/202348531

Astronomy & Astrophysics

JWST discovers an AGN ionization cone but only weak radiatively driven feedback in a powerful $z \approx 3.5$ radio-loud AGN

Wuji Wang[1], Dominika Wylezalek[1], Carlos De Breuck[2], Joël Vernet[2], David S. N. Rupke[3], Nadia L. Zakamska[4], Andrey Vayner[4], Matthew D. Lehnert[5], Nicole P. H. Nesvadba[6], and Daniel Stern[7]

[1] Astronomisches Rechen-Institut, Zentrum für Astronomie der Universität Heidelberg, Mönchhofstr. 12-14, 69120 Heidelberg, Germany
e-mail: wuji.wang@uni-heidelberg.de; wuji.wang_astro@outlook.com
[2] European Southern Observatory, Karl-Schwarzchild-Str. 2, 85748 Garching, Germany
[3] Department of Physics, Rhodes College, 2000 N. Parkway, Memphis, TN 38112, USA
[4] Department of Physics and Astronomy, Bloomberg Center, Johns Hopkins University, 3400 N. Charles Street, Baltimore, MD 21218, USA
[5] Univ. Lyon, Univ. Lyon1, ENS de Lyon, CNRS, Centre de Recherche Astrophysique de Lyon UMR5574, 69230 Saint-Genis-Laval, France
[6] Université de la Côte d'Azur, Observatoire de la Côte d'Azur, CNRS, Laboratoire Lagrange, Bd de l'Observatoire CS 34229, 06304 Nice Cedex 4, France
[7] Jet Propulsion Laboratory, California Institute of Technology, 4800 Oak Grove Drive, Pasadena, CA 91109, USA

Received 9 November 2023 / Accepted 13 January 2024

ABSTRACT

We present the first results from a JWST program studying the role played by powerful radio jets in the evolution of the most massive galaxies at the onset of cosmic noon. Using NIRSpec integral field spectroscopy, we detected 24 rest-frame optical emission lines from the $z = 3.5892$ radio galaxy 4C+19.71, which contains one of the most energetic radio jets known, making it perfect for testing radio mode feedback on the interstellar medium (ISM) of a $M_\star \sim 10^{11}\,M_\odot$ galaxy. The rich spectrum enables line ratio diagnostics, showing that the radiation from the active galactic nucleus (AGN) dominates the ionization of the entire ISM out to at least 25 kpc, the edge of the detection. Subkiloparsec resolution reveals filamentary structures and emission blobs in the warm ionized ISM distributed on scales of ~5 to ~20 kpc. A large fraction of the extended gaseous nebula is located near the systemic velocity. This nebula thus may be the patchy ISM that is illuminated by the AGN after the passage of the jet. A radiative-driven outflow was observed within ~5 kpc from the nucleus. The inefficient coupling ($\lesssim 10^{-4}$) between this outflow and the quasar and the lack of extreme gas motions on galactic scales are inconsistent with other high-z powerful quasars. Combining our data with ground-based studies, we conclude that only a minor fraction of the feedback processes is happening on <25 kpc scales.

Key words. galaxies: evolution – galaxies: high-redshift – galaxies: ISM – galaxies: jets – quasars: emission lines – quasars: individual: 4C+19.71

1. Introduction

Active galactic nucleus (AGN) feedback can be categorized into either quasar mode, where the output from the supermassive black hole (SMBH) is coupled radiatively to the gas, or radio mode, where the feedback is due to the kinetic energy of the jet (e.g., Fabian 2012; Harrison 2017). The quasar mode is known to be prevalent (e.g., Harrison et al. 2014). The radio mode also plays an important role in AGN–gas interactions, leading to quenching. This is especially true in massive galaxies in the early Universe, as shown by both numerical simulations and observations (e.g., Heckman & Best 2014; Mukherjee et al. 2018; Kondapally et al. 2023). Despite the relatively short lifetime of a powerful jet (~10^7 yr), observations do indeed indicate that it can still significantly impact the host galaxy (e.g., total energy output by the jet $\gtrsim 10^{60}$ erg, Nesvadba et al. 2006; Miley & De Breuck 2008). Relativistic jets trigger shocks and drive outflows through an expanding overpressured bubble (e.g., Begelman & Cioffi 1989). While hydrodynamic simulations demonstrated that jets have the ability to interact with the interstellar medium (ISM) out to several kiloparsecs (e.g., creating turbulence, driving outflows, and compressing the gas, Dugan et al. 2017; Mukherjee et al. 2021), observations paint a more complicated picture. Specially, jet–ISM interactions are found to be different between AGN with intermediate radio power ($L_{1.4\,\mathrm{GHz}} = 10^{23-25}\,\mathrm{W\,Hz^{-1}}$, e.g., Mullaney et al. 2013) and those with a higher power (e.g., Mukherjee et al. 2016). Moreover, it is difficult to study the feedback mechanisms of the most powerful jetted AGN due to observational limitations and the simultaneous presence of energetic, quasar mode feedback.

High-redshift radio galaxies (HzRGs) are the best targets to test AGN feedback in massive host galaxies (~$10^{11}\,M_\odot$, De Breuck et al. 2010) because the gas, dust, and stellar populations in their host galaxies can be observed without contamination from the bright, point-like quasar light. In contrast to low-z, where radio mode AGN are believed to have low black hole accretion rates with inefficient radiative luminosity, HzRGs are observed to have both a vigorous radio mode and quasar mode energy output (e.g., Vernet et al. 2001; Nesvadba et al. 2007, 2017a,b). There are numerous studies focused on the outflows on scales from several to tens of kiloparsecs for both low- and high-redshift radio galaxies, which find evidence of them being jet driven (Tadhunter et al. 2001, 2007; Nesvadba et al. 2006, 2007). A closer look (scales of tens of parsecs) at the feedback in the vicinity of radio AGN is possible at low-z (e.g., Tadhunter et al. 2003). However, spotting the warm, ionized quasar outflow around cosmic noon (Madau & Dickinson 2014) down to subkiloparsec scales is challenging. Therefore, it is still unclear how energetic jet mode and quasar mode feedback couple with the ISM, how efficient these mechanisms are in driving outflows, and on which scales the different feedback mechanisms dominate. All of these are critical issues to be addressed before we can achieve a deeper understanding of the quenching of star formation in these massive host galaxies (Falkendal et al. 2019).

We can now finally take a step forward thanks to the Near Infrared Spectrograph (NIRSpec; Jakobsen et al. 2022) on board JWST, which provides an order of magnitude improvement in sensitivity. At least for HzRGs, there is evidence that the morphology and/or kinematics of the ionized ISM and even circumgalactic medium (CGM) gas are impacted by jets (Nesvadba et al. 2008, 2017a; Falkendal et al. 2021; Wang et al. 2023), which may indicate their role in feedback. However, the situation may be different when using deeper observations (e.g., Wylezalek et al. 2017). For example, how does the ISM of HzRGs look in the vicinity of and inside the host galaxies (e.g., ~10 to 20 kpc). NIRSpec integral field unit (IFU) observations of powerful quasars at cosmic noon have already revealed the detailed ionization mechanisms and quantified the outflow rates on galactic scales (e.g., Wylezalek et al. 2022; Vayner et al. 2023, 2024). NIRSpec will revolutionize our view of the inner ISM of HzRGs where the detailed physics are still unclear. A resolution-matched comparison can finally be done for high- and low-z radio AGN. NIRSpec IFU will also enable observational tests of simulated jet feedback (e.g., Mukherjee et al. 2016) in the early Universe.

In this work, we present the first JWST view of the ionized ISM of a $z \sim 3.5$ radio-loud AGN. In Sect. 2, we describe the observations and data processing. We then show in Sect. 3 the morphology of the warm ionized gas and identification of the observed optical emission lines from the extracted spectra. Finally, we discuss the impact of the jet on the ISM using line-ratio diagnostics and summarize in Sect. 4. Throughout this paper, we assume a flat Λ cosmology with $H_0 = 70\,\mathrm{km\,s^{-1}\,Mpc^{-1}}$ and $\Omega_m = 0.3$. Following this cosmology, 1 arcsec = 7.25 kpc at the redshift of 4C+19.71. Throughout this work, we use $z = 3.5892 \pm 0.0004$ as determined from atomic carbon, [C I](1−0) ($\nu_{\rm rest} = 492.16$ GHz), as the systemic redshift (Falkendal et al. 2021; Kolwa et al. 2023). Due to the relatively large synthesized beam ($1.8'' \times 1.9''$, Falkendal et al. 2021) of the Atacama Large Millimeter/submillimeter Array (ALMA) [C I](1−0) observation, it is uncertain whether the molecular gas is located in the host galaxy (Appendix D). Though JWST observes in a vacuum, we label the emission lines with their air wavelengths in Å following the convention, for example [O III]5007.

2. 4C+19.71, observation, and data processing

4C+19.71 (MG 2144+1928) is the first target observed as part of the JWST Cycle 1 General Observers program (ID 1970, PI: W. Wang) "Zooming into the monster's mouth: tracing feedback from their hosts to circumgalactic medium in $z = 3.5$ radio-loud AGN". The program includes four HzRGs with a diversity of star formation rates and radio jet morphologies (van Ojik et al. 1996; Carilli et al. 1997; Nesvadba et al. 2007; Falkendal et al. 2019). We selected them to have similar redshifts ($z \simeq 3.5$) to maximize the number of emission lines in a single observational setting.

4C+19.71 has a FR II-type radio jet with a double-sided lobe extending over $\gtrsim$60 kpc (Fanaroff & Riley 1974; Carilli et al. 1997). Besides the radio data, there are multiwavelength studies available for 4C+19.71 (e.g., Pentericci et al. 1999; Maxfield et al. 2002; Seymour et al. 2007; De Breuck et al. 2010). The HzRG is surrounded by an X-ray halo and [O III]5007 nebula with similar extension. Both are elongated in the same direction as the jet (~60 kpc; Armus et al. 1998; Smail et al. 2012; Nesvadba et al. 2017b). A more extended, ~100 kpc Lyα nebula is also detected around the radio AGN. It also shows an elongated morphology along the jet axis, even beyond the radio lobes (Falkendal et al. 2021; Wang et al. 2023).

The stellar mass of the host galaxy of 4C+19.71 is constrained to be $\lesssim 10^{11.1}\,M_\odot$. It forms stars at the rate of $\sim 84\,M_\odot\,\mathrm{yr}^{-1}$ (Falkendal et al. 2019). Finally, there is significant molecular gas in the host ($2.5 \times 10^{10}\,M_\odot$, Kolwa et al. 2023).

The observation of 4C+19.71 was conducted on UT 2022 October 30 with NIRSpec in IFU mode (Böker et al. 2022; Jakobsen et al. 2022). We selected $G235H/F170LP$ as the disperser and filter setup, which covers 1.70−3.15 µm in the observed frame or ~3700−7620 Å in the rest frame. The combination of filter and grating offers the spectral resolution of $85-150\,\mathrm{km\,s^{-1}}$. This ensures major optical emission lines seen in type-2 AGN ([O II]3726, 3729 to Hα, including [S II]6716, 6731) can be observed at once (e.g., Zakamska et al. 2003). We adopted a 9-point dither pattern and the improved reference sampling and subtraction (IRS^2) read-out pattern. The total on-source exposure time was 3.7 h. We designed the leakage exposure, 0.4 h, to identify light leaking through the failed open shutters on the microshutter array (MSA) at the first dither position.

We downloaded the raw data from the Mikulski Archive for Space Telescopes (MAST). The data were processed with the JWST Science Calibration pipeline[1] (v1.9.4) with the Calibration Reference Data System (CRDS) context file jwst_1041.pmap. Our procedure is similar to Vayner et al. (2023), executing the standard first and second stages of the pipeline with one modification. Specifically, we used the "emsm" method instead of "drizzle" during the data cube construction step to reduce the low-frequency ripples due to undersampling. The third and final stage of the processing is to combine cubes from different exposures into the final cube. We instead used the script from Vayner et al. (2023), who applied the Python package `reproject` because the third stage of the pipeline falsely rejects the bright emission peak while keeping some noise spikes. During this step, sigma clipping (2σ) was also included to reject outliers. The data cube was resampled to have a pixel scale of 0.05″. We processed the raw NIRSpec IFU data of the standard star TYC 4433-1800-1 (PID 1128) for flux calibration. Finally, we performed an additional background subtraction to the flux-calibrated science data cube to alleviate negative background continuum seen in source-free regions. The size of the point spread function (PSF) of the NIRSpec IFU depends on wavelength and spatial position. We mark the full width at half maximum (FWHM) of the PSF constructed in Vayner et al. (2024) in Fig. 1a.

Several works based on NIRSpec IFU observations report a World Coordinate System (WCS) offset in the final data cube (e.g., Wylezalek et al. 2022; Perna et al. 2023). We aligned the

[1] https://github.com/spacetelescope/jwst

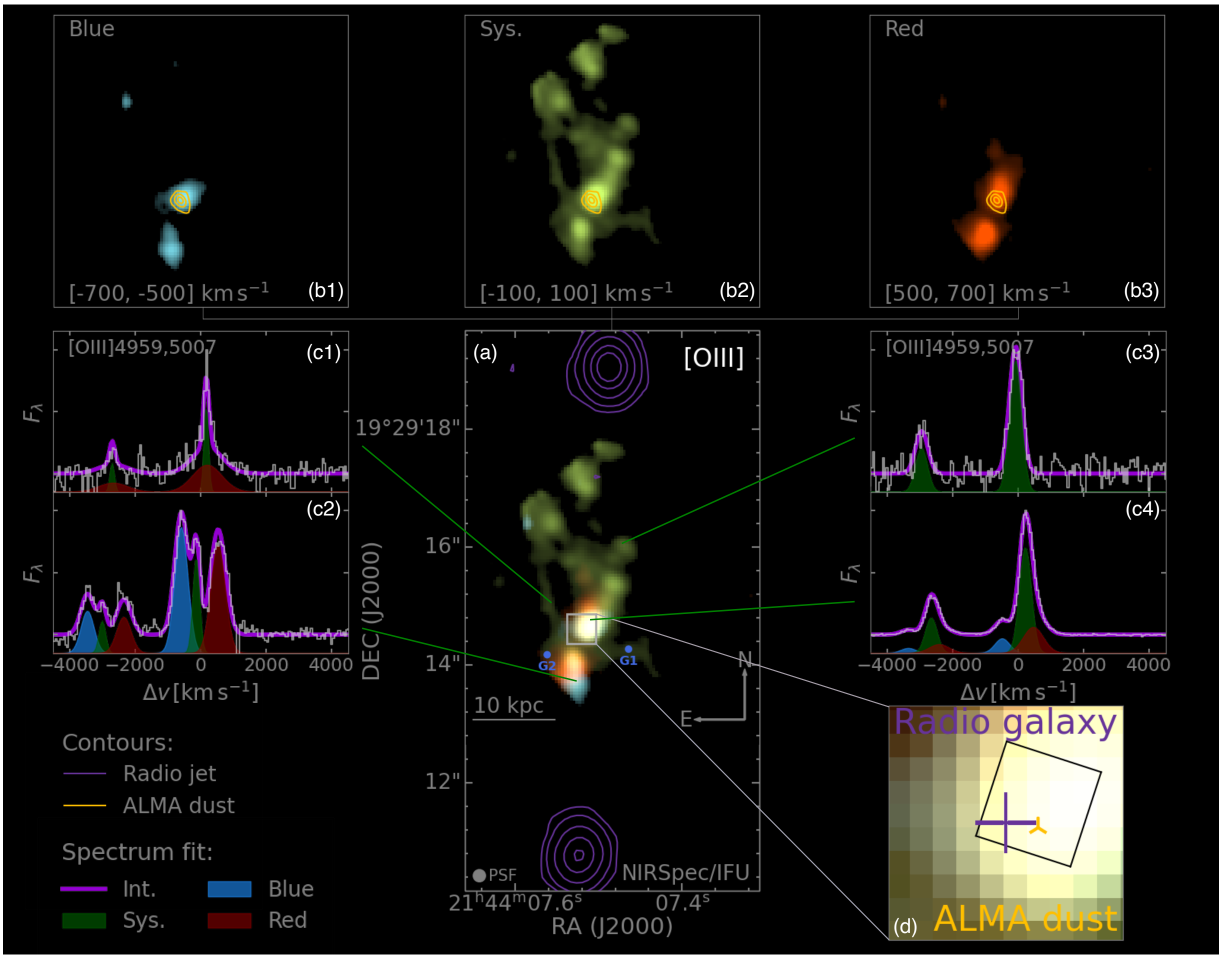

Fig. 1. NIRSpec [O III] color composite and example spectra of [O III] doublet. (a) Three-color composite image of narrowband [O III]5007. We overlay the VLA 4.7 GHz jet hot spots in dark purple contours. Blue dots indicate the position of foreground galaxies (see text). FWHM of the PSF is marked at the left corner. (b) "Monochrome" narrowband images of [O III]5007 collapsed at blue wing (b1), systemic redshift (b2), and red wing (b3), respectively. Yellow contours show dust continuum emission from the ALMA data. (c) Example spectra of continuum-subtracted [O III]4959, 5007 extracted at four different spatial locations normalized to their peak flux density. We fit the spectra using `q3dfit` with up to three kinematic components. The light purple curve indicates the overall fit. The individual components are shown in blue, green, and red with a negative offset from the zero level. (d) Zoom-in view of the central $0.5'' \times 0.5''$ region of the narrowband image (gray box in panel a). Dark purple plus + sign marks the position of the continuum emission of the radio galaxy determined from the NIRSpec cube while the yellow triple-spike triangle shows peak position of the ALMA 400.3 GHz dust. The sizes of the markers represent the position uncertainty, 1.2″ and 0.04″ for radio galaxy and ALMA dust respectively. Black box in the insert shows the aperture where the 1D spectrum (Fig. 2) is extracted.

continuum emission position of the west foreground galaxy in our NIRSpec cube to the *Hubble* Space Telescope (HST) WFPC2 image and used this new WCS in the following analysis (see Fig. 1a and Pentericci et al. 1999). The astrometry of the HST image was corrected by cross-matching with *Gaia* DR3 targets (Gaia Collaboration 2023). Our final WCS solution resulted in a shift of $\Delta\mathrm{RA} = 0.43''$ and $\Delta\mathrm{Dec} = -0.22''$ compared to the pipeline output WCS. We discuss the astrometry correction in Appendix A.

We also present the ALMA Band 8 observation of 4C+19.71. This observation was carried out under program ID 2021.1.00576.S (PI: W. Wang) on UT 2022 June 17. In this work, we use only the archived image at ν_{obs} = 400.3 GHz to show the position of the cold dust emission. A detailed analysis of the ALMA observations is beyond the scope of this paper and will be presented in a forthcoming paper.

3. Results

In this paper, we inspect both the 2D morphology and 1D spectrum of the warm ionized gas. Given the signal-to-noise ratio (S/N) of the optical emission lines covered in our setting, we choose the [O III]5007 ([O III] hereafter if not specified) as the proxy for the morphology. It is extensively used in the studies of AGN narrow line regions (e.g., Husemann et al. 2013; Harrison et al. 2014; Wylezalek et al. 2016). This is the first time that the distribution of ionized gas around a z > 3.5 radio loud AGN is seen with ≲1 kpc resolution.

3.1. Morphology of the extended ionized nebula

Armus et al. (1998) observed the [O III] emission of 4C+19.71 with Keck narrowband imaging. They reported the central [O III] (i.e., a similar region as observed in the field of view of the

Wang, W., et al.: A&A, 683, A169 (2024)

NIRSpec IFU) has an elongated morphology along the north-south direction with two distinctive parts. We show the first zoom-in view of the [O III] nebula of 4C+19.71 in Fig. 1. We produce three pseudonarrowband images and show their composite in Fig. 1a. The individual images are shown in Figs. 1b1–b3 for the blue wing ([−700, −500] km s^{-1}), systemic redshift ([−100, 100] km s^{-1}), and red wing ([500, 700] km s^{-1}), respectively. On each of the images, there are two distinct peaks located south and north which roughly align with the jet axis (dark purple contours in Fig. 1a, Carilli et al. 1997). Based on [O III] gas kinematics probed by VLT/SINFONI near the jet hot spot positions (Fig. A.7 of Nesvadba et al. 2017a), we assume the southern jet is the approaching one. There is no doubt that 4C+19.71 has a hidden quasar (e.g., Seymour et al. 2007; De Breuck et al. 2010; Falkendal et al. 2019, and Sect. 4.1). Assuming the ionization cone of the quasar is aligned with the jet axis (Drouart et al. 2012), it is likely that we are observing, in both the south and north regions, the foreground and background parts of the cone.

To assist in studying the morphology, we show example [O III]4959, 5007 spectra extracted at four different locations (Figs. 1c1–c4). We note that the analysis of the extended emission-line region kinematics is not the focus of this paper. The per-spatial-pixel (spaxel) spectra are fit using `q3dfit` (Rupke et al. 2023), which is a Python tool for analyzing JWST IFU data based on the software `IFSFIT` (Rupke 2014; Rupke et al. 2021)[2]. It is clear that at least three different kinematic components are present on galactic scales ($\lesssim$10 kpc). This is especially obvious for the gas in the south, with three distinct peaks present (e.g., Fig. 1c2). We stress that we refer to the component closest to 0 km s^{-1} as "systemic" and the others as "blue" or "red" depending on their relative velocity shift with respect to the systemic component. At this point, it remains unclear whether they are the blueshifted or redshifted outflowing gas clouds.

The most striking morphological features are the spatially extended emission blobs and filamentary structures around the systemic velocity (Fig. 1b1). For example, both components detected in the east filament (Fig. 1c1) and the gas of the northern spot (Fig. 1c3) all have $|\Delta v| < 300$ km s^{-1}. Neither the previous narrowband imaging nor ground-based IFU could resolve these components spatially and spectrally (Armus et al. 1998; Nesvadba et al. 2017a). With the relatively small field of view (FoV) of the NIRSpec IFU, the jet hot spots are not captured which are presumed to be the regions with the most energetic jet-gas interactions. Given the fact that these extended filamentary features sit at the systemic redshift, we arrive at the conclusion that they are not associated with the outflow but may be high density gas clumps. Their morphologies may have been disrupted by the jet-induced bubble (Mukherjee et al. 2016; Dugan et al. 2017). Indeed, at least in the example spectra extracted at the east filament, we observe a broad component indicative of disruption by the jet ($FWHM$ = 1052 km s^{-1}).

3.2. Continuum emission

We overlay in Fig. 1b the continuum emission detected in our ALMA Band 8 observation, which likely indicates the location of the cold dust emission heated by the newly formed stellar population (e.g., Herrera-Camus et al. 2021). In Fig. 1d we show that the AGN position (NIRSpec continuum, Sect. 4.1) agrees with the ALMA dust location within their uncertainties. The 1σ uncertainty, ~0.02″, of the ALMA dust position is estimated using $\mathrm{pos_{acc}} = \mathrm{beam_{FWHP}}/(S/N)/0.9$ with $\mathrm{beam_{FWHP}} \simeq 0.2''$ and $S/N \simeq 10$ (see Appendix A for the 1σ uncertainty, ~0.06″, of the NIRSpec continuum)[3].

A previous HST image (WFPC2/F702W) indicates other two objects in the NIRSpec IFU FoV (Pentericci et al. 1999). They are also seen in our NIRSpec observations (Fig. 1a). We label them G1 and G2 for the galaxy in the west and east, respectively. G1 is used as the WCS alignment reference in Sect. 2. They are identified as foreground galaxies with $z \simeq 1.786$ for G1 and $z \simeq 1.643$ for G2. Their spectra and emission line identifications are shown in Appendix B.

3.3. Emission line identification

We present the identification of the emission lines in Fig. 2. This is the first time that optical nebular emission lines from [O II]3726, 3729 to [S II]6716, 6731 are observed for $z \simeq 3.5$ HzRGs with the spectral resolution of 85 to 150 km s^{-1}. This makes it possible to investigate the ionization mechanisms and metallicities (e.g., line ratio diagnostic diagrams, Baldwin et al. 1981; Veilleux & Osterbrock 1987; Kauffmann et al. 2003; Groves et al. 2004b, 2006; Kewley et al. 2001, 2006, 2013; Wylezalek et al. 2017).

We extracted a spectrum from a $0.2'' \times 0.2''$ or 1.4×1.4 kpc^2 (4×4 pix^2) square aperture near the position of the continuum emission peak. The aperture and size were chosen to also include the [O III] emission peak which maximizes the S/N for emission line identification. The aperture was aligned with the extension of the brightest [O III] emission blob. We show this aperture in the black box in Fig. 1d. The spectrum is presented in Fig. 2. We summed over five wavelength pixels around the systemic zero (velocity range of ~270 to ~150 km s^{-1}) to calculate the line S/N for identification. We identify ~24 emission lines (doublets) with $S/N > 3$. The ones with $S/N \gtrsim 10$ are marked by red lines. We implemented a visual check by examining the spatial distribution of lines with $3 < S/N < 10$. The spatially resolved ones are marked by black dashed lines.

We fit the spectrum with `q3dfit`. We used three kinematic components. The line center and width of the same component are connected for different lines. We present these kinematic results in Table 1. We refer to them as central, red, and blue components based on their velocity shifts. In Appendix C, we report fit line fluxes from the 1D spectrum.

4. Discussion and summary

4.1. Comparison to Cygnus A

Cygnus A (3C405) is the most powerful radio AGN in the local Universe with comparably high radio power as 4C+19.71 (z = 0.0562, $P_{178\,\mathrm{MHz}} \sim 5.5 \times 10^{28}$ W Hz^{-1}, Carilli & Barthel 1996). This makes it the perfect target to compare with the properties of the warm ionized ISM gas using the common optical tracers (Fosbury et al. 1999; Vernet 2001). Using the spectropolarimeter on the Keck telescope, Ogle et al. (1997) observed the nebular emission lines of Cygnus A. We overlay our 1D spectrum (Fig. 2) with the spectrum of Cygnus A extracted at its nucleus in Fig. 3. The extraction aperture of Cygnus A is $\sim 1'' \times 1.1''$ which corresponds to 1.1×1.2 kpc^2 and is similar to the aperture used for 4C+19.71 (1.4×1.4 kpc^2). This is the first time that a rest-frame optical spectrum of a $z \gtrsim 1$ radio AGN can be studied in comparable detail as a local example.

[2] https://q3dfit.readthedocs.io/en/latest/

[3] https://help.almascience.org/kb/articles/what-is-the-absolute-astrometric-accuracy-of-alma

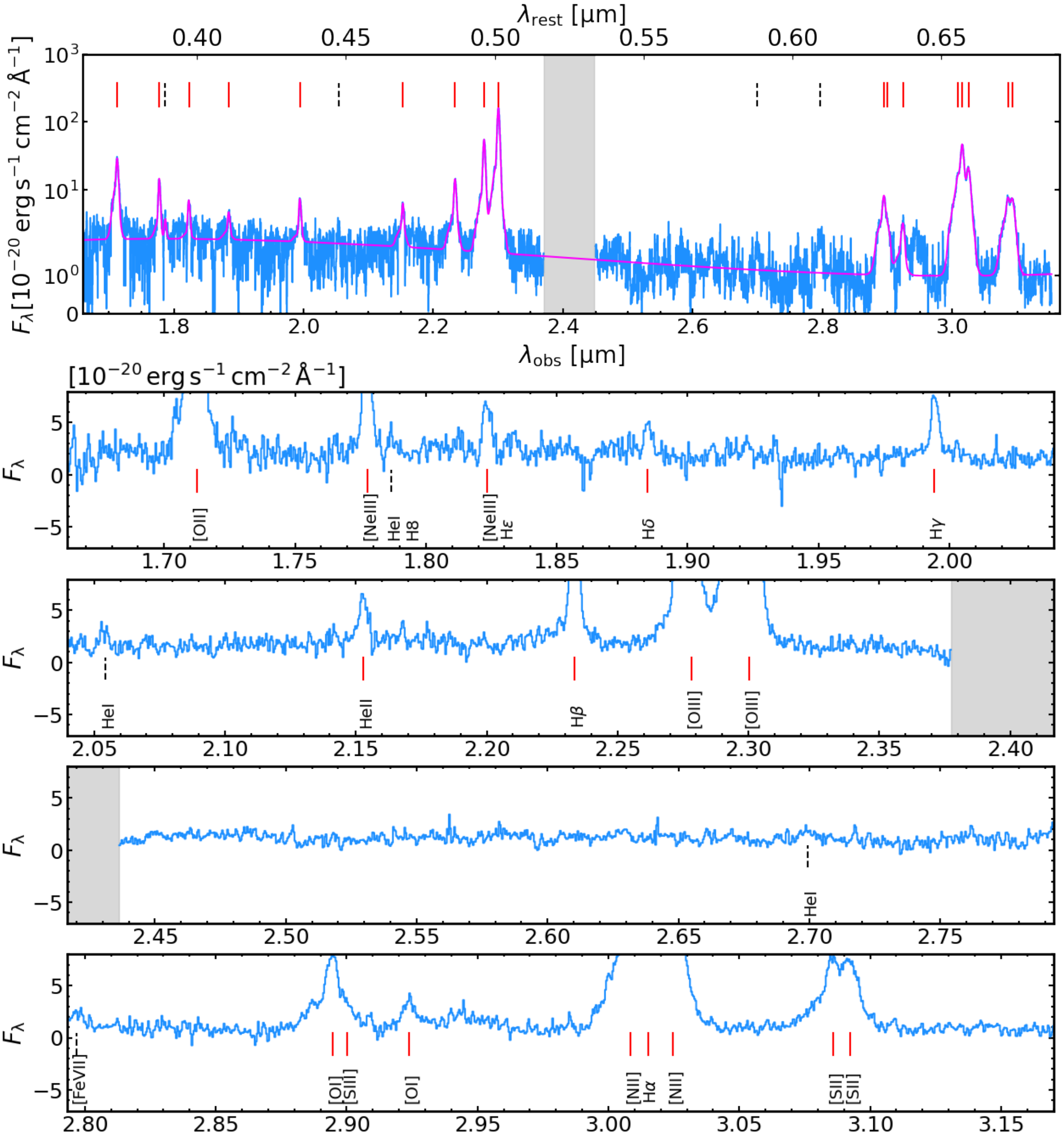

Fig. 2. Full spectrum extracted at the AGN position without continuum subtraction (black box in Fig. 1d). We mark the emission lines detected with $S/N \gtrsim 10$ in red lines. Lines detected with $3 < S/N < 10$ and visually checked to be extended are marked with gray lines. We note that the feature at ~2.945 µm is likely instrumental due to the leakage flux from the MSA. The central gray shaded region is the detector gap. The top panel is the full view of the spectrum while the zoom-in view of the faint lines are shown in the bottom panels. The magenta curves show the best fit of the spectrum (Appendix C).

To first order, the continuum shape of 4C+19.71 is consistent with Cygnus A. We note that the Cygnus A spectrum is corrected for Galactic reddening and had its host galaxy continuum subtracted (Ogle et al. 1997). Though there might be contamination of continuum (i.e., due to the leak of from the MSA) for our NIRSpec data, we conclude that the emission from evolved stellar population in the host of 4C+19.71 is faint, that is, the spectrum is dominated by the (possibly scattered) light of the hidden AGN. This indicates that the stellar population has a subdominant contribution in the regions near the AGN.

The relative emission line fluxes are comparable for 4C+19.71 and Cygnus A at least from [O II]3726, 3729 to [O III]. We conclude that, to first order, AGN photoionization mechanisms dominate the inner parts of these two galaxies. The

Table 1. Fit kinematic results from the 1D spectrum at nucleus.

	Central comp.	Red comp.	Blue comp.
Δv [km s^{-1}]	238 ± 10	572 ± 30	−148 ± 20
FWHM [km s^{-1}]	445 ± 10	412 ± 30	1669 ± 20

Notes. The velocity shift is with respect to the systemic redshift from Kolwa et al. (2023), z = 3.5892.

similarity of the Balmer lines, Hβ, Hγ, and Hδ, suggests the ISM gas conditions are similar (Osterbrock & Ferland 2006). The dissimilarity of the flux at redder wavelength (e.g., [O I], [N II], and [S II]) may suggest differences in gas enrichment. van Bemmel et al. (2003) proposed that the quasar wind-driven outflowing dust clouds scatter the optical line emitting photons in Cygnus A. We know there are at least three kinematic components present in the nucleus of 4C+19.71 (Sect. 3.1). We defer to a future publication the detailed study of the gas kinematics to unveil the spatially resolved gas motions and constrain the ISM distribution.

4.2. Line ratio diagnostics and ionization mechanisms

To study the extended irregular ISM structures around the hidden powerful radio AGN (Sect. 3.1), we construct line ratio maps and compare them to emission line diagnostics (e.g., Groves et al. 2004b, 2006; Kewley et al. 2006). We use `q3dfit` to fit the cube to systematically separate the blended emission lines and account for doublets. The fit region was selected based on the [O III] narrowband image with a S/N cut of >5 (white contour in Fig. 4). We limit the spatial study in this paper to the six brightest emission lines: [O II]3726, 3729, Hβ, [O III]4959, 5007, [O I]6300, [N II]6548, 6583, Hα, and [S II]6716, 6731. These lines are fit simultaneously with the same velocity shift and line width for the corresponding components ("kinematically tied", e.g., Zakamska et al. 2016). Following Vayner et al. (2023), we ran the fit with 3, 2, and 1 as the maximum number allowed Gaussian components. We performed a visual inspection to determine the best fit for each spaxel. In the following discussions, we sum the fluxes of the doublet [O II]3726, 3729 and [S II]6716, 6731, respectively. We use the fluxes of the individual [O III]5007 and [N II]6583 lines, respectively. Hereinafter, we omit the wavelength when referring to the line name. The line ratio maps and diagnostics based on the fit are shown in Figs. 4 and 5, respectively. As mentioned before, a kinematical study of the ionized ISM is beyond the scope of this paper; we only derive the line ratios of the integrated line fluxes of all velocity components.

The Balmer line ratios are sensitive to dust attenuation (e.g., Veilleux & Osterbrock 1987; Osterbrock & Ferland 2006). We present the color excess, $E(B-V)$, maps based on the fit Hα/Hβ flux ratios in Fig. 4a. The map is constructed using an intrinsic flux ratio of 3.1 assuming Case B recombination in AGN ionization and a Calzetti et al. (2000) extinction law following Vayner et al. (2023). We find that there is a dusty region with high $E(B-V)\sim1$ around the AGN position, coincident with our ALMA dust continuum (pink contours in Fig. 4a), confirming the importance of dust causing extinction near the AGN. This spatial coincidence also validates our manual astrometry correction based on foreground galaxy (Appendix A). Fosbury et al. (1999), Vernet (2001) proposed that a dust ring is present around the nucleus of Cygnus A. Given the spectral similarity of 4C+19.71 to Cygnus A (Fig. 3), it is possible that we also detect a dust lane around the center of 4C+19.71. The line ratios shown in Figs. 4b and c are corrected for the dust attenuation based on this $E(B-V)$ map.

In Figs. 4b,c, we show respectively the ratio maps of [O I]/Hα and [S II]/Hα based on the integrated line fluxes of all components. The following line ratios are in logarithmic scale, unless otherwise specified. We group the spaxels in the FoV into five regions (white dashed lines in Figs. 4b,c), following the apparent geometry of the AGN ionization cone, with the nucleus added as an individual region. The southern part of the ISM is distinctive as having lower [O I]/Hα and [S II]/Hα values. In the extended filamentary part of the nebula toward the north, there is a large scatter with the presence of both higher and lower [O I]/Hα and [S II]/Hα values. In general, the east and west regions have higher [O I]/Hα and [S II]/Hα. To simplify, we combine the east and west regions and refer to it as EW.

We inspect our results in line ratio diagnostic diagrams and present in Fig. 5. In addition to [O I]/Hα (Fig. 5b) and [S II]/Hα (Fig. 5c), we present the [N II]/Hα–[O III]/Hβ (Fig. 5a) and [O II]/[O III]–[O III]/Hβ diagnostics (Fig. 5d). The EW region (red diamonds) occupies different locations on the diagnostic diagrams than the other regions, with higher [O I]/Hα, [S II]/Hα, and [O II]/[O III] values. The EW region is also distinctive with a lower [O III]/Hβ compared to the other regions. Although the southern spaxels (blue hexagons) are clustered toward lower [N II]/Hα, [O I]/Hα, [S II]/Hα, and [O II]/[O III] values, we find they fall in the line ratio space spanned by the northern regions (green squares) in all diagrams. Despite having a relatively large dispersion, the median line ratios of the northern region is consistent with the spaxels from the nucleus region (black triangles). We report the median line ratios of each region in Table 2.

We overlay the Groves et al. (2004a) dusty radiation-pressure dominated model grids on the diagnostic diagrams. We chose the $2\,Z_\odot$ models (black) as indicated by the [N II]/Hα ratios (e.g., metallicity from Groves et al. 2006; Nesvadba et al. 2017a). The models are constructed with various combinations of the power-law index, α, of the ionizing source (i.e., $F_\nu\propto\nu^\alpha$) and ionization parameter, $U=S_\star/(n_\mathrm{H}c)$, where c is the speed of light, n_H is the hydrogen number density and $S_\star$ is the flux of ionizing photons entering the cloud. The goal is not to perform a quantitative comparison, but rather to test which parameter(s) could be responsible for the line ratio differences. Although other interpretations are possible, a higher U parameter could explain the lower [O I]/Hα and a higher [O III]/Hβ (e.g., Villar-Martín et al. 1999). Our comparison indicates a scenario where the north, south, and nucleus regions have higher U parameters than the EW region. This is expected given that the jet axis is along the north-south direction which is also the direction of the AGN ionization cone (Drouart et al. 2012). Hence, the ionizing photons of the AGN can reach the ISM with less extinction along the north-south direction. In this configuration, the EW region is outside of the ionization cone where the photons will encounter more obstacles before ionizing the gas (e.g., Fosbury et al. 1999; Vernet et al. 2001). This indicates larger particle density n_H and less ionizing photon flux (smaller $S_\star$) in the EW which leads to lower observed U parameters.

The south region has lower [N II]/Hα, [O I]/Hα, [S II]/Hα, and [O II]/[O III]. The U parameter appears at similar levels in the south as in the nucleus. Comparing with the model grids, this could indicate that the ratio difference is due to lower α (steeper power-law ionizing spectrum). If this is the case, then there may be additional extinction between the ionizing photons and the southern clouds. The attenuation map (Fig. 4a) indeed

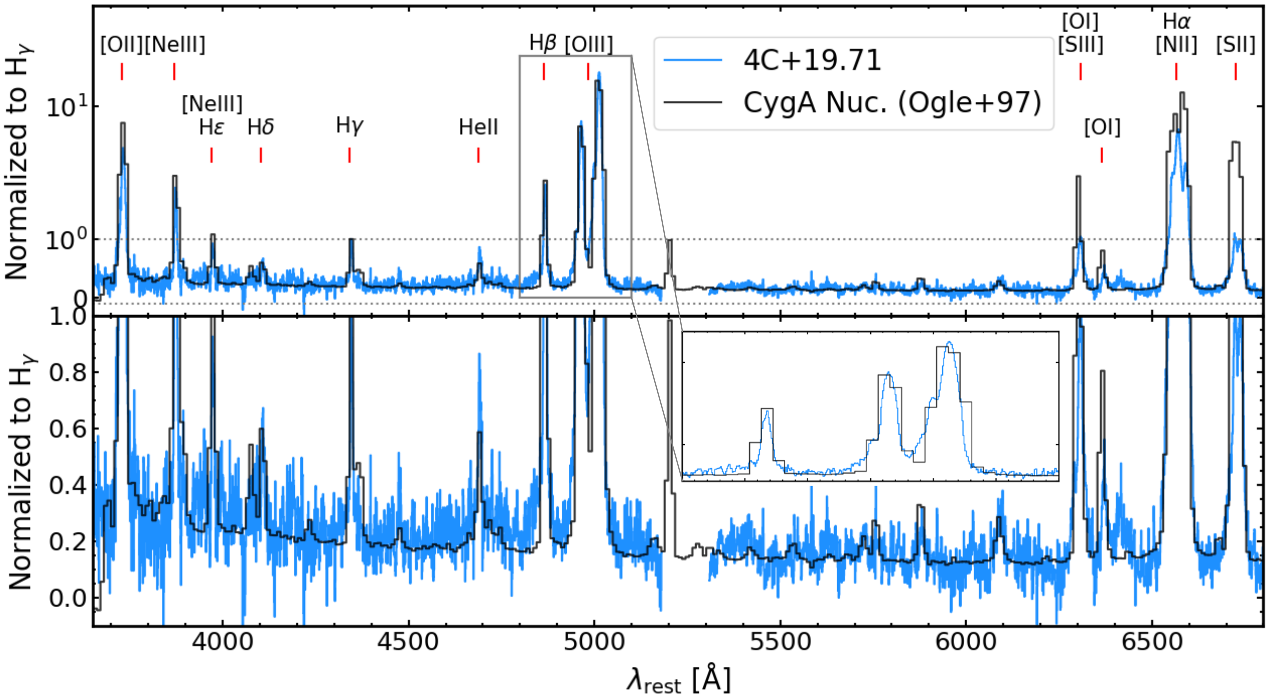

Fig. 3. Spectral comparison of 4C+19.71 to Cygnus A (Ogle et al. 1997). Blue histogram shows the same 1D spectrum as in Fig. 2. The spectrum of Cygnus A is shown in black which is extracted at its nucleus position after Galactic reddening correction and subtraction of a elliptical galaxy template. Both spectra are normalized to the peak flux density of their Hγ. The bottom panel is a zoom-in version of the region between the gray dotted lines in the upper panel. We marked the emission lines detected for 4C+19.71 with $S/N \gtrsim 10$ as in Fig. 2. The inset provides a further zoom-in around Hβ–[O III] complex.

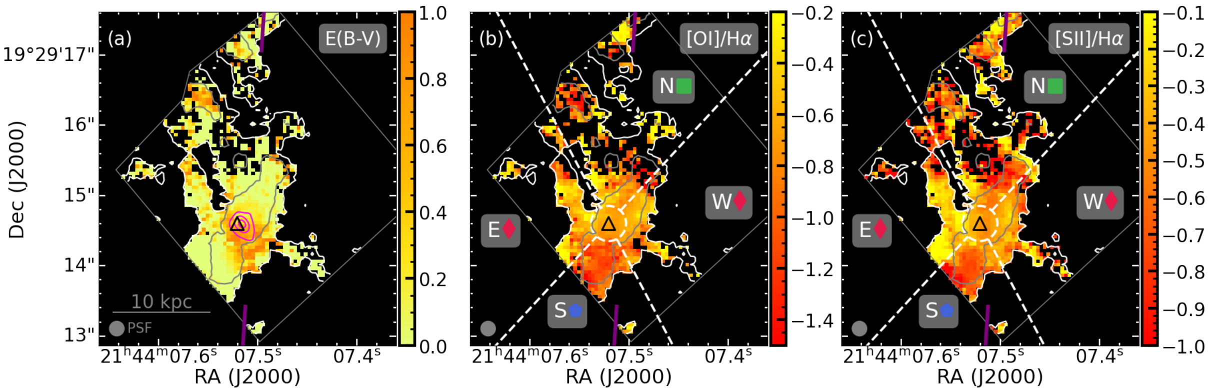

Fig. 4. Dust attenuation (a) and line ratio maps (b), (c) constructed based on the fit fluxes integrated for all components. The white and gray contours indicate the 5σ and 15σ [O III] surface brightness levels of the un-smoothed systemic narrowband image, respectively (Fig. 1). Dark purple lines show the directions toward the radio jet hot spots. Black triangle marks the position of the AGN while magenta contours trace the ALMA continuum (Fig. 1d). The dashed white lines and circle in panel b and c divide the FoV into five regions for line ratio diagnostic analysis (Fig. 5). FWHM of the JWST PSF is marked at the left corner.

shows a higher value toward the south. If this is due to the geometry of the dust torus, it may be inconsistent with the indicated orientation from Nesvadba et al. (2017a). We also overlay the similar radiation model with $0.5\,Z_\odot$ in cyan in Fig. 5c and find that there is an alternative possibility that the southern region is more metal poor than the nuclear region. Additionally, the complex kinematics in the southern region (Fig. 1c3), suggesting a more complex scenario in the south (e.g., a late-stage merger, see Sect. 4.5). The detailed analysis of this southern region requires more lines which is beyond the scope of this paper (e.g., He lines, Groves et al. 2004a; Holden et al. 2023).

To further test the ionization mechanisms, we also overlay the empirical classification from Kewley et al. (2006) in Figs. 5a–c. Although these are calibrated using low-z data (i.e., may not be relaible for high-z, see Kewley et al. 2019), the results provide evidence of the AGN radiation dominating ionization of the ISM within $\lesssim$30 kpc of the hidden quasar. Some spaxels in the north and east regions are located in the low

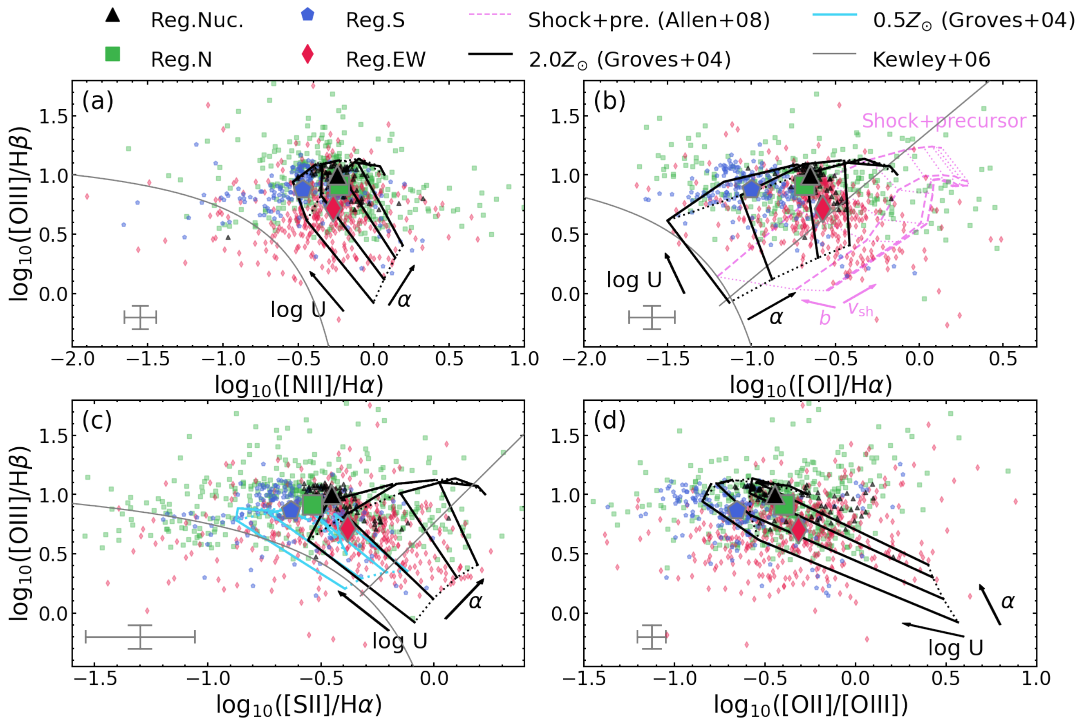

Fig. 5. Line ratio diagnostic diagrams based on fitting and corrected for dust attenuation. Each smaller mark corresponds to one spaxel in the FoV. The larger symbols represent the median. Data points with the same symbol are the same region marked as Fig. 4: Nuc. – nucleus (circle with $r = 0.25''$), N – north, S – south, EW – east+west. The typical 1σ error is shown at the left corner. We show the $2\,Z_\odot$ dusty radiation-pressure dominated photonionization models from Groves et al. (2004a) in black and mark the direction of increasing ionization parameter, $\log U \in [-3.0, -2.0, -1.0, 0.0]$, and power-law index, $\alpha \in [-2.0, -1.7, -1.4, -1.2]$. The similar model with $0.5\,Z_\odot$ is shown in panel c in cyan. Purple grids are the "shock+precursor" models with per-shock density $100\,\mathrm{cm}^{-3}$, (shock velocities of $200 \le v_{\mathrm{shock}} \le 1000\,\mathrm{km\,s}^{-1}$ in steps of $100\,\mathrm{km\,s}^{-1}$ and magnetic parameters of $0.01 \le b = B/n^{1/2} \le 100\,\mu\mathrm{G\,cm}^{-3/2}$ in steps of 1 dex, Allen et al. 2008). The directions of increasing v_{shock} and b are indicated with purple arrows. We include the empirical classification from Kewley et al. (2006) in gray lines in panels a–c.

ionization or H II region. This suggests a different ionization mechanism or mix of different mechanisms at these spatial locations. Indeed, we find a part of them are roughly consistent with the "shock+precursor" models (light purple grids Fig. 5b, Allen et al. 2008). The shock models can cover a large fraction of the parameter space of the line ratio diagnostics. The identification of shock ionization requires combination of flux ratios with kinematics, electron temperature and Hα fluxes (e.g., Alatalo et al. 2016; Baron et al. 2017; Alarie & Morisset 2019). Our discussion is not meant to be decisive but to be inclusive with the possibility of shock. We choose the models with pre-shock number density, $n = 100\,\mathrm{cm}^{-3}$ (e.g., De Breuck et al. 2000). For the shock velocities, we use higher values ($v_{\mathrm{shock}} \ge 200\,\mathrm{km\,s}^{-1}$) following De Breuck et al. (2000) studying the emission lines of HzRGs. We note that shock+precursor model with pre-shock density $n = 1000\,\mathrm{cm}^{-3}$ are also physical for AGN (Liu et al. 2020) which occupies a subset of the line ratio space spanned by $n = 100\,\mathrm{cm}^{-3}$ model using the same set of v_{shock} and magnetic parameters. The driver of the shock is unclear. The EW region is roughly in the direction perpendicular to the ionization cone (jet axis) which suggests a less collimated shock driver or the ionization cone is not perpendicular to the dusty obscuring disk (e.g., Dugan et al. 2017; Tanner & Weaver 2022; Vayner et al. 2023). As for the more extended parts ($\gtrsim$10 kpc) in the north, the passage of the powerful radio jet could also have left remaining shock effects.

Table 2. Median line ratio values for different regions in Fig. 5.

	Nuc.	N	S	EW
[O III]/Hβ	1.00	0.92	0.88	0.72
[N II]/Hα	−0.24	−0.23	−0.47	−0.27
[O I]/Hα	−0.65	−0.68	−1.00	−0.58
[S II]/Hα	−0.45	−0.54	−0.63	−0.38
[O II]/[O III]	−0.44	−0.40	−0.65	−0.31

Our results show that the inner part of the ionized ISM in the $z \sim 3.5$ radio-loud AGN is dominated by photons from the hidden AGN with potential evidence for shock ionization. Its structure agrees with the classical ionization cone. Although the analysis is based on knowledge gained at low-z and there are more unsolved complexities, JWST will be the key to address this (e.g., Nakajima & Maiolino 2022; Sanders et al. 2024).

4.3. *Inefficient quasar-driven outflow at nucleus*

Our NIRSpec IFU observations enable studying outflows on scales $\lesssim$20 kpc. VLT/SINFONI observations captured more extended outflowing gas (Collet et al. 2016; Nesvadba et al. 2017a,b).

In Sect. 3.1, we show that the "high-velocity" clouds are only detected within the ~5 kpc from the AGN and their morphology is aligned with the jet axis (Fig. 1). This is inconsistent with the results from observations of quasars at cosmic noon where fast ($|\Delta v| \sim 500\,\mathrm{km\,s^{-1}}$) outflows are seen at $\gtrsim$10 kpc and are less directionally confined (e.g., Vayner et al. 2024). However, Cresci et al. (2023), Veilleux et al. (2023) also showed one contradicting case. Hence, this discussion is yet settled and required more observations. Through our discussions in Sects. 4.1 and 4.2, these may be the outflows inside the ionization cone. The double-sided radio lobes have a projected extent of ~60 kpc, which is beyond the JWST FoV. Hence, this potential outflow maybe radiatively driven.

The systematic per-spaxel kinematic study is beyond the scope of this work. Additionally, as shown in Sect. 4.2 (also in Sect. 4.5), there may be more complex scenarios happening in the southern cone. Hence, we use the results from the integrated 1D spectrum (Figs. 1d and 2, Tables 1 and C.1) at the nucleus region as a proxy to estimate the kinetic energy of the potential outflow near the AGN. For this calculation, we focus on the red and blue components (Tables 1 and C.1) and assume them to be the redshifted and blueshifted outflow clouds seen on the back and front side of the northern part of the ionization cone, respectively. Then, we assume their relatively velocity shifts with respect to the central component (Appendix D) as their outflow velocities ($\Delta v_{\mathrm{red}} = 334\,\mathrm{km\,s^{-1}}$ and $\Delta v_{\mathrm{blue}} = -386\,\mathrm{km\,s^{-1}}$). We follow Vayner et al. (2024) and use the following equation to calculate the ionized outflow gas mass (Osterbrock & Ferland 2006):

$$M_{\mathrm{ion}} = 1.4\left(\frac{m_{\mathrm{p}} L_{\mathrm{H}\alpha}}{j_{\mathrm{H}_\alpha} n_{\mathrm{e}}}\right), \tag{1}$$

where $L_{\mathrm{H}\alpha}$ and n_{e} are the Hα luminosity and electron density, respectively. We assume an electron temperature $T_{\mathrm{e}} \simeq 15\,000$ K (Nesvadba et al. 2017a; Vayner et al. 2024). We use the fiducial value $n_{\mathrm{e}} = 500\,\mathrm{cm^{-3}}$ from Nesvadba et al. (2017a). Given that the emissivity, j_{H_α}, is not sensitive to n_{e}, we use the value of $2 \times 10^{-25}\,\mathrm{erg\,cm^3\,s^{-1}}$ for $T_{\mathrm{e}} \simeq 15\,000$ K (Vayner et al. 2024). Based on Eq. (1), we find $M_{\mathrm{ion}} = 10^5$ and $10^6\,M_\odot$ for the red and blue components, respectively. We then estimate the outflow rate using the following equation (Vayner et al. 2024):

$$\dot{M}_{\mathrm{ion}} = \frac{M_{\mathrm{ion}} v_{\mathrm{ion}}}{\Delta R}. \tag{2}$$

For the distance ΔR, we use half of the physical size of the extraction aperture, 0.7 kpc. For the velocity, we use the $v_{\mathrm{ion}} = |\Delta v| + \sigma_v$ (Rupke & Veilleux 2013; Vayner et al. 2024). We report the summation of the red and blue components as the estimated total outflow rate. This gives a total $\dot{M}_{\mathrm{ion}}$ of $2\,M_\odot\,\mathrm{yr^{-1}}$. The outflow momentum flux $\dot{P}_{\mathrm{ion}}$ and outflow kinetic luminosity $L_{\mathrm{ion}}^{\mathrm{kinetic}}$ are calculated from

$$\dot{P}_{\mathrm{ion}}^{\mathrm{outflow}} = \dot{M}_{\mathrm{ion}} \times v_{\mathrm{ion}}, \tag{3}$$

$$L_{\mathrm{ion}}^{\mathrm{kinetic}} = \frac{1}{2}\dot{M}_{\mathrm{ion}} \times v_{\mathrm{ion}}^2. \tag{4}$$

We calculate values for $\dot{P}_{\mathrm{ion}}^{\mathrm{outflow}}$ and $L_{\mathrm{ion}}^{\mathrm{kinetic}}$ of 1.5×10^{34} dyne and $8.0 \times 10^{41}\,\mathrm{erg\,s^{-1}}$, respectively. These are much smaller (~2 dex) than the values derived on larger scales by SINFONI (Nesvadba et al. 2017a,b). If we use the infrared AGN luminosity, $L_{\mathrm{AGN}}^{\mathrm{IR}} = 10^{10.91}\,L_\odot$, and assume a conversion factor, $\kappa_{\mathrm{AGN}}^{\mathrm{bol}} = 6$, the bolometric luminosity of 4C+19.71 is estimated to be $L_{\mathrm{bol}} \sim 2.5 \times 10^{47}\,\mathrm{erg\,s^{-1}}$ (Drouart et al. 2014; Falkendal et al. 2019). Then the coupling efficiency of this potential radiatively driven outflow, $L_{\mathrm{ion}}^{\mathrm{kinetic}}/L_{\mathrm{bol}}$, is $\sim 10^{-5}$. Using NIRSpec IFU, Perna et al. (2023) and Vayner et al. (2024) reported higher coupling efficiency for $z \sim 3$ quasars (0.02 and 10^{-3}, respectively). Veilleux et al. (2023) found a relatively low coupling efficiency using the same instrument, 1.8×10^{-4}, for a $z \sim 1.6$ type-1 quasar which is still 1 dex higher than 4C+19.71. Harrison et al. (2018) summarized the coupling efficiency for a large number of AGN (e.g., their Fig. 2). Compared to their statistics, the value from this work is located at the lower end. Our estimation based on the JWST observation is a ~2 to 3 dex lower than the coupling efficiency of the jet kinetic energy probed on larger scales for a sample of ~50 HzRGs (10^{-3} to 10^{-2}, Nesvadba et al. 2008, 2007, 2017a,b).

Our NIRSpec IFU data is only sensitive to the central clumps, $\lesssim$20 kpc, but not to extended diffuse emission. If we assume there are fast outflows (~$500\,\mathrm{km\,s^{-1}}$) and use the distance from the center quasar to the edge of our FoV (~20 kpc), the crossing time of this outflow would be ~40 Myr. This is shorter than the jet age, ~60 Myr, of 4C+19.71 (Nesvadba et al. 2017a). Hence, it is plausible that we do not capture the fast and (presumably) energetic outflowing gas on large scales (e.g., size of the radio lobes). Nevertheless, if the radiative coupling efficiency is 10^{-5} at the nucleus where the radiation is the strongest, it will be less efficient farther outside. Simulations (e.g., Costa et al. 2018) find that the efficiency for the radiation-driven outflows can be ~0.1% in luminous quasars ($L_{\mathrm{bol}} \gtrsim 10^{47}\,\mathrm{erg\,s^{-1}}$) within galactic scales ($\lesssim$10 kpc). The efficiency drops after ~10 Myr which may resemble the case of our observation. Though the ISM and CGM gas of 4C+19.71 seem more quiescent than in other HzRGs (Nesvadba et al. 2017a; Wang et al. 2023), a gas kinetic energy luminosity of $10^{45}\,\mathrm{erg\,s^{-1}}$ was found for this source by including the ISM at the jet lobes. Comparing to the results from Nesvadba et al. (2017a,b), we conclude that, at least for this HzRG, the mechanical feedback from the radio jet takes the leading role for driving the outflow, and it is happening in the radio lobes beyond the galactic scale (e.g., ~30 kpc from the AGN).

One of the main uncertainties is the estimation of M_{ion}, which is inversely proportional to n_{e}. We find that M_{ion} (and thus $L_{\mathrm{ion}}^{\mathrm{kinetic}}$) could be ~2 dex lower if we use the n_{e} estimated based on our observation (Appendix C). Therefore, the radiative coupling could be even more inefficient. Another uncertainty is the outflow speed. We take the unknown orientation of the ionization cone into account by using $v_{\mathrm{ion}} = |\Delta v| + \sigma_v$. Even if the estimated speed is one of the three components in 3D space (i.e., the intrinsic v_{ion} is higher by another factor of three), the radiative coupling efficiency will increase by a factor of nine, $\sim 10^{-4}$, which is still ~1 dex lower than the kinetic efficiency from Nesvadba et al. (2017a).

4.4. AGN illuminates the filamentary ISM after jet passage

In Sect. 3.1, we found that ionized ISM emission with $\lesssim$30 kpc of the AGN is dominated by gas close to the systemic redshift (Fig. 1c). Due to the limitation of the FoV, we only captured the northern extended region. In general, the gas morphology is elongated along the north-south direction, aligned with the jet axis. When we focus on the smaller scale structures (~5 kpc), these gaseous clouds are filamentary and patchy and do not follow the collimated jet but have larger angle separations (~30 deg). As discussed in Sect. 4.2, we are observing the ionization cone-like structures along the jet. This provides enough ionizing photons to illuminate the extended gaseous nebula beyond the galactic scale. The fact that we do not observe the extended ISM in directions outside of the ionization cone, for example in the west where we have the spatial coverage (Fig. 1), may be due to the shortage of ionizing photons. Hence, it may be that the patchy filaments in the north are the "intrinsic" structures, which are not seen in other directions as they are not emitting or simply outside the NIRSpec FoV.

The HzRGs we observed may have entered their flux-limited parent radio surveys because their radio lobes are brightened when they encounter a higher density environment which provides a larger "working surface" for the jet (Eales 1992; Wang et al. 2023). Combining the discussion in Sect. 4.3 and Nesvadba et al. (2017a), the situation of 4C+19.71 may be that the jet was launched ~60 Myr ago, and in its younger years could have pushed some gas outside of the host galaxy. Once the radio lobes have escaped the host galaxy, the radio jet is very collimated and is no longer interacting with the ISM; the observed systemic gas in Fig. 1 is thus no longer kinematically affected by the radio jets, but the gas is still photoionized by the AGN photons within the ionization cone along the jet axis.

Fu & Stockton (2009) found similar quiescent nebulae whose morphology do not fully agree with their radio maps in low-z quasars on comparable physical scales. They proposed that the expanding bubbles following the jet disturb the ISM. 4C+19.71 has one of the most powerful radio jets, $P_{\rm jet} \sim 10^{47}$ erg s^{-1} (using $\log(P_{1.4\,\rm GHz}/\rm W\,Hz^{-1}) = 28.6 \pm 0.1$, Nesvadba et al. 2017a; Cavagnolo et al. 2010). The situation may be different than the low-z low radio power quasars. Nevertheless, we find evidence of shock ionization on the extended northern nebula of which the jet could be the driver (Sect. 4.2). Further analysis (e.g., $T_{\rm e}$ mapping) will be helpful to determine the mechanisms.

4.5. Complex southern ISM

In Sect. 4.3, our discussion of the outflow is based on the northern region near the quasar as the nature of the southern "high-velocity" region is more complicated. In Fig. 1c2, we clearly find that there are three velocity components with the "high-velocity" ones (blue and red) dominating the flux. The morphology of the blue and red parts are not spatially overlapping (Figs. 1a, b1, and b3). Such kinematics resemble that of a rotating disk. If we simply take the velocity shifts of the blue and red components from the one spaxel spectrum (Fig. 1c2), $\Delta v_{\rm blue} = -585$ km s^{-1} and $\Delta v_{\rm red} = 535$ km s^{-1}. This is very high for a rotating disk; using the half size of ~4 kpc, this would imply a dynamical mass of $\sim 2 \times 10^{11}\,M_\odot$. We do not detect any continuum emitting source at this position, though we note that the partially overlapping foreground G2 may obscure some of the emission (Fig. 1a). Extracting from a $r = 0.1''$ aperture, the observed flux density upper limit is $\sim 10^{-20}$ erg s^{-1} cm^{-2} Å^{-1} at 2.5 µm (i.e., rest frame V band). This then gives an upper limit to the absolute V band magnitude of ~−17 which could be a galaxy with $M_\star \sim 10^8$ to $10^9\,M_\odot$ (e.g., Weaver et al. 2022). This corresponds to a $M_\star/M_{\rm dyn.} \sim 10^{-3}$ which is very small for a galaxy at $z \sim 3.5$. The southern region shows lower [O I]/Hα and [S II]/Hα than the rest of the nebula. It also has the potential to have subsolar metallicity (Sect. 4.2). Though our estimates have large uncertainties, we cannot exclude the possibility of it being a late stage merger. A more detailed kinematic study is required to unveil the nature of this region with complex kinematics.

4.6. Summary and future

In this work, we present the first NIRSpec IFU view of the ionized ISM in the vicinity of the $z \simeq 3.59$ radio-loud AGN 4C+19.71. With unprecedented resolution and sensitivity, we study the gas morphology, ionization states and preliminary kinematics within 10 kpc of the AGN. This makes it possible to study the role of the jet and radiative feedback near cosmic noon and to compare to low-z AGN and theoretical models. We find that the radiation from the hidden quasar dominates the ionization of the ISM of 4C+19.71 which resembles the scenario of other powerful quasars at cosmic coon. The radiatively driven outflow is only found within 5 kpc of the AGN and is inefficiently ($\sim 10^{-5}$) coupled to the central $L_{\rm bol} \sim 10^{47}$ erg s^{-1} quasar even at the nucleus. Combining with ground-based studies, we conclude that the jet kinetic energy takes a leading role in the feedback of this HzRG at $z \sim 3.5$. Line ratio diagnostics infer the existence of a ionization cone along the jet axis. The AGN ionizing photons illuminate the filamentary extended ISM along the cone. The observed morphology may be the "intrinsic" shape of the dense gas around this relatively massive galaxy. These conclusions are based on the first source from our sample. The picture of the feedback from the most powerful radio sources will be clearer with our full sample which will allow kinematics studies of the ionized ISM of radio-loud AGN with very different jet morphologies.

Acknowledgements. This work uses the NASA's Astrophysics Data System and a number of open source software other than the aforementioned ones such as Jupyter notebook (Kluyver et al. 2016); `matplotlib` (Hunter 2007); `SciPy` (Virtanen et al. 2020); `NumPy` (Harris et al. 2020); `Astropy` (Astropy Collaboration 2018); `LMFIT` (Newville et al. 2016). We thank Daizhong Liu and Markus Hundertmark for the useful discussion of the WCS alignment. This work is based in part on observations made with the NASA/ESA/CSA *James Webb* Space Telescope. The data were obtained from the Mikulski Archive for Space Telescopes at the Space Telescope Science Institute, which is operated by the Association of Universities for Research in Astronomy, Inc., under NASA contract NAS 5-03127 for JWST. These observations are associated with program JWST-GO-01970. Support for program JWST-GO-01970 was provided by NASA through a grant from the Space Telescope Science Institute, which is operated by the Association of Universities for Research in Astronomy, Inc., under NASA contract NAS 5-03127. D.W. and W.W. acknowledge support through an Emmy Noether Grant of the German Research Foundation, a stipend by the Daimler and Benz Foundation and the MERAC foundation and a Verbundforschung grant by the German Space Agency. N.L.Z. and A.V. are supported in part by NASA through STScI grants JWST-ERS-01335 and JWST-GO-01970. The work of D.S. was carried out at the Jet Propulsion Laboratory, California Institute of Technology, under a contract with NASA. This paper makes use of the following ALMA data: ADS/JAO.ALMA#2021.1.00576.S. ALMA is a partnership of ESO (representing its member states), NSF (USA) and NINS (Japan), together with NRC (Canada), MOST and ASIAA (Taiwan), and KASI (Republic of Korea), in cooperation with the Republic of Chile. The Joint ALMA Observatory is operated by ESO, AUI/NRAO and NAOJ.

References

Alarie, A., & Morisset, C. 2019, Rev. Mex. Astron. Astrofis., 55, 377
Alatalo, K., Cales, S. L., Rich, J. A., et al. 2016, ApJS, 224, 38
Allen, M. G., Groves, B. A., Dopita, M. A., Sutherland, R. S., & Kewley, L. J. 2008, ApJS, 178, 20
Armus, L., Soifer, B. T., Murphy, T. W., Jr., et al. 1998, ApJ, 495, 276
Astropy Collaboration (Price-Whelan, A. M., et al.) 2018, AJ, 156, 123
Baldwin, J. A., Phillips, M. M., & Terlevich, R. 1981, PASP, 93, 5
Baron, D., Netzer, H., Poznanski, D., Prochaska, J. X., & Förster Schreiber, N. M. 2017, MNRAS, 470, 1687
Begelman, M. C., & Cioffi, D. F. 1989, ApJ, 345, L21
Böker, T., Arribas, S., Lützgendorf, N., et al. 2022, A&A, 661, A82
Calzetti, D., Armus, L., Bohlin, R. C., et al. 2000, ApJ, 533, 682
Carilli, C. L., & Barthel, P. D. 1996, A&ARv, 7, 1
Carilli, C. L., Röttgering, H. J. A., van Ojik, R., Miley, G. K., & van Breugel, W. J. M. 1997, ApJS, 109, 1

Cavagnolo, K. W., McNamara, B. R., Nulsen, P. E. J., et al. 2010, ApJ, 720, 1066
Collet, C., Nesvadba, N. P. H., De Breuck, C., et al. 2016, A&A, 586, A152
Costa, T., Rosdahl, J., Sijacki, D., & Haehnelt, M. G. 2018, MNRAS, 479, 2079
Cresci, G., Tozzi, G., Perna, M., et al. 2023, A&A, 672, A128
De Breuck, C., Röttgering, H., Miley, G., van Breugel, W., & Best, P. 2000, A&A, 362, 519
De Breuck, C., Seymour, N., Stern, D., et al. 2010, ApJ, 725, 36
Drouart, G., De Breuck, C., Vernet, J., et al. 2012, A&A, 548, A45
Drouart, G., De Breuck, C., Vernet, J., et al. 2014, A&A, 566, A53
Dugan, Z., Gaibler, V., & Silk, J. 2017, ApJ, 844, 37
Eales, S. A. 1992, ApJ, 397, 49
Fabian, A. C. 2012, ARA&A, 50, 455
Falkendal, T., De Breuck, C., Lehnert, M. D., et al. 2019, A&A, 621, A27
Falkendal, T., Lehnert, M. D., Vernet, J., De Breuck, C., & Wang, W. 2021, A&A, 645, A120
Fanaroff, B. L., & Riley, J. M. 1974, MNRAS, 167, 31P
Fosbury, R. A. E., Vernet, J., Villar-Martín, M., et al. 1999, in The Most Distant Radio Galaxies, eds. H. J. A. Röttgering, P. N. Best, & M. D. Lehnert, 311
Fu, H., & Stockton, A. 2009, ApJ, 690, 953
Gaia Collaboration (Vallenari, A., et al.) 2023, A&A, 674, A1
Groves, B. A., Dopita, M. A., & Sutherland, R. S. 2004a, ApJS, 153, 9
Groves, B. A., Dopita, M. A., & Sutherland, R. S. 2004b, ApJS, 153, 75
Groves, B. A., Heckman, T. M., & Kauffmann, G. 2006, MNRAS, 371, 1559
Harris, C. R., Millman, K. J., van der Walt, S. J., et al. 2020, Nature, 585, 357
Harrison, C. M. 2017, Nat. Astron., 1, 0165
Harrison, C. M., Alexander, D. M., Mullaney, J. R., & Swinbank, A. M. 2014, MNRAS, 441, 3306
Harrison, C. M., Costa, T., Tadhunter, C. N., et al. 2018, Nat. Astron., 2, 198
Heckman, T. M., & Best, P. N. 2014, ARA&A, 52, 589
Herrera-Camus, R., Förster Schreiber, N., Genzel, R., et al. 2021, A&A, 649, A31
Holden, L. R., Tadhunter, C. N., Morganti, R., & Oosterloo, T. 2023, MNRAS, 520, 1848
Hunter, J. D. 2007, Comput. Sci. Eng., 9, 90
Husemann, B., Wisotzki, L., Sánchez, S. F., & Jahnke, K. 2013, A&A, 549, A43
Jakobsen, P., Ferruit, P., Alves de Oliveira, C., et al. 2022, A&A, 661, A80
Kauffmann, G., Heckman, T. M., Tremonti, C., et al. 2003, MNRAS, 346, 1055
Kewley, L. J., Dopita, M. A., Sutherland, R. S., Heisler, C. A., & Trevena, J. 2001, ApJ, 556, 121
Kewley, L. J., Groves, B., Kauffmann, G., & Heckman, T. 2006, MNRAS, 372, 961
Kewley, L. J., Maier, C., Yabe, K., et al. 2013, ApJ, 774, L10
Kewley, L. J., Nicholls, D. C., & Sutherland, R. S. 2019, ARA&A, 57, 511
Kluyver, T., Ragan-Kelley, B., Pérez, F., et al. 2016, in Positioning and Power in Academic Publishing: Players, Agents and Agendas, eds. F. Loizides, & B. Schmidt (IOS Press), 87
Kolwa, S., De Breuck, C., Vernet, J., et al. 2023, MNRAS, 525, 5831
Kondapally, R., Best, P. N., Raouf, M., et al. 2023, MNRAS, 523, 5292
Liu, W., Veilleux, S., Canalizo, G., et al. 2020, ApJ, 905, 166
Madau, P., & Dickinson, M. 2014, ARA&A, 52, 415
Maxfield, L., Spinrad, H., Stern, D., Dey, A., & Dickinson, M. 2002, AJ, 123, 2321
Miley, G., & De Breuck, C. 2008, A&ARv, 15, 67
Mukherjee, D., Bicknell, G. V., Sutherland, R., & Wagner, A. 2016, MNRAS, 461, 967
Mukherjee, D., Bicknell, G. V., Wagner, A. Y., Sutherland, R. S., & Silk, J. 2018, MNRAS, 479, 5544
Mukherjee, D., Bicknell, G. V., & Wagner, A. Y. 2021, Astron. Nachr., 342, 1140
Mullaney, J. R., Alexander, D. M., Fine, S., et al. 2013, MNRAS, 433, 622
Nakajima, K., & Maiolino, R. 2022, MNRAS, 513, 5134
Nesvadba, N. P. H., Lehnert, M. D., Eisenhauer, F., et al. 2006, ApJ, 650, 693
Nesvadba, N. P. H., Lehnert, M. D., De Breuck, C., Gilbert, A., & van Breugel, W. 2007, A&A, 475, 145
Nesvadba, N. P. H., Lehnert, M. D., De Breuck, C., Gilbert, A. M., & van Breugel, W. 2008, A&A, 491, 407
Nesvadba, N. P. H., De Breuck, C., Lehnert, M. D., Best, P. N., & Collet, C. 2017a, A&A, 599, A123
Nesvadba, N. P. H., Drouart, G., De Breuck, C., et al. 2017b, A&A, 600, A121
Newville, M., Stensitzki, T., Allen, D. B., et al. 2016, Astrophysics Source Code Library [record ascl:1606.014]
Ogle, P. M., Cohen, M. H., Miller, J. S., et al. 1997, ApJ, 482, L37
Osterbrock, D. E., & Ferland, G. J. 2006, Astrophysics of Gaseous Nebulae and Active Galactic Nuclei (Sausalito: University Science Books)
Pentericci, L., Röttgering, H. J. A., Miley, G. K., et al. 1999, A&A, 341, 329
Perna, M., Arribas, S., Marshall, M., et al. 2023, A&A, 679, A89
Rupke, D. S. N. 2014, Astrophysics Source Code Library [record ascl:1409.005]
Rupke, D. S. N., & Veilleux, S. 2013, ApJ, 775, L15
Rupke, D. S. N., Schweitzer, M., Viola, V., et al. 2021, Astrophysics Source Code Library [record ascl:2112.002]
Rupke, D., Wylezalek, D., Zakamska, N., et al. 2023, Astrophysics Source Code Library [record ascl:2310.004]
Sanders, R. L., Shapley, A. E., Kriek, M., et al. 2016, ApJ, 816, 23
Sanders, R. L., Shapley, A. E., Topping, M. W., Reddy, N. A., & Brammer, G. B. 2024, ApJ, 962, 24
Seymour, N., Stern, D., De Breuck, C., et al. 2007, ApJS, 171, 353
Smail, I., Blundell, K. M., Lehmer, B. D., & Alexander, D. M. 2012, ApJ, 760, 132
Tadhunter, C., Wills, K., Morganti, R., Oosterloo, T., & Dickson, R. 2001, MNRAS, 327, 227
Tadhunter, C., Marconi, A., Axon, D., et al. 2003, MNRAS, 342, 861
Tadhunter, C., Dicken, D., Holt, J., et al. 2007, ApJ, 661, L13
Tanner, R., & Weaver, K. A. 2022, AJ, 163, 134
van Bemmel, I. M., Vernet, J., Fosbury, R. A. E., & Lamers, H. J. G. L. M. 2003, MNRAS, 345, L13
van Ojik, R., Roettgering, H. J. A., Carilli, C. L., et al. 1996, A&A, 313, 25
Vayner, A., Zakamska, N. L., Ishikawa, Y., et al. 2023, ApJ, 955, 92
Vayner, A., Zakamska, N. L., Ishikawa, Y., et al. 2024, ApJ, 960, 126
Veilleux, S., & Osterbrock, D. E. 1987, ApJS, 63, 295
Veilleux, S., Liu, W., Vayner, A., et al. 2023, ApJ, 953, 56
Vernet, J. 2001, PhD Thesis, Université de Paris Diderot (Paris VII), France
Vernet, J., Fosbury, R. A. E., Villar-Martín, M., et al. 2001, A&A, 366, 7
Villar-Martín, M., Tadhunter, C., Morganti, R., Axon, D., & Koekemoer, A. 1999, MNRAS, 307, 24
Virtanen, P., Gommers, R., Oliphant, T. E., et al. 2020, Nat. Meth., 17, 261
Wang, W., Wylezalek, D., Vernet, J., et al. 2023, A&A, 680, A70
Weaver, J. R., Kauffmann, O. B., Ilbert, O., et al. 2022, ApJS, 258, 11
Whitmore, B. C., Allam, S. S., Budavári, T., et al. 2016, AJ, 151, 134
Wylezalek, D., Zakamska, N. L., Liu, G., & Obied, G. 2016, MNRAS, 457, 745
Wylezalek, D., Schnorr Müller, A., Zakamska, N. L., et al. 2017, MNRAS, 467, 2612
Wylezalek, D., Vayner, A., Rupke, D. S. N., et al. 2022, ApJ, 940, L7
Zakamska, N. L., Strauss, M. A., Krolik, J. H., et al. 2003, AJ, 126, 2125
Zakamska, N. L., Hamann, F., Pâris, I., et al. 2016, MNRAS, 459, 3144

Wang, W., et al.: A&A, 683, A169 (2024)

Appendix A: Astrometric correction

The *JWST* Fine Guidance Sensor (FGS) is responsible for guiding the pointing, and there is no known issue in the guiding process. However, there is a known systematic WCS offset of the NIRSpec IFU[4]. This is due to poorly registered IFU detector coordinates on the *JWST* focal panel with respect to the reference V2 and V3 axes. This corresponds to 0.173″ and 0.178″ in the V2 and V3 direction[5], respectively (Help Desk, private communication through). This offset projection to sky (RA, Dec) coordinates could then be calculated using `pysiaf` by assuming the targeted RA and Dec of the IFU pointing is correct. The projection matrix for converting V2, V3 coordinates to the sky plane can be set by `pysiaf.utils.rotations.attitude_matrix` using the old (V2, V3) reference coordinates, target RA and Dec, and angle between the north and V3. This angle is measured from north to east with a value of 83.0652845 deg for our observation. It is calculated using the angle between the IFU with respect to the North (from the header) and the fixed angle between the IFU and V3. There is an additional $\sim 3''$ systematic rotational angle error between the IFU plane and V3 axis. Since this will only result in a secondary ($\sim 0.007''$) offset, we neglect it here. The final systemic offsets of the pointing, from updated position to the original position, are ΔRA= 0.21″ and ΔDec= −0.15″. We refer to this correction as "Correction1". This error has been reported as partially corrected using the up-to-date context file. We test the new pipeline assigned WCS using jwst_1093.pmap and find it matches closely with our "Correction1". We report an offset of $|\Delta\mathrm{RA}| = 0.09''$ and $|\Delta\mathrm{Dec}| = 0.07''$ using the fit 2D Gaussian centroids of G1 at $\sim 2.7\mu$m. Hence, we consider this systematic WCS error has been fixed. However, other source of uncertainty is still presented and still required manual alignment.

In addition, there is a further offset due to the zero-point shift of the NIRSpec detector and the FGS which adds another term to the aforementioned values in the V2V3 plane. The shifts are -0.016″ and 0.111″ in V2 and V3 coordinates, respectively (Help Desk, private communication). However, a caution is noted that the direction of this shift is not well-understood. We assumed this direction and followed the aforementioned procedure using `pysiaf`. This resulted in the ΔRA= 0.09″ and ΔDec= −0.14″. We refer to this correction as "Correction2++". Since the direction is uncertain, we produced further corrections "Correction2+−", "Correction2−+", and "Correction2−−". The "+" and "−" signs indicate which direction we adopted for the offset with respect to the original direction suggested by, the Help Desk.

Table A.1. Offset between different astrometry and manual shift.

Method	$\Delta\alpha_{\rm manual}$	$\Delta\delta_{\rm manual}$
Correction1	0.22″	-0.06″
Correction2++	-0.34″	0.07″
Correction2+−	-0.10″	0.09″
Correction2−+	-0.10″	0.06″
Correction2−−	-0.34″	0.07″

For the manual correction of the astrometry, we matched G1 positions (Section 3) measured from the $\sim 2.7\mu$m continuum image collapsed from our NIRSpec IFU cube and the *HST*/WFPC2 (Whitmore et al. 2016) image. This was done by matching the centroids of the fit 2D Gaussian profile. We caution that although we updated the astrometry of the *HST* image using *Gaia* DR3 (Gaia Collaboration 2023), the uncertainty of the WCS position is $\sim 0.06''$. This is estimated based on the standard deviation of the offsets of the cross matched *Gaia* targets in the *HST* FoV. This uncertainty ($\sim 1.2''$ given the unknown direction) is marked by the size of the plus marker in Fig. 1d. We further note that the *HST* image was observed in 1997. The proper monition of the stars were taken into account during the correction by adopting the reported epoch=J2000 coordinates in the *Gaia* DR3 catalog. Another source of uncertainty could be the intrinsic continuum emission offset from different bands. The *HST*/WFPC2 image was taken with the F702W filter, which corresponds to 2520 Å in the rest frame of G1. The NIRSpec IFU data covers $\sim 0.57 - 1.15\mu$m for G1. We examined the continuum centroid offset of G1 by extracting narrowband images at the blue and red ends of the data cube. A $\sim 0.09''$ shift is seen.

We present the offsets of these corrections with respect to the manual shift (aligned with *HST*) used in the analysis in Table A.1. Fig. A.1 presents the visual inspection of the WCS correction by comparing the results from different methods. We mark the *HST* positions of the three continuum emission objects with green circles. The radius of each circle is 0.12″ which can be used as the spatial uncertainty of the *HST* object. We see that Correction2+− and Correction2−+ have $\sim 0.1''$ offsets from the manual shift (or *HST* WCS). Given that there is a $\sim 0.1''$ uncertainty in the *HST*-NIRSpec alignment, we decide that the IFU WCS offset can be solved by correcting the systematic error. Since the direction of the error is not well-understood, we use the manual match in this paper.

[4] https://jwst-docs.stsci.edu/jwst-observatory-characteristics/jwst-pointing-performance
[5] https://jwst-docs.stsci.edu/jwst-observatory-characteristics/jwst-field-of-view

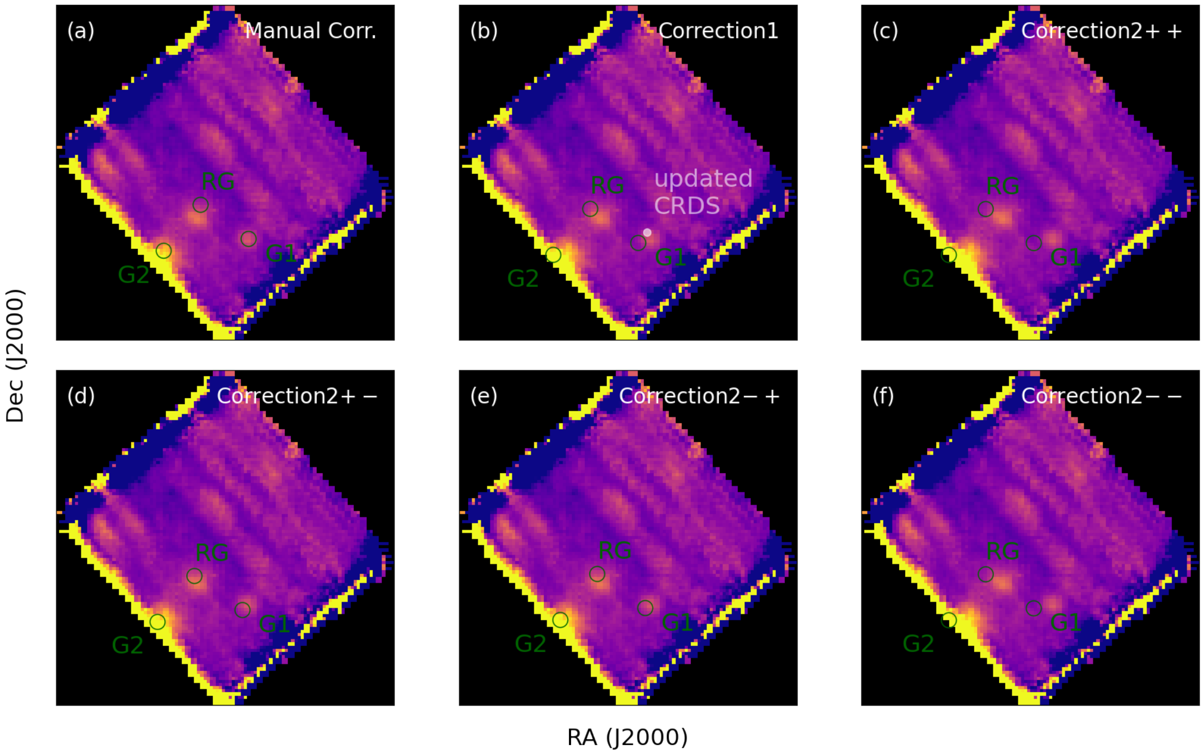

Fig. A.1. Narrowband continuum images (observed frame 2.721 − 2.778μm) with WCS corrected with different methods. The method is labeled at the top right corner of each panel. The three green circles mark the positions of the host galaxy of 4C+19.71 (RG), G1, and G2. The radius of each circle is 0.12″ which can be used roughly as the uncertainty of the *HST* WCS. The white dot in panel (b) marks the centroid of G1 using the updated CRDS (jwst_1093.pmap).

Appendix B: Foreground galaxies

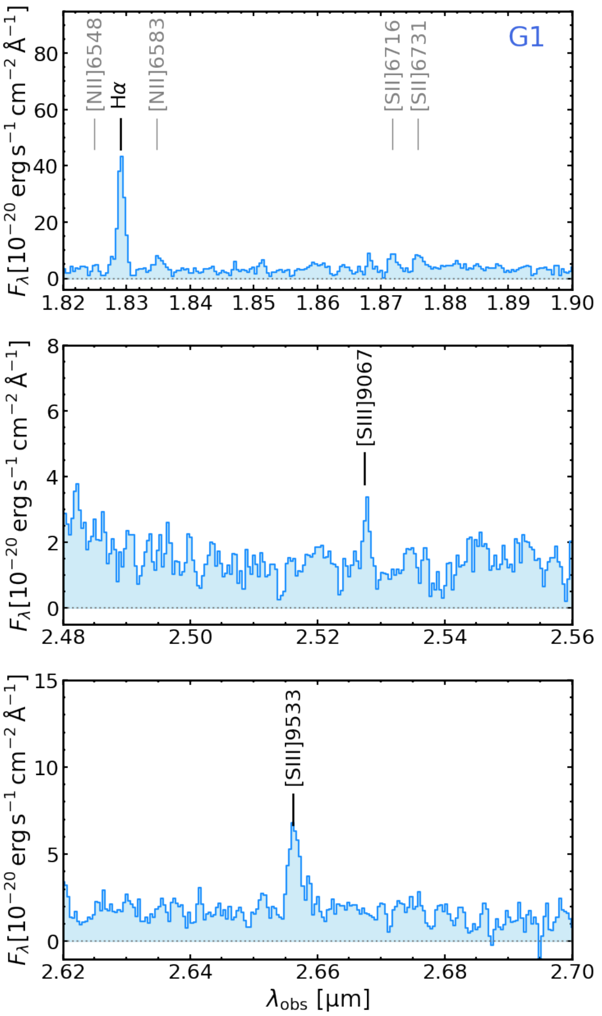

Fig. B.1. Spectrum extracted at the position of foreground galaxy, G1, without continuum subtraction. Upper panel: Zoom-in view of the spectrum around Hα. Middle panel: Zoom-in view of the spectrum around [S III]9071. Bottom panel: Zoom-in view of the spectrum around [S III]9533. We mark the lines detected both spectrally and spatially in thick black lines. The expected positions of the lines around Hα are marked in gray lines.

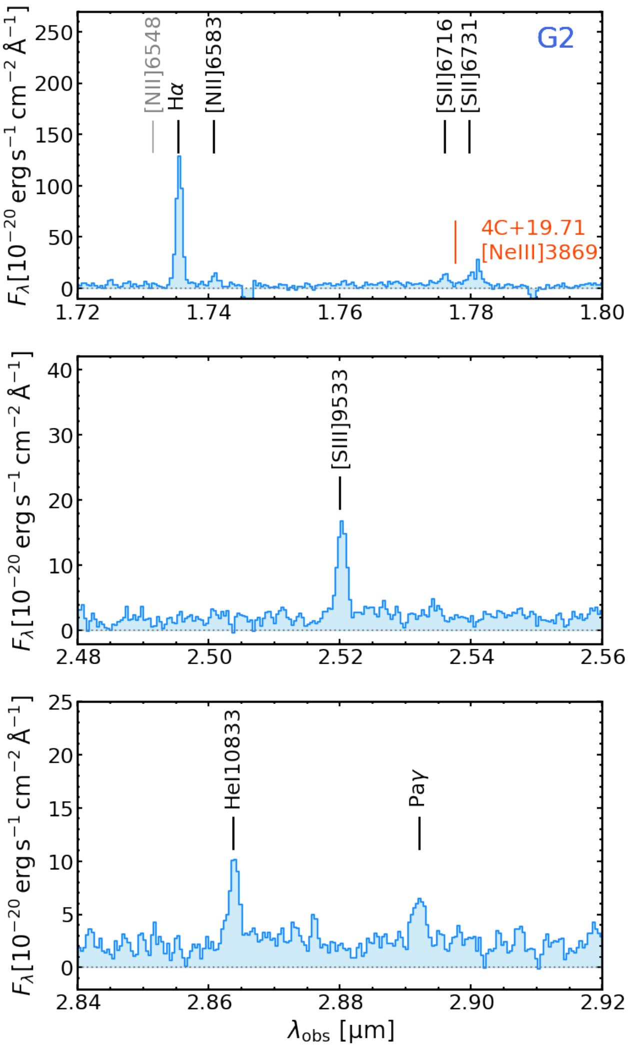

Fig. B.2. Spectrum extracted at the position of foreground galaxy, G2, without continuum subtraction. Upper panel: Zoom-in view of the spectrum around Hα. Middle panel: Zoom-in view of the spectrum around [S III]9533. Bottom panel: Zoom-in view of the spectrum around He I10833. Same line-marking conventions are adopted as Fig. B.1. We further mark in orange the position of [Ne III]3869 emission from 4C+19.71 which is near the [S II]6716,6731 doublet of G2 (upper panel).

We report in Sect. 3 that two foreground galaxies have been identified with continuum and emission lines: G1 to the west of the radio galaxy and G2 to the east. There we present the spectra of G1 and G2. Their positions are marked with blue dots in Fig. 1 which are the centers of their extraction apertures. For both galaxies, we used square apertures with the size of $0.25'' \times 0.25''$ ($\sim 5{\times}5\,\mathrm{pix}^2$) and summed each spectrum from the spaxels inside the aperture. For partially covered spaxels, we multiply the area by the fractional overlap with the extraction aperture. The aperture for G1 was centered at its continuum peak position. As for G2 which is only partially captured in our FoV, we placed the aperture to be as close as possible to its continuum emission peak while minimizing the impact from the detector edge. In Fig. B.1 and B.2, we show the spectra extracted for G1 and G2, respectively. The redshifts of G1 and G2 are determined based on their Hα lines and have values of $z_{\rm G1} \simeq 1.786$ and $z_{\rm G2} \simeq 1.643$. For each foreground galaxy, at least two more emission lines are identified based on their redshifts. We use thick black vertical lines to mark the spatially and spectrally detected emission lines. The expected positions of emission lines near Hα based on the derived redshift of the targets are marked in gray lines if not clearly detected. We note that the [S II]6716,6731 doublet of G2 overlaps with the [Ne III]3869 line of 4C+19.71 in wavelength (orange line in top panel of Fig. B.2). The spatial check confirms that there are distinct emission peaks separated by $\sim 0.4''$.

Wang, W., et al.: A&A, 683, A169 (2024)

Appendix C: Emission line list

Table C.1. Fit emission line fluxes. The reported uncertainty is the direct 1σ output of `q3dfit`.

Line	central comp.	red comp.	blue comp.
		f [10^{-18} erg s^{-1} cm^{-2}]	
[O II]3726,3729	5.8±0.4	2.1±0.4	8.9±1.6
[Ne III]3869	3.3±0.2	0.8±0.2	1.3±0.9
He I3888 + H8*		< 0.5	
[Ne III]3967 + Hϵ	1.5±0.4	0.4±0.3	0.4±1.4
Hδ	0.7±0.3	0.2±0.2	0.6±0.9
Hγ	1.6±0.2	0.4±0.2	0.4±0.7
He I4472*		< 0.4	
He II4686	1.4±0.1	< 0.2†	1.1±0.8
Hβ	3.9±0.2	0.6±0.2	2.9±0.7
[O III]4959	17.5±0.5	1.8±0.4	8.7±1.5
[O III]5007	53.1±1.0	5.6±1.0	26.3±1.6
He I5876*		< 0.6	
[Fe VII]6087*		< 0.7	
[O I]6300	2.4±0.2	0.3±0.2	3.1±0.8
[S III]6312	0.4±0.2	0.2±0.2	0.9±0.9
[O I]6364	0.8±0.3	0.1±0.3	1.0±1.1
[N II]6548	2.0±0.3	0.7±0.3	4.0±1.1
Hα	15.8±0.4	1.2±0.3	14.7±1.1
[N II]6583	6.0±0.4	2.0±0.3	12.0±1.1
[S II]6716	1.6±0.2	0.3±0.2	2.1±0.6
[S II]6731	1.8±0.2	0.6±0.2	4.8±1.1

Notes. *We report 3σ upper limits for lines with low S/N (Sect. 3.3). †Though the He II4686 has $S/N > 10$, the fit reported the flux of its comp. red to be 0. Hence, we report the upper limit here.

We fit the 1D spectrum presented in Section 3.3 (Fig. 2) using `q3dfit`. The continuum is modeled by a third order polynomial and the emission lines ($S/N > 10$) are fit with Gaussian profiles. We set the maximum number of the Gaussian components to be three for the fit. The centroid (width) of each corresponding Gaussian component is set to be the same (Vayner et al. 2023). The fit line fluxes are shown in Table C.1. For the doublet [O II]3726,3729, we set the flux ratio to be 1:1 and report the summation since they are spectrally unresolved. For the low S/N lines (Sect. 3.3), we report 3σ upper limits.

Appendix D: Systemic redshift based on ionized gas

The systemic redshift (velocity zero) used in this work is based on the [C I](1-0) (z=3.5892, Kolwa et al. 2023). Given its relatively faint flux and large observed beam size, it is unclear whether this traces the "authentic" redshift of the host galaxy. The ideal tracer would be the stellar absorption lines (e.g., Ca II HK). However, the continuum emission near the nucleus is AGN dominated (Sect. 4.1) for our target. Nevertheless, we report the [O III] flux-weighted redshift based on the fit "low-velocity" components from the entire FoV (Sect. 4.2). We define the "low-velocity" components as the ones with $|\Delta v| < 300\,\mathrm{km\,s^{-1}}$ (e.g., Fu & Stockton 2009). The redshift is $z_{[\mathrm{O\,III}]} = 3.5908 \pm 0.0017$ which corresponds to $108 \pm 114\,\mathrm{km\,s^{-1}}$ with respect to the [C I](1-0) redshift. The $z_{[\mathrm{O\,III}]}$ and $z_{[\mathrm{C\,I}]}$ are consistent within the relatively large uncertainty.

In our calculation in Sect. 4.3, we assume the central component is the systemic component. Its $\Delta v_{\mathrm{central}} = 238 \pm 10\,\mathrm{km\,s^{-1}}$ agrees with the systemic velocity estimated here from the entire FoV.

Appendix E: Estimation of electron density

We use the fiducial value of n_e in the calculation in Sect. 4.3 (Nesvadba et al. 2017a). The n_e for the red and blue components can also be estimated based on the fit [S II]6716 and [S II]6731 lines ratios (0.50 and 0.44 for red and blue components respectively; Table C.1). This result in a $n_e \sim 8 \times 10^3\,\mathrm{cm^{-3}}$ and $\sim 8 \times 10^4\,\mathrm{cm^{-3}}$ for the red and blue components, respectively (e.g., Sanders et al. 2016). These are much larger than the fiducial value, $n_e = 500\,\mathrm{cm^{-3}}$, from Nesvadba et al. (2017a). However, the fit line ratios for these two kinematic components are in the range where they are not sensitive to n_e. If we nevertheless use n_e based on our estimation, the radiative coupling efficiency becomes $\sim 10^{-7}$, and continues to support the conclusion is valid that the radiative-driven outflow is inefficient in 4C+19.71.

We report that the n_e of the central component is $\sim 800\,\mathrm{cm^{-3}}$ based on its [S II]6716 and [S II]6731 ratio (0.89, Table C.1; Sanders et al. 2016) which is the same order of magnitude as the value reported by Nesvadba et al. (2017a). Further analysis is required to understand the electron temperature and density at the center.

5 Discussion and outlook

I exploited state-of-the-art IFUs to investigate the multiphase CGM and ISM of distant radio-loud AGN. Despite the fact that the boundary between CGM and ISM is not clearly defined (Tumlinson et al., 2017), there is no doubt that jointly they are a key component for studying the fueling and feedback processes in galaxy evolution. The period of focus, Cosmic high-Noon ($z \approx$3-6), bridges the EoR and the peak of star formation rate density, approximately coinciding with the peak of black hole growth. It is the best time for examining the build-up of some of the most massive galaxies. In this thesis, I present new insights into the gaseous medium in the presence of both violent AGN activities, utilizing *JWST*/NIRSpec IFU, VLT/MUSE, and ALMA covering the rest frame UV to FIR.

Chapter 1 serves as the general introduction to this thesis, providing a broader overview of the different chapters in Section 1.6. Readers can also find the detailed summaries at the beginning of each chapter. The work presented in Chapter 2-4 is more or less limited to the focuses on the major datasets analyzed there. Within the current observational ability, the objects investigated in this thesis are stationary comparing to the lifetime of humankind. Nevertheless, one ought to employ both a panoramic and developing perspective when examining AGN, which are not objects but events. In the first part of this following chapter, I provide a short discussion bringing together the different parts of the multi-wavelength 3D views. My work so far is only the tip of the iceberg. These amazing datasets can serve as the basis for ~5 other PhD theses. In the second part of the chapter, I present potential future plans stemming from the current observations of this most well-studied HzRGs sample, and also offer an outlook beyond.

5.1 Discussion

As introduced in Chapter 1, the 3D view provided by the IFUs continues to revolutionize our understanding of galaxy evolution. In addition to presenting thorough analyses of each cube individually, efforts should also be devoted to integrating the information revealed by different instruments to paint a more comprehensive picture. This will not only help us understand the influence of

AGN on the different components of their host galaxies but also the evolutionary paths of active galaxies.

In this thesis (and also during my PhD), 4C+19.71 is the only HzRG that has been analyzed with all cubes (Chapter 3 and 4, see also Falkendal et al., 2021; Kolwa et al., 2023, for ALMA observed $[\mathrm{C\,I}]$). Additionally, VLT/SINFONI analysis was also carried out for it with lower sensitivity but larger spatial coverage (Nesvadba et al., 2017b). I will use this source as an example for discussion, utilizing 3D information coming from different angles: (i) MUSE covers rest frame UV emissions with a spatial resolution of $\sim 1''$; (ii) SINFONI detects bright optical [O III] at similar resolution with a $10'' \times 10''$ field-of-view; (iii) NIRSpec IFU presents the sub-kpc view of optical emissions with higher sensitivity; (iv) ALMA Band 3 traces the [C I] with a beam size of $\sim 2''$; (v) ALMA Band 8 shows the [C II] and dust at comparable resolution as *JWST*.

It is not surprising that the AGN photons dominates the ionization of gas on galactic scales as confirmed by the NIRSpec IFU data. On larger scales, such as around the jet hot spots (projected $\sim 30\,$kpc away from the center), Falkendal et al. (2021) found that photons from the AGN still play an important role, as evidenced by emission lines captured by both MUSE and ALMA. Regarding gas kinematics, *JWST* suggests weak radiatively driven outflows even at the center. Although it is not possible to differentiate each component, results from SINFONI data suggest bulk gas motion and relate it to the driving mechanism by the jet using [O III]$\lambda\lambda 4959, 5007$. However, UV emitting halo observed by MUSE indicates the quiescent nature on of the gas on CGM scales. We caution that the Lyα is not a good kinematic tracer, and it is also affected by sky-lines for 4C+19.71 (Chapter 3). The spectrally resolved C IV$\lambda\lambda 1548, 1551$ doublet, with less perturbed nature, at the jet hot spot is another piece of information of this quiescence. Molecular gas is detected both at the core and at one radio hot spot (Falkendal et al., 2021). This similar spatial distribution of H_2, aligned with the jet axis, has also been found in other HzRGs (e.g., Emonts et al., 2014). Therefore, we may conclude that the AGN radiation has a minor effect on gas kinematics — it cannot even eject the ionized gas, let alone the dense molecular gas. It is not straightforward to link the H_2 (probed by [C I]) to the kinematics of the ionized CGM gas to look for evidence of jet ejection, as their physical conditions are different. On the other hand, we could examine the scenario from an additional angle other than the jet ejection. Given that the indicated metallicity is low at the hot spots, we may witness the jet-induced gas cooling at larger scales for 4C+19.71 (Emonts et al., 2014; Falkendal et al., 2021). The low, yet not negligible, SFR (84 $M_\odot\,\mathrm{yr}^{-1}$) is constrained from integrated SED with little spatial information (Falkendal et al., 2019). Besides, it has only been ~ 60 Myr since the launch of the jet (e.g., Wang et al., 2024). Hence, it is not impossible that the stars are still being formed in the host, i.e., near the radio core center (as seen in ALMA Band 8), even though we presume the jet is doing the quenching. Intriguing questions such as the spatial distribution of the newly formed stars and the subsequent radiative feedback from the quasars will be left for future exploration (Section 5.2).

5.2 Outlook

5.2.1 Fundamental Lyα physics

In Chapter 2 and 3, my analyses of Lyα were based on the basic assumption of neutral hydrogen absorption correction. We discussed the other possible treatment, namely radiative transfer (e.g., Verhamme et al., 2006), in Section 3.5, along with a quantitative test. The ability of MUSE presented us with a coherent view of the line profiles across tens of kiloparsecs, supporting our simple idea where a H I shell (Binette et al., 2000) — with no particular shape needs to be assumed — absorbs or scatters photons outside our field-of-view (i.e., they are lost). Indeed, in reality, both mechanisms likely take effect simultaneously. There has not been much analysis of the Lyα nebulae following the absorption correction technique outside the field of HzRGs (e.g., see Zhang et al., 2023, as an example). Now, we can and should take full advantage of IFUs to reconstruct the intrinsic emissions tracing the CGM. This thesis represents a pioneering effort in providing a careful treatment of the nebulae under this assumption in full 3D view.

Although not an IFU (i.e., outside the topic of this thesis), the VLT/UVES, with a factor of three higher in spectral resolution than MUSE, is perfect for testing this basic physics. A systematic statistical analysis of the absorbing gas using this dataset is ongoing at the time of writing (Ritter et al. in prep.). With these results, we can initiate work by involving both radiative transfer and hydrodynamic modeling set up for emitting gas distribution around HzRGs specifically, utilizing information from MUSE. The predicted spectra can then be compared with the observed ones (e.g., Costa et al., 2022). We can answer questions such as what the line broadening mechanisms are, how much of the intrinsic photons are lost, and where these photons go. This will unveil the Lyα physics at the dense nodes of cosmic filaments in the presence of activate AGN-gas interactions.

5.2.2 NIRSpec IFU + ALMA and multiwavelength data

The details embedded in the NIRSpec IFU data cubes are numerous. Just by simply counting numbers, which is a significant overestimation, we have only explored 25% in Chapter 4. We selected these four radio galaxies into the proposal due to their common redshifts and wealth of ancillary multiwavelength data (Section 1.5.4). Otherwise, they are unique individually. For example, TN J0121+1320 is the only target with compact spatially unresolved radio emission, while others all have double-sided jets with extents of several tens of kiloparsecs. It also has the highest SFR at $\sim 626\,M_{\odot}\,\mathrm{yr}^{-1}$, while TN J0205+2242 seems already quenched with only an upper limit of SFR constrained at $< 84\,M_{\odot}\,\mathrm{yr}^{-1}$ (Falkendal et al., 2019). 4C+03.24 has a clear indication of deflected jet indicating strong jet-cloud interaction. Hence, it would be interesting to look at different scenarios within each of them as well as some common trends as a sample.

My ALMA program provides the resolution matched ($\sim 0.2'' \times 0.15''$) view as the NIRSpec IFU cubes. The [C II]158 μm ([C II]) line and the dust continuum underneath will provide unique information on the ordered gas motion and the newly formed stellar population. Two out of four of the radio galaxies have detection (the others were not fully observed, Section 1.5.4). It will be fascinating to study the cold gas with less disturbance from the AGN. As [C II] is a frequently used dynamic tracer for Cosmic high-Noon galaxies (Faisst et al., 2020b), we can related the kinematics of active and star forming galaxies in this key period.

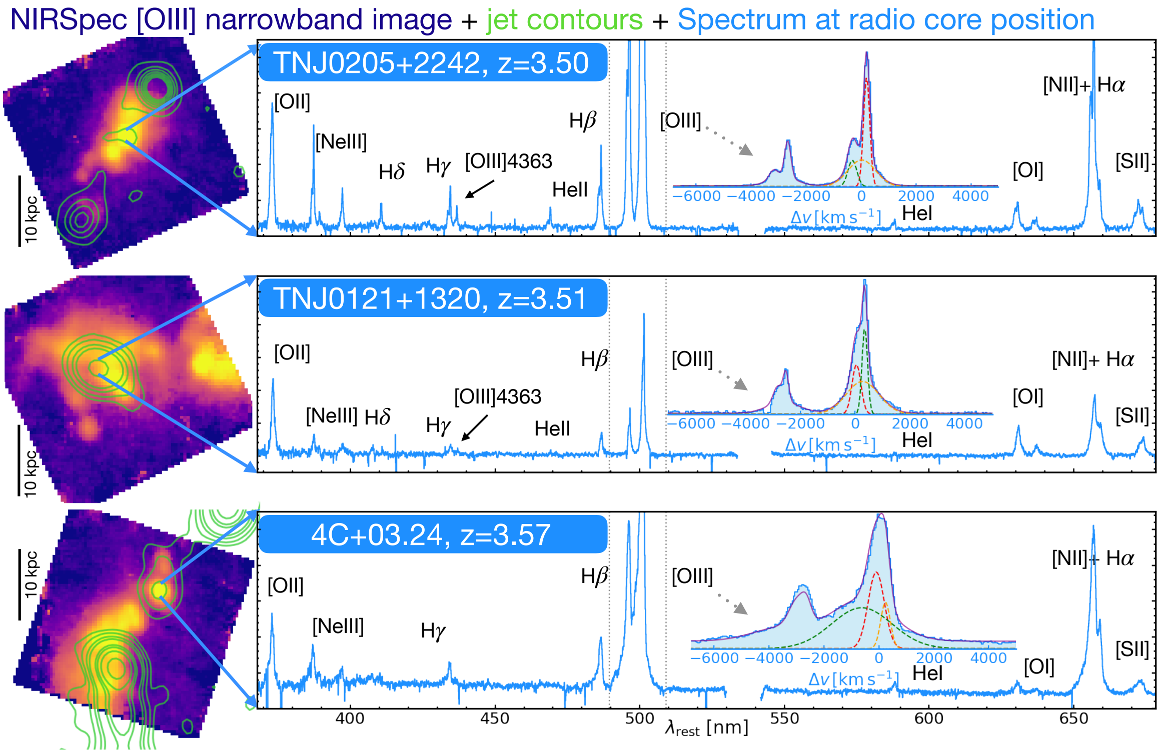

Figure 5.1. [O III]λ5007 narrow band images with full spectra extracted at the radio core from the NIRSpec IFU (aperture size $r = 0.15'' \sim 1.1$ kpc). We show the images and spectra of the three other targets proposed in JWST-GO-1970 in addition to 4C+19.71 (Chapter 4). The green contours are the radio emissions. The major lines are labeled on the spectra. The zoom-ins of the [O III]$\lambda\lambda$4959, 5007 doublet are shown as insets. The fits of the [O III]$\lambda\lambda$4959, 5007 are also presented where the dashed lines illustrate each of the kinetic components for [O III]λ5007.

Gas kinematics

We will investigate the detailed gas kinematics by exploiting the NIRSpec IFU + ALMA cubes. The results shown in Chapter 4 may represent a unique case where the absence of extreme gas motion on galactic-scale in one HzRG are seen, indicating an inefficient radiatively driven outflow. Here, I present a preliminary view of the gas kinematics probed by [O III]$\lambda\lambda$4959, 5007 at the position of the radio core for the other three HzRGs in Figure 5.1. Along with the data, I provide line fittings of the [O III]$\lambda\lambda4959, 5007$ (total fit in dark magenta, different components in dashed lines for 5007 Å line). The fits were conducted together with Hβ, where each of the kinematic component is fixed to the same line width and redshift. As indicated by the line fitting, we expect to see at least three groups of gas at the radio core for all AGN. Are there really outflowing ionized gas? If so, what are the driving mechanisms? In addition to this quick kinetic check, at this spatial resolution and sensitivity, we see more "irregularity" in the [O III]$\lambda\lambda4959, 5007$ morphology, which does not necessarily align with the jet axis. This raised more interesting questions of the role of jets and AGN radiation.

One logical explanation would certainly be the AGN-driven outflow (e.g., as in other quasars at Cosmic Noon, Vayner et al., 2024). The presence of both radio- and quasar-mode feedback further complicates the disentangling of various (outflow/recycling) components. We will work to understand the details of gas kinematics on ISM scales. Exploiting the NIRSpec IFU, we can trace and link different components through the field-of-view, allowing us to spectrally and spatially separate the different gas clouds. This analysis will be helpful in differentiating between the two driving mechanisms, for example. However, it is not trivial to systematically do this separation, as the potential velocity gradient of one group of cloud may be smeared out under the other co-spatial components. Data analysis tool like `q3dfit` will be suitable for this purpose (Rupke et al., 2023; Vayner et al., 2023).

Following the spatial decoupling, the grouped kinematic components can then be characterized. For example, we can estimate the outflow mass rates. Gas velocities will be combined to determine the momentum fluxes ($\mathrm{d}p/\mathrm{dt}=\dot{M}v$) and mechanical powers ($\mathrm{d}E/\mathrm{dt}=\frac{1}{2}\dot{M}v^2+\frac{3}{2}\dot{M}\sigma^2$). These kinetic parameters, $\dot{p}$ and $\dot{E}_{\mathrm{kin}}$, will be compared to the energy output through the jet kinetic energy and the radiative energy of the quasars. Then, we can quantify the efficiency of the various feedback (Costa et al., 2018). Moreover, since we are in the IFU mode, we can map the momentum and power fluxes. We can then compare these to the morphology of other observations (such as radio). These will help us to learn how the AGN feedback dissipates at different distance and position angles (if there is a preferential cone-like structure for the outflow), and therefore the impact of the central engine on the surrounding gas. While the energetic AGN-driven outflow is one contributing factor to the complex gas kinematics, we cannot rule out the possibilities of gas recycling/inflow and/or mergers given the dense living environments. Mapping the kinetic parameters will also serve as a starting point. For example, features like narrow line width and/or regular (i.e., rotation-like) pattern may be hints for motions other than AGN-driven outflows.

While the *JWST* traces the warm ionized gas, which may bias us towards the AGN, my ALMA data, with comparably high spatial resolution, will examine the kinematics of cold gas using [C II]. As shown in Figure 5.2, the kinematics differ significantly between [C II] and [O III]$\lambda5007$. The [C II] emission probes both the atomic and molecular hydrogen gas, enabling us to explore the dynamical states of the galactic regions unaffected by the AGN. For example, [C II] is potent for observing ordered rotating disk structures beyond Cosmic Noon (Lelli et al., 2021; Venemans et al., 2019, see also insets in Figure 5.1). How-

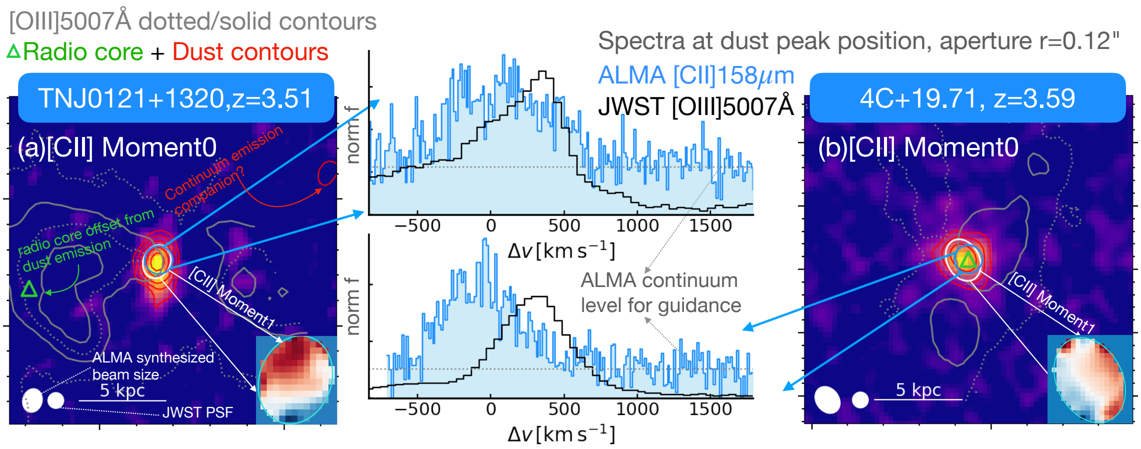

Figure 5.2. [C II] moment 0 maps and spectra of the two HzRGs with detections. The green triangle marks the radio core position. The red contours are the ALMA Band 8 dust continuum emissions underneath the [C II]. The spectra in the middle are extracted from a $r = 0.12''$ aperture at the peak position of the dust continuum. The overlaid [O III]$\lambda 5007$ are extracted at the same place in the same-size aperture from NIRSpec IFU cubes, respectively. The insets present the [C II] moment 1 maps which may indicate rotation.

ever, there is also evidence of observing [C II] in outflows as well (e.g., Herrera-Camus et al., 2022). The case may be more chaotic within the host galaxies of our powerful AGN. In Figure 5.2, we observe that the detected line width is very broad, which could indicate outflows and/or disturbed gas kinematics (especially TNJ0121+1320 in panel a). Given that [C II] can trace a variety of ISM phases, further analysis is needed. For instance, we will fit an ordered rotation model to the [C II] data (e.g., 3D-Barolo) and examine the residual after subtraction for any indication. Preliminarily speaking, two kinematic components could exist, possibly representing the approaching and receding sides of a rotation disk or merger. The kinetic broadening could then be the reason of the observed broad width (FWHM$\sim 600\,\mathrm{km\,s^{-1}}$). Assuming the rotating disk scenario, we can determine the $v_{\rm rot}/\sigma_v$ as an indication of the dynamical stability of rotation over turbulent motion. According to the AGN unification model, the HzRGs are observed from the edge-on direction. The potential disks will help constrain the viewing angle. The inner galactic structures influence the launch of AGN outflows, with the relative angle between the AGN ionization cone (jet axis) and the disk playing a key role (Dugan et al., 2017; Tanner & Weaver, 2022).

In summary, this joint *JWST*+ALMA analysis will characterize the complex ISM to understand feedback details. We will compare the velocity fields and projected morphologies of the multiphase gas with the radio jet morphologies, examining, for the first time, the interactions among jets, gaseous outflows, and the dynamical stability of the ISM at $z \sim 3.5$. This is valuable for providing observational evidence on AGN-gas interaction at Cosmic high-Noon.

Stellar population and AGN impact on SFR:

Falkendal et al. (2019) reported that the HzRG hosts predominantly reside below the star formation main sequence. Suzuki et al. (2022) found the evidence of quenching in a galaxy sample at $z \gtrsim 3.5$ with similar $M_\star \sim 10^{11}\,\mathrm{M}_\odot$. More recent evidence revealed a quiescent massive galaxy ($M_\star \approx 10^{10.9}\,\mathrm{M}_\odot$) at $z = 4.896$ with a short star formation burst of $340\,\mathrm{Myr}$ and rapid quenching (de Graaff et al., 2024). Their proposed quenching time scale (a few 100s of Myr) aligns with the jet age of HzRGs (a few 10s of Myr, Nesvadba et al., 2017b). This indicates that the jets may play a leading role in quenching. The constraint of the SED (Falkendal et al., 2019) was based on photometry data with low spatial resolution. Further questions arise: How is star formation being quenched by the jet-mode feedback? How does quasar-mode feedback contribute to quenching? With my datasets, we can now directly observe these relatively short events in the inner ISM at the onset of Cosmic Noon.

The targets in my sample span a large SFR range which represent different stage of the evolution. My *JWST* data covers the majority of the frequently studied optical nebular emission lines at low redshifts, from [O II]$\lambda\lambda 3726, 3729$ to [S II]$\lambda\lambda$6716, 6731, allowing us to probe the ionization states and gaseous enrichment of the ISM (Figure 5.1). For example, the detection of multiple oxygen lines (including [O III] at 4363 Å) will be essential to constrain the electron temperature (T_e) and metallicity (e.g., Sanders et al., 2024). However, the case may be more complicated for AGN (e.g., Binette et al., 2024). Two of the HzRGs have [O III]$\lambda 4363$ Å detected, namely TN J0205+2242 and TN J0121+1320 (Figure 5.1). More interesting than the 1D spectrum, this line is only spatially resolved for TN J0121+1320, which deserves further scrutiny. In general, the wealth of emission lines enables line ratio diagnostics (e.g., Chapter 4) which will be used to address different excitation mechanisms and separate regions without strong AGN domination (e.g., using on-going calibrations made use of *JWST* analyses at high-z Mazzolari et al., 2024). This will be combined with kinematic results to quantify the potential outflow rate of gaseous clouds powered by different mechanisms. Hence, we can visualize the outflow at different stages for this sample and profile the evolution of the material ejections.

Besides probing the gaseous ISM, my data can also explore the stellar components. Hα serves as one tracer of star formation (e.g., Vayner et al., 2023). The rest-frame optical continuum covered by the NIRSpec IFU is crucial for studying the evolved stellar population. We will constrain the star formation history together with previous data (Falkendal et al., 2019; Seymour et al., 2007), thus assessing the integrated impact of the AGN on the stars. However, the optical continuum may still be dominated by scattered AGN emissions (at least in 4C+19.71, Chapter 4, Wang et al., 2024). The reduction of the cubes needs refinement to provide an unbiased view, for example the leakage emission from the NIRSpec micro-shutter assembly is one of the leading sources of noise. Nevertheless, *JWST*/MIRI will be key in breaking this degeneracy in the SED of HzRGs (see next).

Moreover, the continuum observed in my ALMA data is assumed to be the emission of the dust heated by the young stellar population (Falkendal et al., 2019). We will use these to trace the spatial distribution of the newly formed stars. For instance, we will probe the peak mass density of the young stellar population with a spatial accuracy of $\sim 1\,$kpc. Additionally, this presumed-to-be stellar disk can further constrain the orientation (see above) and dynamics. Hence, we can quantify how the AGN feedback exerts on the young stars. An interesting example is TN J0121+1320 shown in Figure 5.2a. Although the astrometry of the NIRSpec IFU is associated with uncertainties of $\sim 0.3''$, the accuracy of the interferometry is much better (i.e, radio and ALMA). We observe an offset of $\sim 1''$ ($\sim 7.4\,$kpc) between the radio core (host galaxy?) and the [C II]+dust position. This may indicate the existence of companion or ignited star formation due to AGN feedback. Therefore, this analysis is key to gain a chronological view of the evolution of these powerful AGN.

HzRGs with other quasar and galaxy species through cosmic time

The HzRGs possess the highest radio power among AGN, and their host galaxies are located at the high $M_\star$ end (Miley & De Breuck, 2008). The output $E_{\rm kin}$ from these energetic ($P_{500\,\rm MHz}$>$10^{27}\,\rm W\,Hz^{-1}$) and extended (~10s to ~100s of kpc), though short-lived, jets is enormous (Nesvadba et al., 2008). How do these giant radio quasars fit into the picture of the AGN zoo near Cosmic Noon (e.g., radio-quiet quasars and highly obscured luminous quasars)? Is this radio-active phase unique given their proto-cluster-like living environment, or is it a midpoint in a broad evolutionary path? We will address these questions by linking the HzRGs with other powerful quasars covered with multiwavelength data (e.g., Vayner et al., 2024). The knowledge acquired from the aforementioned analyses, e.g., a deeper view of the gas kinematics, a detailed ISM modeling, and a spatial constraint on stellar populations, will be instrumental for this joint study.

For example, the project can focus on the spatial distribution of energy among various components of the host galaxies injected by the quasars. This will provide a comprehensive view of the “blow-out" mechanisms (wind and jet) in different quasar, potentially unveiling their evolutionary connections. In addition to studying diverse quasars, we will also compare our findings with other *JWST* projects investigating high-z massive galaxies to establish a sequential view of quenching. The NIRSpec IFU data taken with the program JWST-GO-3045 will be an excellent starting point which focus on the optical wavelength of star-forming main sequence galaxies. It will be intriguing to examine jointly how the disturbances from AGN compare to those from star formation. Additionally, it is also crucial to link the HzRGs with their low-z counterparts (e.g, Cygnus A, Ogle et al., 1997, see also Chapter 4), which was previously impossible due to observations limitations. Through this comparison, we can study structures below galactic scales and identify similarities and differences to better understand the environment and evolution of radio AGN. Overall, this work will be invaluable for picturing the cosmic quasar feedback on galaxy evolution, building upon the legacy of this thesis work.

5.2.3 The missing puzzle pieces

The spectroscopy observations in the rest frame near-infrared (mid-infrared in observed frame) are still missing for the $z \gtrsim 3$ HzRGs. Apart from the "traditional" feedback, which disturbs and ejects gas, jetted AGN are also known to be able to heat up the molecular gas ($T \sim 100 - 1000\,\mathrm{K}$) to states impossible for fueling star formation (Lanz et al., 2015; Ogle et al., 2010). Specifically, the rotational and/or rotation-vibration transitions of this warm or even hot H_2 can be directly observed in the near to mid-infrared. These transitions fall within the observing window of the "pride" instrument of *JWST*, i.e., MIRI. Particularly, the MIRI Medium Resolution Spectroscopy (MRS) will capture the 3D information of the emission from these direct yet poorly understood tracers. This is also an active topic in theoretical fields (e.g., Kristensen et al., 2023; Togi & Smith, 2016). We will proposal to fill in the last pieces of puzzle in gas phases (first) for this most-well observed HzRGs sample.

Together with the NIRSpec IFU and ALMA data, we can then finally complete the census and access the full impact of AGN on the gaseous medium. My current data cover the warm and cold ionized gas and the cold dust. Warm molecular gas has been found to constitute a large fraction of the total M_{H_2} in AGN host (e.g., Hernandez et al., 2023). Additionally, analysis of the cold H_2 in our sample of HzRGs revealed faint signals (Falkendal et al., 2021; Kolwa et al., 2023). Hence, the missing gas phase needed to establish a panoramic view is the warm H_2. Is the H_2 consumed, ejected, and/or heated up to a warmer state? With MIRI, we can capture the direct warm H_2 tracer, namely the ro-vibrational (ro-vib) emission lines, within the redshift range of our sample. As ro-vib H_2 indicates the extreme conditions of the ISM (e.g., $T > 1000\,\mathrm{K}$ and $n_{\mathrm{H}_2} \lesssim 10^4\,\mathrm{cm}^{-3}$, Kristensen et al., 2023), its detection will already provide some characterization of the additional channel of the quenching of star formation. The possibility of covering multiple H_2 lines allows for modeling of the gas temperature and density. We will then combine these physical parameters to the radio jets (whom were found to be related to warm H_2, e.g., Ogle et al., 2010). For example, we will map the warm H_2 and compare its structure with jet morphologies. It will help us to quantify the energy injection from the jets in addition to driving outflow (Nesvadba et al., 2017b). Without warm H_2, a significant aspect of AGN feedback may be overlooked. Thus, we will move a step forward in distinguishing the coupling between different feedback mechanisms in the radio-loud type-2 AGN using this previous inaccessible ISM tracer in HzRGs at $z > 3$.

In addition to the warm H_2, the simultaneously covered rest-frame near-IR continuum will be key to constraining the evolved stellar population and the AGN-heated hot dust (e.g., De Breuck et al., 2010). With this, we can determine the mass and spatial distribution of the main stellar component and have a much better constraint on the star formation history (through SED). We will also model the AGN dust torus with the MIRI MRS data (e.g., Drouart et al., 2012). This will offer an evolutionary view of the impact from powerful jetted AGN and refine the AGN model at Cosmic high-Noon.

5.2.4 Summary

Thus far, I have discussed several intriguing points for investigation based on the current datasets, as well as plans to fill in the missing data coverage. It is worth noting that we indeed intend to expand the *JWST* + ALMA + MUSE sample (Section 1.5.4). This expansion will offer a more comprehensive view of the feedback from jetted AGN, incorporating additional data on different gas/companion dynamics, ISM compositions, and stellar populations. Moreover, it is crucial to broaden our perspectives on galaxy evolution studies beyond the somewhat *narrow* focus of this thesis by integrating various species together at this transition epoch.

Bibliography

Abbott BP, Abbott R, Abbott TD, Abernathy MR, Acernese F, et al. 2016. Phys. Rev. Lett. 116(6):061102

Adam G, Rocca-Volmerange B, Gerard S, Ferruit P, Bacon R. 1997. A&A 326:501–504

Allington-Smith J, Murray G, Content R, Dodsworth G, Davies R, et al. 2002. PASP 114(798):892–912

Antonucci R. 1993. ARA&A 31:473–521

Antonucci RRJ. 2023. *Galaxies* 11(5):102

Argyriou I, Glasse A, Law DR, Labiano A, Álvarez-Márquez J, et al. 2023. A&A 675:A111

Arrigoni Battaia F, Hennawi JF, Prochaska JX, Oñorbe J, Farina EP, et al. 2019. MNRAS 482(3):3162–3205

Bacon R, Accardo M, Adjali L, Anwand H, Bauer S, et al. 2010. *The MUSE second-generation VLT instrument*. In *Ground-based and Airborne Instrumentation for Astronomy III*, eds. IS McLean, SK Ramsay, H Takami, vol. 7735. International Society for Optics and Photonics, SPIE

Bacon R, Adam G, Baranne A, Courtès G, Dubet D, et al. 1988. *The Integral Field Spectrograph TIGER*. In *Very Large Telescopes and their Instrumentation, Vol. 2*, vol. 30 of *European Southern Observatory Conference and Workshop Proceedings*

Bacon R, Copin Y, Monnet G, Miller BW, Allington-Smith JR, et al. 2001. MNRAS 326(1):23–35

Bacon R, Mary D, Garel T, Blaizot J, Maseda M, et al. 2021. A&A 647:A107

Bacon R, Monnet G. 2017. *Optical 3D-Spectroscopy for Astronomy*. Wiley

Bacon R, Vernet J, Borisova E, Bouché N, Brinchmann J, et al. 2014. *The Messenger* 157:13–16

Beckmann V, Shrader CR. 2012. *Active Galactic Nuclei*

Bégin T, Hlavacek-Larrondo J, Rhea CL, Gendron-Marsolais M, McNamara B, et al. 2023. MNRAS 519(1):767–777

Bertemes C, Wylezalek D, Albán M, Aravena M, Baker WM, et al. 2023. MNRAS 518(4):5500–5521

Binette L, Kurk JD, Villar-Martín M, Röttgering HJA. 2000. A&A 356:23–32

Binette L, Zovaro HRM, Villar Martín M, Dors OL, Krongold Y, et al. 2024. A&A 684:A53

Böker T, Arribas S, Lützgendorf N, Alves de Oliveira C, Beck TL, et al. 2022. A&A 661:A82

Bundy K, Bershady MA, Law DR, Yan R, Drory N, et al. 2015. ApJ 798(1):7

Cai Z, Cantalupo S, Prochaska JX, Arrigoni Battaia F, Burchett J, et al. 2019. ApJS 245(2):23

Cantalupo S, Arrigoni-Battaia F, Prochaska JX, Hennawi JF, Madau P. 2014. Nature 506(7486):63–66

Carilli CL, Walter F. 2013. ARA&A 51(1):105–161

Cavagnolo KW, McNamara BR, Nulsen PEJ, Carilli CL, Jones C, Bîrzan L. 2010. ApJ 720(2):1066–1072

Chambers KC, Miley GK, van Breugel W. 1987. Nature 329(6140):604–606

Chambers KC, Miley GK, van Breugel WJM. 1990. ApJ 363:21

Chapman SC, Sivanadam S, Andersen D, Bradley C, Correia C, et al. 2018. *The multi-object adaptive optics system for the GIRMOS spectrograph on Gemini-South*. In *Adaptive Optics Systems VI*, eds. LM Close, L Schreiber, D Schmidt, vol. 10703 of *Society of Photo-Optical Instrumentation Engineers (SPIE) Conference Series*

Chen HW, Zahedy FS, Boettcher E, Cooper TM, Johnson SD, et al. 2020. MNRAS 497(1):498–520

Colless M, Dalton G, Maddox S, Sutherland W, Norberg P, et al. 2001. MNRAS 328(4):1039–1063

Costa T, Arrigoni Battaia F, Farina EP, Keating LC, Rosdahl J, Kimm T. 2022. MNRAS 517(2):1767–1790

Costa T, Rosdahl J, Sijacki D, Haehnelt MG. 2018. MNRAS 473(3):4197–4219

Davies R, Absil O, Agapito G, Agudo Berbel A, Baruffolo A, et al. 2023. A&A 674:A207

De Breuck C, Brotherton MS, Tran HD, van Breugel W, Röttgering HJA. 1998. AJ 116(1):13–19

De Breuck C, Lundgren A, Emonts B, Kolwa S, Dannerbauer H, Lehnert M. 2022. A&A 658:L2

De Breuck C, Seymour N, Stern D, Willner SP, Eisenhardt PRM, et al. 2010. ApJ 725(1):36–62

De Breuck CAG. 2000. *Very distant radio galaxies: Search techniques and emission line properties*. Ph.D. thesis, University of Leiden, Netherlands

de Graaff A, Setton DJ, Brammer G, Cutler S, Suess KA, et al. 2024. *arXiv e-prints* :arXiv:2404.05683

Dekel A, Zolotov A, Tweed D, Cacciato M, Ceverino D, Primack JR. 2013. MNRAS 435(2):999–1019

den Brok JS, Cantalupo S, Mackenzie R, Marino RA, Pezzulli G, et al. 2020. MNRAS 495(2):1874–1887

Dijkstra M. 2014. *PASA* 31:e040

Dijkstra M. 2017. *arXiv e-prints* :arXiv:1704.03416

Drouart G. 2013. *Relation noyau actif et histoire de la formation d'étoiles dans les radio galaxies distantes.* Ph.D. thesis, Université Paris Sud - Paris XI, Français

Drouart G, De Breuck C, Vernet J, Laing RA, Seymour N, et al. 2012. A&A 548:A45

Drouart G, De Breuck C, Vernet J, Seymour N, Lehnert M, et al. 2014. A&A 566:A53

Dugan Z, Gaibler V, Silk J. 2017. ApJ 844(1):37

Duncan KJ, Windhorst RA, Koekemoer AM, Röttgering HJA, Cohen SH, et al. 2023. MNRAS 522(3):4548–4564

Eales SA. 1992. ApJ 397:49

Eisenhauer F, Abuter R, Bickert K, Biancat-Marchet F, Bonnet H, et al. 2003. *SINFONI - Integral field spectroscopy at 50 milli-arcsecond resolution with the ESO VLT*. In *Instrument Design and Performance for Optical/Infrared Ground-based Telescopes*, eds. M Iye, AFM Moorwood, vol. 4841 of *Society of Photo-Optical Instrumentation Engineers (SPIE) Conference Series*

Emonts BHC, Norris RP, Feain I, Mao MY, Ekers RD, et al. 2014. MNRAS 438(4):2898–2915

Event Horizon Telescope Collaboration, Akiyama K, Alberdi A, Alef W, Algaba JC, et al. 2022. ApJ 930(2):L12

Event Horizon Telescope Collaboration, Akiyama K, Alberdi A, Alef W, Asada K, et al. 2019. ApJ 875(1):L1

Fabian AC. 2012. ARA&A 50:455–489

Faisst AL, Fudamoto Y, Oesch PA, Scoville N, Riechers DA, et al. 2020a. MNRAS 498(3):4192–4204

Faisst AL, Schaerer D, Lemaux BC, Oesch PA, Fudamoto Y, et al. 2020b. ApJS 247(2):61

Falkendal T, De Breuck C, Lehnert MD, Drouart G, Vernet J, et al. 2019. A&A 621:A27

Falkendal T, Lehnert MD, Vernet J, De Breuck C, Wang W. 2021. A&A 645:A120

Falkendal TM. 2018. *Constraining star formation rates and AGN feedback in high-z radio galaxies.* Ph.D. thesis, Sorbonne Université, France

Fanaroff BL, Riley JM. 1974. MNRAS 167:31P–36P

Farina EP, Arrigoni-Battaia F, Costa T, Walter F, Hennawi JF, et al. 2019. ApJ 887(2):196

Fosbury RAE, Vernet J, Villar-Martín M, Cohen MH, Ogle PM, et al. 1999. *Optical continuum structure of <ASTROBJ>Cygnus A</ASTROBJ>*. In *The Most Distant Radio Galaxies*, eds. HJA Röttgering, PN Best, MD Lehnert

Galametz A. 2010. *The Environments of AGN out to z=2*. Ph.D. thesis, Universite de Strasbourg Louis Pasteur, France

Gitti M, Brighenti F, McNamara BR. 2012. *Advances in Astronomy* 2012:950641

Greene JE, Labbe I, Goulding AD, Furtak LJ, Chemerynska I, et al. 2024. ApJ 964(1):39

Gullberg B. 2016. *Exploring star formation in high-z galaxies using atomic and molecular emission lines*. Ph.D. thesis, Ludwig-Maximilians University of Munich, Germany

Gullberg B, De Breuck C, Lehnert MD, Vernet J, Bacon R, et al. 2016. A&A 586:A124

Harrison CM. 2017. *Nature Astronomy* 1:0165

Harrison CM, Alexander DM, Mullaney JR, Swinbank AM. 2014. MNRAS 441(4):3306–3347

Harrison CM, Costa T, Tadhunter CN, Flütsch A, Kakkad D, et al. 2018. *Nature Astronomy* 2:198–205

Harrison CM, Ramos Almeida C. 2024. *arXiv e-prints* :arXiv:2404.08050

Heckman TM, Best PN. 2014. ARA&A 52:589–660

Hernandez S, Jones L, Smith LJ, Togi A, Aloisi A, et al. 2023. ApJ 948(2):124

Herrera-Camus R, Förster Schreiber N, Genzel R, Tacconi L, Bolatto A, et al. 2021. A&A 649:A31

Herrera-Camus R, Förster Schreiber NM, Price SH, Übler H, Bolatto AD, et al. 2022. A&A 665:L8

Ho LC. 2008. ARA&A 46:475–539

Hubble EP. 1925. *Popular Astronomy* 33:252–255

Hubble EP. 1929. ApJ 69:103–158

Humphrey A, Villar-Martín M, Fosbury R, Binette L, Vernet J, et al. 2007. MNRAS 375(2):705–714

Humphrey A, Villar-Martín M, Fosbury R, Vernet J, di Serego Alighieri S. 2006. MNRAS 369(3):1103–1114

Humphrey A, Villar-Martín M, Sánchez SF, di Serego Alighieri S, De Breuck C, et al. 2008a. MNRAS 390(4):1505–1516

Humphrey A, Villar-Martín M, Vernet J, Fosbury R, di Serego Alighieri S, Binette L. 2008b. MNRAS 383(1):11–40

Humphrey AJ. 2004. *Quantitative spectroscopy of the ultraviolet and optical emission lines from high redshift radio galaxies*. Ph.D. thesis, University of Hertfordshire, UK

Jakobsen P, Ferruit P, Alves de Oliveira C, Arribas S, Bagnasco G, et al. 2022. A&A 661:A80

Jarvis MJ, Rawlings S, Eales S, Blundell KM, Bunker AJ, et al. 2001. MNRAS 326(4):1585–1600

Jarvis MJ, Wilman RJ, Röttgering HJA, Binette L. 2003. MNRAS 338(1):263–272

Jones GC, Übler H, Perna M, Arribas S, Bunker AJ, et al. 2024. A&A 682:A122

Kakkad D, Bertola E, Carniani S, Cicone C, Circosta C, et al. 2023. A systematic search for warm molecular gas in AGN and star forming galaxies at z=2 with MIRI. JWST Proposal. Cycle 2, ID. #3257

Kewley LJ, Groves B, Kauffmann G, Heckman T. 2006. MNRAS 372(3):961–976

Kolwa S. 2019. *The kinematic nature of baryons in the multi-phase circumgalactic media of high-redshift radio galaxies*. Ph.D. thesis, Ludwig-Maximilians University of Munich, Germany

Kolwa S, De Breuck C, Vernet J, Wylezalek D, Wang W, et al. 2023. MNRAS 525(4):5831–5845

Kolwa S, Vernet J, De Breuck C, Villar-Martín M, Humphrey A, et al. 2019. A&A 625:A102

Kormendy J, Ho LC. 2013. ARA&A 51(1):511–653

Kristensen LE, Godard B, Guillard P, Gusdorf A, Pineau des Forêts G. 2023. A&A 675:A86

Kukreti P, Morganti R, Tadhunter C, Santoro F. 2023. A&A 674:A198

Kurk JD. 2003. *The cluster environment and gaseous halos of distant radio galaxies*. Ph.D. thesis, University of Leiden, Netherlands

Lanz L, Ogle PM, Evans D, Appleton PN, Guillard P, Emonts B. 2015. ApJ 801(1):17

Lelli F, Di Teodoro EM, Fraternali F, Man AWS, Zhang ZY, et al. 2021. *Science* 371(6530):713–716

Lequeux J. 2005. *The Interstellar Medium*

Madau P, Dickinson M. 2014. ARA&A 52:415–486

Mainieri V, Bertola E, Bianchin M, Bischetti M, Brusa M, et al. 2023. JWST/MIRI unravels the impact of AGN feedback on star-formation at cosmic noon. JWST Proposal. Cycle 2, ID. #3158

Marshall MA, Perna M, Willott CJ, Maiolino R, Scholtz J, et al. 2023. A&A 678:A191

Mazzolari G, Übler H, Maiolino R, Ji X, Nakajima K, et al. 2024. *arXiv e-prints* :arXiv:2404.10811

McCarthy PJ. 1988. *Extended Optical Emission in 3CR Radio Galaxies.* Ph.D. thesis, University of California, Berkeley

McCarthy PJ. 1993. ARA&A 31:639–688

McCarthy PJ, van Breugel W, Spinrad H, Djorgovski S. 1987. ApJ 321:L29

McDermid RM, Emsellem E, Shapiro KL, Bacon R, Bureau M, et al. 2006. MNRAS 373(3):906–958

McGregor PJ, Hart J, Conroy PG, Pfitzner ML, Bloxham GJ, et al. 2003. *Gemini near-infrared integral field spectrograph (NIFS)*. In *Instrument Design and Performance for Optical/Infrared Ground-based Telescopes*, eds. M Iye, AFM Moorwood, vol. 4841 of *Society of Photo-Optical Instrumentation Engineers (SPIE) Conference Series*

Miley G. 1980. ARA&A 18:165–218

Miley G, De Breuck C. 2008. A&A Rev. 15(2):67–144

Miley GK, Overzier RA, Zirm AW, Ford HC, Kurk J, et al. 2006. ApJ 650(1):L29–L32

Morais SG, Humphrey A, Villar-Martín M, Lagos P, Moyano M, et al. 2017. MNRAS 465(3):2698–2713

Morganti R, Oosterloo T, Tadhunter C, Bernhard EP, Raymond Oonk JB. 2021. A&A 656:A55

Morrissey P, Matuszewski M, Martin DC, Neill JD, Epps H, et al. 2018. ApJ 864(1):93

Moster BP, Naab T, White SDM. 2013. MNRAS 428(4):3121–3138

Mukherjee D, Bicknell GV, Sutherland R, Wagner A. 2016. MNRAS 461(1):967–983

Nesvadba NPH, De Breuck C, Lehnert MD, Best PN, Collet C. 2017a. A&A 599:A123

Nesvadba NPH, Drouart G, De Breuck C, Best P, Seymour N, Vernet J. 2017b. A&A 600:A121

Nesvadba NPH, Lehnert MD, De Breuck C, Gilbert A, van Breugel W. 2007. A&A 475(1):145–153

Nesvadba NPH, Lehnert MD, De Breuck C, Gilbert AM, van Breugel W. 2008. A&A 491(2):407–424

Nesvadba NPH, Lehnert MD, Eisenhauer F, Gilbert A, Tecza M, Abuter R. 2006. ApJ 650(2):693–705

Netzer H. 2013. *The Physics and Evolution of Active Galactic Nuclei*

Noirot G. 2017. *The CARLA-Hubble survey : spectroscopic confirmation and galaxy stellar activity of rich structures at 1.4 < z < 2.8*. Ph.D. thesis, Université Paris, France

Noirot G, Stern D, Mei S, Wylezalek D, Cooke EA, et al. 2018. ApJ 859(1):38

Noirot G, Vernet J, De Breuck C, Wylezalek D, Galametz A, et al. 2016. ApJ 830(2):90

Ogle P, Boulanger F, Guillard P, Evans DA, Antonucci R, et al. 2010. ApJ 724(2):1193–1217

Ogle PM, Cohen MH, Miller JS, Tran HD, Fosbury RAE, Goodrich RW. 1997. ApJ 482(1):L37–L40

Osterbrock DE, Ferland GJ. 2006. *Astrophysics of gaseous nebulae and active galactic nuclei*

Ouchi M, Ono Y, Shibuya T. 2020. ARA&A 58:617–659

Overzier RA. 2006. *Emergence of cosmic structures around distant radio galaxies and quasars*. Ph.D. thesis, Leiden Observatory

Papadopoulos PP, Thi WF, Viti S. 2004. MNRAS 351(1):147–160

Parijskij YN, Thomasson P, Kopylov AI, Zhelenkova OP, Muxlow TWB, et al. 2014. MNRAS 439(3):2314–2322

Pentericci L, McCarthy PJ, Röttgering HJA, Miley GK, van Breugel WJM, Fosbury R. 2001. ApJS 135(1):63–85

Pentericci L, Röttgering HJA, Miley GK, McCarthy P, Spinrad H, et al. 1999. A&A 341:329–347

Perna M, Arribas S, Marshall M, D'Eugenio F, Übler H, et al. 2023. A&A 679:A89

Péroux C, Howk JC. 2020. ARA&A 58:363–406

Petitjean P, Pécontal E, Valls-Gabaud D, Charlot S. 1996. Nature 380(6573):411–413

Riechers DA, Pavesi R, Sharon CE, Hodge JA, Decarli R, et al. 2019. ApJ 872(1):7

Röttgering HJA. 1993. *Ultra-steep spectrum radio sources: tracers of distant galaxies*. Ph.D. thesis, -

Rottgering HJA, Hunstead RW, Miley GK, van Ojik R, Wieringa MH. 1995. MNRAS 277:389–396

Roy N, Heckman T, Overzier R, Saxena A, Duncan K, et al. 2024. *arXiv e-prints* :arXiv:2401.11612

Rupke D, Wylezalek D, Zakamska N, Veilleux S, Vayner A, et al. 2023. q3dfit: PSF decomposition and spectral analysis for JWST-IFU spectroscopy. Astrophysics Source Code Library, record ascl:2310.004

Sanders RL, Shapley AE, Topping MW, Reddy NA, Brammer GB. 2024. ApJ 962(1):24

Saxena A, Overzier RA, Villar-Martín M, Heckman T, Roy N, et al. 2024. *arXiv e-prints* :arXiv:2401.12199

Seymour N, Stern D, De Breuck C, Vernet J, Rettura A, et al. 2007. ApJS 171(2):353–375

Silk J, Rees MJ. 1998. A&A 331:L1–L4

Silva M, Humphrey A, Lagos P, Guimarães R, Scott T, et al. 2018a. MNRAS 481(1):1401–1415

Silva M, Humphrey A, Lagos P, Villar-Martín M, Morais SG, et al. 2018b. MNRAS 474(3):3649–3672

Smail I, Blundell KM, Lehmer BD, Alexander DM. 2012. ApJ 760(2):132

Somerville RS, Hopkins PF, Cox TJ, Robertson BE, Hernquist L. 2008. MNRAS 391(2):481–506

Sugai H, Hattori T, Kawai A, Ozaki S, Kosugi G, et al. 2004. *Test observations of the Kyoto Tridimensional Spectrograph II at the University of Hawaii 88-in and Subaru Telescopes*. In *Ground-based Instrumentation for Astronomy*, eds. AFM Moorwood, M Iye, vol. 5492 of *Society of Photo-Optical Instrumentation Engineers (SPIE) Conference Series*

Suzuki TL, Glazebrook K, Schreiber C, Kodama T, Kacprzak GG, et al. 2022. ApJ 936(1):61

Swinbank AM, Vernet JDR, Smail I, De Breuck C, Bacon R, et al. 2015. MNRAS 449(2):1298–1308

Tanner R, Weaver KA. 2022. AJ 163(3):134

Thatte N, Tecza M, Schnetler H, Neichel B, Melotte D, et al. 2021. *The Messenger* 182:7–12

Togi A, Smith JDT. 2016. ApJ 830(1):18

Tsai CW, Eisenhardt PRM, Wu J, Stern D, Assef RJ, et al. 2015. ApJ 805(2):90

Tumlinson J, Peeples MS, Werk JK. 2017. ARA&A 55(1):389–432

Übler H, Maiolino R, Curtis-Lake E, Pérez-González PG, Curti M, et al. 2023. A&A 677:A145

Umehata H, Fumagalli M, Smail I, Matsuda Y, Swinbank AM, et al. 2019. *Science* 366(6461):97–100

van Ojik R. 1995. *Gas in distant galaxies: probing the early Universe*. Ph.D. thesis, University of Leiden, Netherlands

van Ojik R, Roettgering HJA, Carilli CL, Miley GK, Bremer MN, Macchetto F. 1996. A&A 313:25–44

van Ojik R, Roettgering HJA, Miley GK, Hunstead RW. 1997. A&A 317:358–384

Vayner A, Wright SA, Murray N, Armus L, Boehle A, et al. 2021a. ApJ 919(2):122

Vayner A, Zakamska NL, Ishikawa Y, Sankar S, Wylezalek D, et al. 2023. ApJ 955(2):92

Vayner A, Zakamska NL, Ishikawa Y, Sankar S, Wylezalek D, et al. 2024. ApJ 960(2):126

Vayner A, Zakamska NL, Riffel RA, Alexandroff R, Cosens M, et al. 2021b. MNRAS 504(3):4445–4459

Veilleux S, Cecil G, Bland-Hawthorn J. 2005. ARA&A 43(1):769–826

Venemans BP. 2005. *Protoclusters associated with distant radio galaxies*. Ph.D. thesis, Leiden Observatory

Venemans BP, Neeleman M, Walter F, Novak M, Decarli R, et al. 2019. ApJ 874(2):L30

Venemans BP, Röttgering HJA, Miley GK, van Breugel WJM, de Breuck C, et al. 2007. A&A 461(3):823–845

Verhamme A, Schaerer D, Maselli A. 2006. A&A 460(2):397–413

Vernet J. 2001. *Etude spectropolarimétrique des premières phases de l'évolution des galaxies les plus massivesEtude spectropolarimétrique des premières phases de l'évolution des galaxies les plus massivesSpectropolarimetric study of the early evolutionary phases of the most massive galaxies;*. Ph.D. thesis, Universite de Paris Diderot (Paris VII), France

Vernet J, Fosbury RAE, Villar-Martín M, Cohen MH, Cimatti A, et al. 2001. A&A 366:7–25

Vernet J, Lehnert MD, De Breuck C, Villar-Martín M, Wylezalek D, et al. 2017. A&A 602:L6

Villar-Martín M, Alonso-Herrero A, di Serego Alighieri S, Vernet J. 2000. A&AS 147:291–297

Villar-Martin M, Binette L, Fosbury RAE. 1996. A&A 312:751–760

Villar-Martín M, Sánchez SF, De Breuck C, Peletier R, Vernet J, et al. 2006. MNRAS 366(1):L1–L5

Villar-Martin M, Tadhunter C, Clark N. 1997. A&A 323:21–30

Villar-Martín M, Tadhunter C, Morganti R, Axon D, Koekemoer A. 1999. MNRAS 307(1):24–40

Villar-Martin M, Tadhunter C, Morganti R, Clark N, Killeen N, Axon D. 1998. A&A 332:479–492

Villar-Martín M, Vernet J, di Serego Alighieri S, Fosbury R, Humphrey A, Pentericci L. 2003. MNRAS 346(1):273–294

Wagner AY, Bicknell GV, Umemura M. 2012. ApJ 757(2):136

Walter F, Decarli R, Sargent M, Carilli C, Dickinson M, et al. 2014. ApJ 782(2):79

Wang W, De Breuck CA, Lehnert MD, Nesvadba N, Rupke D, et al. 2021a. Zooming into the monster's mouth: tracing feedback from their hosts to circumgalactic medium in z=3.5 radio-loud AGN. JWST Proposal. Cycle 1, ID. #1970

Wang W, Wylezalek D, De Breuck C, Vernet J, Humphrey A, et al. 2021b. A&A 654:A88

Wang W, Wylezalek D, De Breuck C, Vernet J, Rupke DSN, et al. 2024. A&A 683:A169

Wang W, Wylezalek D, Vernet J, De Breuck C, Gullberg B, et al. 2023. A&A 680:A70

Wells M, Pel JW, Glasse A, Wright GS, Aitink-Kroes G, et al. 2015. PASP 127(953):646

Wilman RJ, Jarvis MJ, Röttgering HJA, Binette L. 2004. MNRAS 351(3):1109–1119

Wisotzki L, Bacon R, Brinchmann J, Cantalupo S, Richter P, et al. 2018. Nature 562(7726):229–232

Wylezalek D. 2014. *The large-scale environments of radio-loud active galactic nuclei and their evolution across cosmic time*. Ph.D. thesis, Ludwig-Maximilians University of Munich, Germany

Wylezalek D, Cicone C, Belfiore F, Bertemes C, Cazzoli S, et al. 2022a. MNRAS 510(3):3119–3131

Wylezalek D, Galametz A, Stern D, Vernet J, De Breuck C, et al. 2013. ApJ 769(1):79

Wylezalek D, Vayner A, Rupke DSN, Zakamska NL, Veilleux S, et al. 2022b. ApJ 940(1):L7

Wylezalek D, Vernet J, De Breuck C, Stern D, Brodwin M, et al. 2014. ApJ 786(1):17

Zhang S, Cai Z, Xu D, Afruni A, Wu Y, et al. 2023. ApJ 952(2):124

Acknowledgements

First and foremost, I deeply thank **Dominika Wylezalek**, my amazing PhD supervisor. None of these achievements would have been possible without your guidance, assistance, support and encouragement. The official date marking the very first beginning of my scientific journey with Dominika is 10th April 2018 (See Screenshot). Remarkably, this predates my PhD, underscoring how fortunate I am to have met you so early on. Thank you for agreeing to take me on board initially with the MASCOT data during my Master study (Wylezalek et al., 2022a). I vaguely recalled that my email signature was still in Chinese characters at that time. Luckily, you did not treat that as spam. You have always believed in me, even when I seriously doubted myself most of the time. The most shining example would surely be the approval of JWST-GO-1970, which (may significantly) alter my career path. Of course, I understand that you cannot and should not always provide detailed guidance to me. Thank you also for “pushing” me into the situation for independence which began around December 2022. Additionally, I would like to extend my gratitude to Paul and Arthur, who should be listed as co-authors of Wang et al. (2021b) and Wang et al. (2023), respectively.

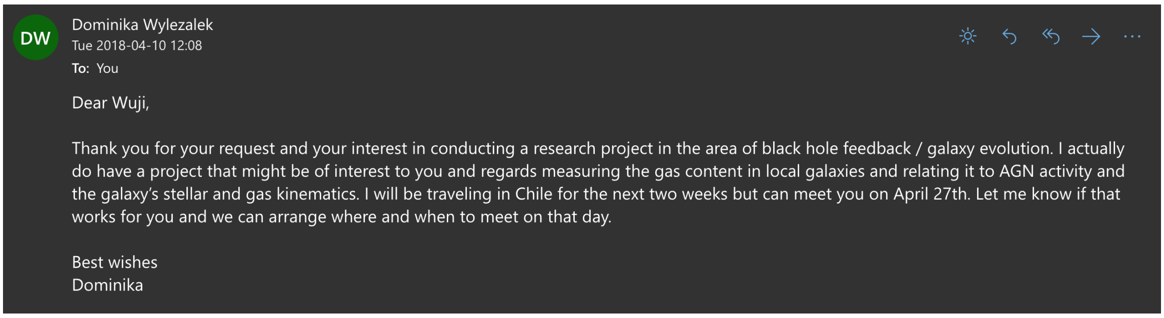

DW
Dominika Wylezalek
Tue 2018-04-10 12:08
To: You

Dear Wuji,

Thank you for your request and your interest in conducting a research project in the area of black hole feedback / galaxy evolution. I actually do have a project that might be of interest to you and regards measuring the gas content in local galaxies and relating it to AGN activity and the galaxy’s stellar and gas kinematics. I will be traveling in Chile for the next two weeks but can meet you on April 27th. Let me know if that works for you and we can arrange where and when to meet on that day.

Best wishes
Dominika

Screenshot of the first email reply from Dominika.

I do not know if anyone else has been fortunate enough to have such a “luxury" PhD advising team as I have had. I want to express my heartfelt gratitude to **Carlos De Breuck** & **Joël Vernet** (alphabetical order), my equally amazing

PhD co-supervisors [1] whom I also met with early on. Your invaluable assistance has contributed significantly to every single aspect of my PhD and even beyond. It is very lucky for me that (at least one of) you will always be there whenever I need help. You not only showed me how to conduct scientific analysis but also how to be a qualified scientific researcher. For example, I enjoyed a lot with your “obsession" about details, though sometimes it distracted us. Additionally, I will also keep in mind the honesty, open-mindedness, and scientific instincts you imparted to me. Thank you sincerely for making the effort to visit Heidelberg all the way from Munich several times to speed up our progress. Beyond our scientific discussions, there are countless fun memories from over the years. If I may share one (apologies to Dominika), the best beer I have ever tasted was the one Carlos brought from Belgium.

I would also like to thank all of my collaborators for your contributions to our publications and proposals. A special thanks to **Matt Lehnert**, who contributed to every one of those. Despite not having had the opportunity to meet in-person yet, I have always learned something from our email communications (and even picked up a few fancy English words along the way). I also want to extend my appreciation to **Sthabile** for providing crucial practical assistance in the early stages of my career, laying a solid foundation for my research. Many thanks to **Montse Villar-Martín** and **Andy Humphrey** for your help in navigating the complexities of Lyα. I am grateful to **Nadia Zakamska** and **Dan Stern** for engaging science discussions and your amazing host during my visits to Johns Hopkins and Caltech. Big thanks to **Dave**, **Andrey**, **Nicole**, **Bitten**, **Mark**, **Guillaume**, **Fabrizio**, **Gaël**, **Nick**, and **Patricio** for your valuable contributions.

I am incredibly grateful to our Galaxy Evolution & AGN (GALENA) group at ARI. A special thanks to **Caroline**, my officemate, who provided invaluable assistance ranging from data analysis to English writing, and from career advice to simple chats about anything. I am also thankful to **Marco** for sharing advanced coding ideas. I am thankful to **Pranav** for discussions about the true *radio* aspect of radio AGN, and for your assisting with re-reducing the $\sim$30-year-old data. Additionally, my thanks go out to everyone in our group for sharing their expertise and for the enjoyable conversations. Although the beginning was challenging during the pandemic, we gradually resumed several interesting social activities over the past year.

I also thank **Eva Grebel** for providing useful advice during my thesis committee meetings throughout the years.

Furthermore, I would like to express my thanks to all the friends and colleagues I met in Heidelberg, Garching, and at various conferences and workshops. Your insights and support have greatly enriched my astronomical journey.

I am grateful to IMPRS-HD, particularly to our coordinator **Christian Fendt** and assistant **Nina Zhao**, for your support, especially in facilitating my visit to the United States. This visit may indeed play a significant role in securing my next position.

[1] Of course, you always called yourselves my “academic grandfathers".

I would also like to thank my parents for their support throughout all the years.

Last but not least, I want to express my deep gratitude to my wife, **Qing Xia**, for your consistent support over the years. You convinced me to stay on the astronomical track, and this PhD thesis stands as proof and a rewarding achievement. Most importantly, thank you for taking care of all the vacation travel plans:)